Computational and rheological studies for coating flows.

Echendu, Shirley Ogechukwu Somtochukwu

Computational and Rheological Studies for Coating Flows

By

Shirley Ogechukwu Somtochukwu Echendu

B.Eng. (Hons)

Swansea University
Prifysgol Abertawe

Thesis submitted to Swansea University in candidature for the degree of

PHILOSOPHIAE DOCTOR

Institute of Non-Newtonian Fluid Mechanics

College of Engineering

Swansea University

June 2013

DEDICATION

To God;

most gracious and merciful

To my mother;

Mrs Florence Ifeoma Echendu

And my son;

Odinakachukwu Jay Kenechukwu (O'Jay) Echendu

Declaration

I declare that this work has not previously been accepted in substance for any degree, and is not being concurrently submitted in candidature for any degree.

.....

(Signed by Candidate)

Statement 1

This thesis is the result of my own investigations, except where otherwise stated. Other sources are acknowledged by footnotes giving explicit references. A bibliography is appended.

.....

(Signed by Candidate)

Statement 2

I hereby give consent to my thesis, if accepted, to become available for photocopying and for inter-library loan, and for the title and summary to be made available to outside organisations.

.....

(Signed by Candidate)

Acknowledgements

I am sincerely and heartily thankful to my supervisor, Professor M.F. Webster, whose encouragement, supervision and support from the preliminary to the concluding level enabled me to develop an understanding of the subject. Over the course of the study, his careful criticism, comments and ideas, I owe a deepest gratitude to, as they have developed me personally and professionally and have made it possible to complete this study and write this dissertation.

It is a great pleasure to specially thank Dr. H.R. Tamaddon-Jahromi, for his organized and strategic support, helpful discussions and friendly suggestions which have helped me write my dissertation successfully.

I acknowledge Dr. F. Belblidia and Dr. H. Matallah, for their helpful support during the early stage of the research.

I owe sincere and earnest thankfulness to Dr. Samuel Larkai for his encouragement, support and persuasion throughout my Career as an Engineer.

I appreciate the support and assistant provided by TATA Steel R & D Department, especially, Dr. Rob Ireson, Dr. Joel Rousseau, and Dr. Sreedhara Sarma.

I am truly indebted and thankful to my mum (Mrs. Florence Echendu) for her continuous encouragement, intense moral support and patience throughout the course.

I am obliged to my son (Master Odinaka Jay Echendu) for his overwhelming love and understanding shown to me over the times I spent during the research.

I offer my regards and blessings to all of those who supported me in any respect during the completion of the project.

And finally, I acknowledge the financial support provided by the Engineering and Physical Sciences Research Council, Swansea University Bridging the Gap and TATA Steel, United Kingdom.

Shirley Ogechukwu Somtochukwu Echendu

June 2013

Abstract

Coating flows can be defined as a laminar free surface flows, whereby a liquid layer is applied onto a solid substrate. A typical industrial application consists of co-rotating cylindrical rollers, which are used to apply a liquid coating (paint) onto a moving substrate, and depending on the direction of the rollers, can be configured in either forward or reverse mode. These types of coating solution flows are industrially important applications, and convey viscoelastic aspects due to their polymeric content and unsteady polymeric behaviour. The process often possesses localized regions of high shear and extension rates (narrow nip and wetting-line zones), which may cause instabilities on the coated substrate (ribbing, leveling, striping). These non-Newtonian and viscoelastic studies for industrial reverse roll coating focus on the use of computational techniques to model these types of coating flows, alongside the analysis of the fluid flow behaviour and under varied rheological properties. Two flow problem configurations have been considered, a model benchmark problem of mixed combined-separating flow, and the industrial application of reverse roll coating flow. Predictions and corresponding solutions are reported for viscous, inelastic and complex viscoelastic fluid properties. The numerical formulation adopts a Taylor-Galerkin pressure-correction (TGPC) scheme, using a finite element method for viscous, inelastic flows and a hybrid finite element/finite volume method for their viscoelastic counterparts.

The research plan is centered around computational fluid dynamics and rheological studies, with the main target focused on industrial roll-coating operations. From simple theory, Newtonian and non-Newtonian coating flows possess specific, yet disparate characteristics. This may lead to distinct and significant differences in their detailed flow behaviour, and in the stressing levels generated, dependent upon the nature of the flow configuration. The study is segmented into several stages: initially, solution was sought for a benchmark flow problem, where a semi-implicit time stepping finite element procedure was employed to simulate a mixed combined-separating flow. Here, both viscous and viscoplastic material approximations have been introduced. Secondly, the industrial application of reverse roll coating flow was addressed for viscous inelastic coating fluids. This incorporated scenarios of inclusion and not of a dynamic wetting line and consideration of the effects of a rubber elastomer-cover upon the applicator roll. Thirdly, viscoelastic paint coatings were addressed for the industrial reverse roll coating flow. Here, a hybrid finite element/finite volume sub-cell method was utilized, and with inclusion of a dynamic wetting line. Of the various viscoelastic material models available, use has been made of the Phan-Thien Tanner (PTT) network class of models, in both linear and exponential variety, and of the FENE class of models, with FENE-CR and FENE-P versions. This has offered a richness in capacity over variation of rheological properties.

The choice of computational methods has been justified and the TGPC algorithm was deemed suitable for problem solution. The methodology tested on combined-separating flow provided high-quality numerical results, which compare favorably against experiments, literature and theory. When applied to the reverse roll coating problem, the TGPC algorithm has been coupled to a time-dependent free-surface update procedure, to determine the dynamic movement of the meniscus and the wetting line. Around the nip-region, the flow problem manifests strong flow features, which have been investigated for a range of rheological properties of varying shear and

extensional response. The direct impact these have on localized peak nip-pressures and distributional lift levels has been observed, where several relief mechanisms have been successfully identified (important to optimize process control). The influence of solvent fraction, extensional viscosity and increasing elasticity, up to critical stress states have been analysed in considerable detail.

In summary, the success of this work indicates optimal flow process settings and preferential rheological coating properties to employ, with respect to this industrial coating process. As such, it lays the foundation and guide towards achieving a stable and consistent coating application – specifically, as high-speed high-gain production is of current demanded.

Shirley Ogechukwu Somtochukwu Echendu

June 2013

Contents

Chapter 1

Introduction

This chapter is concerned with the general introduction to this body of research. Here, effective implementation, knowledge and understanding are all prerequisites. This is done through an in depth literature review. The theory and hypothesis are briefly explained, followed by the problem descriptions including the governing equations and boundary conditions adopted. The numerical techniques and algorithms are appraised and justified, and the computational stages are outlined giving the various means by which the numerical results has been analysed.

1.1 Introduction

In recent years, Computational methods have evolved as the most convenient and economical technique for solving industrial problems without building or commissioning the plant or application itself. Due to mathematical complexity of rheological problems, computation provides the effective solution for many practical engineering problems. Known as computational fluid dynamics, here, numerical methods and their associated algorithms are used to solve fluid flow problems. The main branch developed to implement these has been the relatively new field of computational rheology, where, given the mass and momentum balances, with a choice of constitutive equation and appropriate boundary conditions, the solution has been obtained for the non-linear system of partial differential equations governing the complex flows (Crotchet et al. 1984 and Zienkiewicz and Taylor 1989).

In the field of Rheology, this is defined as the study of deformation and flow of materials. The fundamental theoretical concepts are the kinematics which deals with the geometrical deformation and flow, conservation laws based on the forces and stresses and constitutive relations specific to elasticity. The constitutive equations link the dynamics and forces to describe the flow process, and these are then applied to solve engineering problems arising in industrial polymer processing, coating applications and food technologies. Fluids can be classed as viscous, inelastic, elastic, viscoelastic, plastic, viscoplastic or viscoelastoplastic depending on their individual characteristics (Bird et al. 1987). Viscosity is a measure of a fluids resistance to flow based on the material response. According to Newton's postulate, under isothermal conditions, for simple steady shear flows, shear stress is directly proportional to shear rate. If a fluid does not satisfy this simple linear relationship, then it may be termed as 'non-Newtonian'. These types of fluids may have varying viscosity with shear-rate and non-varnishing normal stress differences.

Coating flows can be defined as laminar free surface flows, whereby a liquid layer is applied onto a solid substrate. A typical industrial application consists of co-rotating cylindrical rollers which are used to apply liquid onto a moving substrate, and depending on the direction of movement of the rollers, it can be termed as forward or reverse mode. These types of flows are important features in industrial coating applications, due to their polymeric content and the complex flow response generated.. As such, knowledge of the coating flow behaviour and the rheological it conveys are essential elements in the design and operation of roller coating applications. These processes are quite complex and often possess localized regions of high shear and extension rates, which can interfere with the process operations, causing instabilities on the coated substrates. Most coating flows employed in industry are of polymeric type (Bird et al. 1987) and a high molecular polymer will increase pressure drops in many applications, as discovered by (Mysels 1949 and Toms 1948).

In order to accurately predict a solution to an engineering problem using computational fluid dynamics, there are three main stages required; pre-process, solve equations and post-process. The pre-processing stage consist of the development of a computational domain with appropriate boundary conditions, the flow governing equations and a set of constitutive equations, and the definition of the flow rheological equations of state. The solving of equations stage constitutes the use of a numerical scheme to solve the flow equations. Such a

method includes finite difference, finite element and or finite volume methods. The post-processing stage involves the analysis and interpretation of the numerical solution from these computational techniques. The aim is for this to provide an optimized process, with improved overall process design and control, whilst for the practitioner,, reducing production cost and increasing commercial competitiveness.

Prior to the modeling of the roller coating process, a combining and separating flow (referred to as 'mixing flow') configuration was selected as a model flow and benchmark problem, to mimic the reverse mode in a reverse roll coating flow. This flow manifests reversing of flow direction, but does not include the fluid free-surfaces aspects. The numerical formulation adopts a Taylor Galerkin Pressure Correction (TGPC) scheme (Tamaddon-Jahromi et al. 1992 and Carew et al. 1994), with finite element method for viscous, and inelastic flows, and a hybrid finite element/finite volume method for complex viscoelastic flow behavior. Such a numerical methodology was tested under the combining and separating flow configuration and highly accurate solutions were obtained which compares qualitatively with experiments and theory. For the combining and separating flow, material models analysed were of viscous and, viscoplastic type of models. For the reverse roll coating, flow simulations for viscous and inelastic, Linear and exponential PTT network class of models, FENE-CR and FENE-P models were investigated.

The field of roll coating has been well studied both experimentally and theoretically, with researchers focusing mainly on forward roll coating and Newtonian fluids. However, reverse mode processes have been somewhat important in the case of instabilities occurring. Several parameters are considered when operating such applications, including nip gap, speed ratios, deformable roll cover and fluid rheological properties. Benkreira et al. [1981, 1982, 2002a] have performed in depth studies on roll coating using experimental techniques. The authors have focused on roll coating of viscous fluids, analyzing ribbing instabilities and dynamic wetting. Coyle et al. [1987, 1990] observed the film splitting flow of shear-thing liquids in forward roll coating and the theory of deformable roll coating. Carvalho et al. [1994 and 1996] investigated the elastohydrodynamic lubrication on roller nips, in terms of capillary and viscoelastic properties of roll cover. Cohu et al. [1995a, 1995b and 1997] also experimentally investigated on forward roll coating with deformable rolls and rheometry of paints. All authors have focused on experimental review of viscous and inelastic flow in forward roll coating with deformable rollers. Until recently, most of the theories and hypothesis of coating flows have all been based on these aspects. Some of the areas concerning industrial needs have not been fully explored. In recent developments to try and tackle practical industrial applications, several reviews and research studies on roll coating have been introduced. Benkreira [2002] experimentally studied the dynamic wetting in reverse roll coating. Ascenio et al. [2006] analysed high speed roll coating with complex rheological fluids. Lopez et al. [2002a, 2002b] presented the rheological effects in roll coating of paints and non-Newtonian effects on ribbing instability. Again, the authors have categorized roll coating applications and focused on specific aspects.

The computational and rheological studies for coating flows brings together the different aspects of the process. The overall aim is to use computational techniques to model coating materials in a reverse roll coating industrial application, involving dynamic wetting lines, the

approximation of complex nip-gap, meniscus and throughput flow, and the interaction with the complex coating fluid rheology. Here, a broad outline to the subject matter and its background are provided for the research study, covering details on fluid rheological properties and computational methods. The plan and outlined of the research conducted is then as follows:

In chapter 2, fluid mechanics is introduced and its relevance in the engineering of fluid flow processes. Here, the fluid model is defined and governing equations are assembled. The introduction covers the fundamental concepts of fluid flow and the three basic laws satisfied in any fluid dynamics processes. (law of conservation of mass, law of conservation of momentum and law of conservation of energy). With particular reference to the coating flows studied herein, this chapter aids in the understanding of the dynamics of coating flows and their governing equations and how the initial and boundary conditions are construed.

Chapter 3 entails the specification of various coating fluid model and assembly of the rheological equations of state. This allows for the analysis of the rheological aspects of the problem and how their influence is determined.

Chapter 4 is concerned with the theory behind numerical methods and development of the numerical techniques and algorithms used in the computational studies and simulation of coating flows, with relevance to the engineering of this industrial fluid flow process. The various numerical techniques are appraised and the choice of numerical analysis justified. The algorithms used in modeling the coating process are defined and mathematical models describing the mechanics behind the physical problems are assembled. Having considered all characteristics of the numerical schemes, a finite element based time stepping algorithm was selected, coupling a Taylor-Galerkin and pressure-correction method of high degree of accuracy, capable of solving viscous and viscoelastic flows. This chapter is devoted to analyzing the several mathematical techniques employed within this algorithm.

A model benchmark problem, combining and separating incompressible flow of Newtonian and inelastic Herschel-Bulkley fluids is studied numerically in Chapter 5. The influence of inertia and fluid rheology is analysed on flow patterns, velocity fields and pressure drops for various flow configurations, with fixed geometric gap-width that itself stimulates the splitting and merging of in the flow. For such Newtonian flows, the numerical procedure was verified with good agreement against previous numerical and experimental observations. To extend consideration to non-Newtonian inelastic materials, the material rheological characteristics were approximated with the use of the Herschel-Bulkley fluid model, incorporating the Ostwald-de Waele Power-law model and viscoplastic yield stress. An unyielded power-law fluid with varying power index (m) was investigated, then variation of the consistency index (k) were analysed. For Bingham model solutions, devoid of shear-thinning and increasing yield stress, the appearance of yielded and unyielded regions was observed. Under Herschel-Bulkley modelling, there was little change noted in the kinematics, but some was apparent in rheological response.

The industrial application is introduced in chapter 6; where a high-speed defect-free roll coating flow with free meniscus surface is simulated. This study has sought to attack

industrial optimisation of coating performance by developing an effective predictive toolset for high-speed defect-free coatings, to address increased process efficiency and commercial productivity. Here, time-stepping/finite element methods are deployed to model this free-surface problem that involves the transfer of a coating fluid from a roller to a substrate (of prescribed wet-film thickness). This procedure is used in conjunction with a set of constitutive equations capable of describing the relevant fluid-film rheology in appropriate detail. Quantities of pressure, lift and drag have been calculated streamwise across the flow domain for which streamline patterns reveal a large recirculating vortex around the meniscus region. Further analysis has been conducted, mimicking the presence of a wetting line, whilst varying boundary conditions at the nip-zone. Observation has shown that such inclusion would serve as a relief mechanism to the positive peak pressures generated around the nip zone. Here, through an elasto-hydrodynamic formulation, the elastic deformation of a rubber roll cover (elastomer) has also been introduced, which offers fresh insight into the process with respect to nip-flow behaviour, and allows for the analysis of both positive and negative nip-gaps.

Subsequently, Chapter 7 addresses the numerical solution of high-speed reverse roller coating flow associated with the industrial process of thin-film paint-coatings of strip-steel. The modelling includes viscous inelastic rheology, meniscus and dynamic wetting lines. Flow structures are examined in detail around the meniscus, nip and wetting line regions, analysed via streamline and shear rates patterns, surface distributional lift and localised nip-pressures. For Newtonian coatings, two vortex transfer modes are visible: one large structure commencing just downstream of the meniscus; and a second miniscule structure in the nip-vicinity, upstream of the wetting line, which is accompanied by increase in localised pressure (this would be influenced by air-entrainment, if that were to become a feature of the problem). Effects of parameter variation are analysed in nip-gap size, adjustment of applicator roller-substrate speed-ratio and levels of surface tension.

The computational modelling of reverse roll coating, in the context of dynamic wetting lines is analysed in Chapter 8, for various non-Newtonian viscoelastic materials. Rheological description appeals to the Phan-Thien Tanner (PTT) network class of models, which parametrically can be made suitable to represent typical *polymeric solution* response, with properties of shear-thinning and strain-hardening/softening. The numerical technique utilises a hybrid finite element-subcell finite volume algorithms with dynamic free-surface location, drawing upon a fractional staged, predictor-corrector, semi-implicit time-stepping procedure. The numerical solution is investigated following a systematic study which allows for parametric variation in elasticity (We-variation), extensional hardening-softening (ε), and solvent fraction (β). Under incompressible liquid flow conditions, LPTT and EPTT constitutive equations were modelled for flow simulation through a two-dimensional planar reverse roll coating domain. Solution cover a range of Weissenberg numbers (We) up to critical levels, addressing velocity fields and vortex developments, pressure and lift profiles, shear-rate and stress fields. At low values (ε>0.5, β =0.1) of extensional viscosity, EPTT model flow fields were considerably easier to solve, attaining critical We levels up to 0.4, in contrast to those for the LPTT model for which critical We levels were 0.3; this situation is reversed at high extensional viscosity levels. On the influence of strain softening in EPTT

solutions, increasing the level of extensional hardening/softening stimulates the vortex structure around the nip region, with a reduction in peak pressure and lift values.

In chapter 9, further rheological exploration is examined in contrast to that above. Here, simulations are conducted for high speed reverse roll coating flow of polymer solutions using viscoelastic FENE constitutive models, appealing specifically to FENE-CR and FENE-P models, with properties of strain hardening and shear-thinning, respectively. A systematic computational and rheological study allows for parametric variation in elasticity (We-variation), level of extensional hardening (ε), shear-thinning and solvent fraction (β). Various problem aspects are investigated to reveal the influence of viscoelasticity on vortex developments, pressure and lift profiles, shear and extensional rates, and critical stress states. Specific advantages of the viscoelastic rheological properties are observed by analysing stress and flow structures over a range of Weissenberg numbers. The novel aspects of the work lie in the application of the algorithm to the reverse roll coating process under such viscoelastic flow approximation. Furthermore, the effects of shear-thinning are observed comparing FENE-CR with LPTT and the effects of strain softening between FENE-P and EPTT.

Chapter 10 presents the conclusions and future directions to this study. Overall, this provides a guide to the suitable rheological properties required in an industrial coating for a stable and consistent application.

Chapter 2

Fluid mechanics and governing equations

This chapter is concerned with the introduction of fluid mechanics and its relevance in the engineering of fluid flow processes. The fluid model is defined and governing equations are assembled. The introduction covers the fundamental concepts of fluid flow and the three basic laws satisfied in any fluid dynamical process (law of conservation of mass, law of conservation of momentum and law of conservation of energy). With particular reference to the coating flows studied, this chapter aids in the understanding of the dynamics of coating flows, the formulation of their basic governing equations and how the initial and boundary conditions are configured.

2.1 Introduction

A fluid can be defined as a substance that flows and undergoes deformation when a shear force is applied. Fluids can include gases or liquids. Fluid mechanics is the branch of applied mechanics concerned with the study of statics or dynamics of fluid flow. Now a modern discipline, computational fluid dynamics constitutes computational methods used to develop solutions to fluid mechanics problems.

Between fluids and solids, a fluid undergoes strain when subject to applied (shear) stress, but solids resist stress to a certain limit (elastic limit) before deformation. Under applied shear force, a fluid undergoes continuous deformation which is analysed by the continuum concept. From the basic concepts of fluid mechanics, there are two types of approach used; the Lagrangian approach and the Euler approach. The Lagrangian approach describes the path of a fluid particle exactly (i.e. at a particular moment in time), where the coordinate system is dynamic and moves with the particle. This approach is quite complex for fluids, since they are in continuous motion, and is mainly used in solid mechanics. The latter, Euler approach describes the path of the fluid particles with respect to space and time, such that spatial reference is fixed e.g. for a fluid flow through a pipe, the Euler approach considers only a section of the pipe and tracks the fluid particles in that section. This type of approach is mainly used in fluid mechanics and is that used in this study.

There are various flow analysis techniques used in fluid mechanics; these are, control volume or integral analysis, differential analysis, and experimental analysis. Here the focus lies mainly on differential analysis. In any of the flow analysis techniques, the law of mechanics, thermodynamics and associated boundary conditions must be satisfied. These three laws are developed from the theories and principles of fluid mechanics; the law of conservation of mass, the law of conservation of momentum and the law of conservation of energy.

Other fundamental concepts in fluid mechanics are no slip conditions which are boundary conditions. For a fluid flowing through a pipe, the pipe wall is stationary, therefore having zero velocity. Thus, the fluid in contact with the pipe wall will flow at the velocity of the wall. For no slip conditions to apply, the relative velocity between the solid wall and the adjacent fluid particles is zero.

The flow visualisation can be performed by identifying the flow patterns taken up by the fluid particles, using streamlines, pathlines or streaklines.

The main aim of this chapter is to study and understand the various types of coating fluids used in the numerical modelling and to formulate the basic governing equations of the flow according to the fundamental theories and principles of fluid mechanics.

2.2 Fundamental concepts of fluid flow

Fluids can be classified in various ways depending on the rheology, dilatational tensor, temporal variation, spatial dimension, motion characteristics and fluid type. A particular fluid type can be either liquid or gas based on the individual molecular behaviour. Depending on the density property of the fluid, it can be compressible or incompressible, where compressible fluids have varying density and incompressible fluid have constant density under applied pressure. Flows can also be classed as steady or transient, whilst considering the variation of the fluid properties with respect to time. Depending on the viscosity of a particular fluid type, it can also be classed as a viscous or inviscid fluid, where viscous fluids have varying viscosity and inviscid fluid have vanishingly small viscosity.

In solving fluid mechanics problems, all fluid flows physically arise in three dimensional form (x, y, and z). Yet, for ease in mathematical complexity, fluid flow analysis can be performed in one, two, or three spatial dimensions.

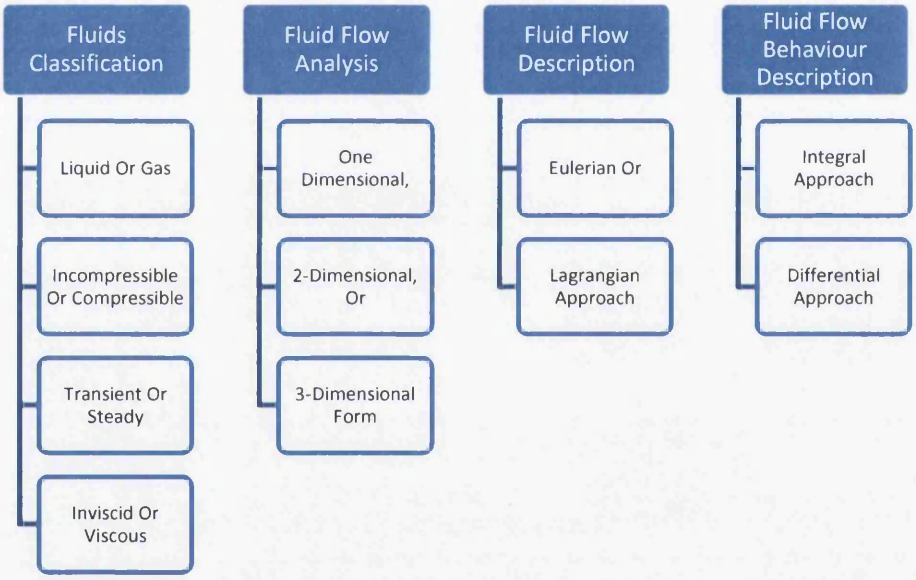

In modelling of fluid flows, the continuum concept is applied assuming that;

- The contribution to the motion of individual molecules can be ignored,
- The fluid undergoes continuous deformation, and
- The fluid variables, attached to each point in the fluid domain, have a unique value.

In order to analyse any fluid flow problem, one has to define the system and its control volume. The system is a collection of matter of fixed identity, and a control volume is a volume in space in which fluid flows. In fluid dynamics one can define an open or closed system, depending on the type of problem, or indeed the finite nature of the control volume.

The various basic concepts of fluid mechanics considered are;

Fluid modelling

For any particular fluid flow problem, the kinematics of the fluids has to be determined. Kinematics is the study of how fluid moves. For static fluids, the fluid velocity field can be determined without reference to the force on the fluid depending on the spatial distribution of the particles in a fluid at any particular time. This can be expressed as,

$$V = u(x,y,z,t)i + v(x,y,z,t)j + w(x,y,z,t)k \tag{2.2}$$

For moving fluids, the dynamics of the fluid must be determined. Hence, fluid dynamics is the study of fluids in motion, a topic for this chapter, where the associated dynamics of fluid flow are investigated.

Flow field description

There are two approaches which can be used to represent the motion of a fluid flow. These include the Lagrangian and the Euler approach. In the Lagrangian approach, coordinate reference is relative to the motion of the particles themselves in a fluid element. The velocity of a particular element in the fluid at a particular point in time is studied and traced through the flow. This is done for every other element of the fluid and gives a complete description of the flow field. For fluids, this approach is fairly complex to follow, as they are in continuous motion. Alternatively, this approach is a popular choice in solid mechanics.

Under the Euler approach, the motion of the particles in the fluid element are studied with reference to a fixed spatial reference, as a function of space and time. Here, the motion of the flow is given by prescribing the properties of the fluid relative to the space coordinate system and time. This approach is generally easier to adopt in practice and is commonly used in fluid mechanics.

Time derivatives in a fluid

The properties of a fluid, such as density, pressure, acceleration, are relative to spatial distribution and time. In an Eulerian approach, one may describe the rate of change of a particular property with respect to time, t, at a fixed point in space. Therefore, suppose a property of a fluid is specified as α,

In an Eulerian scheme, $$\alpha = \frac{\partial \alpha}{\partial t}(x,y,z,t) \tag{2.3}$$

In a Lagrangian scheme, $$\alpha = \frac{\partial \alpha}{\partial t}(t) \tag{2.4}$$

In the Lagrangian representation, the rate of change of that property is described with respect to time following an individual molecular element of the fluid.

Reynolds transport theorem

Reynolds transport theorem is one of the fundamental principles of fluid mechanics and a part of the integral theorem which is considered when deriving the governing equations of fluid mechanics. It conveys the relationship between the time rate of change of an extensive property for a system and that for a control volume. Basically, the Reynolds transport theorem is a law governing the fluid motion using both system concept and control volume concepts.

Considering a volume V and a certain property α, associated with the fluid. The integral part of the material derivative, with both steady and unsteady effects, can be represented as;

$$\frac{D\alpha}{Dt} = \frac{\partial \alpha}{\partial t} + V.\nabla(\alpha) \tag{2.5}$$

where $(\frac{D\alpha}{Dt})$ is the time rate of change of the property of a system, and $(\frac{\partial \alpha}{\partial t})$ is the time rate of change of the property within the control volume as the fluid passes through it and finally, $[V.\nabla(\alpha)]$ is the net flux of the property across the entire control surface.

Analysis of fluid flow behaviour

There are two different approaches which can be used to analyse the behaviour of a fluid flow, the integral approach and the differential approach. In the integral approach, quantities are evaluated within a volume of fluid. This is accomplished by obtaining integrated equations expressing behaviour of fluid properties for a control volume in a flow field. This can be performed in two steps; firstly, to scrutinise the problem and check if the system is appropriate for control volume analysis; and secondly, to examine the behaviour of the control volume, i.e. moving, fixed or elastic. The properties which can be analysed in integral form are; volume flow rate, mass (integral of density over volume), and force (integral of stress over area).

In the differential approach, it involves the evaluation of unknown dependent variables at any spatial point in fluid flow for all time. The differential equations express the fluid flow behaviour with detailed knowledge of a flow field at a point.

2.3 Fluid flow and associated governing equations

The fundamental concepts of fluid flow are all based on three principle laws, the law of conservation of mass, the law of conservation of momentum and the law of conservation of energy.

Conservation of mass

The law of conservation of mass applies to all fluid elements. This law states that the mass of a closed system will remain constant over time i.e. mass cannot be created nor destroyed, the mass flowing into a system must equal the mass flowing out of that system.

Considering a volume of fluid bounded by a closed surface,

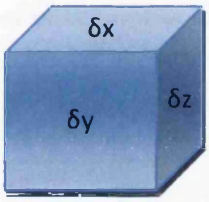

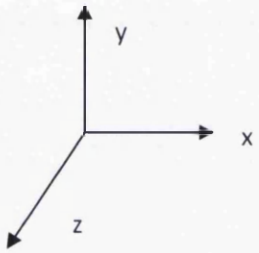

The fluid flows is three dimensional, therefore with velocity component, (u, v and w) in the (x, y, and z) directions, respectively. In differential form, the continuity equation can be derived from the law of conservation of mass as follows;

$$mass = \frac{density}{volume} \tag{2.6}$$

$$\frac{Dmass}{Dt} = 0 \tag{2.7}$$

$$\frac{\partial \rho}{\partial t} + \frac{\partial (\rho u)}{\partial x} + \frac{\partial (\rho v)}{\partial y} + \frac{\partial (\rho w)}{\partial z} = 0 \quad \text{or} \quad \frac{\partial \rho}{\partial t} + \nabla \cdot (\rho U) = 0 \tag{2.8}$$

From equation 2.8, the fundamental continuity equations of fluid mechanics are obtained, which is valid for all types of flows including; steady, unsteady, compressible, incompressible, viscous and inviscid flows.

Considering an incompressible fluid with constant density, the density can be negligible, therefore one derives,

$$\frac{\partial u}{\partial x} + \frac{\partial v}{\partial y} + \frac{\partial w}{\partial z} = 0 \quad \text{Or} \quad \nabla \cdot U = 0 \tag{2.9}$$

Conservation of momentum

In fluid dynamics, the study of fluids in motion, it is assumed that all fluid elements obey the basic laws of mechanics. The motions of these fluids are predicted using the fundamental laws of physics and physical properties. These are based upon the laws of Newton;

1) A body will remain at rest in a straight line until acted upon by an external force.
2) The rate of change of momentum of a body is proportional to the force applied and takes place in the direction of the force.
3) Action and reaction are equal and opposite.

The fundamental law which applies to fluid dynamics is Newton`s second law, as stated above. The forces which influence the motion of the fluid include; gravitational forces, pressure, forces due to molecular viscosity, surface tension, compressibility and inertial Reynolds stresses. For a Newtonian incompressible fluid with constant viscosity and density, the momentum transport equation can be expressed as;

$$\rho\frac{\partial U}{\partial t} = \mu\nabla^2 U - \rho U\cdot\nabla U - \nabla p \tag{2.10}$$

For Newtonian compressible fluids, the external forces are gravity, (g) and surface tension. The surface tension is described by the Cauchy stress tensor (σ), therefore the momentum equation is expressed as:

$$\frac{D(\rho u)}{Dt} = \nabla\cdot\sigma + \rho g \tag{2.11}$$

Where (σ) is the Cauchy stress tensor, which can be reduced to an isotropic pressure and an extra stress tensor, expressed as;

$$\sigma = -p\mathrm{I} + \mathrm{T} \tag{2.12}$$

The total material derivative, $\frac{D}{Dt}$ can be defined as,

$$\frac{D}{Dt} = \frac{\partial}{\partial t} + u\cdot\nabla \tag{2.13}$$

Combining equations 2.13 into 2.11, ignoring the forces due to gravity, one extracts,

$$\rho\left(\frac{\partial}{\partial t} + u\cdot\nabla\right)u = \nabla\cdot\sigma \tag{2.14}$$

Therefore, replacing the Cauchy stress with expression 2.12, the momentum transport can be expressed through the Navier-Stokes equation as;

$$\rho\left(\frac{\partial u}{\partial t}\right) = \nabla \cdot \mathrm{T} - \rho U \cdot \nabla U - \nabla p \tag{2.15}$$

The extra stress tensor (T) is defined as;

$$\mathrm{T} = 2\mu D \tag{2.16}$$

and the rate of deformation tensor, D over space and time, with the temporal derivative (U_t) and the matrix transpose (†) defined as;

$$D = \frac{1}{2}\left(\nabla U + \nabla U^{\dagger}\right) \tag{2.17}$$

For conversion to dimensional quantities, adopting characteristics scales on velocity U (Standard foil speed), length L (steady state coating height) and characteristic viscosity (μ_0) set at a zero-shear rate level, the non-dimensional variables may be defined as:

$$u^* = \frac{u}{U}, p^* = \frac{L}{\mu_0 U}, \mu_i^* = \frac{\mu_i}{\mu_0}$$

$$\dot{\gamma}^* = \frac{U}{L}\dot{\gamma}, x^* = \frac{x}{L}, t^* = \frac{U}{L}t$$

Thus, the non-dimensional quantity (Re) is introduced as;

$$\mathrm{Re} = \frac{\rho U L}{\mu_0} \tag{2.18}$$

As such, the non-dimensional Navier-Stokes equation for momentum transport may be expressed as;

$$\mathrm{Re}\frac{\partial u}{\partial t} = \nabla \cdot \mathrm{T} - \mathrm{Re} U \cdot \nabla U - \nabla p \tag{2.19}$$

Initial and boundary conditions

In the modelling of flow, initial and boundary conditions must be specified, in conjunction with the governing equations. The initial and boundary conditions can be specified in terms of velocity or pressure, depending on the type of flow problem. For viscous fluids, it is assumed that at solid boundaries the fluids are not in motion, therefore the no-slip condition applies:

$$u = v = 0 \tag{2.20}$$

For inviscid fluids, it can also be assumed that there are no fluid motions at the solid boundaries, but a tangential-slip condition applies:

$$u \cdot n = 0 \,. \tag{2.21}$$

For free surface flows, appropriate interface boundary conditions must be adopted and in a similar manner, initial conditions must be specified for time dependent flows.

Chapter 3

Rheology

This chapter is concerned with the introduction of the subject matter of rheology, the theory of complex fluid flow and associated material fluid properties, the introduction of mathematical models to represent the same, and their relevance in the engineering of fluid flow processes. The work entails the definition of how coating fluids are modelled and the assembly of the rheological equations of state. This allows for the in-depth analysis of the various rheological parameters and their influence on both, a model flow problem and an industrial roll coating application. The physical meaning and concepts behind the properties of complex non-Newtonian and viscoelastic fluid material are also described

3.1 Introduction

Rheology is the study of flow and deformation of fluids [Barnes 2000]. Fluids are said to be flowing when the elements of the fluid deform and adjacent particles in the fluid are moving relative to one another. The flow of fluids can be divided into two classical deformation states; i.e. shear flows and extensional flows [Macosko 1994, Tanner et al. (1998), Tanner (2000), and Morrison (2001)]. In shear flows, the fluid particles flow over or past each other, while in extensional flows, the adjacent particles in the fluid flows towards or away from each other.

The property of fluid that offers resistance to shear is called viscosity (inverse fluidity). Fluids are made to flow by imparting a velocity or applying a force. For any given velocity, the force increases with increasing viscosity, whereas for a given force, the velocity reduces with increasing viscosity. The gradient of the velocity in the direction at right angles to the flow is termed the 'shear rate' (shear strain or velocity gradient), and the resulting force per unit area created, applied or produced by the flow is referred to as the 'shear stress'. Fluids with high viscosity (μ) have high resistance to shear stress. Therefore, for any viscous fluid, shear stress (τ) is proportional to shear strain ($\dot{\gamma}$). This can be expressed as;

$$\tau = \mu \dot{\gamma} \tag{3.1}$$

According to Newton's law of viscosity, these fluids can be sub-divided into those expressing Newtonian and non-Newtonian fluid properties. Newtonian fluids possess a shear stress that is directly proportional to shear strain, while non-Newtonian fluids reflect a more complex dependency upon shear strain.

With respect to the variation of shear strain in relation to shear stress, when a shear force is applied, fluids can be classified into the following various categories depending on the viscosity:

Apart from Newtonian fluids with constant viscosity where shear stress is linearly proportional to shear strain, other fluid properties include those of:

- Shear-thinning fluids or pseudo plastic fluids; where viscosity decreases with increasing shear stress, e.g. ketchup, blood, paint, nail polish.
- Shear-thickening fluids or dilatants fluids; where viscosity increases with increasing shear stress, e.g. mixing of corn starch and water.
- Bingham plastic; where shear stress must reach a certain limit before flow commences, e.g. squeezy-bottle ketchup.
- Thixotropic fluids; where viscosity decreases with time at constant shear stress.
- Rheopectic fluids; where viscosity increases with time at constant shear stress.
- The 'Ideal fluid'; constantly shearing with little or no stress applied.

- The 'Ideal solid'; no shear strain, with the maximum shear stress applied (no flow).
- Viscoelastic fluids; that expose viscous and elastic properties, when shear stress is applied. Under pure viscous response, a fluid strains linearly with time; whilst under pure elasticity, the fluid strains instantaneously and returns back to its original state once the stress is removed.

The main aim of this chapter is to provide the underpinning theory to model industrial coating flows, using constitutive equations of state to represent the state of stressing in a fluid under flow. This then emerges as mathematical differential-type models to describe their equations of state. A study is performed of the associated rheological properties of some typical fluids of this type and relevance.

3.2 Newtonian fluid approximation

A Newtonian fluid can be defined simply as a fluid that possesses a constant viscosity with deformation rate and time; still viscosity may vary with adjustment in prevailing temperature and/or pressure conditions. This type of fluid does not display any elastic or extensional behaviour under flow; hence it does not support non-zero 'Normal stresses'. Therefore, for Newtonian fluids, shear viscosity may be interpreted through the ratio of shear stress to shear rate.

$$\tau = \mu \dot{\gamma} \tag{3.1}$$

Common expectation for such fluid viscosity is to decrease with increase in temperature, and the larger the viscosity, the greater the rate of decrease [Barnes at al. 1989]. With respect to pressure dependency, the fluid viscosity normally increases with rise in pressure, but at a slightly lower rate than under temperature changes and for situations encountered in everyday life.

All fluids become non-Newtonian at sufficiently large shear rates, but Newtonian fluids considered here will only do so at extremely high levels of shear rate.

3.2.1 Flow equations for Newtonian fluids

For a Newtonian fluid with a constant viscosity (as above), some assumptions can be made about its flow in certain simple geometric settings. Here, one may consider the importance of viscosity in flows, the effects of turbulence for high-speed flows, and the importance of surface tension as well as viscosity in some flow situations.

For flow through a tube:

For a fully developed laminar flow of a Newtonian fluid through a tube, of radius a, length L, flow rate Q, and pressure P, it has been long established by Poiseuille [Barnes 2000], that the velocity of the fluid at any given radius will have a parabolic profile [Holland et al. (1995)] as given by;

$$u(r) = \frac{P}{4\eta L}\left(a^2 - r^2\right) \tag{3.2}$$

This shows that the shear rate or the velocity gradient varies linearly in the tube, from a maximum at the wall to zero at its centre. This also implies to the shear stress in the liquid. Therefore in such a scenario, the velocity is maximum at the centre of the tube where shear rate is zero and velocity is zero at the walls where shear rate is maximum. This is based on the 'no slip' concept, that there is no slippage at the walls, which is true for most Newtonian fluids considered here. Accordingly, the general equation for the streamwise pressure drop [Barnes et al. (1989)] governing Newtonian laminar flow through a tube is given by;

$$P = \frac{8Q\eta L}{\pi a^4} \tag{3.3}$$

where P represents the pressure drop (in Pascal units), Q is the flow-rate, L is the tube length, a is the tube radius, and η is the fluid viscosity.

For turbulent flows:

For turbulent flows, the Reynolds number (which is the ratio of inertial forces to viscous forces) is introduced and expressed in non-dimensional form as;

$$\mathrm{Re} = \frac{\rho U \ell}{\eta} \tag{3.4}$$

where ρ represents the fluid density, U a characteristic velocity-scale (based on say, mean flowrate Q), ℓ is a characteristic length-scale (based on say, tube-diameter), and η is the fluid viscosity.

For free-surface coating flows

For free-surface coating flows, governed by a surface tension coefficient, ς, when a thin sheet-substrate is pulled across a Newtonian fluid at a constant velocity V, with the fluid lying on one side of the sheet, the final thickness of the liquid coating formed on the sheet-substrate is approximately given by, (for capillary numbers up to 2, see below, [Barnes 2000])

$$h = 0.75\left(\frac{\eta V}{\rho g}\right)^{\frac{1}{2}}\left(\frac{\eta V}{\varsigma}\right)^{0.132} \tag{3.5}$$

Then, the influence of surface tension may be judged from the capillary number (a ratio of viscous to surface tension forces), as expressed by;

$$Ca = \frac{\eta V}{\varsigma} \tag{3.6}$$

3.3 Non-Newtonian fluid flows

Non-Newtonian fluids usually have limiting values of viscosity at low and high shear rates, called the zero-shear and infinite-shear viscosities, respectively. At sufficiently low shear rates, the viscosity is constant, but begins to decrease thereafter at some point, with a straight line response (in log-log form) indicating a power-law behaviour [Barnes 2000]. When fluid viscosity decreases with increasing shear rate, these so-called fluids are referred to as shear thinning. These are distinguished from those manifesting a decrease in viscosity with time under constant shearing, then termed thixotropic fluids. On the other hand, when viscosity increases with increasing shear rate, the fluids are termed shear-thickening (or dilatant fluids). When an increase in fluid viscosity with time under constant shearing is observed, then the fluids are called rheopectic fluids.

3.3.1 Considering shear-thinning/shear-thickening fluids

The material flow response for a non-Newtonian shear-thinning fluid can be captured using simple equations which relate viscosity to shear rate via a minimum number of parameters.

The Cross model:

The Cross model was named after Malcolm Cross [1965], an ICI rheologist who worked on dye-stuff and pigment dispersions. He expressed an equation which describes the viscosity of many suspensions on the whole viscosity curve as follows;

$$\frac{\eta - \eta_\infty}{\eta_0 - \eta_\infty} = \frac{1}{1 + (\kappa\dot{\gamma})^m} \tag{3.7}$$

When describing a non-Newtonian fluid with this model, the degree of shear-thinning is dictated by the value of power-index m, with $m = 0$ for Newtonian fluids and m tending towards unity for shear-thinning fluids. For such a 3-parameter dependency, the viscosity function is shown schematically in log-log scale non-dimensional form in Fig. 3.1, reflecting linear form in the power-law region and no second-Newtonian limiting plateau at large deformation rates.

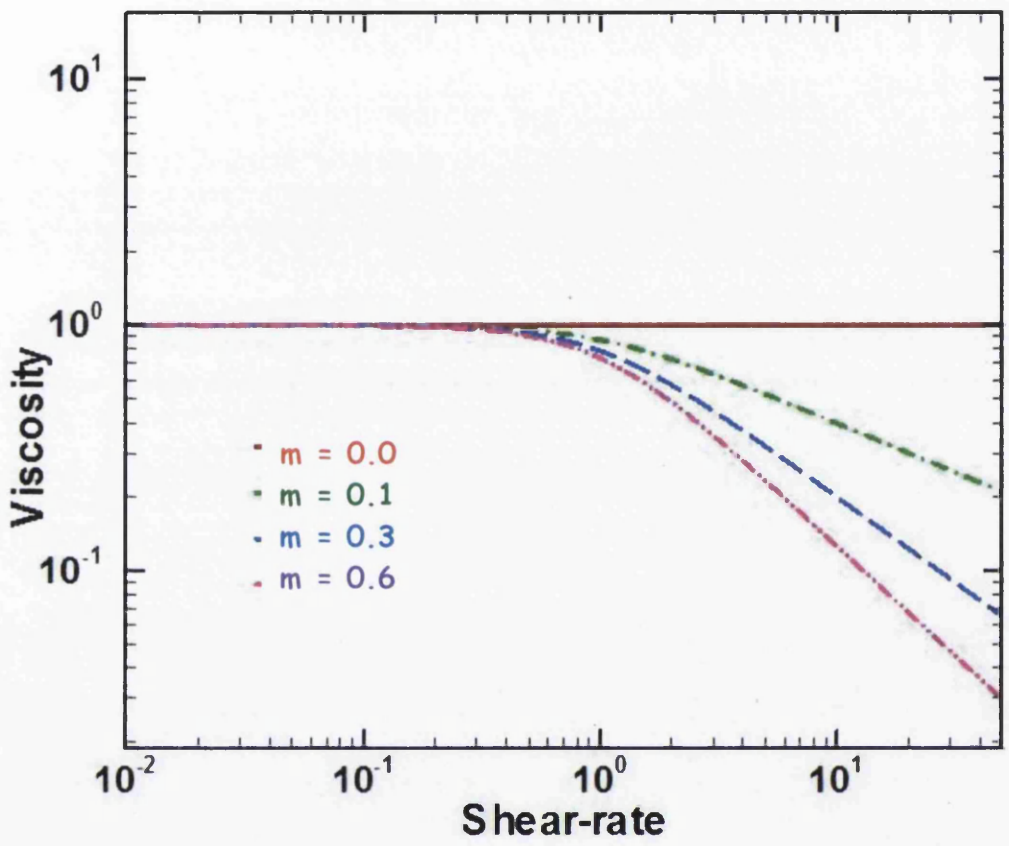

Figure 3.1: Log-log viscosity against shear-rate, Cross model

The Carreau model:

Similarly, the Carreau model, as illustrated in Fig. 3.2, adopts a close functional representation to that of the Cross model, expressed as:

$$\frac{\eta-\eta_\infty}{\eta_0-\eta_\infty}=\frac{1}{\left(1+\left(\kappa\dot{\gamma}\right)^2\right)^{\frac{m}{2}}} \tag{3.8}$$

The Carreau and Cross model are somewhat equivalent at low and high shear rates. Departure is noted in the powerlaw-region (with more curvature) and towards the second-Newtonian limiting plateau at larger deformation rates, $\kappa\dot{\gamma} \geq 10^{-2}$. In this research study, the Carreau model has been used to match the viscosity for a typical industrial coating fluid.

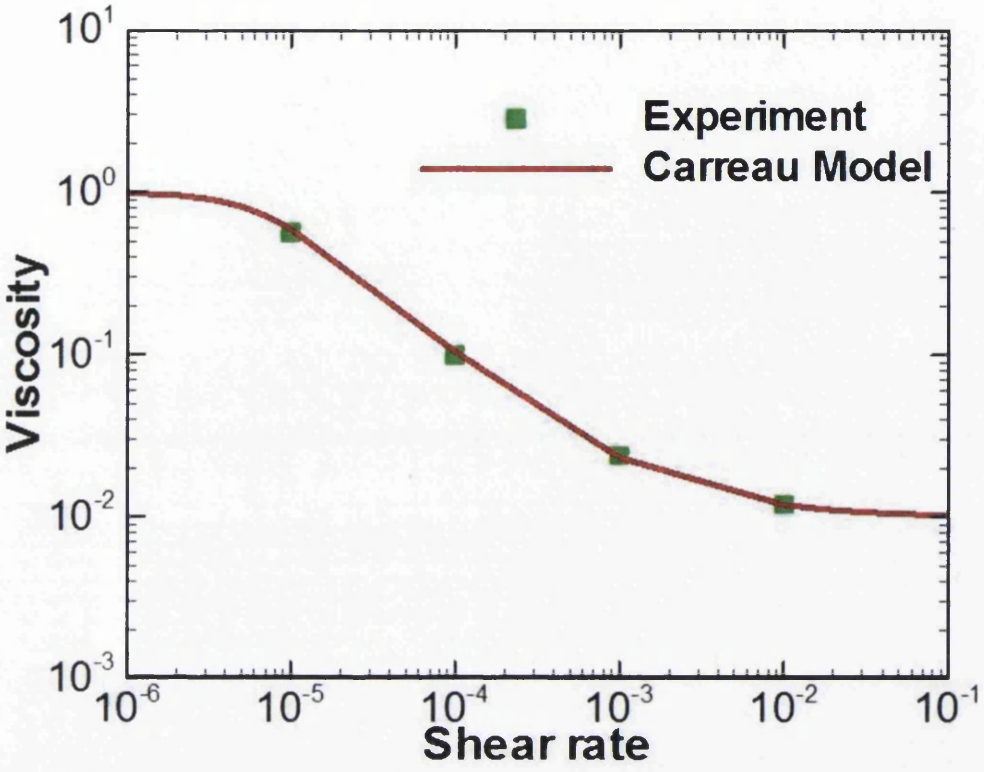

Figure 3.2: Log-log viscosity against shear-rate, Carreau model; matching a typical industrial coating fluid

The Power-law model:

The power law model expresses any non-Newtonian fluid, where the infinite shear viscosity is small, the Cross model reduces to the Ostwald-de Waele power-law model, given by;

$$\sigma = \kappa \dot{\gamma}^{m} \qquad \text{Or} \qquad \eta = \kappa \dot{\gamma}^{m-1} \qquad (3.9)$$

The power-law index (m) is non-dimensional and ranges from $m = 1$ for Newtonian behaviour, with m towards zero for shear-thinning representation, to m above 1 for dilatant fluid response. The power-law model can well describe most structured fluids with shear rates in the range of about 1 to 1000 s^{-1} (see Fig. 3.3.). In practice and above these values, the physical viscosity curves show a tendency to flatten in slope tailing-off towards a limiting high-rate shear viscosity plateau (second-Newtonian level).

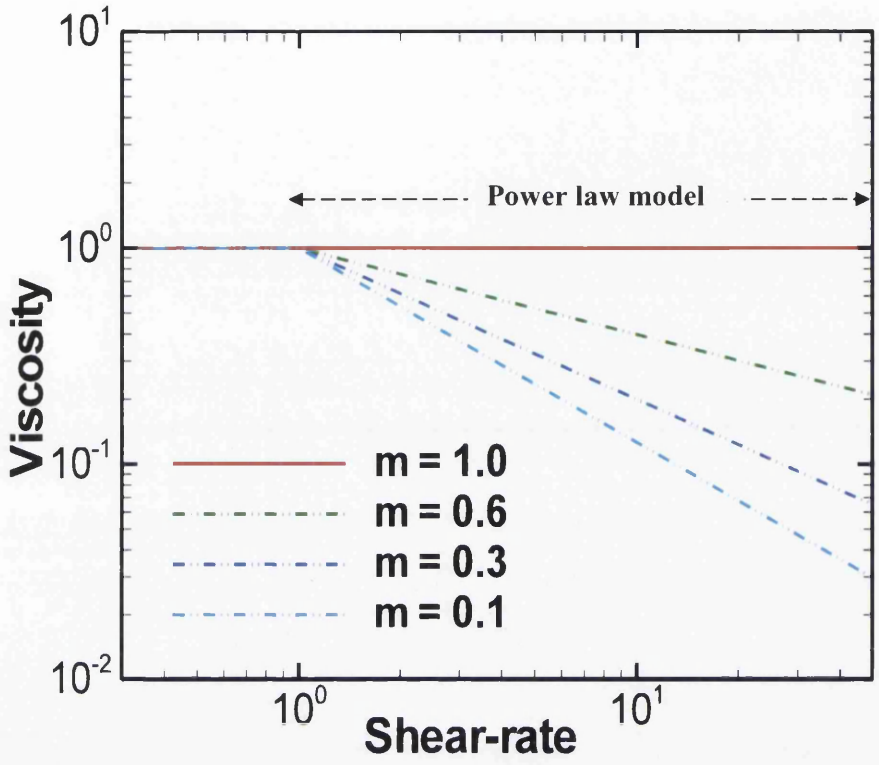

Figure 3.3: Log-log viscosity against shear-rate, Power law model.

3.3.2 Considering yield-stress fluids

For yield stress fluids, there has been useful progress in modelling the behaviour of viscoplasticity, by using simple yield stress containing equations that fit steady-state behaviour [Bird et al. (1983)]. These equations include the Bingham [1922], Casson [1959] and Herschel-Bulkley models [Papanastasiou (1987)]. All such models exhibit a regularization technique for the solid-fluid interface discontinuity and have been developed to make tractable yielded/unyielded regions within a flow (fluid-like being yielded; solid-like being unyielded).

The Sisko and Bingham equations:

For most structured liquids at high shear rates, the Cross model simplifies to the Sisko form, as follows;

$$\eta = \eta_\infty + \frac{\eta_0}{(\kappa\dot{\gamma})^m} \tag{3.10}$$

where for most shear-thinning fluids, power-index m=1. As such, equation 3.10 can be recast as the Bingham model equation, by multiplying through by shear rate, providing;

$$\sigma = \frac{\eta_0}{\kappa} + \eta_\infty \dot{\gamma} \qquad \text{Or} \qquad \sigma = \sigma_0 + \eta_p \dot{\gamma} \qquad (3.11)$$

Here, the Bingham parameters are the yield stress (σ_0) and the plastic viscosity (η_p).

The Casson model:

In simple shear flow, the Casson model takes the form:

$$\sqrt{\sigma} = \sqrt{\sigma_0} + \sqrt{\eta_p \dot{\gamma}} \qquad (3.12)$$

The Herschel-Bulkley model:

The corresponding form for the Herschel-Bulkley model is:

$$\sigma = \sigma_0 + \kappa \dot{\gamma}^n \qquad (3.13)$$

In recent research, there have been several modifications to these models, and here one focuses on the regularization procedures suggested in the Papanastasiou model [1987] based on the Bingham model. In addition, consideration is also given to shear-thinning inclusion via the Herschel-Bulkley approximation. The viscosity function governing the behaviour of this material is described in Fig. 3.4a, utilizing a viscous regularization technique as illustrated in Fig. 3.4b.

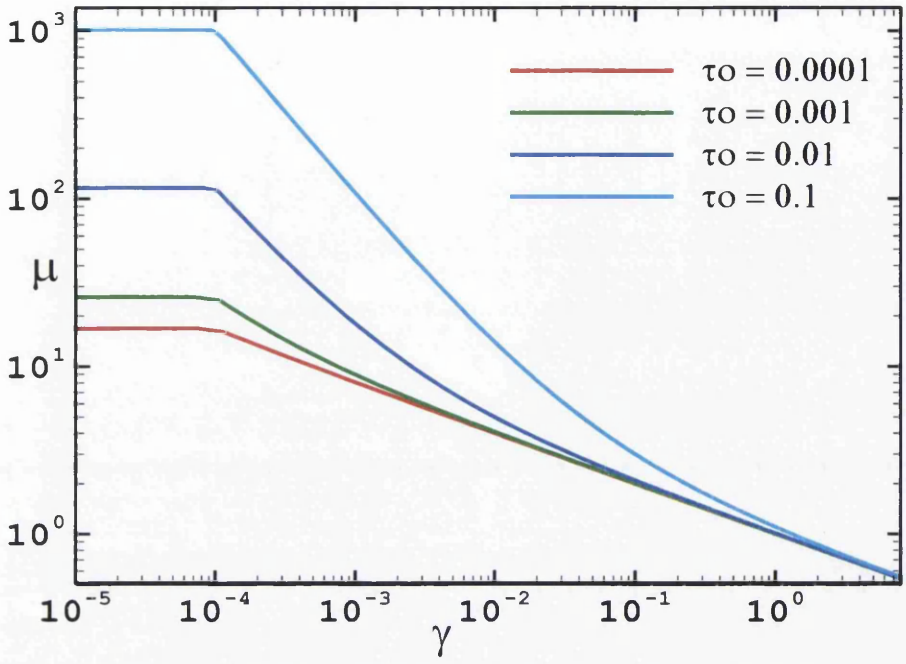

Figure 3.4a: Log-log viscosity against shear-rate; variation in yield stress; Herschel-Bulkley model.

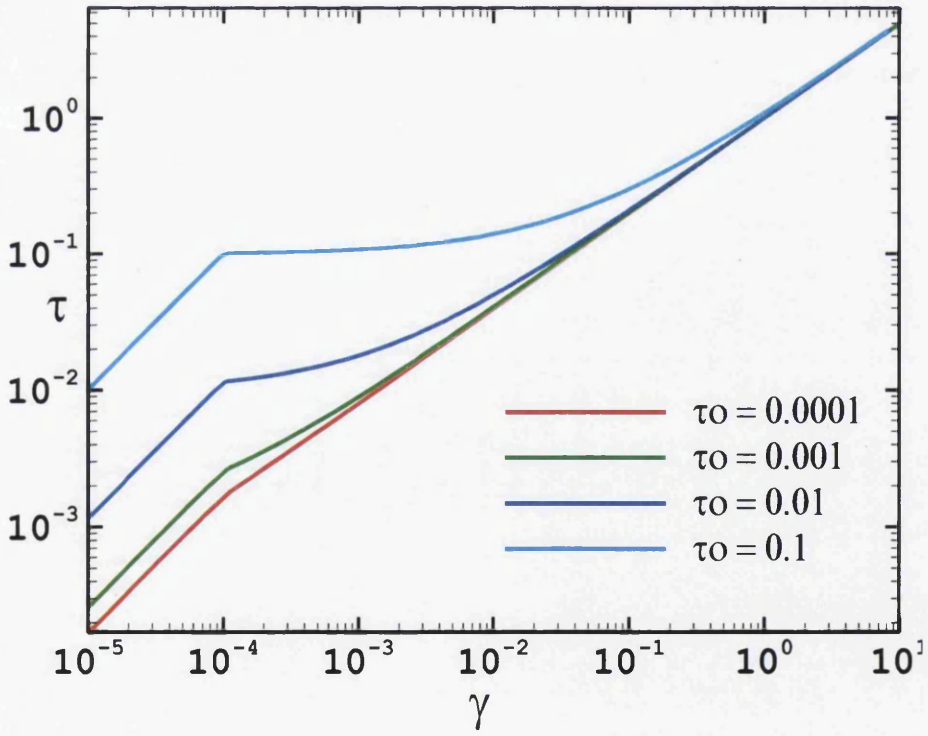

Figure 3.4b: Log-log shear stress against shear-rate; Herschel-Bulkley model under viscous regularization.

3.3.3 Constitutive equations for viscoelastic fluids

Viscoelasticity describes the flow behaviour for complex fluids such as polymers, emulsions and paste. Such material behaviour is dominated by research targeted at industrially relevant materials, with properties intermediate between ideal solids and fluids. The stress response of viscoelastic materials exhibits viscous and elastic characteristics that depart from that governed by Newton's law of viscosity. As such, rheological science advances the fundamental understanding of flowing matter by establishing constitutive equations of state, via relationships expressed between stress, rate-of-change of stress and deformation-rate.

For general viscoelastic flow, the constitutive law relates force, through applied stress per unit area subject to deformation, assuming the fundamental principles as follows. The stress at any fluid-material point is determined from the deformation history of the fluid motion, where that stress is determined by the flow deformation history of the environment around that fluid-material point. As such, the constitutive equation, so derived, must be independent of coordinate variance, and any superimposed rigid body motion.

The constitutive model introduces the extra stress tensor [Crotchet et al. 1982] as:

$$T = \tau_1 + \tau_2 \tag{3.14}$$

where for a Newtonian fluid, the solvent purely-viscous stress component tensor is given by,

$$\tau_1 = 2\mu D \tag{3.15}$$

and for a Generalized Newtonian fluid, by

$$\tau_1 = 2\mu(\dot{\gamma})D \ . \tag{3.16}$$

For a viscoelastic fluid, stress is considered as a combination of viscous and elastic influences, and as such, the simplest such construction of the Maxwell model introduces a convective term to describe the corresponding non-linear material response [Maxwell 1867] as,

$$f\tau_2 + \lambda \overset{\nabla}{\tau}_2 = 2\mu D \tag{3.17}$$

where λ represents a material relaxation time and the convective derivative term is expressed as:

$$\overset{\nabla}{\tau}_2 = \frac{\partial \tau}{\partial t} + U.\nabla\tau - \tau.\nabla U - \tau.(\nabla U)^{\dagger} \ . \tag{3.18}$$

Substituting the convective term into the constitutive model, equation 3.17, yields,

$$f\tau+\lambda\left(\frac{\partial\tau}{\partial t}+U.\nabla\tau-\tau.\nabla U-\tau.(\nabla U)^{\dagger}\right)=2\mu D\ . \tag{3.19}$$

Now, introducing the dimensionless Group Weissenberg number, We as:

$$We=\frac{\lambda U}{\ell} \tag{3.20}$$

where U/ℓ, represents an adopted scale on rate (inverse time-scale) here determined via characteristic velocity and length scales.

Hence, in non-dimensional form the constitutive model for viscoelastic flow may be expressed as:

$$f\tau+We\left(\frac{\partial\tau}{\partial t}+U.\nabla\tau-\tau.\nabla U-\tau.(\nabla U)^{\dagger}\right)=2\mu D\,. \tag{3.21}$$

Here, the role of the f-functional is to describes the material flow type, with f = 1 corresponding to material properties for an Oldroyd B model [1950]; other forms of functionality for f, result in alternative viscoelastic material properties, and these are explored below.

The Phan-Thien/Tanner (PTT) class of models:

This class of models emerges from rubber-network theory and offers finite-extensibility variants to the Oldroyd-B model. Such models, introduced by Phan-Thien and Tanner [1977], rectify the unbounded extensional response at finite rates of the Oldroyd-B model. Though alternative parametric settings, this model is effective in representing industrial viscoelastic flows, such as polymer melts and solutions, in that it can be manipulated to exhibit shear thinning, extensional hardening/softening and extensional hardening/sustained hardening material behaviour.

The f function in general exponential form, yields the Exponential PTT model (EPTT), via:

$$f=\exp\left(\frac{\varepsilon\lambda}{\mu}Tr(\tau)\right)\ . \tag{3.22}$$

Upon expansion of the exponential form f, using Taylor series approximation and truncating at first-order terms, the linear PTT (LPTT) model is obtained, from

$$f=1+\frac{\varepsilon\lambda}{\mu}Tr(\tau) \tag{3.23}$$

Likewise, truncating further at second-order terms leads to a quadratic form (QPTT), based on,

$$f = 1 + \frac{\varepsilon\lambda}{\mu} Tr(\tau) + \frac{1}{2}\left(\frac{\varepsilon\lambda}{\mu} Tr(\tau)\right)^2 \tag{3.24}$$

Upon such a class of PTT models, the Gordon-Scholwalter combined-convected derivative may be introduced, with both upper and lower convective derivatives appearing, via

$$\overset{\square}{\tau}_2 = \overset{\nabla}{\tau} + \xi\left(D.\tau + D.\tau\right) \tag{3.25}$$

This calls upon the material model parameters, ε, ξ (so-called slip-parameter) and η_s to control the extensional and shear behaviour. Accordingly, the material functions are then expressed as,

$$\eta_s = \beta\eta_0 + \frac{\eta_0(1-\beta)}{f}$$

$$N_1 = \frac{2\eta_0(1-\beta)\lambda_1\dot{\gamma}^2}{f^2}$$

$$\eta_e = 4\eta_0\beta + 4\eta_0(1-\beta)\frac{f}{(f-2\lambda_1\dot{\varepsilon})(f+2\lambda_1\dot{\varepsilon})}$$

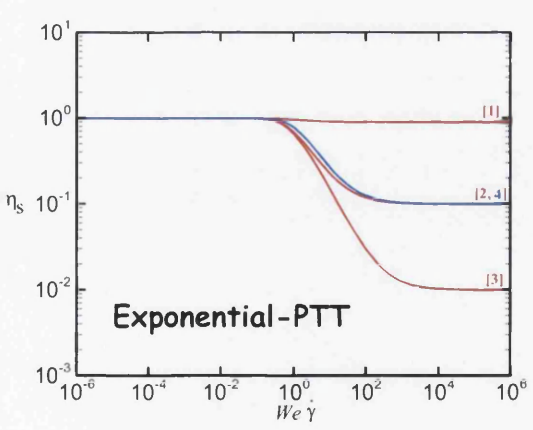

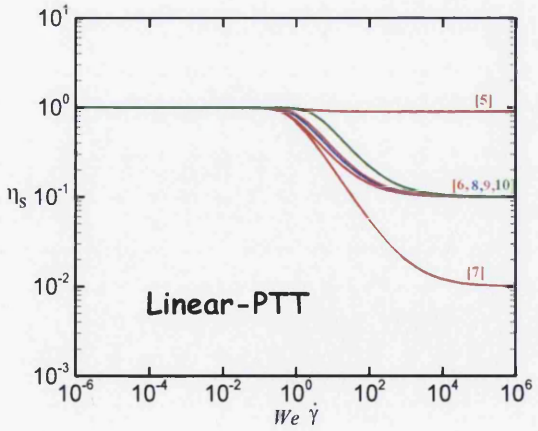

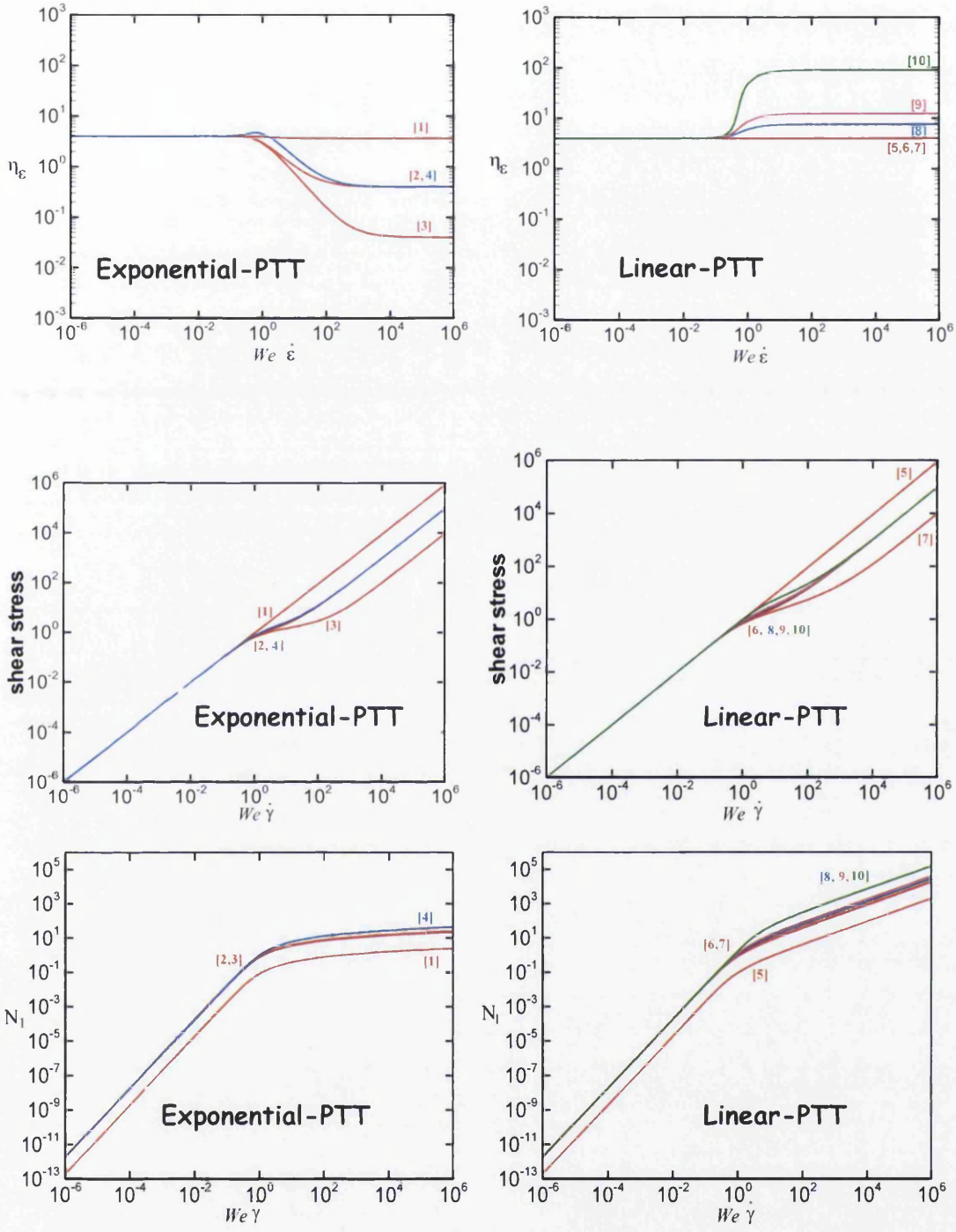

Figure 3.5: a) Shear viscosity, b) extensional viscosity, c) shear stress, d) first normal stress difference

EPTT model; [1] $\beta = 0.9$, $\varepsilon = 0.5$, [2] $\beta = 0.1$, $\varepsilon = 0.5$, [3] $\beta = 0.01$, $\varepsilon = 0.5$, [4] $\beta = 0.1$, $\varepsilon = 0.25$.
LPTT model; [5] $\beta = 0.9$, $\varepsilon = 0.5$, [6] $\beta = 0.1$, $\varepsilon = 0.5$, [7] $\beta = 0.01$, $\varepsilon = 0.5$, [8] $\beta = 0.1$, $\varepsilon = 0.25$, [9] $\beta = 0.1$, $\varepsilon = 0.15$, [10] $\beta = 0.1$, $\varepsilon = 0.02$.

Fig 3.5 describes the behaviour of the respective PTT models selected. Shear viscosity for all PTT models decreases with increasing shear rate; hence, manifesting shear-thinning. Extensional viscosity for LPTT model rises with increased extensional rate and is capped at high rate (sustained extensional hardening). In contrast, under the EPTT model, extensional viscosity response falls with increasing rate (strain softening). N_1 the first normal stress differences are quadratic and weaker for EPTT model than LPTT. The selection range for values of the parameter (ε), which largely governs the extensional behaviour, falls within the range $0.01 \leq \varepsilon \leq 0.5$, although larger values may be used [Tanner 1989 and Phan-Thien 1988]. The solvent fraction (β) decreases and is sampled from the range $0.01 \leq \beta \leq 0.9$, to represent the highly shear-thinning nature of the industrial paints used as coating fluids.

The FENE class of models:

This class of models is substantiated from the base-theory of Hookean dumbbells, finite extensible nonlinear elastic (FENE) models. Such models refer to material representations that describe a long chain polymer, consisting of a chain of monomers connected by a nonlinear spring. The spring force is approximated by Warner's relationship [1972] to describe the polymer dynamics. The two versions of FENE models employed in this thesis are termed FENE-P and FENE-CR models.

FENE-P model describes a continuous form of polymer based upon a closure approximation, proposed by Peterlin [1966]. This reveals a significant reduction of the original FENE constitutive equation. The FENE-P model constitutive equation consists of a configuration tensor (A) and a viscoelastic stress tensor (τ):

$$\overset{\nabla}{\mathrm{A}} + \frac{f\left(Tr(\mathrm{A})\right)}{\lambda}\mathrm{A} = \mathrm{I}$$

where, $f\left(Tr(\mathrm{A})\right)$ is given by the Warner spring-force expression, as:

$$f\left(Tr(\mathrm{A})\right) = \frac{1}{1 - Tr(\mathrm{A})/L^2} \ .$$

Both tensor variables, A and τ, are then connected by a means of Kramer expression, given as,

$$\tau = \frac{\mu_p}{\lambda} f(\mathrm{A})(\mathrm{A} - \mathrm{I}) \ .$$

An alternative version of *FENE* model may be identified by adopting the functional form;

$$\overset{\nabla}{\mathrm{A}}+\frac{f\left(Tr\left(\mathrm{A}\right)\right)}{\lambda h\left(Tr\left(\mathrm{A}\right)\right)}\left(\mathrm{A}-\mathrm{I}\right)=0$$

where $h\left(Tr\left(\mathrm{A}\right)\right)$ is the conformation-dependent contribution to the friction coefficient, expressed through a one-parameter family dependence on κ as,

$$h\left(Tr\left(\mathrm{A}\right)\right)=1-\kappa+\kappa\sqrt{\frac{1}{2}Tr\left(\mathrm{A}\right)}\ .$$

With $\kappa = 0$, the FENE-CR model [Chilcott et al. (1988)] is recovered, and $\kappa = 1$, the FENE-CD model is extracted. Here, it is the FENE-CR model that is utilized.

From Figure 3.6, the material functions for FENE-P and FENE-CR differ significantly, yet only in their respective shear viscosity forms. These material functions are governed by the following expressions:

FENE-CR model:

$$\eta_s=\eta_0$$

$$N_1=\frac{2\eta_0(1-\beta)\lambda_1\dot{\gamma}^2}{f}$$

$$\eta_e=4\eta_0\beta+4\eta_0(1-\beta)\frac{f^2}{(f-2\lambda_1\dot{\varepsilon})(f+2\lambda_1\dot{\varepsilon})}$$

FENE-P model:

$$\eta_s=\beta\eta_0+\frac{\eta_0(1-\beta)}{f}$$

$$N_1=\frac{2\eta_0(1-\beta)\lambda_1\dot{\gamma}^2}{f^2}$$

$$\eta_e=4\eta_0\beta+4\eta_0(1-\beta)\frac{f}{(f-2\lambda_1\dot{\varepsilon})(f+2\lambda_1\dot{\varepsilon})}$$

Notably, the FENE-P model possesses similar material behaviour as that observed for the EPTT material above – shear-thinning and strain-hardening-softening. From Fig. 3.6, the shear viscosity is of constant form for all FENE-CR models analysed, whereas under the FENE-P form, the shear viscosity is a decreasing function, with rate dependent upon the solvent fraction selected. At β = 0.9, with varying parameter L=5.0 and 10.0, the shear-thinning rate is observed to be closely matched for both fluids; whilst at β=0.1, L=3.0 reveals a higher shear-thinning rate than that extracted for L=5.0.

With regards to extensional viscosity, both FENE-CR and FENE-P versions are observed to reach identical levels of extensional viscosity when matched at the same parameter value (L). It is apparent that, the larger the L-value, the larger the level of sustained hardening achieved for any particular solvent fraction (β).

With respect to response under first normal stress difference (N_1), the FENE-P model supports is quadratic behaviour, and therefore, is observed to be weaker (reaching lower levels) at larger shear rates than that substantiated by the FENE-CR model. Here, under shear deformation, it is the influence of shear-thinning that also impacts on N_1 generating this FENE-P response.

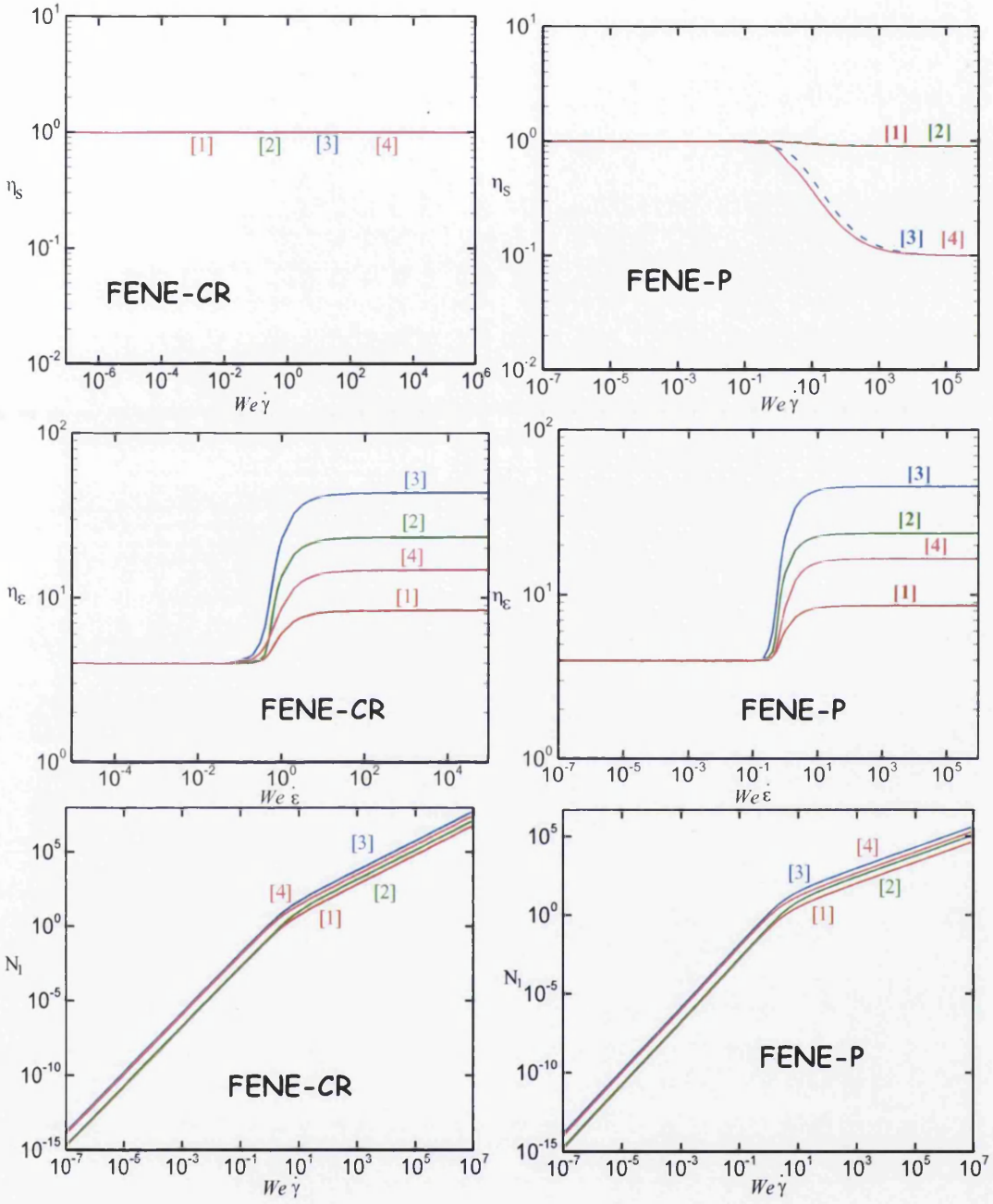

Figure 3.6: a) Shear viscosity, b) extensional viscosity, c) first normal stress
FENE-CR model; [1] β = 0.9, L = 5.0, [2] β = 0.9, L = 10.0, [3] β = 0.1, L = 5.0, [4] β = 0.1, L = 3.0
FENE-P model; [1] β = 0.9, L = 5.0, [2] β = 0.9, L = 10.0, [3] β = 0.1, L = 5.0, [4] β = 0.1, L = 3.0

Chapter 4

Theory & Implementation of numerical methods

This chapter is concerned with the theory behind the numerical methods available and development of the numerical techniques and algorithms used. Specifically, in the computational studies and simulation of coating flows, with relevance to the engineering of fluid flow processes. The various numerical techniques are appraised and the choice of numerical analysis justified. The algorithms used in modeling the coating process are defined and mathematical models describing the mechanics behind the physical problems are assembled. Having considered all the characteristics of the numerical schemes available, a finite element based time stepping algorithm was chosen, coupling a Taylor-Galerkin and pressure-correction method, as this offered a high order degree of accuracy capable of solving viscous and viscoelastic flows. This chapter is devoted to analyzing the several mathematical techniques employed within this algorithm.

4.1 Introduction

Numerical techniques referred to here are those in which mathematical statements of differential flow problems are formulated and solved, from continuous to discrete, providing algebraic solution through appropriate choice of algorithms and numerical solvers. There are various numerical aspects involved, but one common thread is the involvement of a large number of complex partial-differential mathematical calculations. Recently, there has been an enormous focus in the development and application of numerical schemes to tackle scientific and engineering problems. These have proven possible due to widespread availability of fast and efficient digital computers. Prior to the use of high-powered computation, engineering problems were mainly solved in three ways: firstly, by using analytical or exact methods, these methods are limited to linear problems with simple geometries and low dimensionality, whereas most realistic industrial problems are nonlinear and complex. Secondly, by using graphical techniques to characterize the behaviour of systems. Usually these solutions are not too precise and are extremely complex to implement without the use of computers. Lastly, by using a calculator, to manually implement numerical calculations which are elaborate, often complicated and slow.

Today, computers and numerical techniques provide an easy to use solution method, where more emphasis is directed towards formulating the relationship of the problem, to fundamental laws and interpretation of the solution. In order to implement any numerical procedure into engineering practice, one requires the practical need (the problem), the prerequisite mathematical background (theory) and computational expertise (algorithms-software implementation). The mathematical modeling involves the specification of the mathematical problem, which covers the description of the physical problem domain and an assumption of the physical conservation laws governing the system.

The use of numerical techniques naturally arises in all fields of engineering and physical science, and in particular for this research, within the field of computational fluid dynamics (CFD). The main aim here is the design and analysis of mathematical methods to give high precision discrete solutions to complex industrial flow problems. Herein, there are two main solvers employed within the numerical schemes devised, these include both direct and iterative matrix-solvers. The direct method computes the solution to a matrix-problem, working from the matrix itself (sparse, with storage-overhead requirements), in a finite number of steps. Alternatively, iterative methods are indirect (avoid matrix storage overhead) and devised to compute equivalent iterative sequences to a replaced iteration-matrix problem, where iterative convergence is determined as based upon an imposed tolerance threshold. Such iterative schemes must start from an initial guess and iterate through successive approximations that converge to a solution in the limit of the sequence. This involves passing a convergence threshold tolerance for proximity to the limit. Examples of such schemes may be seen in Newton's method, and a Jacobi iteration method.

The first step in the numerical solution of a partial-differential equation system involves discretization. This process is where a continuous (differential) problem is replaced by a discrete equivalent (algebraic) problem with known solution that approximates to that of the original continuous problem. This is provided for by dividing a physical problem domain into

a number of discrete regions. This can be carried out through several different procedures - as in finite difference (FDM), finite element (FEM), finite volume (FVM) and/or spectral schemes (SM). The theory surrounding such procedures is comprehensively documented and can be found in the literature, see [Owens et al. 2002].

Historically, finite difference methods (FDM) have proven a highly effective numerical technique that has dominated the CFD community. This method utilizes finite-difference operators within each differential equation to approximate the derivatives in a pointwise fashion, and thus, provides approximate numerical solutions to the original continuous differential problem. In an attempt to solve an engineering problem using the finite difference method, the problem domain is first divided into a grid network; where the FDM solution is specified as a discrete function upon that grid. Due to its simplicity in formulation and computation, FDM has played an important role in the advance of CFD. However, there are two main sources of error that arise in finite difference methods (as with other similar methods), round-off error and discretization/truncation error. In some complex flow situations, and particularly where there is flow-domain complexity, a conventional FDM Cartesian grid may produce an inaccurate FDM formulation, due to the associated large discretization errors encountered. This has given rise to the need for domain mapping, where real-world complex domains are first mapped into appropriate Cartesian representation, suitable for FDM, and hence conformal mapping techniques have emerged.

For non-uniform complicated computational flow-domains, the finite-element method and finite-volume methods have proved themselves to be more suitable and flexible in use. FEM divides up the domain into a finite tessellation of elements, which can be solved in relation to each other, by finding approximate solutions to the partial differential equations (PDE) and their associated assembled systems. FEM was developed from the work of Alexander Hrennikoff [1941] and Richard Courant [1943]. Although these researchers used different approaches, both targeted mesh discretization of a continuous domain into a set of discrete sub-domains, called elements. Hrennikoff divided the problem spatial-domain using a lattice analogy, while Courant discretized into finite triangular elements. The approach of Courant proved somewhat of a breakthrough and unified earlier results for PDEs, developed by Lord Rayleigh in 1894 and 1896, Ritz in [1908] and Galerkin in 1915, which were all based on finite triangular elements. Then, momentum and major implementation of FEM followed, in the late 40s by Zienkiewicz, and was further developed in the 1960s through the work of Clough [1960] for structural engineering. Key advantages of the FEM over FDM lies in: (i) its ability to handle complicated geometries with ease; (ii) its natural treatment of boundary conditions; (iii) its differential order reduction properties and integral-variational form; (iv) in weighted-residual form, its richness in classification through various choices of weighting functions. On the counterside, the FDM is conceptually simpler and easier to implement. There were mathematical hurdles to overcome under FEM, not least being the consistent application to dynamic fluids problems, necessitating departure from static solid mechanics derivations. Nevertheless, a first order FEM is identical to a FDM for a Poisson equation, most especially if the domain is divided into regular rectangular elements which can be subdivided into two triangles. The quality of FEM approximations is potentially higher between grid points than that afforded through FDM; therefore, FEM has been strongly preferred in structural mechanics.

Other numerical schemes, like finite volume methods (FVM), are mainly used in CFD, where domains are discretized into large number of cells (2D: rectangular or triangular), with relatively low-order approximation within each cell. This method is easily formulated to allow for unstructured meshes. Similar to both FDM and FEM, FVM evaluates a PDE in the form of an algebraic system where the domain is discretized into a mesh and nodal-grid values are calculated at discrete locations on a finite number of cell-volumes (control-volumes), providing the cell environment surrounding each node-point on the mesh. In using the FVM to solve a PDE that contain a differential divergence term (evolution-conservation equation), cell-volume integrals are conventionally converted to cell-surface integrals at cell-boundaries, through the divergence theorem. Such a divergence term is then evaluated as fluxes on the surface boundary of each finite volume cell. To satisfy the law of conservation, the flux entering a given cell-volume is equated to the flux leaving that cell-volume, hence providing a balance with its adjacent neighbours.

Spectral schemes are yet further examples of alternative numerical techniques for solving ordinary differential equations (ODE), PDE and eigenvalue value problems involving differential equations. The spectral scheme is closely related to the FEM in that the former uses a global defined function that are non-zero over the whole domain while the latter, uses a local approach with a basis function that is non-zero only over the local compact support region of that function (region of small sub-set of elements). The implementation of spectral methods are usually accomplished through a Galerkin approach, or collocation method, where approximate solutions are sought over a finite space, requiring the differential equation to be satisfied exactly at a finite number of collocation points. Such spectral schemes provide iteratively fast solutions for steady state problems, and are computationally inexpensive but less accurate for complex domains.

In recent times, most engineering problems have fallen within this framework, so that they may be described using PDEs and are frequently governed by the same underlying physics. In numerically solving these PDEs, generates discrete problems of finite linear algebraic equation systems, governed by large sparse system matrices. This demands efficient and effective solvers: hence the need for iterative and direct solvers.

In this thesis, the computational studies for coating flows utilizes a numerical technique termed, Taylor-Galerkin pressure-correction (TGPC) algorithm. Prior to the development of this algorithm, early in the 1970s, a Galerkin mixed formulation were implemented with components of stress tensor discretized with velocity components and pressure to reach a steady state. There is a practical inability to model convection-dominated form, transient behaviour and three-dimensional geometries with this technique. New techniques proposed to remedy this effect, have emerged from Petrov-Galerkin [Brooks et al. 1982, and Barrett et al. 1984] methods for steady flows, and Taylor-Galerkin [Zienkiewicz et al. 1989] and Lagrange-Galerkin method [Benque et al. 1982 and Douglas et al. 1982] for transient flows . Based upon Euler, Leap frog and Crank-Nicholson time-stepping, Donea [1984] first proposed the Taylor-Galerkin schemes. Taylor-Galerkin and Lagrange Galerkin methods adopt a similar philosophy in that the spatial discretization is considered along the characteristics of the differential system, solving along particle paths, where particles are

tracked over a limited time step interval. The drawback such an approach involves the solving of the pressure terms and the incompressibility constraint. For transient behaviour, one of the most successful methods is the projection or pressure-correction (PC) method introduced through the pioneering work of Chorin [1968] and Temam [1969]. This is a pressure-based fractional-staged scheme, which decouples the velocity and pressure terms of the momentum equation and considers a Poisson equation for the pressure at each time-step utilizing correction stages for velocity and pressure. For viscoelastic flow problems, in 1987, Townsend and Webster [1987] proposed the first instance to consider incremental pressure-correction via FEM, when combined with the Taylor-Galerkin method. Initially, this was derived in an *explicit time-stepping* form. This approach offered some distinct variational advantages with respect to boundary condition treatment and implementation. Nevertheless, this explicit scheme posed some severe limitations at low Re (in the viscous regime, crucial in the viscoelastic context) and naturally inherited a stability Courant-type time-step restriction. Subsequently in the early 1990s, Hawken et al. [1990] proposed further algorithmic modifications towards a *semi-implicit form*, where diffusion-terms were treated implicitly and the advection explicitly for viscous flow problems. The computation of solution was successful over a wide range of Re. Considering the stability over the fractional step scheme, pressure solution was found to be particularly sensitive and a source for destabilization. Van Kan [1986] provided theoretical advance to enhance stability of the PC-scheme without degrading accuracy by developing the pressure-correction methodology into a second-order form under finite difference discretization and Crank-Nicholson time splitting. These ideas were incorporated within the Townsend and Webster approach, described above. More recently, these ideas have been improved still further to include multiple time-step reference for governance of pressure terms [Keshtiban et al. 2008, Tamaddon-Jahromi et al. 2011].

Within finite element discretization for complex flow problems, the treatment of the convective term and appropriate spatial conditions in the choice of approximating functions for velocity, pressure and extra stress are considered most important. Applying the conventional standard Galerkin method guarantees minimum error for elliptic problems, but for hyperbolic functions, the convective term generates non-self adjoint typing-properties, causing rapid solution changes with spurious oscillations. Also the Galerkin method can lead to under-diffusive solutions due to negative artificial diffusion [Raithby et al. 1974]. In order to overcome these deficiencies and obtain stabilized solutions, several stabilization techniques have been proposed which are often based on artificial diffusion, such as the inconsistent Streamline Upwinding (Galerkin) technique and modification to the convective term through quadrature rules. A consistent implementation which is adopted in this study is termed, the "Streamline upwinding Petrov Galerkin technique" SUPG [Brooks et al. 1982], which is suitable for complex multi-dimensional problems, being devised to minimize stream-wise diffusion.

Having considered such enhancements and further developments, this thesis employs the TGPC algorithm to study coating flows. The algorithm is based on a semi-discrete spatial representation, with a hybrid finite element/finite volume approximation, where finite elements are applied for velocity and pressure on triangular parent elements, and cell-vertex finite volume schemes are applied for stress on subtended-child triangular control-volumes

(within each parent cell). As above, the Taylor-Galerkin method adopts a Lax-Wendroff approach, using a Taylor series expansion in time to develop the split-stage time-stepping schemes. The TGPC framework is divided into three stages. The first stage involves a two-step approach, simply known as the predictor-corrector doublet (Lax-Wendroff) for velocity and stress [see Townsend et al. 1987] solved through an efficient low-iteration count Jacobian iterate scheme. The Galerkin projection method applied here in provides the finite element spatial approximation for the discretization process. The second stage introduces the projection method specifically designed to deal with the incompressibility constraint. This involves solving for the pressure-difference over a time-step as a primary variable in a Poisson equation, and employs a direct Choleski decomposition procedure. With the Crank-Nicholson representation for the pressure term in the projection method, stage three recaptures the divergence-free velocity field at the end of the time step loop; where once again solution is provided via a Jacobi iteration.

4.2 Finite element method

In this study, the basic governing equations are discretized through a finite element method. In FEM, the computational domain is divided into a number of elements and a number of nodal points. FEM is a powerful numerical technique for obtaining approximate solutions to PDEs and their associated systems in a wide variety of engineering problems. In a complex domain, it becomes necessary to obtain these approximate numerical solutions rather than exact closed form solutions. The first step in describing a physical phenomenon is to establish the governing equations and suitable initial and boundary conditions for any particular engineering problem. Herein, one can observe the difficulty in obtaining a simple analytical solution stimulated by an irregular complex geometry. To overcome these difficulties, the FEM discretizes the domain into discrete elements with a finite number of unknown variables, in terms of assumed approximating functions within each element. These interpolating or approximating functions are defined in terms of nodal points. These nodes usually lie in the interior and or boundaries connecting to the adjacent elements. The nodal values of the field variables and the interpolation functions over the elements define the behaviour of the field variable within each element and therefore become the new unknowns. The accuracy of the solution and degree of approximation depends on the size and number of elements used and the interpolation functions themselves. The FEM formulates a solution for each element before assembly to represent the entire domain. Within FEM, there are several ways in which one can formulate the variables of each elements; a direct approach, a variational approach, a weighting residual approach and an energy balance approach. Regardless of the approach used, the following common basic steps are always required to obtain a finite element approximation for any engineering problem;

1. Domain discretization – the first step is to construct a mesh by dividing the domain into elements of different shape. The type, size and number of elements depends on the kind of domain and engineering judgment. For some complex domains, it may be necessary to use different element shapes, structured or unstructured elements, or gradual mesh refinements.
2. Interpolation functions – the second step is to assign nodes to each element and select a type of interpolation function to represent the variation of the field

variables over a single element. Depending on the number of nodes assigned to each element, the nature and number of unknowns at each node, the degree of the interpolating function may be assigned – for example, as quadratic or linear.

3. Express element properties – once the mesh is established and nodes assigned, the variables of each element are formulated using matrix equations. This can be accomplished as indicated above. (direct, variational, weighting residual, or the energy balance approach) For the numerical method utilized in this thesis, the Galerkin method involves the weighted residual approach.
4. Assemble each element equation system into the complete system of equations – here the local matrix equation for each element is combined together to obtain a global matrix equation representing the behaviour of the entire system. This is then modified to introduce the initial and boundary conditions.
5. Solve Equations – the system of equation is solved to obtain the unknown nodal variables. The equations may be linear or non-linear; several standard solution techniques may be adopted.
6. Additional computation – sometimes this is required to obtain subsequent variables, once one nodal variable is established, and/or if the equations are highly complex and cannot be solved simultaneously.

The finite element method is used in a range of applications; time independent problems, eigenvalue problems of solid and fluid mechanics, or time dependent problems of continuum mechanics. Within the present body of research, the coating flows are commonly time-dependent problems, and since FEM has recently become a most active field of interest in the numerical analysis of continuum problems, therefore the FEM is a natural choice of selection.

4.2.1 Discretisation and interpolation

In FEM, the basic idea is to systematically generate basis functions on arbitrary regions by dividing into sub-regions. For a one-dimensional case, the sub-regions are intervals or line segments (see Fig. 4.1). Triangle, rectangles or quadrilateral for two dimensions, and tetrahedrons or hexahedrons in three dimensions. The sub regions must satisfy certain criteria;

a) Finite number of sub-regions
b) If there are two sub-regions, they must have a common point in one dimension, a common edge or common vertex in two dimensions, a common face, common edge or common vertex in three dimensions.
c) The union of all sub-regions must precisely define the domain.

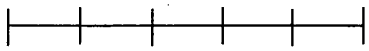

Figure 4.1a: Sub-regions in one dimension

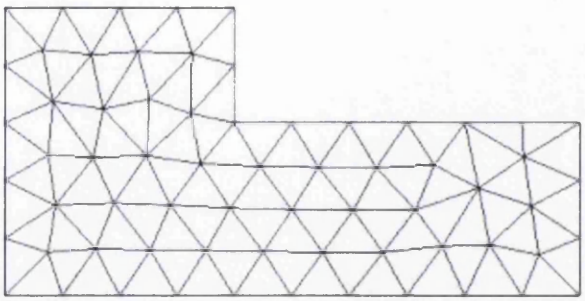

Figure 4.1b: Triangular mesh in two dimensions

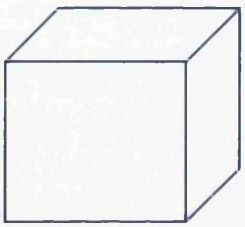

Figure 4.1c: Tetrahedral element in three dimensions

The next step is to define a finite number of points/nodes on the boundary of the sub-regions/elements. The solution of the nodal variable expresses the behaviour of the field variable satisfying the law of conservation. Depending on the type of problem (1D, 2D or 3D case), the definition of these nodes may be in linear or quadratic form. Examples of these nodal points are shown in Fig. 4.2. These nodal points are then interconnected to define each element field variable using the interpolation function.

In one dimension, 2 nodal points, or 3 nodal points,

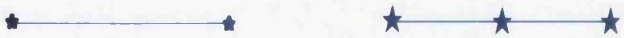

In two dimensions, 3 nodal points, or 6 nodal points,

In three dimensions, 4 nodal points,

Figure 4.2: nodal point on elements in various problem dimensions

For a single field variable u(x,y) determined at each nodal point (x,y) in a three node triangle, the basis function to describe the approximate relation is given as,

$$u(x,y) = N_1(x,y)u_1 + N_2(x,y)u_2 + N_3(x,y)u_3 \qquad (4.1)$$

where N_1, N_2 and N_3 are the spatially dependent interpolation or shape functions. In the FEM, the interpolating functions are usually polynomials. These functions are based on the underlying fundamental conditions that: the function takes the value of each variable at a nodal point and varnishes at all other nodal points; the function has prescribed behaviour on each sub region i.e. linear or quadratic; and the function is continuous on the domain. In the FEM, these unknown variables u_1, u_2 and u_3, can then be determined by the weighted residual approach or the Ritz method. The Ritz method is basically a predecessor of the more general FEM, where interpolation functions obey certain continuity requirements. The main difference is that, the assumed trial functions in FEM are defined over each interconnected element, while in the Ritz method; they are defined over the whole domain. Therefore, the Ritz method is only suitable for simple geometries.

In this study, the domains are discretized into planar two dimensional non-overlapping triangular elements, specifically a six-node triangle with linear pressure interpolations and quadratic velocity interpolations. For the construction of linear finite elements for pressure (see Fig. 4.3), the vertex nodes are assigned with 3 nodal degrees of freedom and for quadratic finite elements for velocity, the vertex and mid-side nodes are assigned with 6 nodal degrees of freedom, respectively.

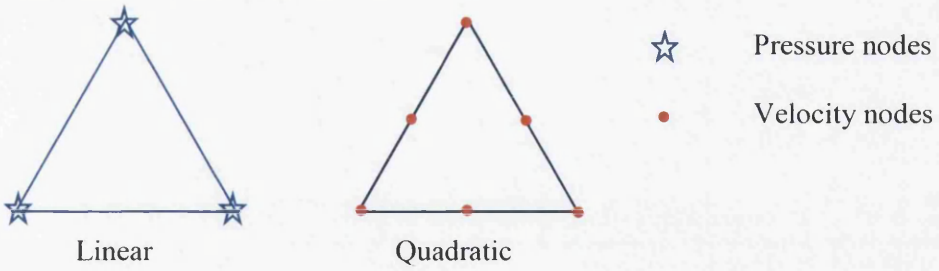

Figure 4.3: Triangular element with linear and quadratic interpolations.

Polynomials are employed as the type of shape functions and are relatively easy to manipulate. The velocity is approximated quadratically as,

$$u(x,t) = \sum_{i=1}^{6} u^i(t)\phi_i(x) \qquad (4.2)$$

$$\tau(x,t) = \sum_{i=1}^{6} \tau^{i}(t)\phi_{i}(x) \tag{4.3}$$

and pressure linearly as,

$$p(x,t) = \sum_{j=1}^{3} p^{j}(t)\psi_{j}(x) \tag{4.4}$$

The order of a polynomial representing a field variable depends on the number of degrees of freedom assigned to an element; therefore the number of coefficients in a polynomial equates to the number of nodal variables.

For linear pressure representation,

$$p(x,y) = \psi_1 + \psi_2 x + \psi_3 y \tag{4.5}$$

For quadratic velocity representation,

$$u(x,y) = \phi_1 + \phi_2 x + \phi_3 y + \phi_4 x^2 + \phi_5 xy + \phi_6 y^2 \tag{4.6}$$

In order to evaluate the integrands over each triangular element in a finite element discretisation, natural area coordinates or barycentric coordinates are selected. Considering a point x_p within an element (see Fig. 4.4), coordinates L_1, L_2, L_3 are area coordinates chosen to describe the location of this point.

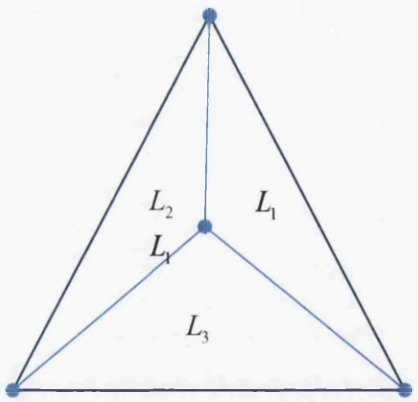

Figure 4.4: Natural area coordinates for a linear triangular element

The location of x_p may be expressed linearly as:

$$\begin{aligned} x &= L_1 x_1 + L_2 x_2 + L_3 x_3 \\ y &= L_1 y_1 + L_2 y_2 + L_3 y_3 \end{aligned} \tag{4.7}$$

The coordinates may be interpreted as interpolating functions, relating the vertex or end nodes to the interior nodal point, therefore,

$$L_1 + L_2 + L_3 = 1 \tag{4.8}$$

The natural coordinates then become the interpolating functions and can be used to express the field variable (u) as,

$$u(x) = u_1 L_1 + u_2 L_2 + u_3 L_3 \tag{4.9}$$

Interpreting u as a function of L_1 and differentiating u via the chain rule formula provides,

$$\begin{aligned} \frac{\partial u}{\partial x} &= \frac{\partial u}{\partial L_1}\frac{\partial L_1}{\partial x} + \frac{\partial u}{\partial L_2}\frac{\partial L_2}{\partial x} + \frac{\partial u}{\partial L_3}\frac{\partial L_3}{\partial x} \\ \frac{\partial u}{\partial y} &= \frac{\partial u}{\partial L_1}\frac{\partial L_1}{\partial y} + \frac{\partial u}{\partial L_2}\frac{\partial L_2}{\partial y} + \frac{\partial u}{\partial L_3}\frac{\partial L_3}{\partial y} \end{aligned} \tag{4.10}$$

Then, any product combination of L_i and its powers to n_i, may yield an integrand over an elemental region Ω of area Δ, for which the following exact integration formula applies,

$$\int_{\Omega} L_1^{n_1} L_1^{n_1} L_1^{n_1} \partial\Omega = \frac{n_1! n_2! n_3!}{(n_1 + n_2 + n_3 + 2)!} 2\Delta \tag{4.11}$$

4.2.2 Weighted residual approach

The method of weighted residuals is a generalised approach for obtaining approximate solutions to linear and non-linear partial differential equations. It is basically one of the means of formulating the finite element matrix equations principally employed in this thesis. There are two steps involved in this method. One is to employ a trial function and satisfy the essential boundary conditions through an integral (weak-form) formulation minimizing discretisation error (residual) over the entire domain. This is done by assuming a general functional behaviour of the dependent field variable to approximately satisfy the differential equation and its boundary conditions. When this approximation and boundary conditions are substituted into the original differential equation, on average, its residuals will vanish over the entire domain. The second step is to solve the resulting equations from step one, and specialize the general functional form to a particular form representing the approximate solution sought. Consider a differential equation in the form,

$$D(\phi) = f \tag{4.12}$$

To find an approximate functional representation for a field variable (ϕ) in a domain bounded by the surface Σ, f is a known function of the independent variable. Assuming appropriate boundary conditions are prescribed on the surface, the method of weighted residual is applied in two steps; First, the unknown exact solution of the field variable (ϕ) is

approximated by $(\tilde{\phi})$ where the functional behaviour is completely specified based on unknown parameters, as

$$\phi \approx \tilde{\phi} = \sum_{i=1}^{n} \phi_i N_i \tag{4.13}$$

where for all the nodes in the surface $(i:n)$, (N_i) are the assumed interpolation functions and (ϕ_i) are the unknown parameters of one of the independent variables. Substituting the approximate solution into the differential equation will result in some residual given as:

$$D(\tilde{\phi}) - f = R \tag{4.14}$$

The residual results from approximating (ϕ) by $(\tilde{\phi})$. The notion in the MWR is to determine the number of unknown parameters such that the projected error R over the entire solution domain varnishes. Hence, in integral form,

$$\int_a^b R W_i dx = 0 \tag{4.15}$$

The error R is distributed over the domain $a < x < b$ by using a weighting function W_i exactly equal to the number of unknown constants in the field variable. The choice of test or weighting functions also varies and dictates the associated method:

1) Pseudo-spectral method or collocation method,
2) Sub-domain method,
3) Least squares method,
4) Method of moments,
5) Galerkin method.

In a pseudo-spectral method, the weighting functions are chosen to be Dirac delta functions, so that the residual errors are forced to be zero at the specific points (chosen nodes). The sub-domain method divides the domain into sub-domains and forces the weighted residual to be zero over various subsections of the domain. In the least squares method, the derivatives of the residuals are used as weighting functions in order to minimize the square error. In a method of moments, the weighting function is chosen from a family of polynomials, and if the interpolations functions were polynomials then this is identical to the Galerkin method. For the purpose of this research, the numerical algorithm utilized, employs a Galerkin-type weighted residual method.

According to the Galerkin method, the weighted functions are the same as the interpolation functions.

$$W_i = N_i, \text{ for } i = 1:n \tag{4.16}$$

4.3 Finite volume method

As mentioned earlier, the numerical algorithm utilized in this research study employs a finite element discretisation method for velocity and pressure, solving viscous and inelastic flows, and a hybrid finite element/finite volume sub-cell scheme for the stress constitutive equation in viscoelastic flows. The former are described previously. Herein, attention is drawn to the finite element/finite volume sub-cell scheme for the viscoelastic stress constitutive equation.

The governing equations for the coating flows assembled in chapter 2, consist of mass and momentum equations and extra-stress constitutive equations. These equations are decoupled in the TGPC algorithm whereby a finite element method is employed for the discretization of velocity components at both vertex and mid-side nodes, and pressure at vertex nodes only, while a finite volume cell vertex approach is adopted for stress components at vertex nodes. To aid in the description of the finite element/finite volume sub-cell approach, the finite triangular element serves as a platform for constructing the finite volume sub-cell. In Figure 4.5, a finite element triangle is drawn with 3 vertex nodes and 3 mid-side nodes. Within this finite element triangle, four finite volume sub triangles are constructed. For the finite element method, the velocity is approximated by quadratic element (on vertex and mid-side nodes), pressure by linear element (vertex nodes only). However, on each parent finite element triangle with four finite volume sub-cells, stress is approximated by quadratic elements with 6 vertex nodes on four finite volume sub-cells fitted in each finite element triangle. Each finite volume presents a linear combination of the stress values on the vertices of that finite volume.

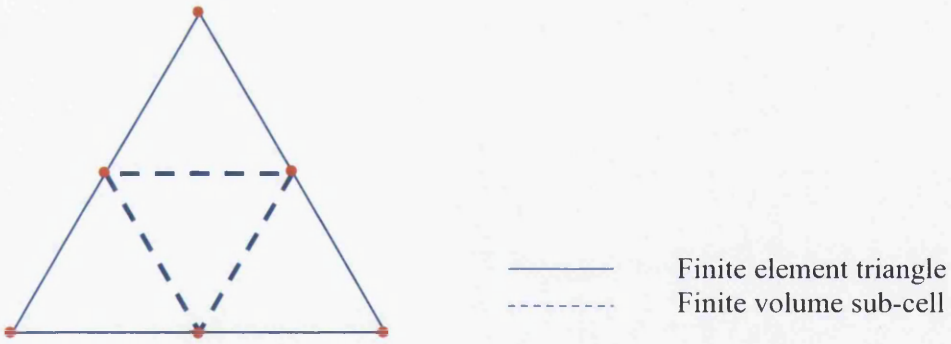

Figure 4.5: Schematic representation of finite element/finite volume sub-cell

Due to the dominant advective term in the constitutive equation, the finite volume method was deemed more suitable in solving the constitutive equation. The fv cell vertex scheme is adopted based upon fluctuation distribution where control volume residuals are distributed through an upwinding technique. Therefore for each scalar stress component acting in an arbitrary volume, the variation of the quantity is controlled via fluctuation of flux vector R and scalar source Q.

For the FV method, the Maxwell constitutive equation may be written in terms of flux R, and source Q as [Wapperom et al. 1998 and Webster et al. 2005],

$$\frac{\partial \tau}{\partial t} + \nabla . R = Q \tag{4.17}$$

where

$$R = ur \tag{4.18}$$

and

$$Q = \left(f\tau + We\left(\tau .(\nabla U)^{\dagger} + \tau .\nabla U \right) + 2(1-\beta)D \right) \tag{4.19}$$

For a scalar stress component (τ), integrating the Maxwell equation (4.17) over a control volume Ω on the domain, using the Gauss divergence theorem on the flux term gives;

$$\int_{\Omega} \frac{\partial}{\partial t} \tau d\Omega + \int_{\Omega} R d\Omega = \int_{\Omega} Q d\Omega \tag{4.20a}$$

Typically, for planar steady simple shear flows, the scalar stress components of an Oldroyd-B fluid are given in dimensional form as;

$$\dot{\gamma} = -2U_{\max} \frac{y}{Y^2} \tag{4.21}$$

$$\tau_{xy} = \mu \dot{\gamma} \tag{4.22}$$

$$\tau_{xx} = 2\lambda\mu \left(\dot{\gamma} \right)^2 \tag{4.23}$$

where Y is the channel width, $U_{\max}$ is the maximum velocity and $\dot{\gamma}$ is the shear-rate.

The cell vertex scheme evaluates the conserved variable on the vertices of the FV grid, therefore for each FV node; the discrete domain integrated covers all regions of all the FV cells with all nodes as vertex nodes. This type of scheme generally maintains their accuracy for non-uniform meshes.

Considering a surface element on a control volume via a line integral, eqn 4.20 can be written as,

$$\int_{\Omega} \frac{\partial}{\partial t} \tau d\Omega + \int_{S} R dS = \int_{\Omega} Q d\Omega \tag{4.20b}$$

where dS is the outward pointing surface element vector. For reasons of accuracy, surface element integration for fluxes, as in equation 4.20b, has been found inferior to area-element integration, as in equation 4.20a; henceforth, this is the selection of choice. The cell-vertex scheme is considered in such a way that the FV scheme evaluates the conserved variable on

the vertices of the finite volume grid. Therefore, for each finite volume vertex node, the integration domain is the region of all the finite volume cells that have that node as a vertex.

Flux distribution schemes: Flux and source residuals can be evaluated over different control volumes. The flux distributions scheme is an approach whereby fluxes of a finite volume cell are non-uniformly distributed to its member nodes. Herein, the flux R_T is calculated over individual finite volume cells T and distributed to the nodes (i) of that cell as;

$$R_i \equiv \sum_T \alpha_i^T R_T \tag{4.24}$$

Where $\left(\alpha_i^T\right)$ are weights determining the flux $\left(R_T\right)$ distribution to the vertex $\left(i\right)$ in a triangle $\left(T\right)$. The suitable choice of $\left(\alpha_i^T\right)$ is based on various criteria;

Conservation: The sum of all coefficients $\left(\alpha\right)$ over the vertices of each triangle $\left(T\right)$ must equal to 1.

Positivity: Flux contribution of each triangle must be taken as positive to guarantee pure convection and prohibition of false extrema in the discrete steady state solution.

Linear Preservation: The coefficients $\left(\alpha_i^T\right)$ must be independent of the data. The scheme maintains the exact steady state solution.

Treatment of time derivative: The time derivative term is distributed over the finite volume cell by means of Median Dual Cell (MDC) approach and is treated using a forward Euler scheme. The MDC is such that the flux distribution treats each individual cell and the activities within a cell will only affect the nodes that are vertices of that cell. The integral of the time derivative for each node (see equation 4.17), is distributed over the finite volume by assuming its piecewise constant over the MDC.

Therefore, to satisfy linear preservation, the weights can be expressed as:

$$\alpha_i^T = \frac{\beta_i^T}{R_T} \tag{4.25}$$

where the coefficients $\left(\beta_i^T\right)$ linearly depends on the data summing to $\left(R_T\right)$. This proves the fact that linear schemes cannot be both positive and linear preserving. The flux distribution can either be expressed in terms of $\left(\beta\right)$ or $\left(\alpha\right)$. Notably, linear schemes can now be divided into two classes, one satisfying positivity and one linearity preserving. In determining the flux distribution, we can distinguish between triangles with one inflow and two inflow sides. Triangles with one inflow side can be both positive and linear preserving, whereas for triangles with two inflow sides, there are numerous choices which depend upon what property are required in the scheme [Struijs et al. 1991]; The β-scheme, and the low diffusion scheme.

For non-linear schemes, a Positive Streamwise Invariant (PSI) scheme is found to be more appropriate in that it satisfies conservation and positivity. It is somewhat equivalent to β-scheme which is linear positive. The scheme is first-order accurate at steady state, however Wapperom and Webster [1998] recognized the important of linearity preserving to achieve high order accuracy and positivity on transient stability by redefining the β-scheme coefficients. Therefore, the determined PSI distribution coefficients satisfy those conditions.

Treating the source terms: As described above for the flux distribution, the total source Q_T is calculated over individual finite volume cells T and distributed to the nodes (i) of that cell as,

$$Q_i \equiv \sum_T Q_i^T \tag{4.26}$$

where $\left(Q_i^T\right)$ is the source contributing to the vertex (i) in a triangle (T). The source integral could also be evaluated over the MDC triangle. If so, this generates two contributions flux and the source terms as, one upwinded and governed over the *fv*-triangle T, (R_T, Q_T), and a second area-averaged and subtended over the median-dual-cell zone, (R_{mdc}, Q_{mdc})

4.4 Taylor-Galerkin pressure-correction

The Taylor-Galerkin and projection algorithm based on the finite element method is considered to solve the governing equations and finite element/finite volume sub-cell scheme for viscoelastic stress constitutive equations. For an incompressible isothermal flow, these equations are the mass balance, momentum balance and the stress constitutive equation. The mass balance equation is

$$\frac{\partial \rho}{\partial t} + \nabla \cdot \left(\rho U\right) = 0 \tag{4.27}$$

where U is the fluid velocity. The momentum balance equation for a Newtonian fluid is;

$$\rho \frac{\partial U}{\partial t} = \mu \nabla^2 U - \rho U \cdot \nabla U - \nabla p \tag{4.28}$$

and for a Generalized Newtonian fluid,

$$\rho \frac{\partial U}{\partial t} = \nabla . \sigma - \rho U \cdot \nabla U \tag{4.29}$$

where ρ is the fluid density (constant for incompressible) and σ the total stress tensor given as;

$$\sigma = -p\mathrm{I} + \mathrm{T} \tag{4.30}$$

where p is the hydrodynamic pressure, I the unit tensor and T the extra stress tensor, given as

$$\mathrm{T} = 2\mu D + \tau \tag{4.31}$$

For the viscoelastic stress τ,

$$\tau + \lambda \overset{\nabla}{\tau} = 2(1-\beta)D \tag{4.32}$$

where λ is a relaxation time, $(\beta = \mu)$ and $(1-\beta)$ is a polymeric viscosity and D is the rate of deformation tensor (refer to Chapter 2). This now leads to a Maxwell constitutive equation of the form;

$$f\tau + \lambda\left(\frac{\partial \tau}{\partial t} + U.\nabla\tau - \tau.\nabla U - \tau.(\nabla U)^{\dagger}\right) = 2(1-\beta)D \tag{4.33}$$

where f represents the non-linear viscoelastic contribution.

Considering the following non-dimensional quantities, Reynolds number and Weissenberg number;

$$\mathrm{Re} = \frac{\rho U \ell}{\mu} \text{ and } We = \frac{\lambda U}{\ell} \tag{4.34}$$

the mass balance, momentum balance and stress equation are non-dimensionalised in the form;

$$\nabla.U = 0 \tag{4.35}$$

$$\mathrm{Re}\frac{\partial U}{\partial t} = \nabla.(2\mu D + \tau) - \mathrm{Re}U \cdot \nabla U - \nabla p \tag{4.36}$$

$$\tau + We\left(\frac{\partial \tau}{\partial t} + U.\nabla\tau - \tau.\nabla U - \tau.(\nabla U)^{\dagger}\right) = 2(1-\beta)D \tag{4.37}$$

where (β) is equivalent to (μ) the solvent viscosity and $(1-\beta)$ is the polymeric viscosity contributions, and U is a characteristic velocity scale of the flow.

The Taylor-Galerkin pressure-correction algorithm is a time stepping procedure with fractional stages, semi-discretized in the temporal domain using Taylor series expansion in time, resulting in second order accuracy.

Consider a differential equation,

$$\frac{\partial u}{\partial t} = F \tag{4.38}$$

Using Lax-Wendroff time stepping scheme,

$$\frac{\partial^2 u}{\partial t^2} = \frac{\partial F}{\partial t} = \frac{\partial F \partial u}{\partial u \partial t} = \frac{\partial F}{\partial u} F \tag{4.39}$$

The resulting second-order Taylor series expansion of the function in time is;

$$u^{n+1} = u^n + \Delta t \frac{\partial u^n}{\partial t} + \frac{1}{2}(\Delta t)^2 \left(\frac{\partial^2 u}{\partial t^2} \right)^n \tag{4.40}$$

where, u^{n+1} and u^n are a function of the u at time levels t_{n+1} and t_n, respectively.

In order to obtain an $O(\Delta t^2)$ accurate scheme, yet to avoid explicit evaluation of the Jacobian $\frac{\partial F}{\partial u}$, a two-step simple predictor corrector approach is introduced. The half-step solution $u^{n+\frac{1}{2}}$ is predicted to approximate with an error of $O(\Delta t^2)$ by an explicit Euler step, and then corrected with u^{n+1} approximated with an error of $O(\Delta t^3)$.

Step 1: $$u^{n+\frac{1}{2}} = u^n + \frac{\Delta t}{2} \left(\frac{\partial u}{\partial t} \right)^n, \tag{4.41}$$

Step 2: $$u^{n+1} = u^n + \Delta t \left(\frac{\partial u}{\partial t} \right)^{n+\frac{1}{2}}, \tag{4.42}$$

This second order accurate scheme is now applied to the constitutive equations as follows;

For the momentum equation,

Step 1: $$U^{n+\frac{1}{2}} = U^n + \frac{\Delta t}{2\rho} \left((\nabla . T - \rho U . \nabla U)^n - \nabla p^n \right), \tag{4.43}$$

Step 2: $$U^{n+1} = U^n + \frac{\Delta t}{\rho} \left((\nabla . T - \rho U . \nabla U)^{n+\frac{1}{2}} - \nabla p^{n+\frac{1}{2}} \right), \tag{4.44}$$

And for the constitutive viscoelastic stress,

Step 1:

$$\tau^{n+\frac{1}{2}} = \tau^{n} + \frac{\Delta t}{2\lambda}\left(f\tau + \lambda\left(U.\nabla\tau - \tau.\nabla U - \tau.(\nabla U)^{\dagger}\right) - 2(1-\beta)D\right)^{n}, \quad (4.45)$$

Step 2:

$$\tau^{n+1} = \tau^{n} + \frac{\Delta t}{\lambda}\left(f\tau + \lambda\left(U.\nabla\tau - \tau.\nabla U - \tau.(\nabla U)^{\dagger}\right) - 2(1-\beta)D\right)^{n+\frac{1}{2}}, \quad (4.46)$$

Concerning the **pressure-correction** procedure; this is fractional-staged method, where velocity and pressure terms of the momentum equation (Step 2 above) are decoupled, and a Poisson equation is considered for pressure at each time-step.

For the explicit scheme, a Crank-Nicholson treatment with $\theta = \frac{1}{2}$ is employed for pressure, therefore from Equation 4.43, $p^{n+\frac{1}{2}}$ is approximated by;

$$p^{n+\frac{1}{2}} = \theta p^{n+1} + (1-\theta)p^{n} \quad (4.47)$$

where $\left(p^{n+1} - p^{n}\right)$ represents the pressure difference on a single time-step $(t_{n+1} - t_n) = \Delta t$.

For the incompressibility constraint in the mass balance equation, an intermediate velocity U^{*} is introduced and projected (momentum equation step 2 above), such that;

$$U^{*} = U^{n} + \frac{\Delta t}{\rho}\left(\left(\nabla.T - \rho U.\nabla U\right)^{n+\frac{1}{2}} - \nabla p^{n}\right), \quad (4.48)$$

Incorporating the pressure $p^{n+\frac{1}{2}}$ into U^{n+1} and substracting U^{*} from U^{n+1} gives;

$$U^{n+1} = U^{*} + \frac{\theta\Delta t}{\rho}\nabla\left(p^{n+1} - p^{n}\right), \quad (4.49)$$

Taking the divergence of U^{n+1} and applying continuity, the resulting pressure difference equation is given as;

$$\nabla^{2}\left(p^{n+1} - p^{n}\right) = \frac{\rho}{\theta\Delta t}\nabla.U^{*} \quad (4.50)$$

Therefore, this pressure-correction scheme embodies as explicit time fractional staged method, where stage 1 introduces a non-divergence free velocity term U^{*} for velocity, and

pressure at stage 2 solves explicitly for the pressure difference $\left(p^{n+1}-p^{n}\right)$, whilst stage 3 corrects the velocity U^{n+1}, to a divergence-free end of time-step velocity.

Stage 1: $$U^{*}=U^{n}+\frac{\Delta t}{\rho}\left(\left(\nabla.T-\rho U.\nabla U\right)^{n+\frac{1}{2}}-\nabla p^{n}\right), \tag{4.51}$$

Stage 2: $$\nabla^{2}\left(p^{n+1}-p^{n}\right)=\frac{\rho}{\theta\Delta t}\nabla.U^{*} \tag{4.52}$$

Stage 3: $$U^{n+1}=U^{*}+\frac{\theta\Delta t}{\rho}\nabla\left(p^{n+1}-p^{n}\right) \tag{4.53}$$

The Taylor-Galerkin pressure-correction algorithm embraces both velocity and stress equations in the governing system of equations at a fractional stage:

Step 1a:

$$\frac{2\,\mathrm{Re}}{\Delta t}\left(U^{n+\frac{1}{2}}-U^{n}\right)=\left(\left(\nabla.T-\mathrm{Re}U.\nabla U\right)^{n}-\nabla p^{n}\right), \tag{4.54}$$

$$\frac{2We}{\Delta t}\left(\tau^{n+\frac{1}{2}}-\tau^{n}\right)=\left(f\tau+We\left(U.\nabla\tau-\tau.\nabla U-\tau.(\nabla U)^{\dagger}\right)-2(1-\beta)D\right)^{n}, \tag{4.55}$$

Step 1b

$$\frac{\mathrm{Re}}{\Delta t}\left(U^{*}-U^{n}\right)=\left(\left(\nabla.T-\rho U.\nabla U\right)^{n+\frac{1}{2}}-\nabla p^{n}\right) \tag{4.56}$$

$$\frac{We}{\Delta t}\left(\tau^{n+1}-\tau^{n}\right)=\left(f\tau+We\left(U.\nabla\tau-\tau.\nabla U-\tau.(\nabla U)^{\dagger}\right)-2(1-\beta)D\right)^{n+\frac{1}{2}} \tag{4.57}$$

Stage 1 solves the velocity and stress components of the momentum and constitutive equation at half time step $\left(n+\frac{1}{2}\right)$ from data gathered at time step (n). This provides the initial non-divergence free velocity $U^{n+\frac{1}{2}}$ to the two-step predictor-corrector procedure, where U^{*} is introduced into the pressure fields. Here, the corresponding matrix systems of equations are solved iteratively by a Jacobi method [22].

Step 2 $$\nabla^{2}\left(p^{n+1}-p^{n}\right)=\frac{\mathrm{Re}}{\theta\Delta t}\nabla.U^{*} \tag{4.58}$$

Stage 2 uses the U^* on it rhs, via a Poisson equation over a full time step $(n, n+1)$ to solve for the pressure difference $\left(p^{n+1} - p^n\right)$, utilizing a direct Choleski decomposition method.

Step 3 $$\frac{\mathrm{Re}}{\theta \Delta t}\left(U^{n+1} - U^*\right) = \nabla\left(p^{n+1} - p^n\right) \tag{4.59}$$

Stage 3 corrects the non-divergence free velocity field U^{n+1} using U^* and $\left(p^{n+1} - p^n\right)$ applied through a Jacobi iteration method.

For the **semi-implicit Scheme**, introduced by Hawken et al [1990, and 1991]. A diffusion term is incorporated into the momentum equation in order to enhance stability and circumvent severe time-step size constraint, as given below;

Step 1a becomes

$$\frac{2\mathrm{Re}}{\Delta t}\left(U^{n+\frac{1}{2}} - U^n\right) = \left(\left(\nabla.T - \mathrm{Re}U.\nabla U\right)^n - \nabla p^n\right) + \nabla.\mu\left(D^{n+\frac{1}{2}} - D^n\right) \tag{4.60}$$

Step 1b becomes

$$\frac{\mathrm{Re}}{\Delta t}\left(U^* - U^n\right) = \left(\left(\nabla.T - \rho U.\nabla U\right)^{n+\frac{1}{2}} - \nabla p^n\right) + \nabla.\mu\left(D^* - D^n\right) \tag{4.61}$$

For the **finite element/finite volume sub-cell scheme**, the results from the flux distribution and source contributions are applied to the two-step simple predictor corrector approach for the viscoelastic stress constitutive equations (4.54) and (4.56) as,

$$\tau^{n+\frac{1}{2}} = \tau^n + \frac{\Delta t}{2}\left(Q - \frac{R}{\Omega}\right)^n, \tag{4.62}$$

$$\tau^{n+1} = \tau^n + \Delta t\left(Q - \frac{R}{\Omega}\right)^{n+\frac{1}{2}}, \tag{4.63}$$

refer to finite volume section (4.3) for expressions of R and Q.

Boundary conditions: Once the domain has been discretised with nodes and interpolation functions selected, appropriate boundary conditions are then specified. For this purpose, Dirichlet and Neumann boundary conditions are deployed. At fixed outer boundaries where Dirichlet conditions apply, the trial field variable is set to zero and solutions values are not calculated (Dirichlet conditions). On other boundaries, natural weak form solutions are incorporated in the full equation system (Neumann conditions).

To implement the finite element formulation for the TGPC algorithm, a space of test function ϕ is introduced for the momentum equation and ψ for the incompressibility constraint. The differential equation are multiplied by the test function and integrated over the domain using the Gauss divergence theorem. On those parts of the boundary where Dirichlet boundary conditions apply, the components of the test function vanishes, whereas under non-Dirichlet boundary conditions, the corresponding boundary integral applies.

4.5 Gradient recovery scheme

Velocity and velocity gradients appear in the constitutive equations for the solution of the stress equations. Accurate calculations of these velocity gradients enhance the stability and accuracy of the finite element discretization. At fixed boundaries in a domain, velocity gradients and stress values can be large. It is here that Dirichlet recovery of velocity gradient fields assists to capture highly accurate discrete representation of the finite element solution. There are two main techniques which can be used for gradient recovery; a local direct method [Hawken et al. 1991 and Matallah et al. 1998] and a Galerkin least squares method. The Galerkin method can either be global or locally. For the purpose of this work, a local direct method is selected for its superior properties. With this method, there is avoidance of large matrix storage, in that; the finite element gradient contributions are locally averaged for each node in a triangular element. For the mid-side nodes, average velocity gradients benefits from superconvergence properties [Levine 1983 and 1985] and for vertex nodes, gradient values include an average element contribution and the average mid-side nodal value. With quadratic interpolation of the six nodal recovered gradients per element, the velocity gradient components are local in nature and discontinuous from one element to another. The expression for velocity gradient is written in the form;

$$G_k^e(x,t) = \frac{\partial u}{\partial x_k}(x,t) \tag{4.64}$$

where k = 1, 2. The velocity vector can be approximated by the finite element interpolating function with N number of nodes to give;

$$u^h(x,t) = \sum_{j-1}^{N} \phi_j(x) u_j(t) \tag{4.65}$$

The velocity gradient components for each element are based on local element information. By combining the two equations above, the velocity gradients may be calculated directly as;

$$G_k^{e,h}(x,t) = \sum_{j-1}^{N} \frac{\partial \phi(x)}{\partial x_k} u_j(t) \tag{4.66}$$

4.6 Free-surface location

Some of the boundaries associated with the application of coating flows involve free surface movement and these can be computed with various techniques; the Largragian/ALE approach and the volume of fluid (VOF) approach. The VOF approach splits the domain into wet and dry sections. The interface between the wet and dry regions defines the free surface. This method is orientated about an Eulerian approach, where fluid flows over a fixed mesh (solid/dry section). The free surface deformation is modelled on the fluid through a purely axial movement and axial mesh mapping redistribution strategy.

The ALE technique is powerful in describing the dynamics of the space-time domain. This technique is applied through the concept of a mesh velocity allocation, combining both a Largragian and an Eulerian framework.

The local kinematic condition is another suitable procedure to govern the evolution of the deforming flow domain using a height function [Sujatha et al. 2006].

$$\frac{\partial h}{\partial t} = v_y - u_x \frac{\partial h}{\partial x} \qquad (4.67)a$$

This method is adopted in this thesis for the modeling of free surfaces in the coating application. This approach was earlier employed by Phan-Thien [1988] to determine the deformation of the flow domain. In this approach, the free surface is estimated from a previous solution using a height function which must be updated at every time step.

For flat free surfaces, the above equation (4.67a) applies, with constant y-coordinates. Whereas, on curved free boundaries, polar coordinates apply as,

$$\frac{\partial h}{\partial t} = v_r - u_\vartheta \frac{1}{r}\frac{\partial h}{\partial \vartheta} \qquad (4.67)b$$

where u = $u = (u_\vartheta, v_r) = \left(\frac{\partial \vartheta}{\partial t}, \frac{\partial r}{\partial t}\right)$ is the velocity vector and $h = h(r, \vartheta, t)$

Surface solution re-projection: To satisfy the zero normal velocity boundary condition at the free surface, $(v_r n_r + u_z n_z = 0)$, where $(n_r n_z)$ components of unit normal to the free surface, the domain may be re-meshed and nodal coordinates modified. This is done by projecting the velocity solution onto the new surface positions.

4.7 Convergence criteria

For the finite element scheme, the solution convergence is monitored through a convergence criterion satisfaction of which enables termination of the program. A suitable error estimation criterion is expressed as;

$$\| E(x) \|_{\infty} = \frac{\| x^{n+1} - x^{n} \|_{\infty}}{\| x^{n+1} \|_{\infty}} \leq e \tag{4.68}$$

Chapter 5

Modelling combined-separating flows *

Combined-separating incompressible flow of Newtonian and inelastic Herschel-Bulkley fluids were studied numerically employing a semi-implicit Taylor-Galerkin pressure correction algorithm, where steady solutions are obtained through a transient finite element procedure. The influence of inertia and fluid rheology is analysed on flow patterns, velocity fields and pressure drops for various flow configurations, with fixed geometric specification on gap-width that stimulates the merging and splitting in the flow. Initially, Newtonian fluids were simulated for this benchmark problem, and the numerical procedure was verified with good agreement against previous numerical and experimental observations. To extend consideration to non-Newtonian inelastic materials, the material rheological characteristics were approximated with the use of the Herschel-Bulkley model, incorporating Ostwald-de Waele Power-law and viscoplastic yield stress approximations. Corresponding solutions for unyielded power-law fluids are observed followed by a variation of the consistency index. Devoid of shear-thinning and increasing yield stress, Bingham model solutions have been investigated and under Herschel-Bulkley modelling, some changes were apparent in rheological response.

*Material in this chapter have been published in the paper "Modelling with viscous and viscoplastic materials under combining and separating flow configurations" by S. O. S. Echendu, F. Belblidia, H. R. Tamaddon-Jahromi, M. F. Webster in *Mechanics of Time-Dependent Materials, November 2011, Volume 15, Issue 4, pp 407-428.*

5.1 Introduction

Combined-separating flows occur as most important unit operations in chemical engineering applications, and many configurations involve complex fluids. The term "mixing" (here, used as merging of flows) attributes mainly to the process of reducing the degree of non-uniformity or gradient of a particular property, that is, concentration, viscosity or colour [Chhabra and Richardson, 1999]. Most of these fluids include polymeric liquids with a variety of rheological behaviour ranging from Newtonian to viscoelastic. These types of fluid processing procedures are abundantly found in the food industry, liquid manufacturing, steel processing, pharmaceutical, chemical petroleum and oil industries. They can include different classes of non-Newtonian materials, such as, polymers, paints, food products and drilling fluids [Bird et al. 1983; Barnes et al. 1989; Tanner and Walters. 1998; Tanner 2000; Bird et al. 1977]. Focusing on the assumptions of a simple single-phase liquid mixing flow around a horizontal cylinder with incompressible fluids, ignoring heat transfers, mass transfers or any chemical reaction, complications can arise with highly viscous Newtonian and non-Newtonian materials.

In practical situations, combined-separating flows may occur in industrial or biomedical processes, for instance, to produce a uniform product, separate or blend fluids as occurs under swallowing of food stuffs [Nicosia 2007; Nicosia and Robbins. 2001] transported down the pharynx and oesophagus. Concerning the swallowing impaired, the correct functioning of the throat valve strongly influences flow splitting alongside food material characteristics. In this research, an investigation is conducted using finite element modeling to analyse the Newtonian and non-Newtonian fluid flow of a merging and splitting flow through a channel. Under Newtonian conditions, the study concentrates on the flow patterns that result under various boundary conditions and an inertia parameter analysis. This covers variation in Reynolds number, velocity fields and pressure drop. For this a finite element simulation of the flow configuration is presented, based on a semi-implicit Taylor Galerkin Pressure Correction Algorithm [Townsend and Webster. 1989; Hawken et al. 1990]. The flow is analysed for a variety of bifurcations to investigate the influence of inertia on Newtonian flow under various flow settings. With reference to a mixing and separating flow cited in the literature [Cochrane et al. 1981; Walters and Webster, 1982], where both unidirectional and reverse-directional flow occur simultaneously, this benchmark problem manifests flow characteristics for both Newtonian and non-Newtonian fluids and the analysis of the numerical solutions generated for this complex flow.

Newtonian fluids are both shear-rate and strain-rate independent, manifesting a constant shear viscosity, zero first normal stress difference, and a constant extensional viscosity. Yet, there are other fluid types that exhibit somewhat different rheological response. For Bingham fluids, flow commences only when shear stress reaches a certain limit; therefore there is presence of yielded and unyielded flow regions, observed from early studies on entry and exit flows of Bingham Fluids by Abdali et al. [1992]. Savreux and Jay [2007] studied viscoplastic fluid mixing in a rotating tank, observing static and moving unyielded zones, and the disappearance of vortices as yield stress was introduced. Marouche et al. [2002] performed studies on the numerical modeling for such yield stress fluids in a mixing vessel and Zisis and Mitsoulis [2002] worked on viscoplastic flow around a cylinder held between

parallel plates. All authors observed the appearance of yielded and unyielded zones as yield stress was introduced. To accommodate this scenario, where both flow and no-flow occur simultaneously, several modifications to the constitutive equations have been proposed and this includes viscous regularization, where a smooth transition in stress is mathematically ensured as shear-rates asymptote to vanishingly small values [cf. Papanastasiou 1987].

Inelastic-viscoplastic rheological behaviour can be represented using the Herschel-Bulkley (HB) model, which incorporates Ostwald-de Waele power-law and a viscoplastic yield stress approximations. Previous research has shown several type of viscous regularization method for Herschel-Bulkley model. Zhu et al. [2005] studied non-Newtonian fluid with yield stress; proposing a generalized model found to be better than the Herschel-Bulkley-Papanastasiou model. Rudman et al [2004] studied pipe flow of shear thinning fluids using the Herschel-Bulkley model; Alexandrou et al. [2003] studied flow instabilities for Herschel-Bulkley fluids (employing a regularized Herschel-Bulkley-Papanastasiou model) and verified the importance of having a finite yield stress for Herschel-Bulkley flows;. also, Alexandrou et al. [2001] studied steady Herschel-Bulkley flow in a three-dimensional expansion (employing a regularized Herschel-Bulkley-Papanastasiou model). All authors found good qualitative agreement with experimental data.

Summarizing, the Herschel-Bulkley form is the most general choice from the constitutive model employed in the present work for material representation, which incorporates the Power-law (inelastic) and Bingham models (yield stress). Initially, unyielded-inelastic power-law properties are resolved, with shear-thinning behaviour observed for (m) less than unity, and Newtonian response achieved with m=1. Subsequently, viscoplastic analysis is conducted via the Bingham model (shear independent), with parameterization over increasing levels of yield stress. Finally, full Herschel-Bulkley modeling combines analysis for inelastic behaviour with the viscoplastic response.

The present flow problems of interest have been investigated numerically with validated experimental evidence by Cochrane at al [1981], Walters and Webster [1982] (experimental, finite difference solutions) and Baloch et al [1995(b)] using a transient finite element approach that employed a pressure-correction scheme. The flow domain and problem is that of two thin insert plates positioned along the horizontal central plane of a channel and parallel to the channel walls with a separating gap between the two plates. Previous studies [Baloch et al. 1995(b)] have employed thin plates and various merging and separating configurations with comparison for three different plate separation gap-width s and increasing flow rates. These authors employed a network model, Phan-Thien/Tanner (PTT), to represent the behaviour of a Boger fluid, and demonstrated numerically the effects of variations in gap-width, inertia material parameters, increasing elasticity and flow conditions. Recently, Afonso et al. [2010] studied viscoelastic flows in mixing-separating cells using finite-volume techniques, to assess the effects of Deborah number (De), Reynolds number and gap size on the two-dimensional flow dynamics. They employed the upper-convected Maxwell model to describe the creeping flow of viscoelastic fluids. The flow configurations follow from the previous studies by Cochrane at al. [1981], Walters and Webster [1982] and Baloch et al. [1995(b)]. Result shows that for Newtonian creeping flow, the ratio of the reversed flow-rate increases with increase in gap size. For viscoelastic flows, below a critical

and supercritical gap-size, increasing Deborah number slightly enhances the reversed flow and leads to a consistent increase in reversed flow-rate ratio. Additionally, various techniques have been used by other researchers to examine flow characteristics in typical mixing and separating configurations. Sendilkumar et al. [2007] studied the fluid mixing characteristics in a jet mixer for Newtonian and non-Newtonian fluids using computational fluid dynamics. That study involved flow patterns that result inside a jet mixer under a number of configurations. These authors focused mainly on the mixing time, when comparing Newtonian and non-Newtonian fluids under different jet nozzle configurations. Findings revealed that Newtonian fluids showed a better flow pattern on the streamlines and mixing times were far less than those for non-Newtonian fluids. Moreover, Fox et al. [1956] studied single-phase blending of liquids, also focusing on the mixing time; results indicated that the mixing time is dependent on the jet Reynolds number. Jayanti [2001] studied the hydrodynamics of jet mixing using CFD analysis and showed the effects of flow circulation patterns in the reactor. Until recently, most researchers in this area have concentrated on jet mixers, striving to correlate the mixing time to a factor of the jet Reynolds number.

In the context of the present study, the model problem manifests dominant flow splitting and separating characteristics. Here, the consequent kinematics and the various bifurcations that arise are demonstrated, to reveal the effects of increasing inertia on vortex development, velocity fields and pressure drops. In doing so, the problem concentrates on a channel configuration with thin insert plates, fixed geometric gap-width and equal flow rates in all channel arms, whilst varying boundary conditions. Steady solutions were obtained through a transient finite element approach that employs a semi-implicit incremental Taylor-Galerkin pressure-correction Scheme, developed in the earlier work of [Hawken et al. 1990; Keshtiban et al. 2008]. This leads to a time-stepping algorithmic framework, with multiple and fractional-staged equations performed within each time step.

5.2 Computational domain and specifications

The details of the particular combined-separating flow problem considered are presented schematically in Fig. 5.1. The insertion of the plates into the domain creates two inlet and two outlet channel arms of equal dimension on opposing sides of the partition and a plate-separation gap of width β. The plate-separation gap considered is $\beta = 2.875L$, where L is a characteristics length taken as the height of an inlet channel arm. The thickness of the plate is taken as $\alpha = 0.1L$ and a sufficiently long length of channel of 23L is selected to reflect fully developed flow at entry and exit of the domain.

In order to compare our numerical approach directly with Baloch et al. [1995(b)], the specification in Fig. 5.1a has been considered as the standard benchmark problem. Firstly, creeping flow of a Newtonian fluid was simulated until fully developed steady conditions are reached. Then, increasing levels of inertia were introduced by varying the Reynolds number. This permits an analysis of the influence of inertia on the flow patterns, velocity fields and pressure drops (analogous to a time-dependent flow with increase of flow-rate). Firstly, a Poiseuille flow was generated in the two-dimensional domain as presented in Fig. 5.1a. Here, the Newtonian problem employs a Poiseuille-type flow at both inlets to the channel and both channel exits, with stationary boundary walls. Secondly, in order to vary the geometric-flow

design of the problem, a separating flow is presented in Fig. 5.1b. Here, the Newtonian problem employs a Poiseuille-type flow at only the top inlet of the channel, with exit flow permitted at all other channel-flow boundaries.

The two-dimensional flow domain was discretised through structured triangular elements, employing a mixed-order Taylor-Hood type of finite element with piecewise-continuous quadratic interpolation for velocity and linear for pressure. Then, velocity nodal variables are located at the vertex and mid-side nodes, whilst pressure variables are restricted to the vertex nodes only. Three meshes were explored and in all three such cases, converged solutions were achieved with minimum influence of the mesh size. As illustrated in the zoomed mesh representations of Fig. 5.2, Mesh 1 employs 800 elements, Mesh 2 has 3200 elements and Mesh 3 has 12800 elements. Comparing the mean velocity component at the central inlet and outlet region on both channel arms in each of the three meshes, a spatial convergence rate of $h^{3.57}$ was estimated, as shown in Fig. 5.3. In assessing quality of mesh convergence, reference is taken to the most highly refined mesh with 12800 elements.

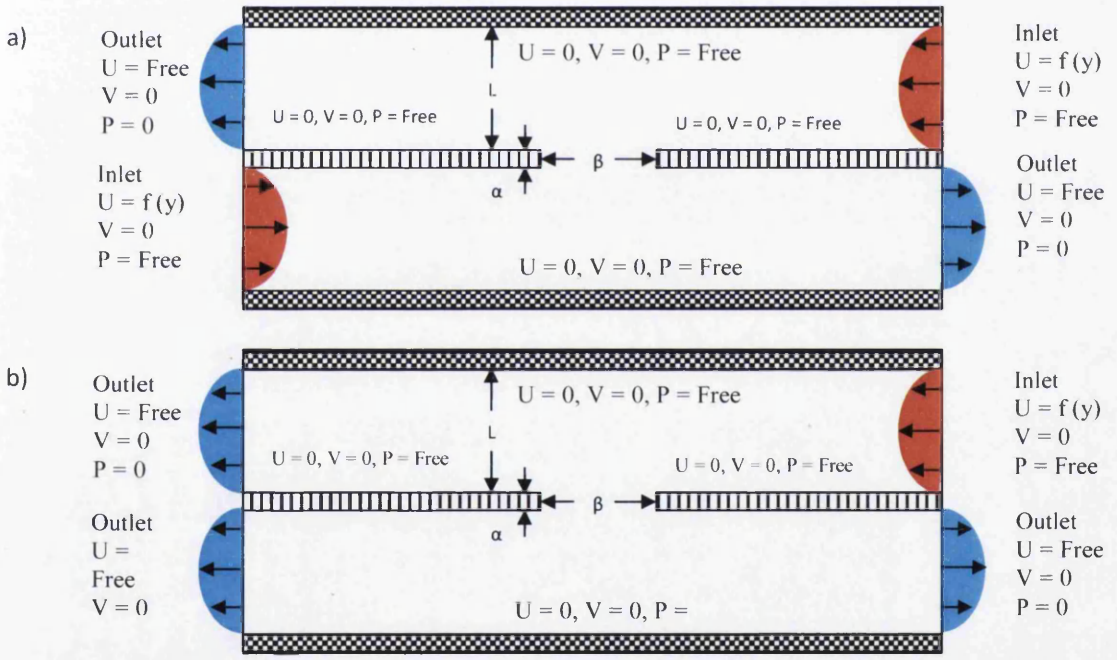

Figure 5.1: Boundary conditions: (a) combined-separating flow, (b) separating flow

Considering a spatially bounded domain with piecewise smooth boundary and a temporal domain, under incompressible isothermal flow conditions. The fluid properties of density and viscosity are constant. Therefore, the system of equations governing the Newtonian steady flow problem, are the continuity equation for the conservation of mass and the momentum equation (see chapter 2). The numerical algorithm employs a temporal-spatial Galerkin finite element approach, Taylor-Galerkin Pressure-correction scheme for viscous and inelastic flows. Here, the resulting Navier-Stokes and inelastic equations (see Chapter 2 and 3

respectively) are solved together with the incompressibility constraint using a semi-implicit incremental time-stepping procedure. The scheme is based on a fractional-step method (described in Chapter 4), utilising semi-discretization in the temporal domain, through a Taylor series expansion in time [Donea 1984] and a pressure correction procedure, to extract a time-stepping scheme of second-order accuracy [Van Kan 1986].

a) Mesh 20x20

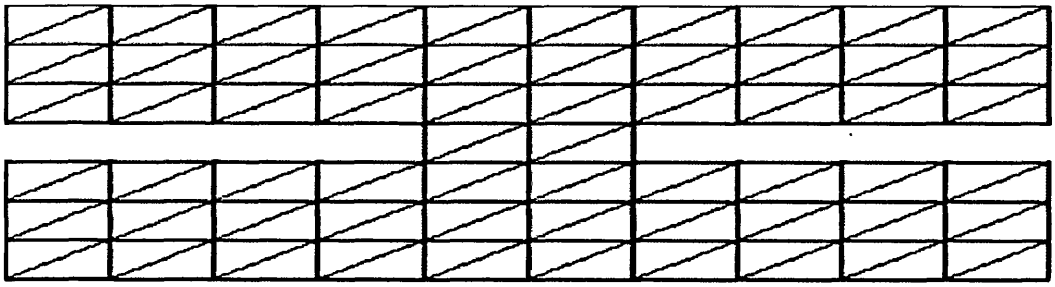

b) Mesh 40x40

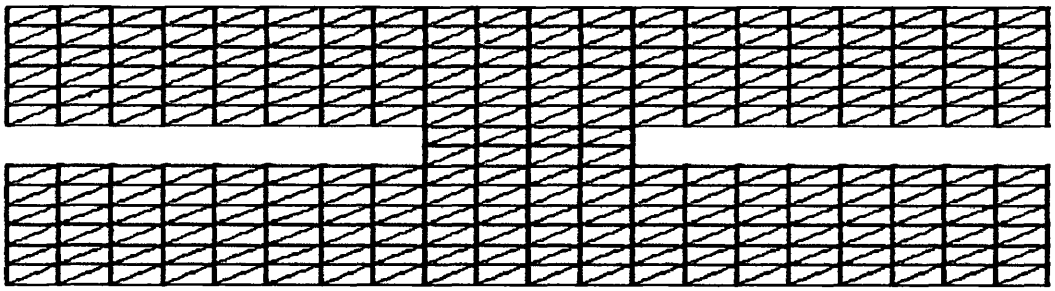

c) Mesh 80x80

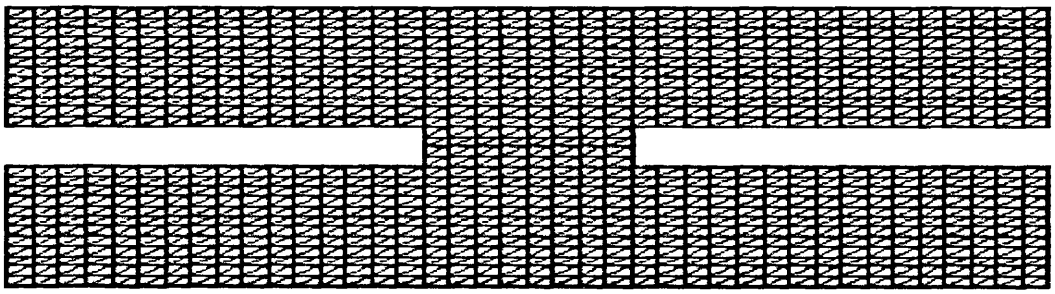

Figure 5.2: Zoomed section of meshes: (a), coarse, (b), medium and (c), refined.

5.3 Newtonian flow solutions

This study of combined-separating flow of a Newtonian fluid through a 2D planar-channel was performed on various bifurcations of different type of flow boundary conditions. In this

section, the numerical results governing the investigation into the influence of inertia on flow streamline patterns, vortex size, velocity field and pressure drops are presented. These results were obtained numerically using the computational meshes presented in section 5.2. Previous numerical observations validated against experimental results were available, therefore this instance was chosen as an appropriate benchmark test problem. The flow domain for the problem, of Fig. 5.1, was discretized into triangular elements. The mesh design was such that the minimum size of element was 0.025L. A finite element mesh of the domain consists of 12800 total numbers of elements, 25921 total numbers of nodes and 1900 total boundary nodes. Typical time-steps involved were $\Delta t=10^{-4}$ for Newtonian flows. Steady state solutions are extracted subject to a time-stepping relative increment tolerance of 10^{-6} employing five mass iterations per Jacobi step.

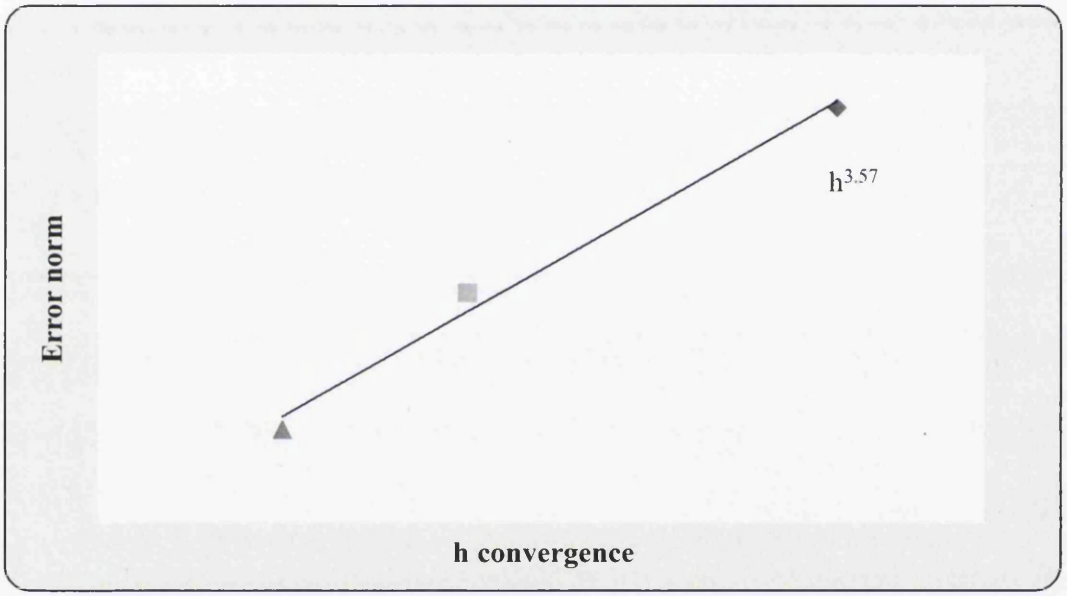

Figure 5.3: Spatial mesh convergence, based on mass conservation: combined-separating flow

5.3.1 Influence of inertia

Streamline patterns: Flow patterns in a combined-separating flow configuration (Fig. 5.4a) are an important feature, found useful to establish the presence of stagnant regions, and the efficiency of the overall flow process. Herein, solutions are analysed by presenting streamline patterns that are plotted at equal intervals in each of the two flow regions of reversed and unidirectional flow. The type of flow pattern representation is that of stream traces, these depending mainly on the geometrical domain of the flow process. The particular flow domain used is important in that it aids determination of the bulk flow and the quantification of vortex formation (relatively static zones). In order to interpret the effects of inertia, with increasing Reynolds number, the flow of a Newtonian fluid has been examined and numerical predictions are presented for the wide-gap geometry (β=2.875L). It is observed that the flow responds to the presence of the gap and breaks up, with some flow

reversal and flow merging in both upper and lower exit sections of the geometry. For a relatively low Reynolds number flow, viscous forces dominate those due to inertia and these prove sufficient enough to sustain unidirectional flow throughout the channel.

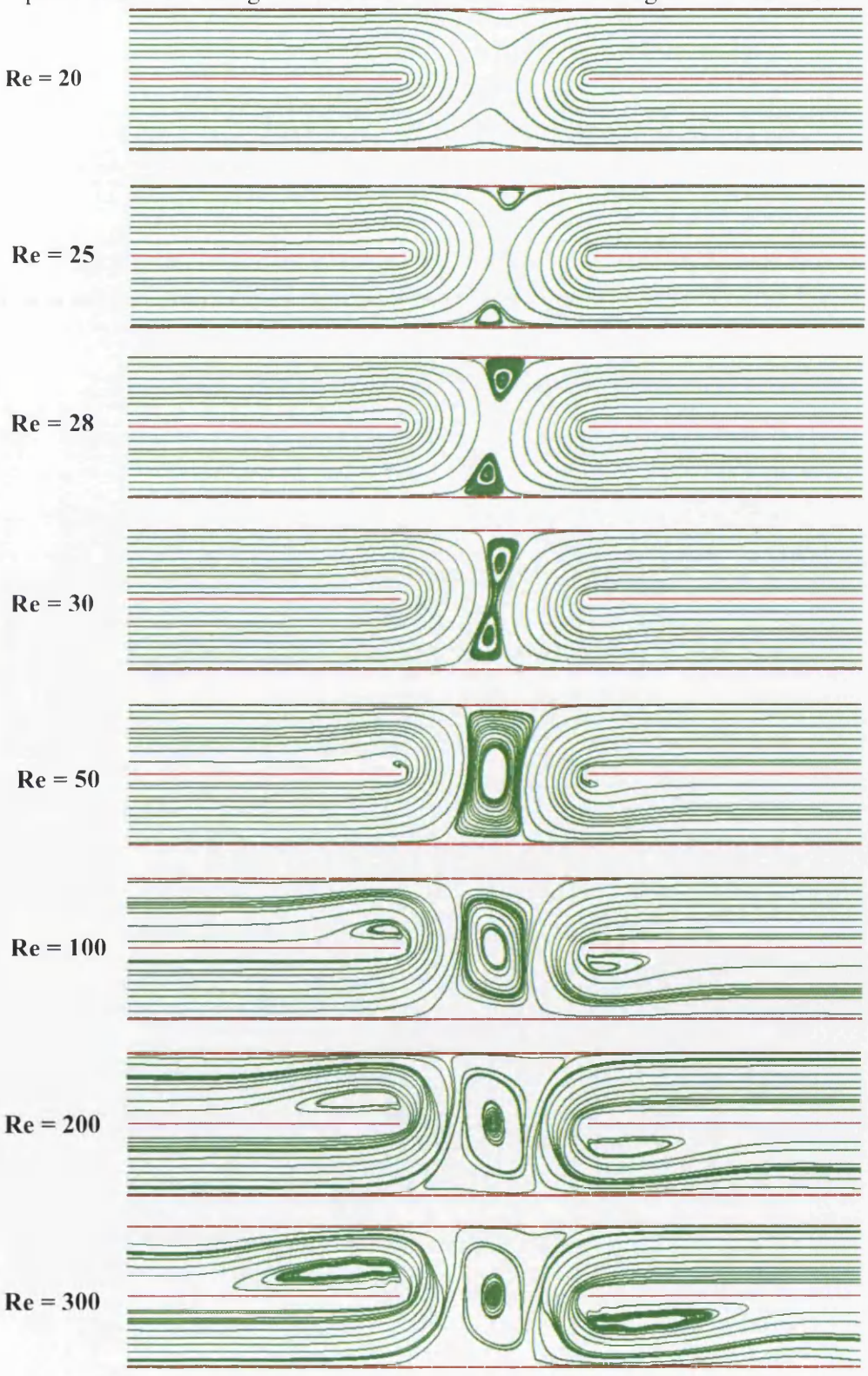

Figure 5.4: (a) Streamline patterns: Newtonian combined-separating

For a Poiseuille-type separating flow (see Fig. 5.4b), solutions are obtained up to Reynolds number Re=20 without significant change in flow structure, with two stagnant regions emerging from the solid channel walls in the middle of the geometry. With increasing inertia (25<Re<50), these stagnant regions begin to recirculate and grow in size, being symmetrically placed with respect to each other and about the central horizontal and vertical lines of symmetry through the geometry. In this progression, for 25<Re<30, a pair of twin vortices form, which strengthen and collide to form one large vortex in the central geometric gap of the domain. A zoom behind the centrally positioned insert plates in the exit flow channel arms (100<Re<300), reveals the formation of recirculating vortices (from around Re~100), lying parallel to the plates initially and becoming more inclined away from the plates as the level of inertia increases, with the strength of the central vortices decreasing somewhat to compensate. These observations lie in close correspondence with available numerical observations [Walters and Webster. 1982; Baloch et al. 1995(b)] validated against experimental results up to Re=30.

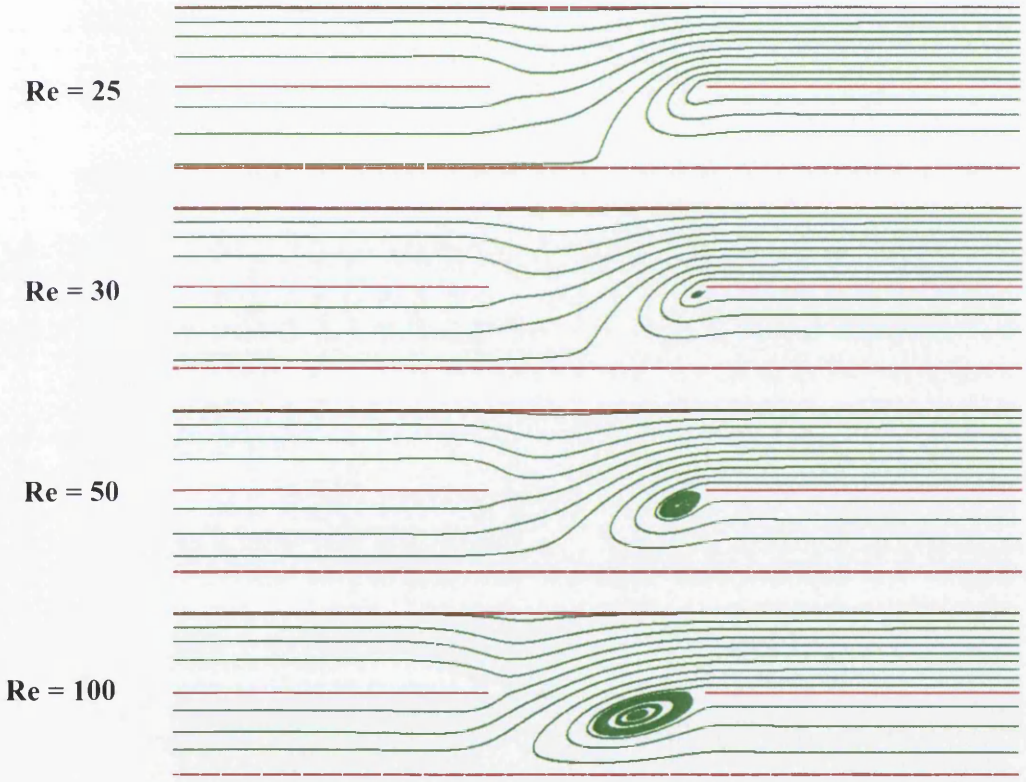

Figure 5.4: (b) Streamline patterns: Newtonian separating flow

For the simulation of a Poiseuille-type Newtonian separating flow (typical representation of a Newtonian-like food system in the swallowing canals [Nicosia and Brasseaur 2002]) through the 2D domain as in Fig. 5.1b, the streamline patterns generated are recorded in Fig. 5.4b, with results obtained up to Re=100. Vortices were observed at Re=30 and above. From these observations, the outcome illustrates how a food-like material, classified as Newtonian fluid,

would flow through a separating channel. In particular, a distinct vortex is observed to be initiated just behind the plates at the center of the channel. This reflects the sort of anticipated patterns that might emerge in the vicinity of the epiglottis, at the end of the pharynx and at the opening to the oesophagus (gap reflecting an open value setting), during a typical swallowing process. These vortices are further developed and expanded at Re=50 and above.

Velocity profiles: In Fig. 5.5, the velocity profiles along the (lower-red and top-green) centre of the channel arms are shown for the Poiseuille-type combining-separating flow. From such graphs, one may clearly observe the impact on the velocities due to the development of the vortex. Up to Re=20, no vortex development is observed; this can be gathered from the distinct gap between the bottom flow and the top flow, as Reynolds number increases. This gap decreases leading to the initial development of the vortex at Re=25. This central vortex, once formed, then fully develops as shown at Re=50, where the two velocity profiles overlap each other. Also a tiny vortex, which begins to form behind the insert plates, is apparent here at Re=50, as the velocity suddenly increases just passed the geometric gap. Both the central vortex and the vortex behind the insert plates, fully develops as Reynolds number is increased up to Re=300. The two line-plots in the graph reveal that, whatever changes occur to the fluid velocity profiles in the lower channel arms also occur in the top channel arms.

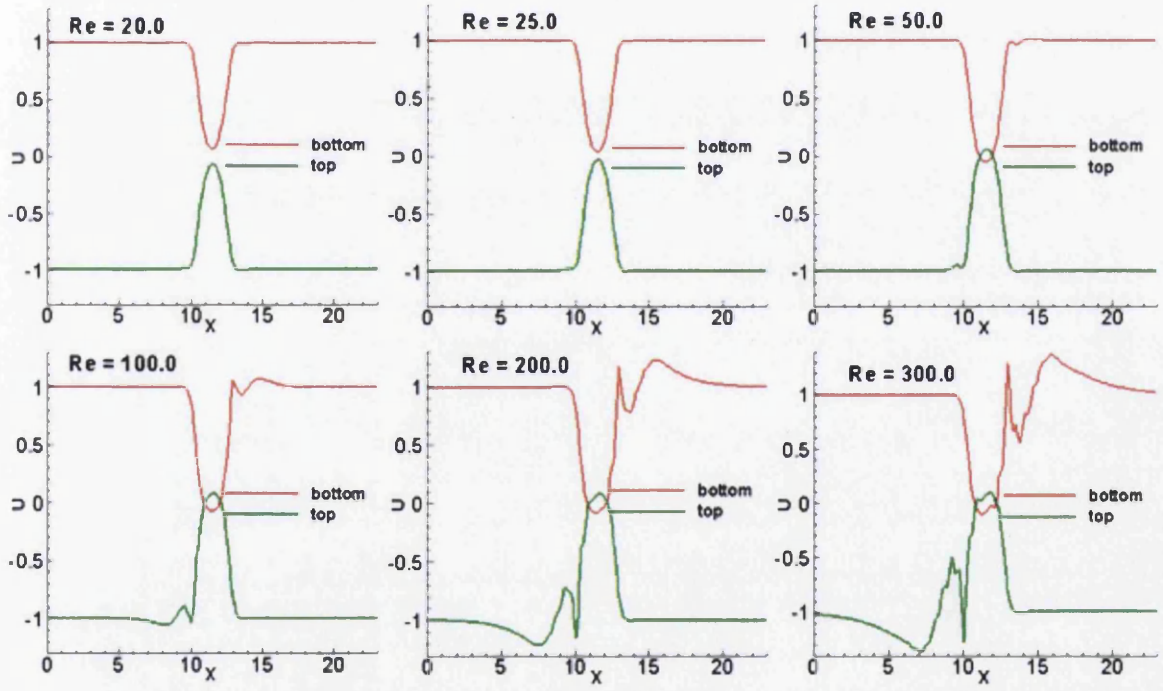

Figure 5.5: Variation of velocities with increasing inertia

The total velocity differences demonstrate the velocity drop from entry to exit for both the lower and top channel arms. As Reynolds number increases from Re=20 to 300, the perturbation in velocity across the geometric gap increases, and hence the total velocity differences gradually rise. There is a rapid increase in the velocity differences from

50<Re<300, this observation reflects the influence of inertia on the velocities as the large central vortex develops.

Pressure profiles: The pressure profiles are observed along the centre x-axis of the bottom channel arms. The results are shown in Fig. 5.6 and are useful in determining the growth-path of vortex development. Vortices are formed around areas of low pressure and these zones attract the fluids towards its centre. From Fig. 5.6, one observes that both inlet flows are drawn towards the channel-centre and respond to the presence of the gap; this results in an increase in pressure towards the centre of the channel. With an increase in inertia/flow rate, the fluid pressure also increases, causing higher pressures at the channel-centre zone. From the streamline patterns for Poiseuille-type flow, vortex development is clearly visible at Re=25, where the level of inertia/flow rate of the fluid causes the pressure to slightly increase towards the channel-centre. This same trend is observed with increase in Re up to 50. At the larger levels, from Re=100 to 300, due to the rapid increase in pressure towards the inlet channel arm, a decrease in pressure is observed towards the outlet channel arm, causing another vortex to form behind the insert plates. From the streamline patterns, this vortex is clearly appearing by Re=100, which correlates as shown in Fig. 5.6 with a decrease in pressure. The numerical solutions demonstrate that as the Reynolds number rises, the pressure across the channel also increases.

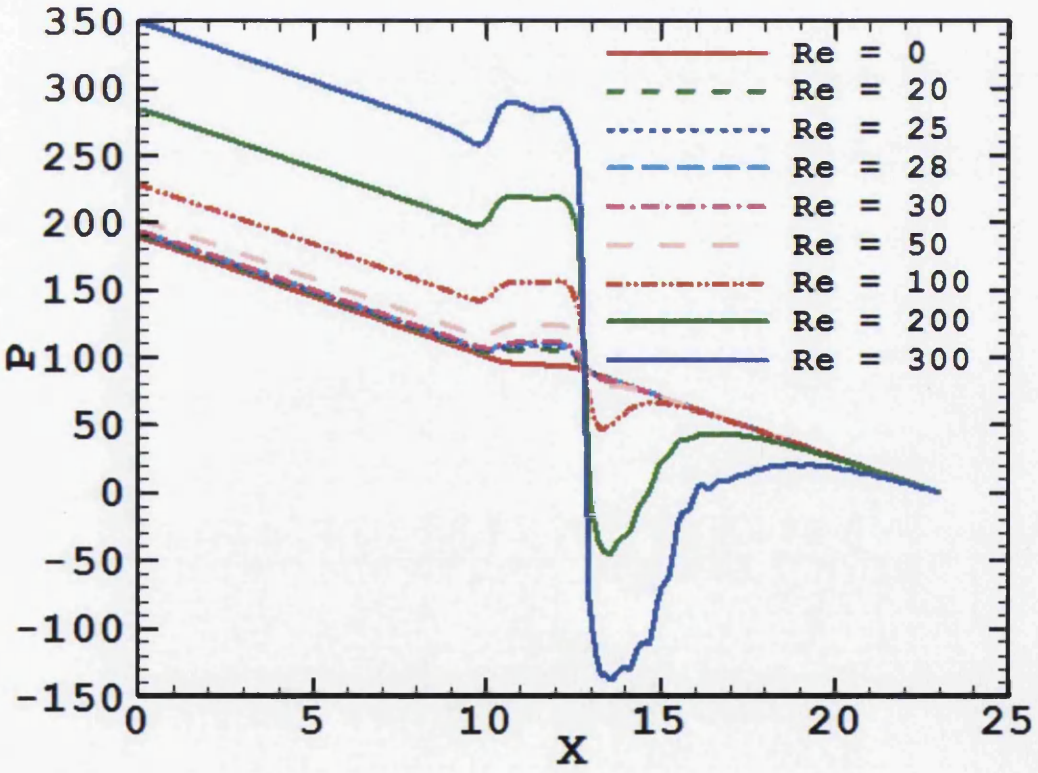

Figure 5.6: Pressure profiles along the bottom channel arms with increasing inertia

5.4 Inelastic and viscoplastic flow solutions

Following the above analysis, it is instructive to give some consideration to material change and introduce yield stress effects, via inelastic and viscoplastic fluid representation. Hence, again, the combined-separating Poiseuille-type flow configuration was considered (of Fig. 5.1a), through a 2D planar-channel. As above, the mesh discretization was precisely that used for the earlier Newtonian flow, with the minimum size of element as 0.025L, 12800 total numbers of elements, 25921 total numbers of nodes and 1900 total boundary nodes.

These inelastic and viscoplastic flows are characterized under three parameters, through the combination of power-law model and Bingham model. These three parameters are the power-index m, the consistency index k, and the yield stress τ_0. As such, one is interested in studying the independent variation of these parameters and investigating the corresponding effects upon the resultant steady-state solutions.

5.4.1 Inelastic shear-thinning power-law representation

Focusing on the combined-separating flow configuration, the first parameter of interest is the power-index m, which manifests itself through the fluid viscosity, so that when m<1 shear-thinning behaviour is apparent (see chapter 3, Fig. 3.3 for material function). Typical pseudo-plastic fluids used in industrial applications, include starch solutions, emulsions, paints and some drilling muds. In this work, particular interest lies in analyzing the effects of variation in the power-index (m) and consistency index (k), on the flow.

5.4.1.1 Effects of variation in power-index (m)

Vortex development: The vortex development with power-index (m) is shown in Fig. 5.7, under a consistency-index of unity, k = 1.0. Here simulations were conducted for Re=25 and Re=50 in the moderate thinning range of 0.7<m<0.9, in order to observe the vortex development patterns. From Fig. 5.7a, (Re = 25) the trends show that decreasing m affects the development of the vortex by slightly increasing the size of the vortex formation, at the top and bottom channel-centre zones. Also, in Fig. 5.7b, with a decrease in m, a vortex formed behind the insert plates, at Re=50 and m=0.9, which develops slightly more as m was decreased to 0.8.

Velocity profiles: Fig. 5.8 shows the velocity variations with decreasing m for shear-thinning fluids, focusing on the mixing flow region and the flow along the bottom channel arms. As m was reduced, the maximum core-velocity in the bottom channel arm is observed to decrease with increased shear-thinning; this position is maintained along the channel. The velocity reduces rapidly towards the channel-centre, where the recirculation takes place, and the departing flow increases rapidly in velocity up to that of inlet flow. From Fig. 5.8, at the beginning of the outlet channel arm, a small variation in velocity is observed, highlighted on the graph; this variation is caused by the vortex formation behind the insert-plates, as shown in the streamlines patterns of Fig. 5.7a. At m=0.9 and up to m=0.7, the vortex is not visible in the streamline patterns, but a small variation in velocity is observed, as in Fig. 5.8. Hence, this data signals the onset and initial development of this vortex.

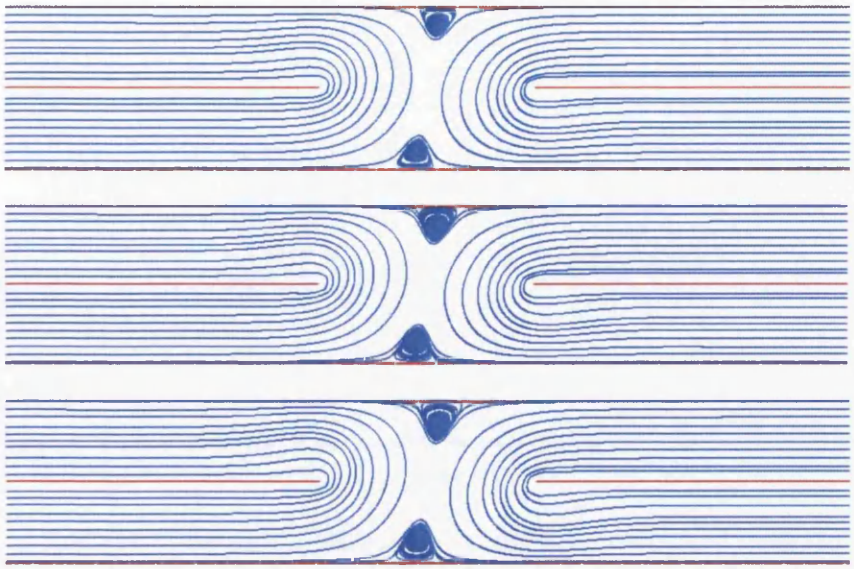

Figure 5.7: (a) Effect of power-law index *m* on vortex size for combined-separating flow (Re=25, *k*=1)

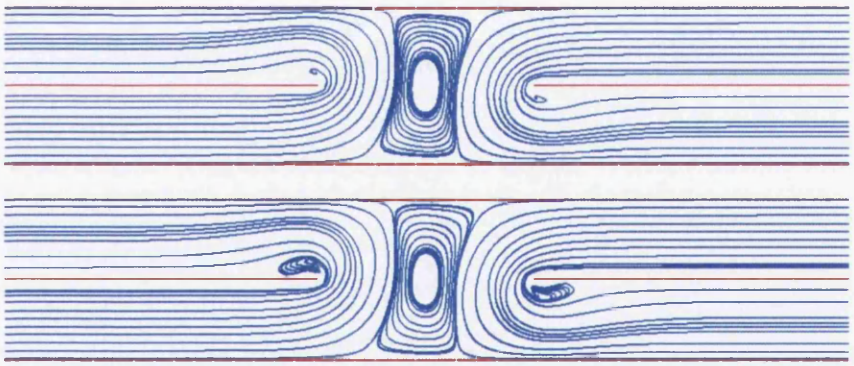

Figure 5.7: (b) Effect of power-law index *m* on vortex size for combined-separating flow (Re=50, *k*=1)

Velocity difference relates to the decline in velocity from U_{max} to U_{min}. It is observed for shear-thinning fluids that as m decrease the velocity differences increase. Viscosity of the fluid decreases as power-index m increases, and the maximum shear rate also decreases with increasing m. Typical fluids with these types of viscosity and shear rate variations include natural polymeric fluids used in the liquid manufacturing industries. The increase in the viscosity of these fluids causes an increase in resistance to flow due to the internal fluid friction, and hence, velocity differences increase with distance normal to the flow direction.

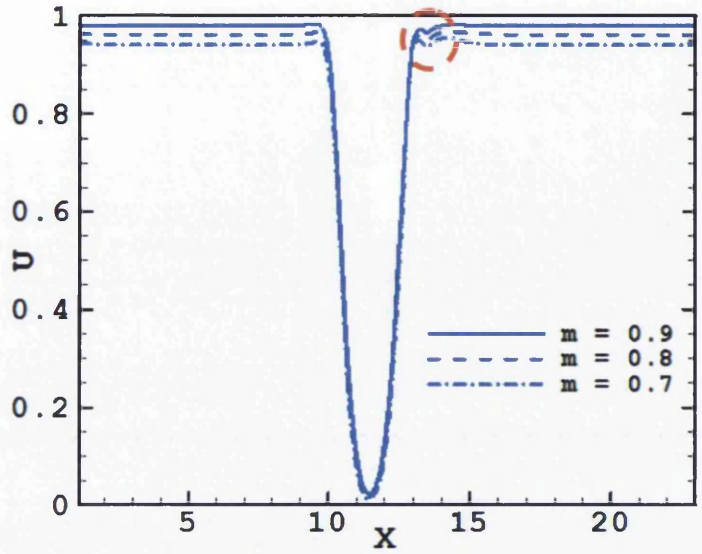

Figure 5.8: Velocity profiles along the bottom-channel arms with power-law index *m* (Re=25, *k*=1)

Pressure profiles: The variation of pressure against power-index m is monitored through the effect on the pressure profiles for the bottom channel arm, as illustrated in Fig. 5.9. It is observed that as m decreases, there is somewhat of a decline in pressure across the channel. Hence, for example with m=1, the pressure at the inlet is at the level of 192 units; then as m is decreased to 0.9, the pressure reduces to 168 units; at m=0.8 and 0.7, the pressure gradually drops to 146 and 126 units, respectively. This explains why there is an increase in vortex size with decreasing m, as shown in Fig. 5.7.

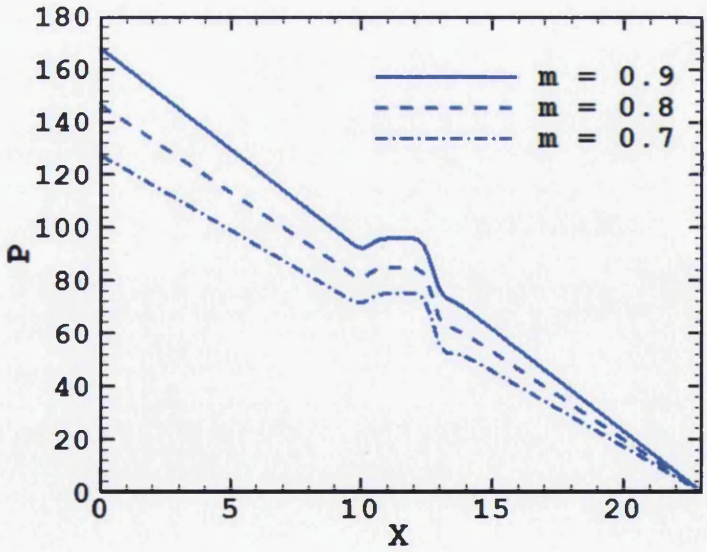

Figure 5.9: Pressure profiles along the bottom-channel arms with power-law index *m* (Re = 25, *k* = 1)

5.4.1.2 Effects of variation in consistency-index (k)

Vortex development: The second parameter of interest is the consistency index k. Adjustment in this parameter also causes viscosity change in the steady solutions generated. Based on power-index of m=0.7, at Re=25, the streamline patterns generated may be analysed as a function of the consistency index k, through values of k=0.75, k=0.5 and k=0.25, as shown in Fig. 5.10. It is clearly observed that as k is decreased, the twin vortex, which begins to form at the centre of the channel, fully develops into a large vortex. A second vortex is also visible behind the insert-plates, and this further develops at k=0.5 and k=0.25. This response in behaviour remains valid for other levels of shear-thinning fluids likewise.

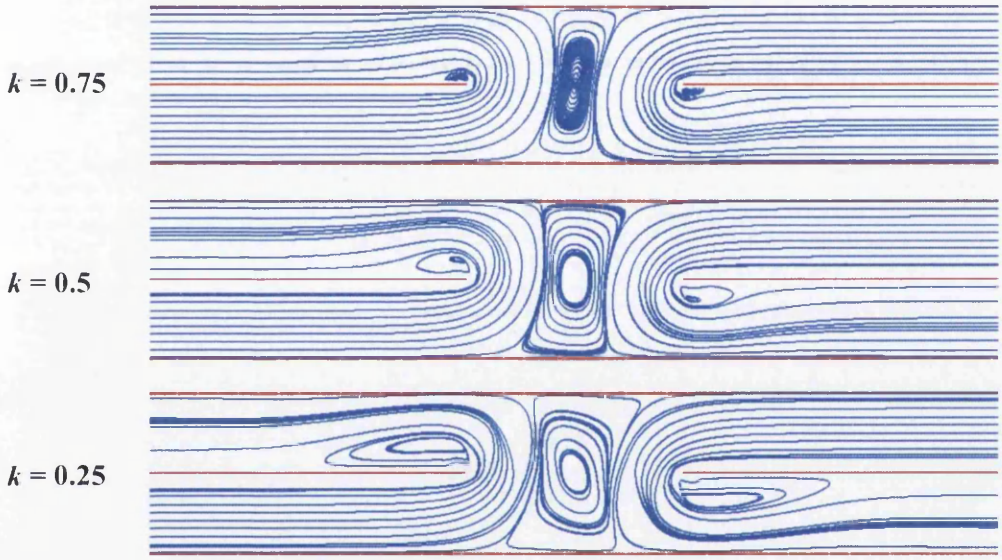

Figure 5.10: Effects of consistency-index *k* on vortex size (Re=25, *m*=0.7)

Velocity profiles: The analysis of the velocity profiles across the channel, as a function of k, is illustrated in Fig. 5.11. This shows the variation of velocity with decreasing k and shows the impact this has on vortex development. Towards the centre of the channel and behind the insert plates, varying velocity profiles are observed, leading to the development of the vortex, as seen in Fig. 5.11. With decreasing k, the fluid viscosity decreases, therefore the internal friction of the fluid decreases which leads to less resistance to flow and hence elevates levels of deformation rate. Hence as k decreases, the velocity difference is seen to rise.

Pressure profiles: The pressure profiles, as a function of the consistency index k, are shown in Fig. 5.12. The trends show that as k decreases, the pressure at the inlet drops rapidly. At k=1, the pressure level lies initially at 128 units; as k is reduced to k=0.75, k=0.5 and k=0.25, the pressure reduces to 98, 68, and 40 units, respectively. Therefore with lower k values, equivalent flow structures are achieved, but sustained by lower pressure drop at the inlet. With increasing k, the pressure drop across the channel tends to increase rapidly.

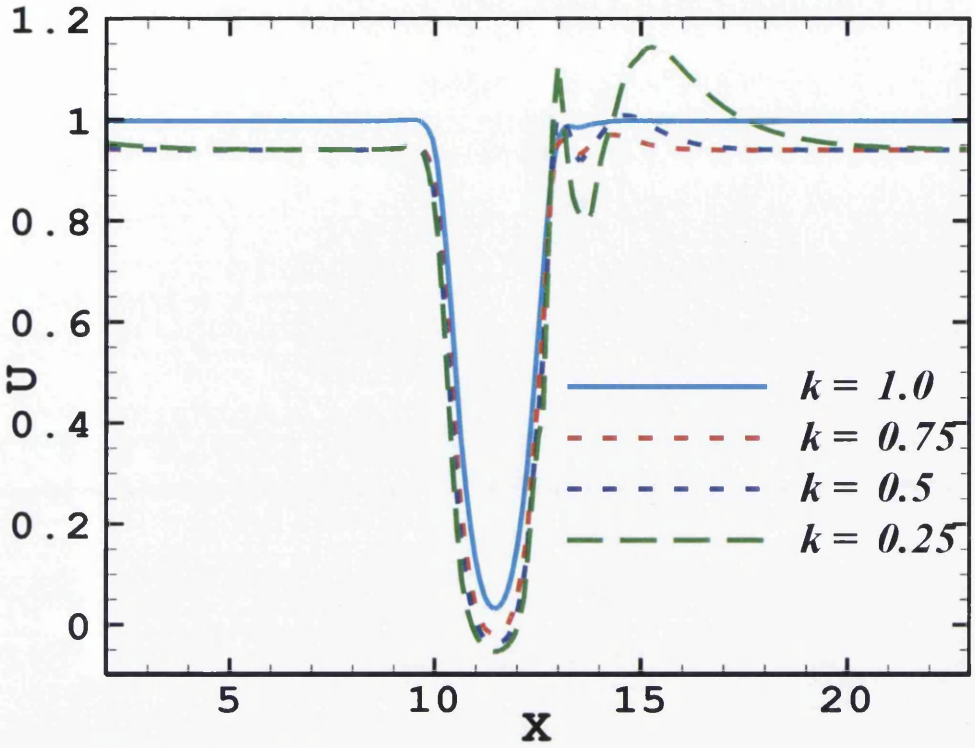

Figure 5.11: Velocity profiles along the bottom-channel arms with consistency-index k (Re=25, m=0.7)

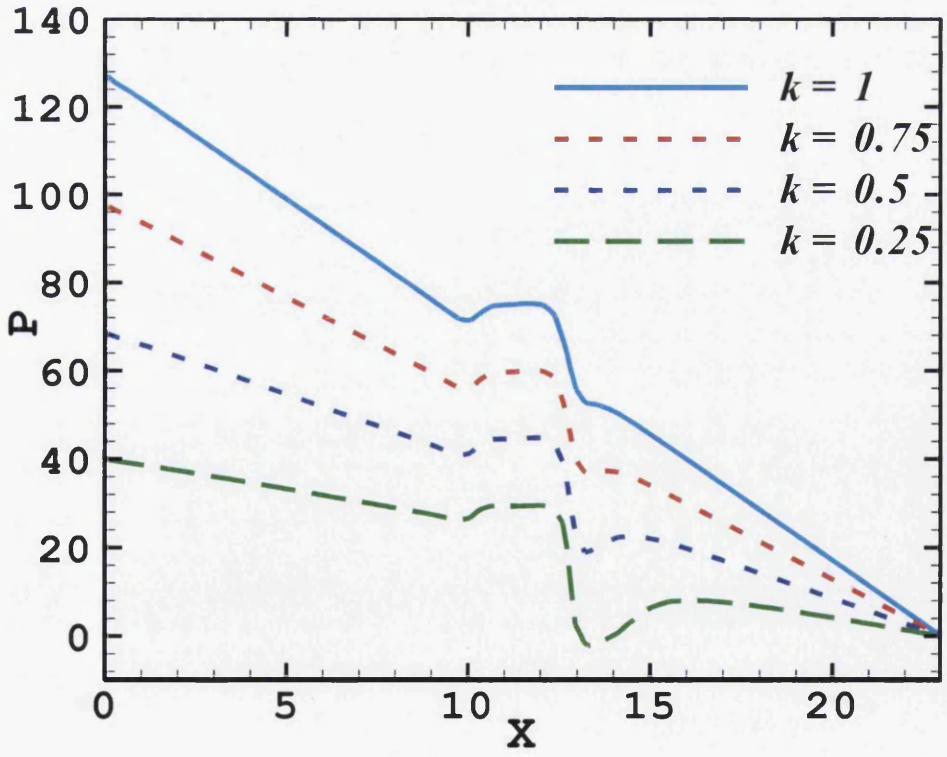

Figure 5.12: Pressure profiles along the bottom-channel arms with consistency-index k (Re=25, m=0.7)

5.4.2 Viscoplastic Bingham yield stress representation

Coal suspensions, slurries, paints, printer inks, sludge are typical viscoplastic-Bingham fluids which can be mixed under industrial processing. Here analysis has been conducted on the influence of yield stress on the flow of such types of fluids in related combined-separating flow configurations.

5.4.2.1 Effects of yield stress (τ_0)

Vortex development: The stream traces for yield stress fluids in these flows are shown in Fig. 5.13. Observations are that as yield stress values are decreased, there is a substantial increase in the size of the vortex region. Hence, for Re=25, at lower values of yield stress ($\tau_0 = 0.001$), vortex formation is observed at the centre of the channel; and these vortices increase in size as yield stress values are further reduced (to $\tau_0 = 0.0001$). It is important to note that when the level of yield stress rises, more inertia is required in order to drive a central vortex. This is in agreement with the observations of Savreux and Jay [2007] that vortices are found to diminish and disappear as yield stress is introduced and subsequently increased.

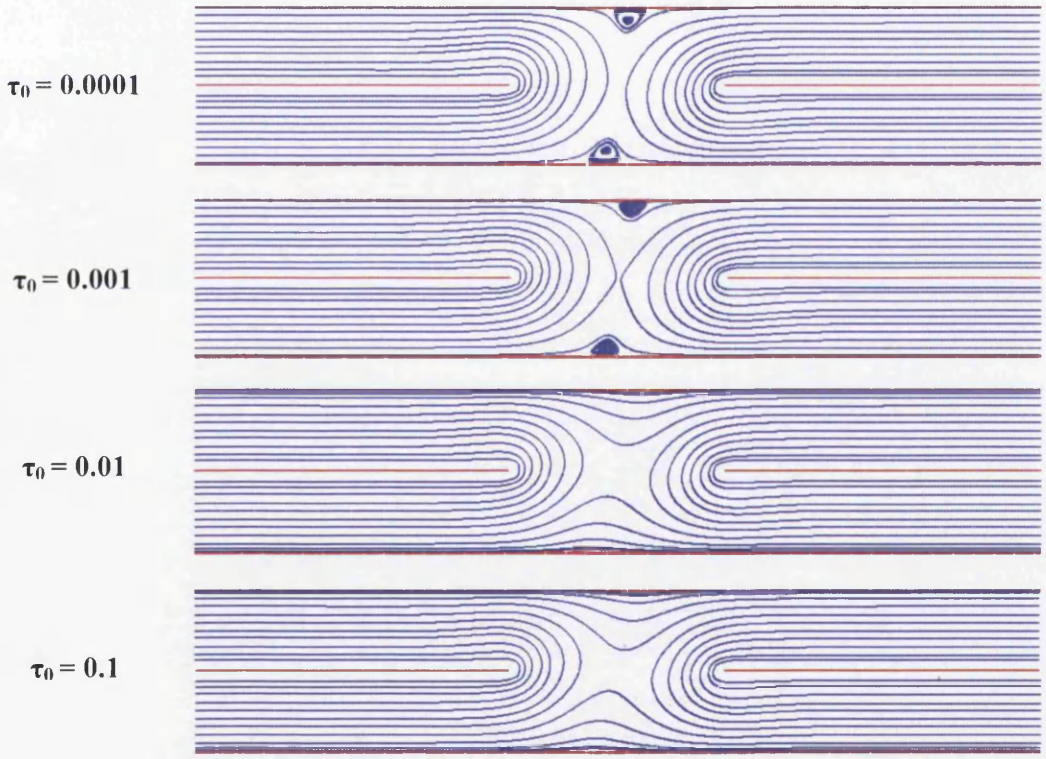

Figure 5.13: Streamline patterns: viscoplastic Bingham fluids (Re=25)

Shear rate and viscosity: The viscosity and shear rate contours as a function of yield stress, τ_0 (Re=25) are displayed in Fig. 5.14. The flow regions at the inlet and outlet walls and around the insert plates are identified as being exposed to high shear rates, therefore the viscosity in these flow-areas tends to be reduced for $\tau_0 = 0.1$ and this is valid for any level of yield stress.

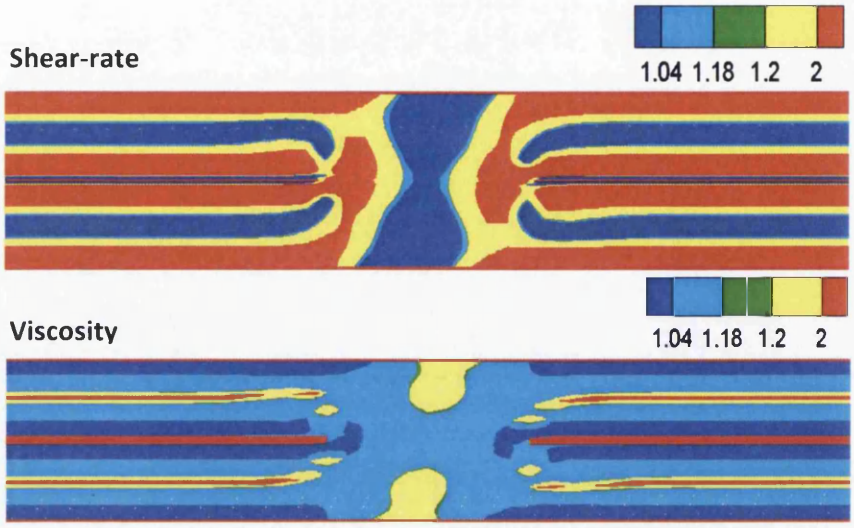

Figure 5.14: Shear rate and viscosity contours across the channel: visco-plastic Bingham fluids, (Re=25, τ_0=0.1)

Yielded and unyielded regions: Fig. 5.15 shows the growth of unyielded regions for the flow of the viscoplastic Bingham fluid across the combined-separating flow domain. The yielding-unyielding cut-off criteria, that captures the interface within the plots, is based on the magnitude of stress exceeding the yield stress level which is set in any given instance (and assessed via deformation-rate). At the relatively large yield stress level of τ_0=0.1, the unyielded region increases and there is no evidence of vortex formation. This is a direct consequence of the lack of any significant deformation present in these zones.

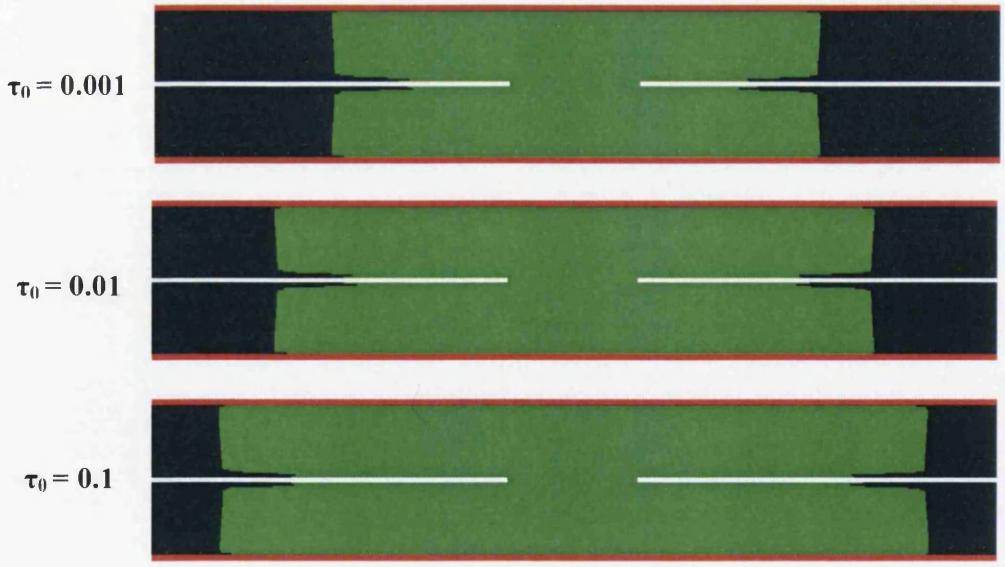

Figure 5.15: Growth of unyielded region (light green): visco-plastic Bingham fluids (Re=25)

5.5 Herschel-Bulkley (HB) flow solutions

This HB-analysis was conducted with the combination of the power-law and yield stress models, at Re=25, m=0.7, k=1.0 and yield stress levels of 0.01, 0.001, and 0.0001 (for combined-separating flow), taking into account variation under the two parameters, the power-law index m and the yield stress τ_0 (see chapter 3, Fig. 3.4a and 3.4b for material function). From Fig. 5.16 and the streamlines patterns for the HB-fluid, observations agree with like trends for the visco-plastic Bingham fluid - that as yield stress increases; the formation of a vortex disappears at yield stress values of 0.01 and above. Also due to the change in the power-index (m) (omitted under Bingham fluid modeling), the vortex size tends to be slightly more exaggerated than that observed with the visco-plastic Bingham fluid. Compared against the power-law fluid at the same levels of power-index (m) and consistency index (k), variations in the streamlines patterns would indicate that there is little to no vortex formation at higher yield stress levels. Fig. 3.4a illustrates the viscosity and shear rate profiles (in log-scale) and tends to explain why there is some vortex formation at low levels of yield stress. With the increase of τ_0 up to yield stress of 0.1, the unyielded region expands with no vortex formation evident at these stress levels (see Fig. 5.17). These observations show clearly the influence of rheological variation on the flow patterns and structures thereof.

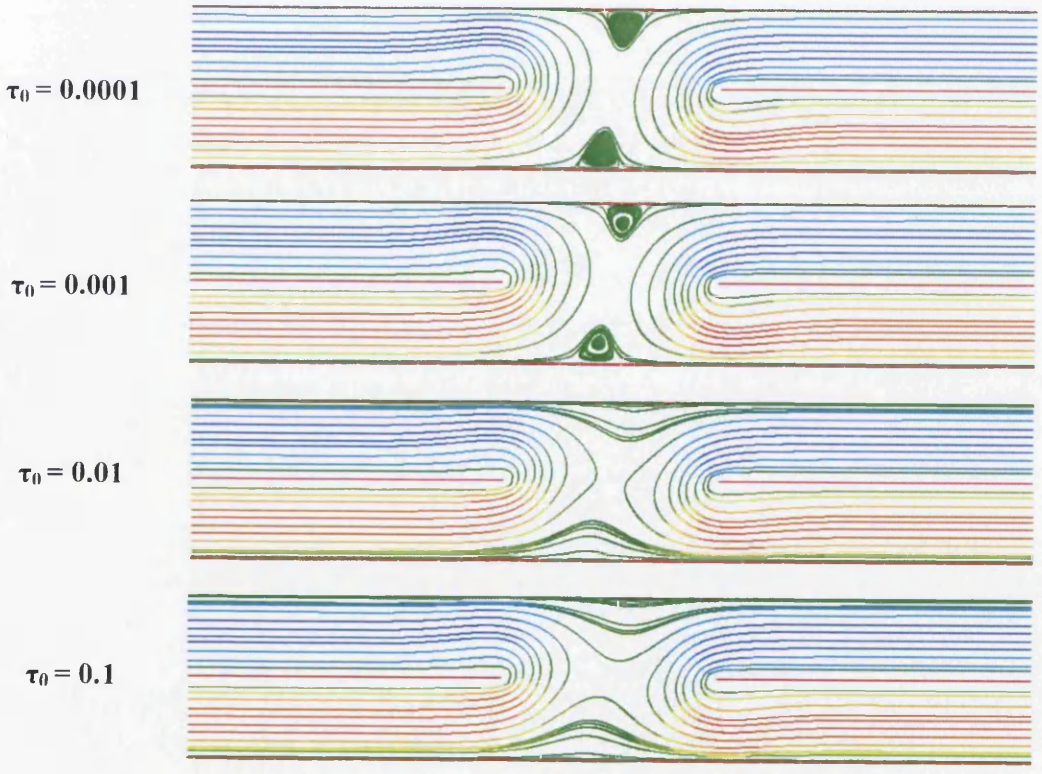

Figure 5.16: Streamline patterns: Herschel-Bulkley fluids (Re=25, *m*=0.7, *k*=1.0)

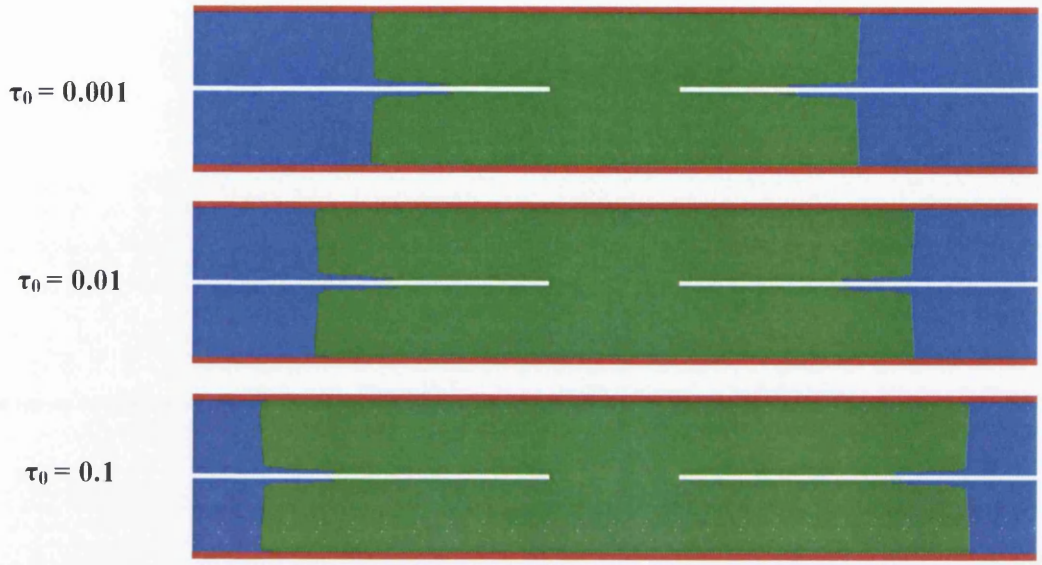

Figure 5.17: Growth of unyielded region (light green): Herschel-Bulkley fluids (Re=25, *m*=0.7)

In comparison for separating flow configurations, some simulations have been conducted for different inertial levels (flow rates) and shear-thinning levels at a fixed yield stress value of τ_0 = 0.01. Observations reveal that at low inertial levels (Re = 50) and high levels of shear thinning (m = 0.6), vortices are again formed under the separating insert plate, as shown in Fig. 5.18a. Then as inertial levels rise to Re = 100, with a decrease in the level of shear thinning (m = 0.8), these vortices expand rapidly due to the prevailing conditions, see Fig. 5.18b. From the shear rate and viscosity contours of Fig. 5.19, one can clearly detect that viscosity levels tend to be extremely low around the inlet wall regions; hence shear rate in these regions will rise.

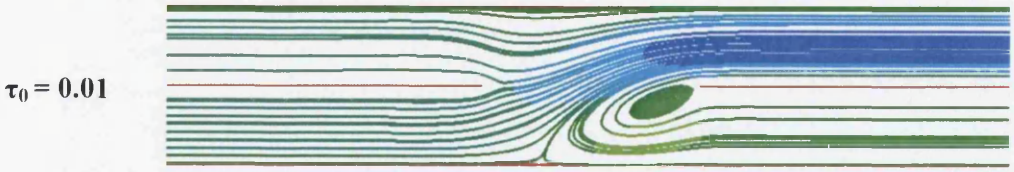

Figure 5.18: (a) Streamline patterns: Herschel-Buckley fluids, Re=50, m=0.6, k=1.0

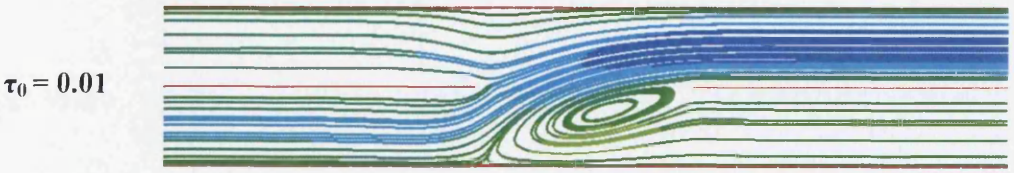

Figure 5.18: (b) Streamline patterns: Herschel-Buckley fluids, Re=100, m=0.8, k=1.0

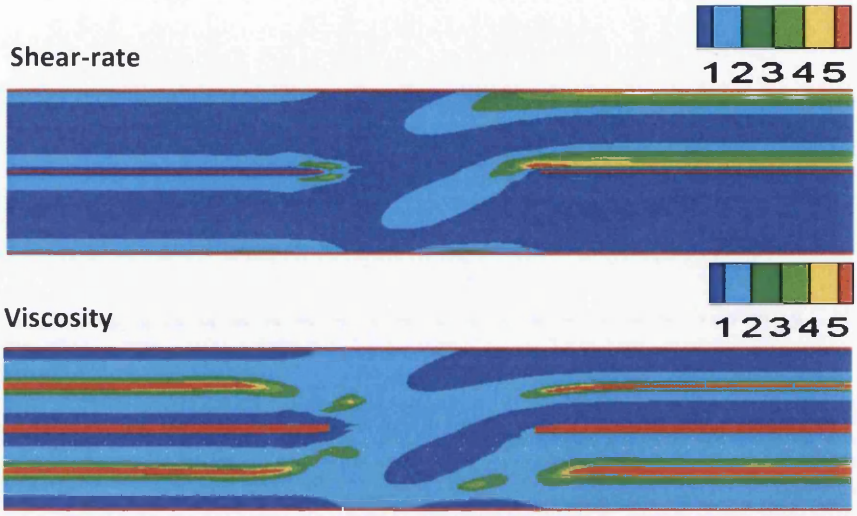

Figure 5.19: Shear rate and viscosity contours across the channel: Herschel-Buckley fluids, (Re=50, m=0.6)

5.6 Overview

Numerical simulation has been conducted for Newtonian and viscoplastic fluid models under combined-separating flow configurations in planar-channels. Solutions are described through streamline patterns, velocity profiles and pressure profiles. The overall study demonstrates the effective performance of a fractional-staged Taylor-Galerkin Pressure-Correction Scheme for these complex inelastic flows, when used in combination with a Herschel Bulkley fluid model and its variants. The numerical solutions generated prove to be qualitatively in close agreement with available numerical and experimental results. The Newtonian problem serves as a benchmark to analyse its prominent features and upon which to introduce fluid rheological properties. Numerical results were obtained for steady flow situations and validated against published data. For Newtonian fluids, the flow was investigated for the influence of inertia under two forms of flow configurations with Poiseuille-type flow, a dual-inlet/outlet combined-separating flow and a single-inlet/dual-outlet separating flow. Corresponding streamline patterns have been extracted from which alternative vortex formations have been observed. For both the dual-inlet flow process and the single-inlet separating flow process, with increasing inertia, flow reversal patterns have been detected, with an increase in the central core vortex sizes, and a vortex was formed behind both insert plates at Re=100 level and above. This trend agrees well with previous experimental and numerical published data. Analysis on the velocity and pressure profiles demonstrates that with increasing inertia, the velocity and pressure also rise across the channel.

Under rheometrical variation, initial consideration was then given to an unyielded fluid, focusing on the effect of power-index m on vortex sizes, velocity profiles and pressure drop. Findings showed that with decreasing power-index m, the vortex sizes slightly increase; the

velocity gradient also increases whilst the pressure gradient decreases. Analyzing the variation of viscosity against shear rate, at low power-index m, larger viscosities were observed in and around the wall regions with lower shear rates. Visco-plasticity was then introduced through a Bingham approximation, taking into account only yield stress variation. Results for this have shown that decreasing yield stress levels, increases the yielded regions in the splitting and combining flow regions. This has led to the formation of a vortex at inertia levels of Re=25 and above; also a slight increase in pressure is observed at yield stress values of 0.01 and above.

Lastly, further investigation has endeavoured to generalize the rheological variation, introducing the Herschel-Bulkley (HB-) model, where there is the combination of inelastic behaviour and yield stress response. Here, and at the larger yield stress levels of 0.1, there is then little to no vortex formation at inertial levels of say around Re=25 (providing vortex suppression characteristics).

Chapter 6

Reverse roll-coating: computational investigation*

This chapter introduces the industrial flow problem where computational techniques are sought to investigate flow through a high-speed defect-free reverse roll coating application. The study aims to develop an effective predictive toolset for high-speed defect-free coatings. The computational domain involves the transfer of a coating fluid from a roller to a moving substrate (reverse mode) up to the nip-region. Time-stepping finite element methods are deployed to model the free-surface problem, in conjunction with a set of constitutive equations (for Newtonian and inelastic flows) capable of describing the relevant fluid-film rheology in appropriate detail. Flow structures and quantities of pressure, lift and drag have been calculated stream-wise across the flow domain and findings are applicable to a wide range of coating sectors in optimisation of coating performance, targeting adaptive and intelligent process control. Further analysis has been conducted, mimicking the presence of a wetting line, whilst varying boundary conditions at the nip, and several relief mechanisms are observed to the positive peak-pressures generated around the nip-zone. Through an elasto-hydrodynamic formulation, the elastic deformation of a rubber roll cover (elastomer) was introduced. This has offered fresh insight into the process with respect to nip-flow behaviour, which allows for the analysis of both positive and negative nip-gaps.

*Material in this chapter have been published in the paper "Reverse roll-coating: a computational investigation towards high-speed defect free coating" by F. Belblidia, H. R. Tamaddon-Jahromi, S.O.S. Echendu, M. F. Webster in *Mechanics of Time-Dependent Materials, December 2012, DOI 10.1007/s11043-012-9204-y*

6.1 Introduction

Roll coating is used extensively in the application of functional organic coatings onto strip steel, in the application of water-borne adhesives to tapes and in structural laminating applications. This process involves coating one side of a substrate (web, sheet) with a fluid formulation as it passes between co-rotating cylindrical rollers (reverse roll mode). As such, film and foil converting applications are considered, being the second most commonly used coating application technique that is after rotogravure. As a process, roll coating is highly versatile, but requires a technically skilled operator to maintain consistency. Currently, the application of coated strip steel in the construction industry is diversifying into more novel functions such as the use of photovoltaic coatings for solar energy collection or coatings that afford acoustic protection. More importantly, there is a continuous drive towards increased coating line-speeds for reasons of economy, whilst maintaining the requirements of controlling film weight and freedom from defects.

From previous studies, (Chandio et al. 2002a, 2002b, 2001) developed a numerical scheme for Newtonian flows, based purely on finite element methodology with free-surface prediction in time. Transient instabilities were analysed with varying speed ratios. Observations reveal that flow instabilities were stimulated upon increase in foil-speed rather than roll-speed. Industrially, a major drawback is presented through the occurrence of flow instabilities at high line speeds, which cause defects that take the form of 'ribbing' of the applied coating (3D effects). To date, there has been considerable focus on the mechanistic origins of such instabilities, mainly based on numerical modelling in which the liquid coating is represented as a Newtonian fluid (as a first approximation) – the onset of ribbing being associated with a critical capillary number (Ca). However, from a practical industrial perspective, a straightforward empirical correlation does not exist between the rheology of a given coating, and the line-speed marking the onset of instability. Generally, such industrial coating liquids contain a number of polymeric additives and surfactants, which may significantly affect the operating conditions, as well as product quality. When minute amounts of polymer are present, the onset of instabilities may occur at much lower line-speeds than for Newtonian coatings (Zevallos et al. 2005). Notwithstanding this fact, still the majority of theoretical work undertaken to date has employed Newtonian fluid approximation.

The proposed study seeks to address these issues and aims to develop effective predictive software tools for use in the development of high-performance coatings, capable of consistent application at high speeds. The work involves the application of novel approaches to the predictive modelling of the free-surface of the coating fluid (i.e. meniscus height in the applicator nip, wet-film thickness transferred to substrate) used in conjunction with constitutive equations capable of describing the fluid-film rheology in appropriate detail (shear-thinning, tension-thinning/thickening, elasticity). The findings of this research are applicable across a wide range of coating sectors in optimisation of coating performance (see review of Mackerle 2005). The ultimate research goal is to develop adaptive-intelligent control of the roll coating procedure to allow for rapid optimisation of machine variables and process productivity.

Coyle et al. (1990c) furnishes the appropriate background material on finite element (fe) studies, and experimental studies for reverse roller coating (RRC) with non-Newtonian fluids. Findings have revealed that at high speed-ratios and large capillary numbers, the metered film flow deviates somewhat from lubrication theory prediction. Also, Fourcade et al. (1999) investigated fluid-solid interaction in a reverse roller-coating process, focussing principally on the deformation of the elastomer on the coated roll. Similarly, Cohu et al. (1997) conducted experiments on forward roller-coating for Newtonian fluids between deformable rolls, with the primary aim of predicting the coating thickness. Informatively, Carvalho et al. (1997) studied the effect of soft-roll deformation with respect to the onset of ribbing. Their main findings showed how a deformable cover may be used to lessen the ribbing on the liquid layer to achieve a required coating thickness. Additionally, Hao et al. (1999) employed a Galerkin fe-method to analyse the reverse roll coating process. They demonstrated that roll-speed ratio is the most significant factor influencing the process, and that a critical speed ratio always exists, observing significant increase in Reynolds (Re) and capillary numbers (Ca) with increasing speed ratio. Ascanio et al. (2004) performed an experimental study on a Newtonian fluid in a deformable nip-gap within a high-speed forward roll-coating process. No cavitation was generated as the negative peak-pressure was not sufficiently low when compared with the vapour pressure of the fluid. Fernando et al. (1988) investigated the importance of dynamic uniaxial extensional viscosities (DUEVs) relative to shear viscosity and viscoelastic parameters. That is, with regard to the onset of ribbing, web growth, and fibre formation in roll-coating applications, where they used non-Newtonian water-soluble polymer blends. Experiments on various blends with increasing DUEV, whilst maintaining identical shear viscosities over a given shear rate range up to $10^4 s^{-1}$, pointed to the fact that this provoked earlier onset of ribbing. Once ribbing has onset, these authors observed a decrease in the number of ribs under increasing DUEV (associated with growth in web-size). Hence, there is compelling evidence that extensional properties are significant in the process. Moreover, in a pertinent and recent computational study, Zevallos et al. (2005) investigated forward roll coating with viscoelastic fluids using Oldroyd-B (constant shear viscosity, strain-hardening) and FENE-P models (shear-thinning, strain-hardening). They employed a fe-method, and found that liquid elasticity has a greater propensity to destabilise the flow. At any given surface tension level (governed by Ca), there was a critical Weissenberg number (We) above which the flow became unstable. Furthermore, one may refer to Mmbaga et al. (2005) for discussion on the topic of treatment of dynamic wetting lines.

On purely experimental grounds, four categories of coating flows were classified and reviewed by Benkreira et al. (1994). These are: free, metered, transfer and gravure coating flows. In addition, Benkreira (2002a) has analysed the movement of the dynamic wetting line in reverse-roll coating in a series of experiments, providing conditions for dynamic failure that may occur due to air entrainment (Benkreira 2002b). Most recently, Benkreira and Khan (2008) examined experimentally the effect of reduced air pressure on dynamic wettings for dip-coating. To assess the role of air/gas viscosity and substrate roughness on dynamic wetting failure, a series of silicone oils (of various viscosities) were tested in a vacuum chamber, allowing for the pressure to be reduced, along with various substrates of differing degrees of roughness. This allowed these authors to gather data capturing the effects of viscosity, roughness and air pressure on dynamic wetting line conditions. Benkreira and Ikin

(2010) also assessed experimentally the role surrounding air/gas viscosity importance in dynamic wetting, a factor that has been missing in more fully describing the wetting phenomenon. The authors concluded that as processing speed increases, the viscous forces exercised by the liquid predominate over surface tension forces resulting in thin pockets of entrained air. Furthermore, findings also confirmed the complex role of roughness, in increasing or decreasing air entrainment speed, depending on the value of the viscosity on the coating solution. Alternatively, a two-roll apparatus was used by Gaskell et al. (2000) to investigate the detailed fluid mechanics of meniscus roll coating, in which inlets were starved and flow rates were small. Both forward and reverse modes of operation were investigated using optical sectioning, combined with dye injection and particle imaging techniques. Similarly, Ascanio et al. (2006b) presented a technique for measuring the pressure distribution of Newtonian fluids flowing through a deformable nip-gap created between rolls, counter-rotating at high speed. They employed a high sensitivity piezoelectric transducer mounted on the rigid roll of a laboratory film coater.

The present study advances the earlier research findings cited (Chandio et al. 2002a, 2002b, 2001) in a number of different aspects listed below, where the roll coating parameters involved have been subdivided into distinct groups:

(i) The operating conditions of roll-speed;
(ii) Variation of nip-gap between rolls;
(iii) Boundary conditions adjustment at the nip (as pressure relief mechanism 1);
(iv) Slip conditions at the nip (pressure relief mechanism 2);
(v) Inelastic representation of fluid properties (pressure relief mechanism 3);
(vi) Roll-cover properties consisting of roll-radius, elastic/plastic/viscoplastic cover material and layer thickness (as relief mechanism 4).

In particular, this work focuses on the effects of parameter variation on the process and analysis of the film rheology.

6.2 Computational domain and specifications

The region of interest in the present analysis of the reverse roll coating line is identified in Fig. 6.1. In recognising appropriate boundary conditions for this problem, all nodes attached to the foil-substrate are assigned with the velocity of the foil. The substrate coating thickness is chosen as the characteristic length (L) and the foil-speed is set to the characteristic velocity (U_F), so that the standard setting yields a non-dimensional foil velocity of unity (U_F=1). Since foil-roller velocity ratio is an important quantity, the standard roller velocity setting equates to that of the foil, providing a ratio of unity (thus, U_R=1). Initially during this first phase of the work, no-slip velocity boundary conditions are applied on all solid surfaces. At the nip-region (end of the flow domain considered), a finite miniscule gap of about 1% of foil thickness (calibration length-scale), is assumed to separate the roller and substrate moving surfaces.

The inflow at the roller, and the coating outflow, on the foil-substrate, are set assuming plug-type flow, ensuring an overall mass balance, so that the flow-rate at the roller ($Q_R = U_R\, h_R$)

equates to the flow-rate at the foil ($Q_F = U_F\ h_F$). This ensures that the desired film thickness is achieved through $h_F = h_R\ U_R/U_F$.

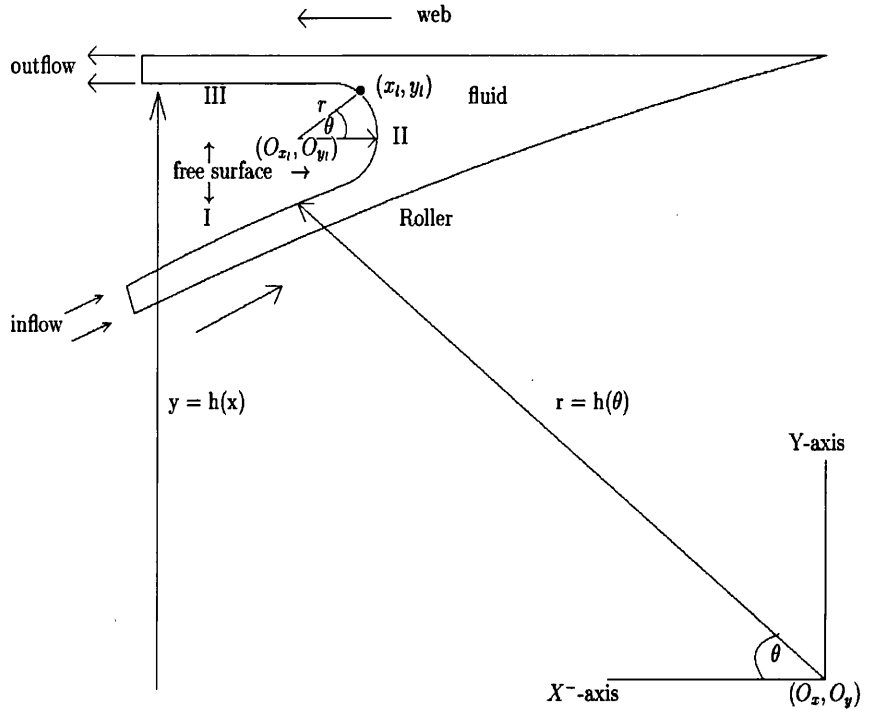

Figure 6.1: Schematic diagram of the flow domain

Free-surface boundaries are assumed at the inflow (region I in Fig 6.1), meniscus (region II), and outflow (region III) locations, respectively, being resolved through the representations described in Chapter 3, eqn (4.67) [see Sizaire and Legat 1997]. During the transient movement of the free-surface toward a steady-state position, a re-meshing time-stepping technique is performed to adjust the mesh within the domain (locally). On the free-surface boundary sections (meniscus, inlet flow, substrate coating) vanishing tractions are imposed and only atmospheric pressure is considered initially. For simplicity, the effects of surface tension are ignored. Thus,

$$-p + \tau_{nn} = -p_0 + \beta_{curv.}\,\sigma_s \quad \tau_{nt} = 0 \tag{6.1}$$

where p and p_0 are local and atmospheric pressures, respectively; τ_{nn}, τ_{nt} are normal and tangential stress components, respectively. Surface tension inclusion is defined through its coefficient, σ_s, and account of the mean curvature of the free-surface, $\beta_{curv.}$. Hence, if the

surface tension is neglected, on the free-surface boundary, the normal stress balances with the pressure terms and the tangential stress vanishes.

Lift and drag calculations: Lift and drag constitute mechanical forces that arise between solid and liquid surfaces. Here, calculations are performed for the lift on the foil-substrate (L_{foil}) and the drag on the feed-roller (D_{roller}). For a Newtonian fluid, the lift and drag forces may be expressed through the following integral expressions over respective surfaces:

$$L_{foil} = \int_{\Gamma_{foil}} \left(-p + \tau_{yy}\right) d\Gamma = \int_{\Gamma_{foil}} L_f \, d\Gamma,$$
$$D_{roller} = \int_{\Gamma_{roller}} \{-p\cos\vartheta + \tau_{xx}\cos\vartheta + \tau_{xy}\sin\vartheta\} d\vartheta = \int_{\Gamma_{roller}} \left(-D_r\right) d\vartheta, \tag{6.2}$$

where $\tau = 2\mu D$ and L_f and D_r (integrands) are the distributional (localised) lift and drag quantities. Note that these quantities, cited below under non-dimensional reference with * superscript notation, may be accessed through experimental measurement, hence providing for direct comparison with the numerical solutions generated.

The modelling approach addresses various themes systematically through *(a)* development of an appropriate numerical techniques; *(b) fe* discretization; *(c)* setting appropriate boundary conditions; *(d)* fluid modelling (paints) through complex viscous-inelastic constitutive equations (rheological considerations); *(e)* computation to mimic a dynamic wetting line and with slip conditions imposed.

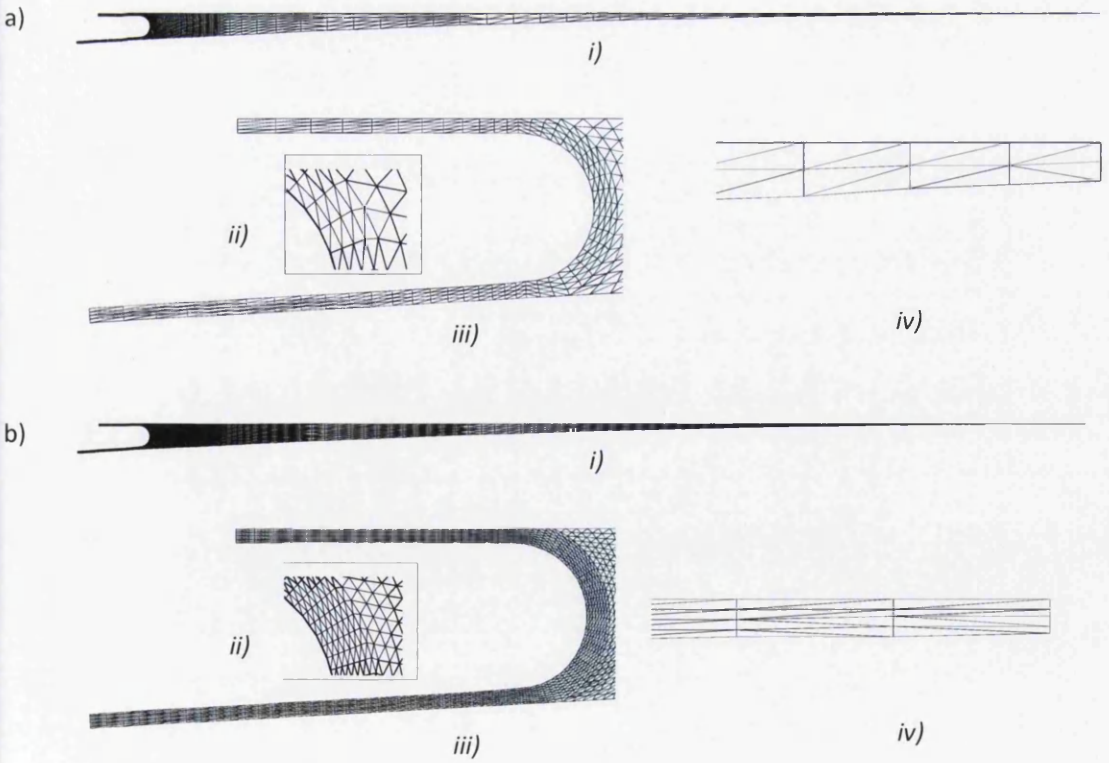

Figure 6.2: FE discretisation; (a) mesh 2; i) full mesh, ii) meniscus region, iii) zoomed meniscus, iv) nip region (nip expanded radially by a factor of 50, for illustration purposes); (b) mesh 3; more refined (scaled and zoomed, as above)

Typical industrial coating fluids of interest are weakly shear-thinning and moderately tension-thinning in extension. This study constitutes a primary analysis, where attention is paid to setting up the free-surface problem and incorporating viscous properties alone, first of Newtonian form and, secondly, through inelastic shear-thinning modelling.

Under isothermal setting for incompressible Newtonian and non-Newtonian flows, the governing conditions consist of a continuity and momentum equation. These equations are coupled with the free-surface boundary equations and are solved through a finite element based time-stepping fractional-staged Taylor-Galerkin incremental pressure-correction (TGPC) framework (see chapter 4). A section of the roller coating domain is isolated (Fig. 6.1) and discretised through triangular tessellation. Three comparative meshes (mesh 1, mesh 2, mesh 3) have been developed for this purpose, as illustrated in Fig. 6.2a (mesh 2) and Fig. 6.2b (mesh 3); (nb: coarser mesh 1 is not shown). Mesh 2 and mesh 3 are obtained by refining mesh 1 and mesh 2, successively. Quantitative parametric detail on these meshes is provided in Table 1. Mesh 2 has been shown to provide sufficient resolution when compared to mesh 1 and mesh 3. Here, the difference in computed solutions for velocity and pressure fields has been observed to be $\approx 9\%$ between mesh 1 and mesh 2, and less than 1% between mesh 2 and mesh 3. Therefore, for reasons of efficiency, yet still retaining sufficient accuracy, mesh 2 is the standard choice used for computation and for the solutions presented below.

Table 1: Mesh characteristics	*Mesh 1*	*Mesh 2*	*Mesh 3*
Total number of nodes	1560	2925	**10536**
Total number of pressure nodes	433	812	**2925**
Total number of elements	650	1302	**5208**
Total number of degrees of freedom	**3553**	**6662**	**23997**

6.3 Newtonian flow solutions

As a standard benchmark setting, Newtonian flows are simulated initially at $t = 0$, starting from a quiescent state. Solution variables (velocity, pressure) will then develop in time to reach a limiting steady-state after a finite number of time-steps (iterations). This procedure is monitored for convergence against an incremental relative-norm tolerance and viewed against a minimal target threshold, set at $O(10^{-6})$.

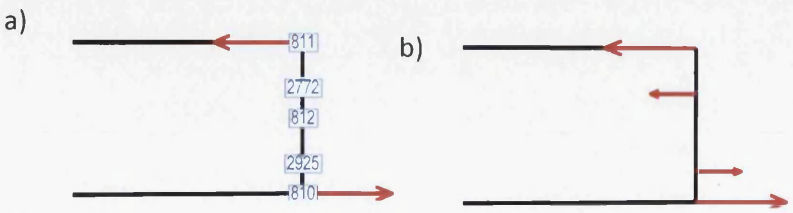

Figure 6.3: Nip velocity boundary conditions; a) blockage type, b) Couette-type

With a unit foil velocity (U_F=1), flow blockage at the nip and similarly balanced roller speeds, solutions are implemented in stages within the inflow/outflow, meniscus and nip-regions: case (a) fixed meniscus free-surface, and case (b) with meniscus free-surface inclusion. Two types of velocity profile are considered (zero-flux) at the nip-region. (i) vanishing stream-wise velocity across the nip-gap (blockage); and (ii) Couette-type velocity conditions, with driving lower (roller) and upper (substrate) boundaries. Both scenarios ensure a zero mass flow balance at this region (see Fig. 6.3). Radial velocity vanishes at the nip under either scenario.

Through flow patterns, Fig. 6.4 indicates the consequences of inclusion/exclusion of meniscus free-surface movement. This points to the important fact that there is no flow reversal in the vicinity of the meniscus under fixed boundary approximation, which enter the problem when traction-free-conditions are fully incorporated (introducing cross-stream tension in the coating), although meniscus shape does not appreciably alter, (Fig. 6.4). Thus, the flow entering from the roller-feed must travel up to the nip before returning back to the domain-exit to form the coating on the foil-substrate (as demonstrated through the streamline patterns).

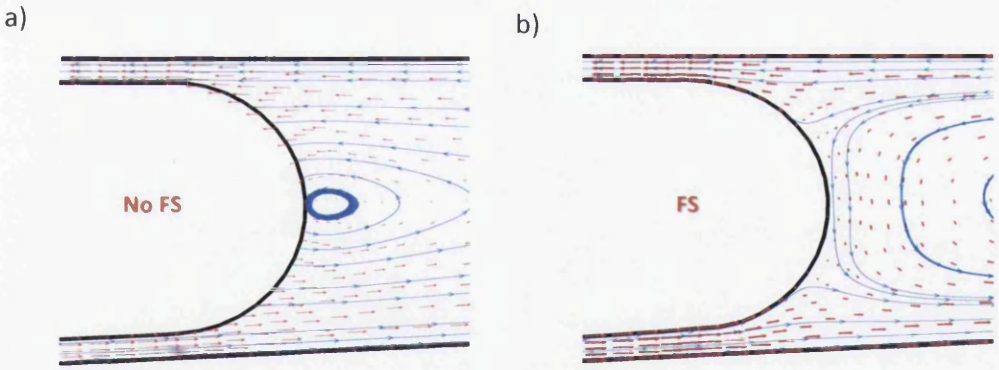

Fig. 6.4: Streamline patterns and effect of free surface; a) excluding free surface movement, b) including free surface movement

For the traction-free setting under (U_F=U_R=1.0), Fig. 6.5a exposes the calibration of the non-dimensional distributional lift, localised pressure on the foil substrate, and the distributional drag on the roller. A sharp rise in pressure (and hence lift) is observed, occurring locally at the nip and building up from a distance of 5% of foil-length considered (measured from the nip). The peak-pressure-value is O(10^3) larger than that in drag on the roller, which itself assumes a distribution that rises to a positive peak at ~2% of foil-length from the nip-gap (-10 length units on roller), and then suddenly drops away at the nip-plane. The variation in

distributional drag from positive to negative peak values is O(1.2*10^2) units, whilst the equivalent variation in pressure is O(175*10^3) units (likewise, in lift, O(70*10^3) units).

Furthermore and under the standard setting protocol, Fig. 6.5b (i) reveals large levels of shear-rate along the foil and roller, being slightly imbalanced near the nip-region between the two solid boundaries, this is due to the geometric design with a flat foil and circular roller. The streamline contours also reveal the large recirculation zone, commencing from the meniscus region and persisting as far as the nip zone, being almost symmetrical under the standard setting (see Fig. 6.5b (ii)).

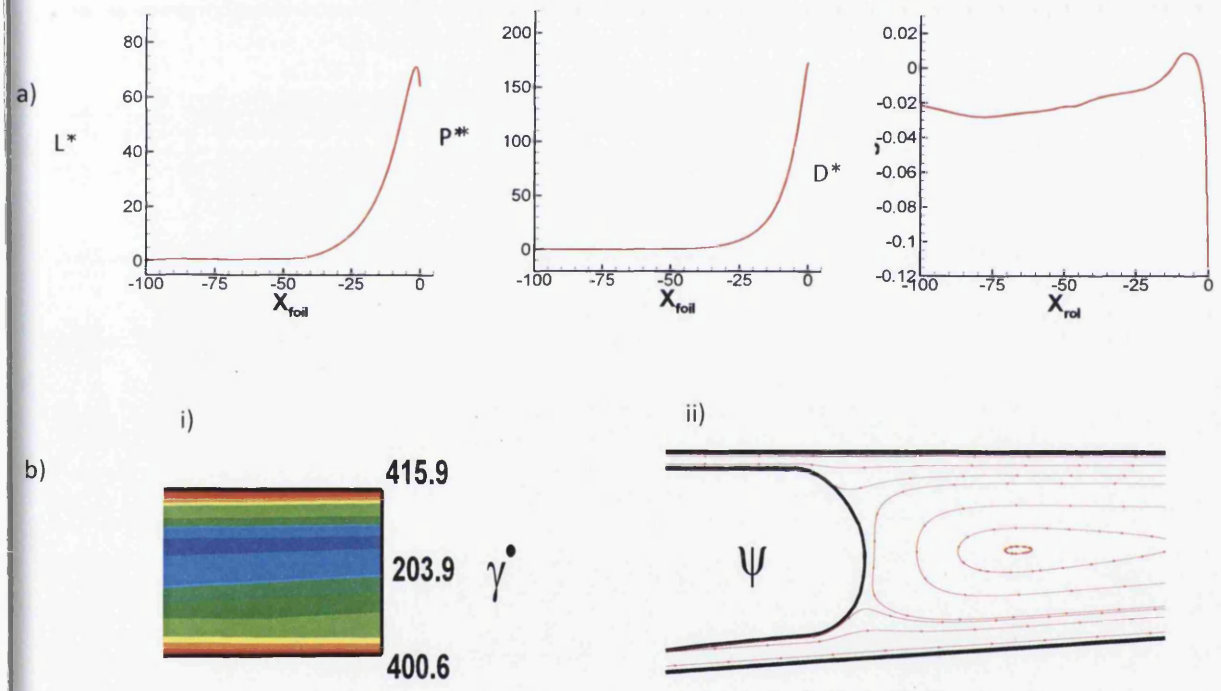

Figure 6.5: Non-dimensional (a) distributional lift and pressure on foil, and drag on roller; (L* = lift * 10^3; P* = Pressure * 10^3; D* = Drag * 10^3)
(b)i Shear-rate across the nip-gap, (b)ii Streamlines at meniscus region

6.3.1 Variation of foil and roller speeds

In all the simulations performed, the foil-coating thickness was retained as constant at the desired level (h_F=1unit). Hence, any increase in foil-speed will generate an increase in exit-coating flow rate, which must be balanced by either increasing roller-speed or inlet-flow metering thickness (inlet-feed thickness on roller). Through experimental trials and based on lubrication approximations, Benkreira *et al.* (1982b); Coyle *et al.* (1990b), and others have

concluded that, there exists a minimum thickness as the speed-ratio of applicator-metering rolls $\left(\frac{V_2}{V_1}\right)$ increases. Furthermore, at a fixed level of inertia (Re) and surface tension (Ca), this thickness decreases linearly with increasing velocity ratio, at a rate that lies in the range of A=[0.615-0.667].

$$h = A\left(1 - \frac{V_2}{V_1}\right). \tag{6.3}$$

Coyle et al. (1990b) also report that minimal thickness, according to lubrication theory, is attained when the wetting line crosses the minimum nip-gap location. Their findings are for both Newtonian and shear-thinning Carreau liquids of Power law index m=0.5 (see below), covering three levels of surface tension. Here, both film-thickness and wetting line position are a function of roller-speed ratio. These findings highlight the challenges faced in achieving a low film-thickness at high foil-speed, whilst avoiding air entrainment.

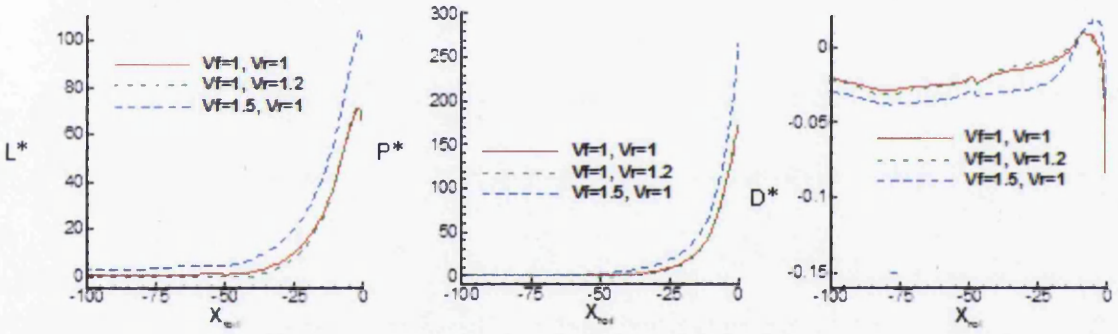

Figure 6.6: Distributional (left) lift and (centre) pressure on foil, and (right) drag on roller; (L* = lift * 10^3; P* = Pressure * 10^3; D* = Drag * 10^3)

Illustration of typical findings in variation of foil and roller-speeds are documented, in Fig. 6.6, comparatively against the standard setting (U_F=U_R=1.0) and a scaled unit flow rate (of Q=1) and h_F=h_R=1.0. Two settings are investigated: (*i*) increasing foil-speed from 1.0 to 1.5 at fixed roller-speed (increasing foil or roller-speed ratio from 1.0 to 1.5, with Q=1.5 and h_F=1.0, h_R=1.5); and (*ii*) increasing roller-speed from 1.0 to 1.2 at fixed foil-speed (decreasing foil or roller-speed ratio from 1.0 to 0.833, with Q=1 and h_F= 1.0, h_R=0.833). Note, that for direct comparison across scales (three cases), a common reference is adopted, hence retaining the same Reynolds number setting, Re=0.32. For the various alternative speed settings, the shear-rates at the nip-region are displayed in Table 2.

Table 2: Shear-rates across the nip-gap

Roll-speed	$\dot{\gamma}$ - Roll side	$\dot{\gamma}$ - Foil side	$\dot{\gamma}$ - Middle nip
Vf=1, Vr=1	400.6	415.9	**203.9**
Vf=1, Vr=1.2	494.5 (+23%)	403.8 (-3%)	**224.4**
Vf=1.5, Vr=1	**365.9 (-8%)**	**654.2 (+57%)**	**254.9**

Findings reveal that peaks in distributional lift on the foil-substrate increase as foil-speed increases and are not influenced by variations in roller-speed. Similarly, the peak in distributional drag on the roller varies with roller-speed and remains unaffected when subject to variations in foil-speed. Likewise, pressure distribution peaks observed on the foil-substrate increase with increasing foil-speed, a finding independent of roller-speed. In contrast to the standard setting (U_F=U_R=1.0) and interpreted from the nip-region, increasing foil-speed (by a factor 1.5) causes the localised shear-rate to rise (by 57%) towards the foil-side (to a maximum); similarly, shear-rates rise (by 23%) on the roller-side (to a maximum) when the roller-speed is increased (by a factor 1.2), see Table 2.

6.3.2 Variation in nip-gap size

Under standard setting (U_F=1, U_R=1), the influence of nip-gap size variation has been analysed, where a nip-gap size of unity is treated as the calibration standard. In relative perspective, this represents 1% of film-thickness (h_F~O(10-6m)). Findings, depicted in Fig. 6.7, reveal that most variation in the important quantities of distributional lift/drag, localised pressure/shear-rate within the nip-region, occur at small nip-gap sizes, below 5% h_F. A plateau-like region for pressure and shear-rate is observed above the 2.5% h_F-level (2.5 nip-gap); there is also a sharp rise in pressure and shear-rate below nip-gap size of 1 unit (with peak-values in units of 173*103 for pressure and 415 for shear-rate); the intermediate zone between 1 and 2.5 sized nip-gaps yields only gradual change in these quantities. The profile in distributional lift varies much more gradually, being delayed in its decline against nip-gap choice, beginning to plateau out around the 5% h_F-level. Variations in distributional drag (not shown) remain contained and relatively low in contrast to other quantities, reaching a maximal negative level (-1.3*103) for a nip-gap size of 2.5 units.

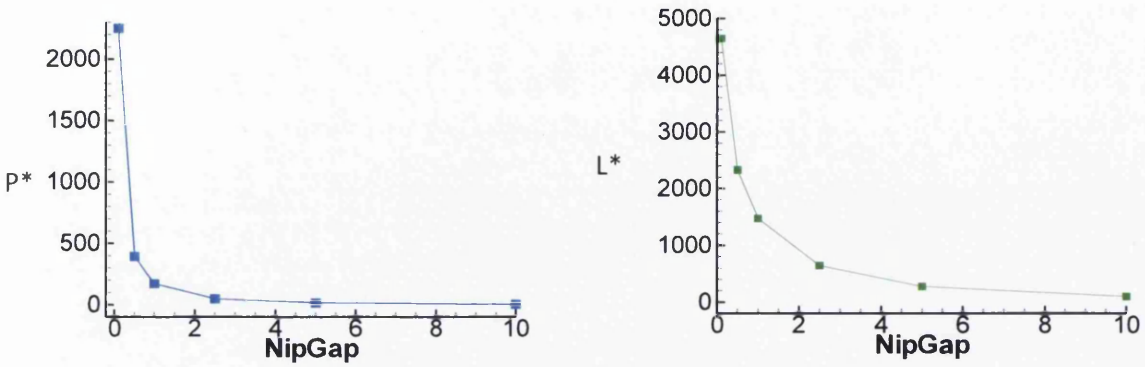

Figure 6.7: Nip-Gap effects; distributional lift and pressure profiles; standard setting (V_F=1, V_R=1), (L* = lift * 10^3; P* = Pressure * 10^3)

6.3.3 Boundary condition adjustment at the nip: relief mechanism I

An initial trial of various nip-flow profiles has been considered, either of blockage or Couette-type, both with zero mass balance across the nip-plane. This is prior to the implementation of slip conditions and further modelling complexities, where a wetting line may be incorporated. Initially, for blockage-type flow, there is no flow permitted across the nip-gap plane, so that only non-zero velocity is retained at the foil (U_F) and roller (U_R) (see Fig. 6.3a). Here, there is sharp solution change between that at the final mid-side node of the neighbouring finite element and the bounding moving surface (quadratic fe-function approximation assumed across the element line edge). Note that, this is the standard profile choice unless stated otherwise. The alternate, and more physically realistic setting, is that of Couette-type flow (see Fig. 6.3b), where the shear-rate across the nip-gap approximates a constant (exactly so between parallel boundaries).

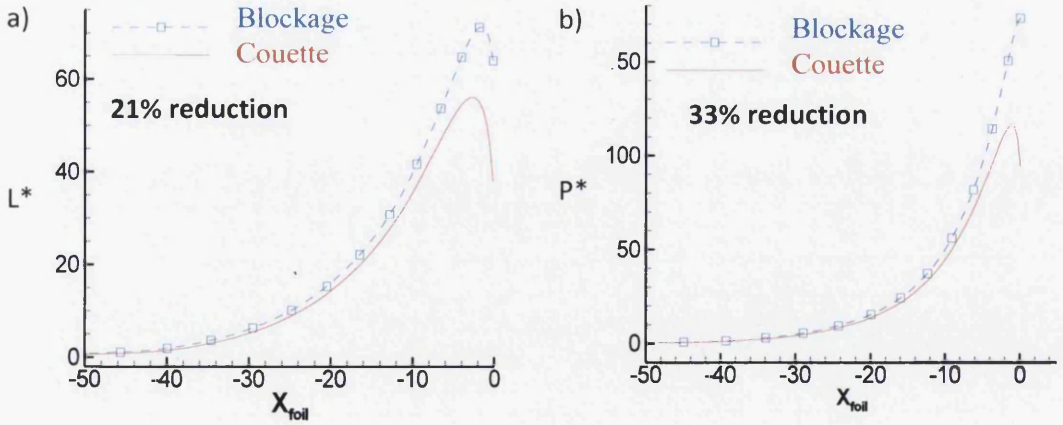

Figure 6.8: Effect of the node boundary condition on the nip gap line (with Ca set to standard on the meniscus side), (L* = lift * 10^3; P* = Pressure * 10^3)

By way of trial, the study focuses on the plane (2D-line) across the flow, representing the nip-gap width. Both extreme nodes on this line have either the kinematic condition of the roller (lower) or the foil-substrate (upper). Under the imposed kinematics of (U_R=1.0, U_F=1.0), the central node across the nip-gap width will have a zero velocity condition, in either boundary condition type considered, Couette or blockage. By solving for the solution at this location (U_y=0, U_x=free), then relief is generated in peaks of lift (21%) and pressure (33%), as depicted in Fig. 6.8. Note, this finding is independent of the introduction of surface tension forces applied to the meniscus region.

6.3.4 Slip conditions at the nip: relief mechanism II

Gravitating towards a full wetting line implementation, the next factor to introduce relates to the effect of slip boundary conditions, as applied to the foil-substrate in the nip-gap, which directly links to respective surface qualities and roughness. Initially, only the final nip-node on the foil is treated as susceptible to this slip mechanism, following the theory conveyed in:

$$u_{slip} = \beta_{slip}\, \tau_{xy} \tag{6.4}$$

where β_{slip} is the slip coefficient and τ_{xy} is the shear stress. For Newtonian fluids, the u_{slip} is given by:

$$u_{slip} = \delta \frac{\partial u}{\partial y} \tag{6.5}$$

Here, δ is the slip length and $\partial u/\partial y$ is the shear velocity-gradient.

Experience reveals that exposure to slip has reduced the maxima in pressure and lift levels encountered, in contrast to those instances without slip, as shown in Fig. 6.9. Here, for realistic flow response, the level of imposed slip-length used lies in the range of $2*10^{-4}$ and $2*10^{-3}$; which for current perspective, corresponds to 50% of the local shear-stress/shear-rate magnitude. Note that larger levels of slip-length coefficient will produce still lower peak levels of pressure and lift; hence this finding identifies a second relief mechanism on such forces.

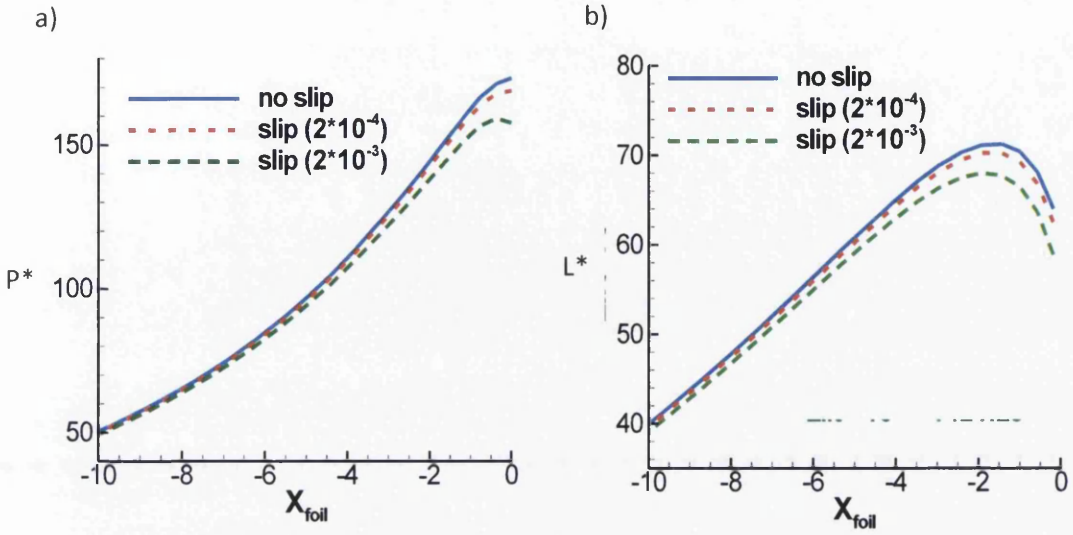

Figure 6.9: Effect of slip boundary condition on the foil at the nip-gap line, (P* = Pressure * 10^3; L* = lift * 10^3)

6.4 Inelastic material modelling: relief mechanism III

Shear-thinning material properties and their impact within the processing conditions are analysed by appealing to various viscous inelastic models. Initially, a power law approximation is introduced with a power index range of m<1. This is followed by a more generalised Carreau model, used to represent typical industrial coating materials.

6.4.1 Power-law model solutions

With this model, the relationship between shear rate and viscosity is governed by $\mu(\dot{\gamma})/\mu_0 = K\dot{\gamma}^{m-1}$, for various levels of power index m. For initial testing and calibration over m-parameter below, the consistency parameter is set as unity (K=1 unit) at unit shear-rate. As such, the region at the nip has been identified as being exposed to high shear rate, and therefore, lower viscosity is observed there with declining power index m.

On the foil and with falling m-parameter, maximum levels of pressure and lift are observed to dramatically reduce. Hence, this substantiates a further possible relief mechanism in the process, as aptly demonstrated in Fig. 6.10.

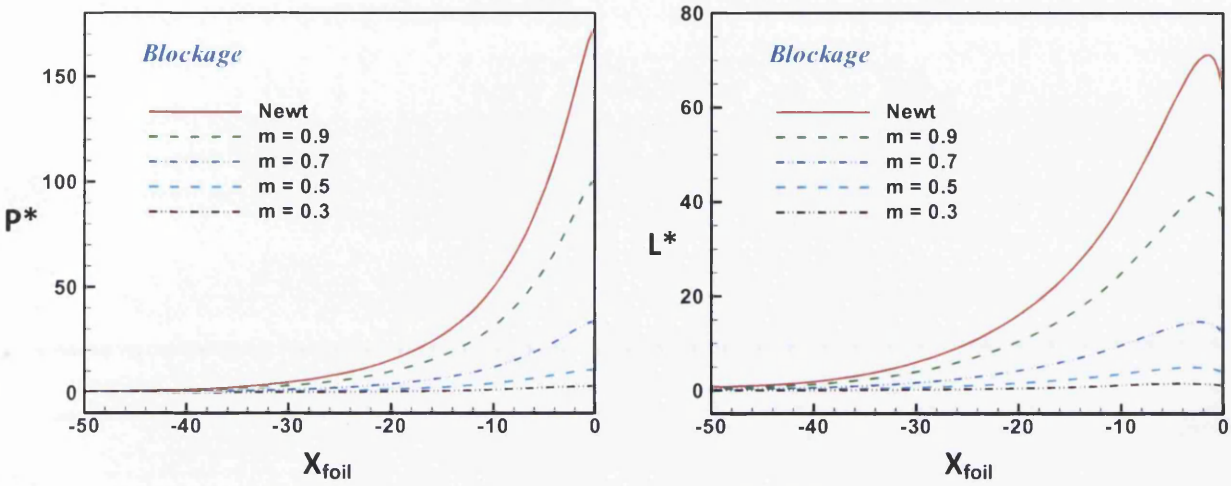

Figure 6.10: Power-law model: distributional pressure and lift with various power indices, (L* = lift * 10^3; P* = Pressure * 10^3, K=1)

To quantify such change over the nip-region, shear rates decrease by about 7% from the Newtonian setting to the inelastic case with m=0.3, as shown in Fig. 6.11a, whilst localised pressure (and lift) reduce dramatically by two orders of magnitude with declining m (from P=173*10^3 for m=1 to as low as 3*10^3 for m=0.3), as depicted in Fig. 6.11b.

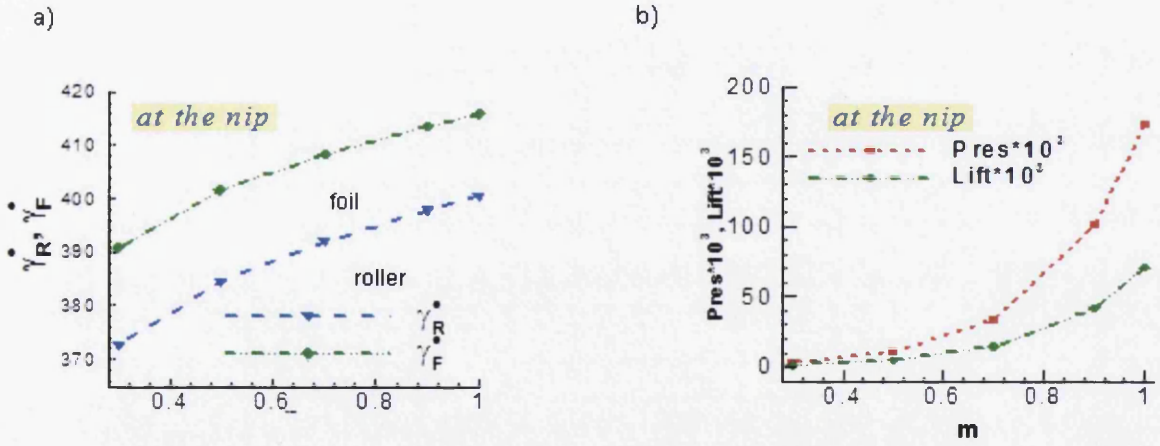

Figure 6.11: Power-law model: non-dimensional shear rates, and distributional pressure and lift across the nip plane with various power indices

In Fig. 6.12, contours of shear rate and viscosity for a power-law index of m=0.5 are displayed, covering the meniscus region and nip zone. As anticipated, shear rates levels are

some three orders of magnitude larger at the nip-region in contrast to the meniscus zone; whilst, viscosity is reduced by two orders of magnitude in comparison across these two zones. This is in-line with viscometric variation for the power-law model. Interestingly, blue/red (low/high) coloured shear rate plots generate red/blue (high/low) viscosity plots in the regions of interest.

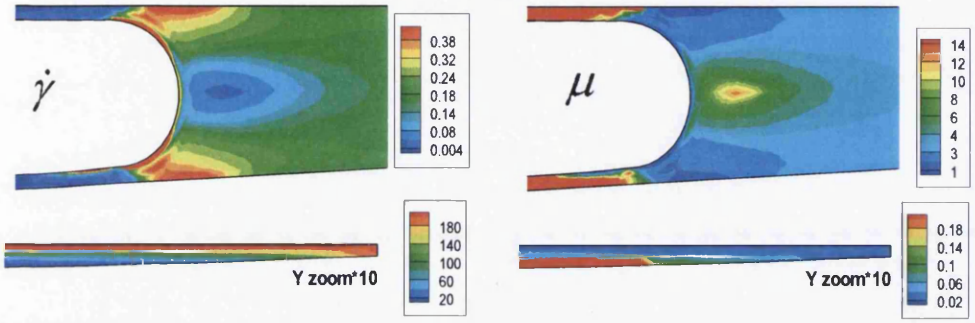

Figure 6.12: Power-law model: non-dimensional shear rates (left), and viscosity (right) contours: meniscus region (top), nip zone (bottom), m=0.5

The adjustment of the kinematics (streamlines) with decreasing power index is illustrated in Fig. 6.13. There is a clear widening of the recirculation zone eye, with a shift in location towards the nip as m-parameter declines. In all instances, there is no flow across the meniscus boundary, and ultimately, all the fluid entering (metered to the inlet-roller) must travel up to the nip before returning to exit the domain and coat the flat foil-substrate.

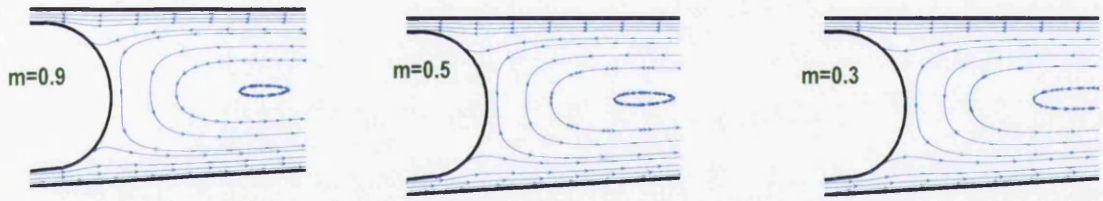

Figure 6.13: Power-law model: streamline contours at the meniscus region with power index

The conclusion is that there is clear evidence here of the strong impact that shear-thinning properties have upon processing design decisions, as recognised through the relief mechanism of lowering nip-levels of pressure and lift. That is, in contrast to considering only Newtonian coating fluids, noting the strong dependence of viscosity on pressure levels. Here, there are some similarities observed in other industrial processes such as journal bearing systems. In these applications, viscosity relates to pressure through the Barus law ($\mu(\dot{\gamma},p)=\mu(\dot{\gamma})e^{\alpha p}$).

6.4.2 Carreau model solutions

Below in order to better represent limiting viscosity levels at high deformation rates, it is also appropriate to introduce alternative material models of the Carreau-type, to improve data fitting at high and low deformation rate extremes, thereby varying infinite shear viscosity plateaux (second plateau levels).

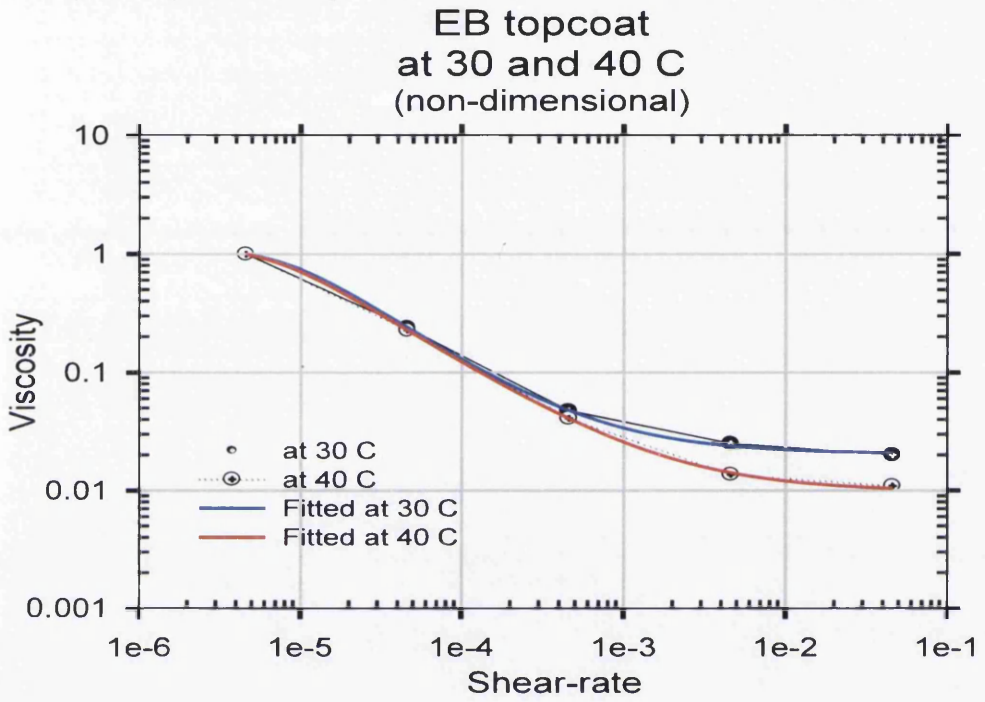

Figure 6.14: Carreau model: non-dimensional shear rates vs. viscosity, viscometric data at 30° and 40°C

Viscometric data have been provided for some model and industrial fluids, sampled at two temperatures of 30°C and 40°C, showing viscosity trends over a shear rate range of 0.1 to 103s^{-1}. Such data is fitted by a Carreau-model and provided in non-dimensional format in Fig. 6.14. The functional form for the Carreau model is given by:

$$\mu(\dot{\gamma}) = \mu_\infty + (\mu_0 - \mu_\infty)\left(1 + K^2\dot{\gamma}^2\right)^{\frac{m-1}{2}} \qquad (6.6)$$

Here, μ_0 is the viscosity at zero shear-rate, μ_∞ is the viscosity at infinite shear-rate, K is a consistency parameter, and m is a dimensionless constant. Deformation rates encountered in the nip-region are excessively high (around 400 non-dimensional units), and as a result, the local viscosity is correspondingly low there, around $\mu_\infty = 0.02$ at 30°C and $\mu_\infty = 0.01$ at 40°C. Such data is associated with second limiting plateau levels at high shear rates. This generates lower relative levels in pressure and lift on the foil, by some two orders from that of the

Newtonian case, as illustrated in Fig. 6.15. Furthermore, the temperature has a direct impact on maximum pressures attained at the nip, as the pressure for the coating at 40°C (1.7*103) is halved in contrast to that for the same fluid at 30°C (3.6*103). Similarly, the peak in distributed lift on the foil is also halved through an increase of temperature by 10°C, as clearly demonstrated in Fig. 6.15. The use of an industrially-applicable fluid with these characteristics is therefore beneficial in dramatically reducing the pressure levels exerted on the foil-substrate.

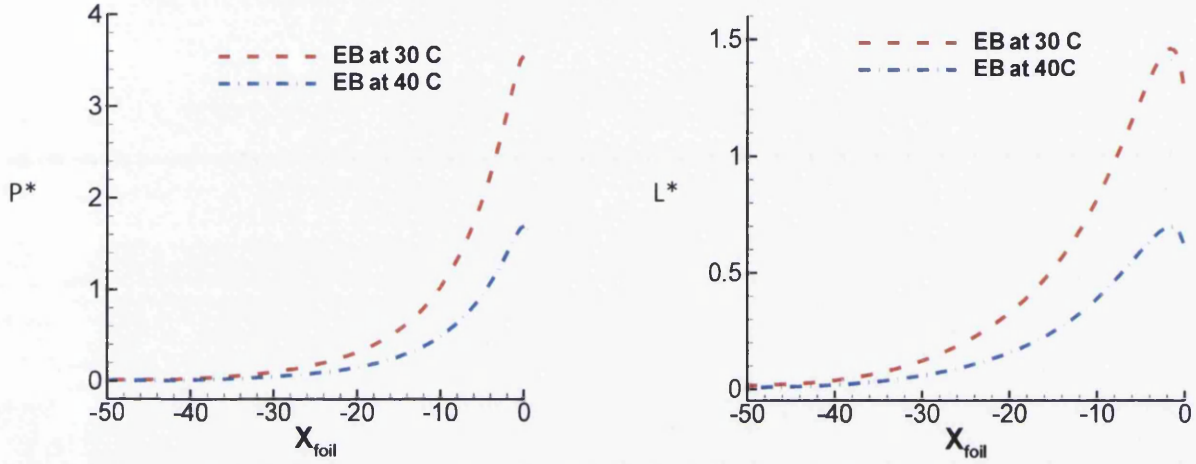

Figure 6.15: Carreau model: distributional pressure and lift for EB topcoat at 30° and 40°C, (L* = lift * 10^3; P* = Pressure * 10^3)

The viscometric data does not span the full range of shear rates encountered within the actual coating process, as the nip-region experiences extremes of shear-rate level, some two order of magnitude larger than elsewhere. In fact, the viscosity reaches the lower (second) plateau at 0.1 shear-rate level located in a region at about 50% of the distance from the nip towards the meniscus. Nevertheless, this engenders significant reduction in localised pressure and lift levels observed – a finding that demands experimental verification by extracting viscometric data in situ, directly from the process.

6.5 Modelling elasto-hydrodynamics: relief mechanism IV

In this final section, the roller is considered as being covered with a deformable (rubber) elastomer, so that an elastohydrodynamic analysis may be incorporated within the context of the roller coating dynamics considered thus far. The principle behind such theory is to associate the degree of deformation of the elastomer cover (which accounts for its shore hardness, or Youngs' Modulus), as a function of the dynamic loading (local forces) it is exposed to over the roll-surface section in question (nip pressure). Effectively, this will introduce a localised neo-Hookean model into the problem description, via a linearised functional representation, through which the activated nip-pressure is related linearly to local displacement. This mimics the fluid-structure interaction which takes affect between the

liquid film and the roller. This will then permit comparison of the effects of employing varying levels of shore hardness to the candidate elastomer cover (*fourth* relief mechanism in lowering loading exerted in the nip-gap). The thickness of the elastomer is therefore implicitly incorporated within the parameterisation. The deformation is interpreted through results in elastomer spatial displacement (Δx), in the form (Carvalho and Scriven 1997, Ascanio and Ruiz 2006b, Gostling *et al.* 2003)

$$\Delta x = \alpha P = \frac{b}{E_b} P = \frac{P}{k}, \tag{6.7}$$

Here, E_b represents the elasticity modulus per unit elastomer thickness, b the elastomer cover thickness and k the elastomer elasticity. Hence, decreasing elastomer elasticity corresponds to increasing elastomer softness. Note, that the resulting α-parameter relates to the commonly used 'shore hardness' measure, and depends on the level of elastomer elasticity/rigidity (E_b). In this respect, one might consider two possible nip-gap scenarios, that of: (i) positive nip-gap, or (ii) negative nip-gap width. The negative nip-gap setting is defined as that measurable gap generated by roller deformation, such that in the absence of roller deformation, there would be penetration of roller surface into the substrate surface.

6.5.1 Positive nip-gap scenario

From a practical implementation viewpoint, two different dynamic approximations may be proposed to represent the effects of elastomer deformation on localised pressure, lift and drag at the nip-gap region. First, there is a full transient analysis, in which the dynamic deformation of the nip-gap (and associated mesh movement) is pursued through time until a balanced position is obtained, according to the dynamic loading exerted through the distributed localised pressure generated at the nip. This approximation will closely represent the dynamics of the process conditions, but will engender considerably large computational times, to resolve the dynamics involved (subject of future study). To overcome this difficulty, and for efficiency, a second pseudo-transient approximation is proposed: whereby, the elastomer-roller is initially deformed to a maximum indentation that would have been attained, given the conditions of the steady pressure level endured under a non-deformable roller. The corresponding deformed nip-gap (and mesh) is then anchored (through time) and employed to predict a pseudo-final pressure level (first look), accordingly.

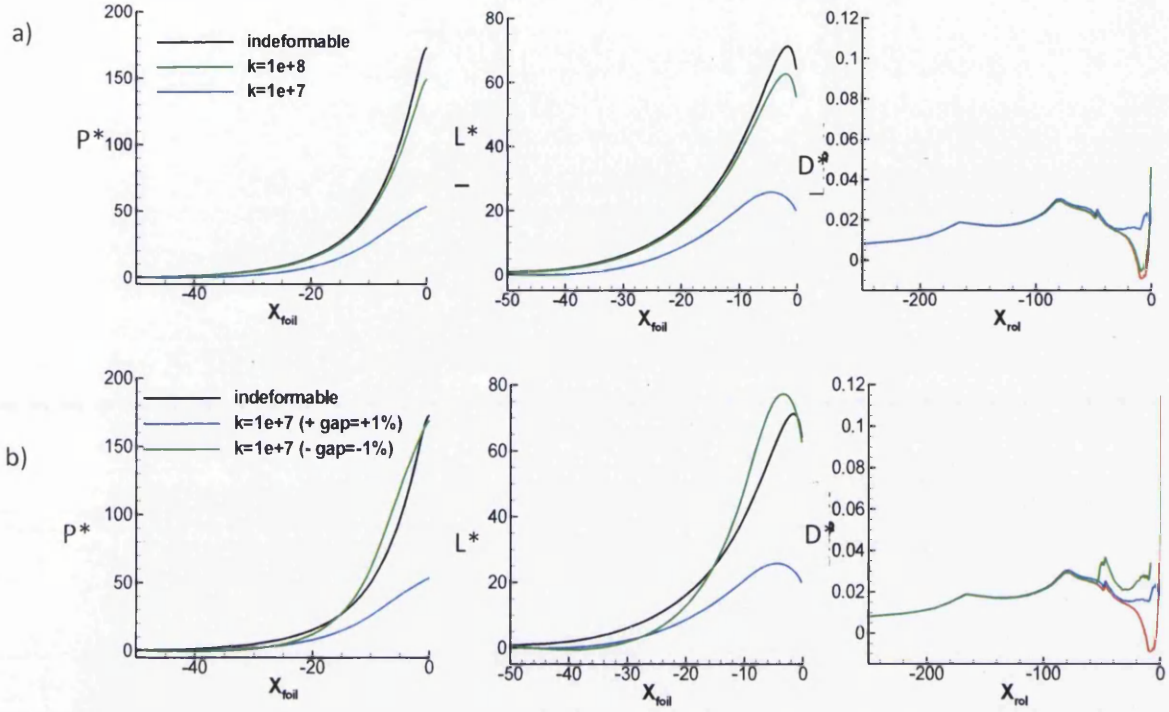

Figure 6.16: Effect of elasticity coefficient of deformable elastomer (roller) on distributional pressure, lift and drag; (a) Positive gap on, (b) Negative gap, (L* = lift * 10^3; P* = Pressure * 10^3; D* = Drag * 10^3)

For comparison purposes and to gain further insight, a series of analyses have been conducted with variation in the level of elastomer elasticity, based on the standard setting (U_F=1, U_R=1 and initial nip-gap of 1%). **Fig. 6.16a** (top) illustrates variation in the distributed patterns for pressure on the foil, lift on the foil and drag on the roller for two sets of elastomer hardness (hard: k=10^{+8}, and soft: k=10^{+7}). As anticipated, the application of an elastomer cover is observed to somewhat relieve levels in localised pressure and lift; subsequently these levels are decreased as the elastomer elasticity is decreased (hardness reduced). Beyond an elasticity threshold (here around k=5*10^{+6}), a non-sustainable negative nip-pressure on the foil will appear causing numerical divergence (meaning, in practice, the elastomer becomes too 'spongy'). The hard elastomer case has deformed by an order of 0.1% in contrast to that of an undeformable roller, reducing the level of both the localised pressure and lift by some 15% from the undeformable state. Moreover, the indentation (deformation) of the soft elastomer is significantly more broadly pronounced (by about 3%), creating a U-stretch roller surface-shape over the x-breadth of the nip-region. Accordingly, the levels of localised pressure and distributional lift are even more reduced (both by 70%). Nip-gap sizes are depicted in the figures according to the various levels of elastomer hardness.

6.5.2 Negative nip-gap scenario

The following procedure is adopted in order to simulate the squeezed coating situation under negative nip-gap imposition and the use of deformable rollers. In this, it is important to maintain realistic nip-gap widths and to avoid excessive corresponding mesh distortion. First, based on the standard setting, the maximum deformation of the roller is estimated, based on a positive equivalent gap-size. From this position, the nip-gap is narrowed, by shifting the roller surface upwards towards the substrate by a distance of twice the initial gap-size. The final deformed nip-zone and mesh-domain is then employed to simulate a scenario and level of pressure equivalent to a negative nip-gap. **Fig. 6.16b** illustrates comparatively corresponding pressure and lift distributions on the foil, and drag distribution on the roller, for a 1% positive gap with a non-deformable roller and a soft roller ($k=10^{+7}$), and a negative gap of -1% for the same soft roller. Notably, there is some rise in the nip-pressure and lift distributions for a deformable elastomer with a negative gap, in contrast to those of a positive gap (deformable or not). Still, under the negative-gap setting, lift-elevation is more localised to the nip-gap zone and hence less influential away from this zone (with less disturbance offered as a consequence to the coating). This demonstrates the positive benefits that can be extracted from negative-gap imposition, so that negative-gap force-results can be devised that reach a level equivalent to the non-deformable roller at the nip, yet relieve those of the positive gap deformable elastomer away from the nip ($x<-20$). Hence, the available performance advantages of running squeezed negative nip-gaps are exposed.

6.6 Computational outcomes

The modelling of a high-speed defect-free reverse roll coating process has been performed employing a Taylor-Galerkin pressure-correction algorithm. The novelty of the research is stimulated by the demand from the coating industry to coat faster uniform, stable thin films, by manipulating coating rheology and coater operating conditions, including elements of hydrodynamic assistance. Specifically, the main points analysed are summarised as:

- Variation of roll speeds
- Variation of nip-gaps
- Boundary conditions adjustment at the nip (Pressure relief mechanism 1)
- Slip conditions at the nip (Pressure relief mechanism 2)
- Inelastic material representation (Pressure relief mechanism 3)
- Roller elastomer hydrodynamics (Pressure relief mechanism 4)

Findings have been presented through streamline patterns. No flow reversal is evident in the vicinity of the meniscus when traction-free conditions are imposed. Thus, the flow entering from the inlet-roller must travel up to the nip before returning back to exit as the coating on the foil-substrate. Velocity variations reveal that as foil-speed increases, distributed lift and pressure on the foil increase and are not influenced by variations in roller-speed. Similarly, the drag on the roller varies with roller-speed and remains unaffected by variation in foil-

speed. More importantly, pressure distributions generated on the foil decrease with increasing roller-speed. This suggests the optimum settings sought, where it is expected that the roller should rotate at a faster rate than the foil. Moreover, there is significant variation in maxima of localised pressure, shear rate and distributional lift, as the nip-gap size is reduced below 5% of foil thickness. Notably, there is a sharp rise of the above quantities below nip-gaps of 1%. A nip-gap size around 5% provides a threshold, above which all measures quantified are insensitive to change. There is also a significant reduction in localised pressure, lift and shear-rate maxima, when nip boundary conditions *(first relief mechanism)* are modelled through a Couette-type velocity condition, halving over that for the blockage alternative. By allowing some kinematic freedom to the central nodal degree of freedom, a relief mechanism governing the forces on the foil/roller has been identified. This indicates the necessity of incorporating a free-surface wetting line beyond the nip-region. The introduction of a slip condition *(second relief mechanism)* has, as anticipated, reduced the level of localised pressure, lift and shear-rate at the nip-gap region. Further increase in slip-length coefficient will produce still lower levels of localised nip-pressure and lift; hence this discloses a second relief mechanism on such nip loading.

For the fluid modelling and considering inelastic shear-thinning coating fluids under power-law modelling, pressure and lift maxima are reduced dramatically with decreasing power index (m) (so, under increased shear-thinning effects), offering a *third* source of relief mechanism to the process. In addition, a strong dependence of viscosity on pressure is observed. In a similar fashion and by employing an inelastic Carreau model, reduction in pressure and lift on the foil is observed for a typical industrial coating material. This indicates the importance and influence of temperature-rise, with the lowering of the second-plateau in viscosity that subsequently reduces the forces exerted on the foil.

As anticipated, the application of a roller-elastomer relieves nip-pressures and lift. Subsequently, these levels are decreased as the elasticity of the elastomer is decreased (softness increased, *fourth relief mechanism)*. Moreover, beyond a certain elasticity threshold, a non-sustainable negative pressure on the foil is reached, which implies that the elastomer is too spongy for practical use. Necessarily the nip-gap size is larger for softer elastomers, with larger indentation (deformation) of the roller in comparison to harder elastomers; this creates a U-shaped stretched roller-surface throughout the nip-region. Similarly, under negative-gap size setting, one observes a change in the manner the localised pressure and lift are distributed for a deformable elastomer, in contrast to that for a positive-gap (deformable or not). Under the negative-gap setting, lift-elevation is more localised to the nip-gap zone and hence less influential away from this zone (with less disturbance offered as a consequence to the coating). Hence, negative-gap configurations may be used to advantage, where preferential squeezed local loading is achieved at the nip equivalent to that for the non-deformable roller setting; yet, they relieve loading patterns of the positive-gap deformable elastomer away from the nip. Thus, it is possible to replicate final nip-gap conditions, under a negative-gap scenario, close to that of the standard positive-gap position; although in this case the shape of the roller is deformed.

Chapter 7

Reverse roll-coating with dynamic wetting lines*

Numerical solution of reverse roller coating flow associated with the industrial process of thin-film paint-coatings of strip-steel is addressed. The modelling includes viscous inelastic rheology, meniscus and dynamic wetting lines, accomplished through a semi-implicit time-stepping finite element Taylor-Galerkin/pressure-correction scheme, coupled with a differential free-surface location technique. Flow structures are examined in detail around the meniscus, nip and wetting line regions, analysed via streamline and shear rates patterns, surface distributional lift and localised nip-pressures. Effects of parameter variation are investigated in nip-gap size, adjustment of applicator roller-substrate speed-ratio and levels of surface tension. Upon surface tension increase, significant features are observed on the dynamic wetting lines and at the contact zone.

*Material in this chapter have been accepted for publication in the paper "Modelling Reverse Roll Coating flow with dynamic wetting lines and inelastic shear thinning fluids" by S.O.S. Echendu, H. R. Tamaddon-Jahromi, M. F. Webster in *Applied Rheology, June 2013*

7.1 Introduction

In the roller coating process of interest rotating cylindrical roller applicators are used to apply a thin-film of liquid coating onto one side of a moving substrate (steel-strip). This flow process is of extreme importance in modern industrial procedures, arising typically in the application of organic coatings onto strip steel. Common roller coating flows can be sub-divided into two principal categories, namely: forward-roller coating and reverse-roller coating (RRC). This computational study focuses on reverse roll coating, investigated via dedicated finite element and free-surface handling schemes. Reverse roller coating has proven itself extremely versatile, and hence remains the topic of various studies for viscous Newtonian and inelastic shear thinning coating fluids (paints with additives). For economic reasons, a driving objective behind the process has been to continuously increase coating line speeds, whilst maintaining stable constant film-thickness with smooth appearance along and across the strip-substrate. As a consequence, one of the major barriers posed, has been the onset of flow instabilities at higher line speeds; this may cause surface defects that take the form of ribbing or stripping on the applied coating. Some earlier studies on reverse roller coating are reviewed, having focused mainly on zonal influences (i.e. within nip, inflow, meniscus, out-flow regions), fluid rheology and flow instabilities. Therein, ribbing onset has been associated with a critical capillary number (Ca_{crit}). Coyle et al. [1987, 1990b, 1990c] analysed an experimental configuration for reverse-roller coating with non-Newtonian liquids, drawing upon finite element simulations. This study showed that at high-speed ratios and high capillary number (Ca), the metered film-thickness increased more than at low capillary number. Experimentally, Gaskell et al. [1995, 2000] investigated meniscus roll coating, again under reverse roll coating conditions. There, the flow was characterized by a single large eddy structure, with primary and secondary fluid transfer jets from the roller to the substrate. These structures tended to merge, as either flow-rate or speed-ratio was increased. For Newtonian fluids, Cohu et al. [1997] also investigated experimentally forward-roller coating between deformable rollers. Findings revealed that a decrease in rubber cover thickness on the applicator roll tended to decrease coating thickness. Also on experimental analysis, Benkreira et al, [1981, 1982] reviewed the four categorical regions in coating flows and studied the movement of dynamic wetting line, [Benkreira et al. 2002] providing the cascade operating conditions of dynamic failure due to air entrainment [Benkreira et al. 2008]. Moreover, Carvalho et al. [1997b] studied the effects of soft-roll deformation with respect to the onset of ribbing, for which findings demonstrated that a deformable roll cover may be used to lessen the ribbing on the strip to achieve a required coating thickness. Chandio and Webster [2001, 2002c] also used finite element methods to numerically predict reverse roller coating solutions for Newtonian fluid coatings. These simulations employed a semi-implicit Taylor-Galerkin/Pressure Correction scheme, where the study focused on flow patterns, variation in roll-speed and foil-speed. Their findings revealed that no flow reversal occurred in and around the vicinity of the free-surface meniscus. With respect to flow instabilities on the strip, this phenomenon tended to occur upon increase of foil-speed rather than increase of roll-speed. Moreover considering dynamic wetting lines, Shiode et al. [2009] numerically analysed reverse roller coating using a volume of fluid (VOF) method. Therein and due to drag forces encountered, their results revealed that, the wetting line moved closer to the nip as speed-ratio was increased. Jang et al. [2009] performed 3D non-Newtonian flow modeling for RRC, employing a finite volume method

and a VOF free-surface technique. This relevant work was conducted for inelastic non-Newtonian fluids, with power-law index (m) ranging from 0.95 to 1.05, mainly focusing on factors such as resulting coating thickness and effect of roll-speed-ratio on ribbing instabilities. The results demonstrated that as power-law index increased, coating film-thickness increased with decrease in coating film-leakage. In contrast, as foil:roller speed-ratio increased, the coating film-thickness decreased with increase in leakage film-thickness; in agreement with Chandio and Webster [2002c]. Thus, for a fluid with power-law index larger than unity (shear-thickening), ribbing instabilities are visible with more waviness on the strip surface. In the computational reverse roller coating study of Belblidia et al. [2012] for high-speed defect-free coatings, with and without elastomer-covered rollers, various relief mechanisms for pressure were identified. Whilst elastomer elasticity decreased (Shore hardness increased), the levels of localized pressure and distributional lift were also observed to decrease.

Prior to this phase of study, simulations were conducted with viscous, inelastic and viscoplastic fluids under confined mixing and separating flow configurations [Echendu at al. 2011]. This counterpart flow problem, with flow-splitting, provided some insight into the complex flow dynamics expected under roller coating and with similar rheology, yet devoid of free-surface issues. As such, the present article is a continuation of the viscous inelastic reverse roller coating study of Belblidia et al. [2012], but with the inclusion of a full dynamic wetting line analysis; hence drawing upon similar finite element procedures with a semi-implicit Taylor-Galerkin pressure-correction algorithm [Hawken et al. 1990, Webster et al. 2005]. For location of the free-surface, kinematic boundary adjustment with a differential mesh stretching algorithm is employed. This scheme is such that the shape can be shifted from one coordinate system to another, locally or globally, according to free-surface orientation and compatibility conditions [Ramaswamy et al. 1990, Carvalho et al. 1997b]. Then solutions are analysed through: flow streamline patterns in separate zones; the effects of boundary condition change and free-surface adjustment; nip-gap size parameterization; speed-ratio change; surface tension effects; variations in distributed lift and localized pressure profiles; and movement of dynamic wetting line.

7.2 Computational domain and specifications

The practical laboratory setup of a typical reverse roll coating process is shown in Fig. 7.1 with the problem description schematically detailed in Fig. 7.2 employing a standard setting with regards to material properties and roller coating design. From Fig. 7.1, it is apparent that in the experimental process the pick-up roll, metering roll and applicator roll are all mounted horizontally, with the pick-up roll half submerged in a bath of coating liquid. Industrially in the present context, the applicator roll meets the strip-substrate to deliver the applied coating. This pick-up roll dips down into the coating bath and picks up the liquid whilst rotating; the liquid is then transferred to the metering roll, which meters the liquid to form a thin film; this is then transferred to the strip-substrate as a coating. Within the simulation, the part of the flow considered is the out-flow from the metering roll to the applicator roll, to the nip-gap, and proceeding to the coating region onto the substrate.

Process description: From Fig. 7.2, the computational domain consists of a cylindrical roller applicator, rotating in the forward direction, with the strip-substrate moving in the opposite direction; then, the liquid-film lies between the roller and the strip-substrate. The roller carries the fluid moving in the forward direction towards the nip and the strip picks up the coating fluid, whilst moving in the opposite direction. This involves fluid-splitting, to form the meniscus-strip coating (outflow), and the flow that is passed into-out of the nip-gap region. The flow zone occupying the localised, narrowest area between the roller and the strip is referred to as the nip-gap; this has positive width with an undeformable roll (no change in roll-shape). The application conditions are described by the capillary number (Ca), which is a ratio between viscous and surface tension forces. Fluid rheology is also an important factor that determines flow behaviour, in relation to stress generated in the coating process. Here, initially Newtonian fluids with constant shear-viscosities are simulated, regardless of the applied shear rates, and later inelastic shear-thinning liquids are introduced to discern differences in flow response.

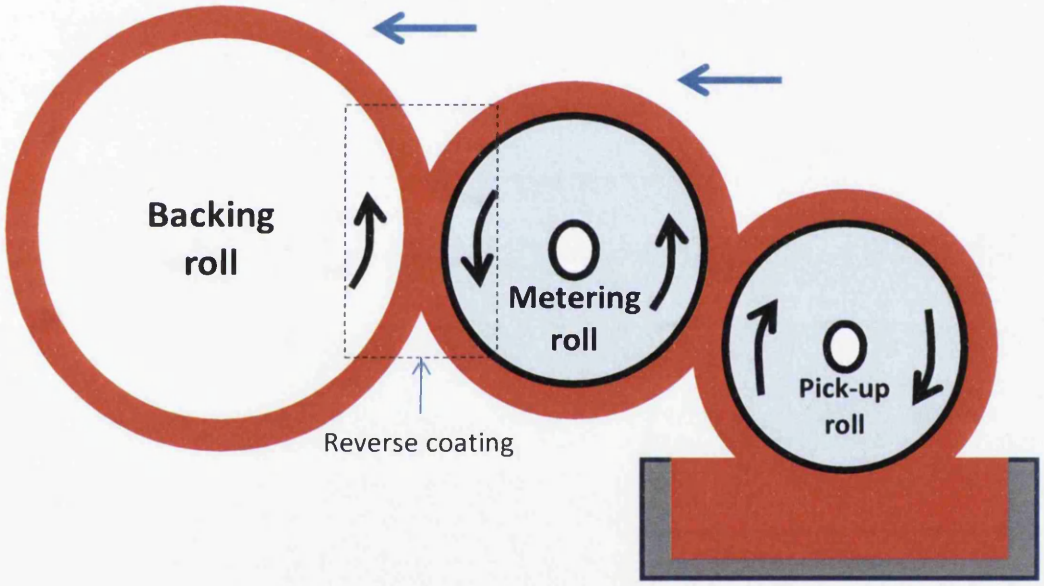

Figure 7.1: Reverse roll coating design setup

Problem domain design data: On process design and in non-dimensional units, the applied standard settings are: roller inlet film-thickness specified as 1.01 units, foil-substrate outlet coating thickness as 1 unit, nip-gap width as 0.1 unit (set at 10% of foil-outlet height h), and leakage film-thickness as 0.01 unit (at 1%h). Assuming suitable velocity scales, the foil-speed was set up as V_F=-1 unit (moving in the reverse direction of the roller) and roll-speed as V_R=1 unit, density and viscosity are set to unity (characteristic viscosity scale, μ_0). This choice leads to a non-dimensional group Reynolds number, *Re*, set at a typical value of 0.32.

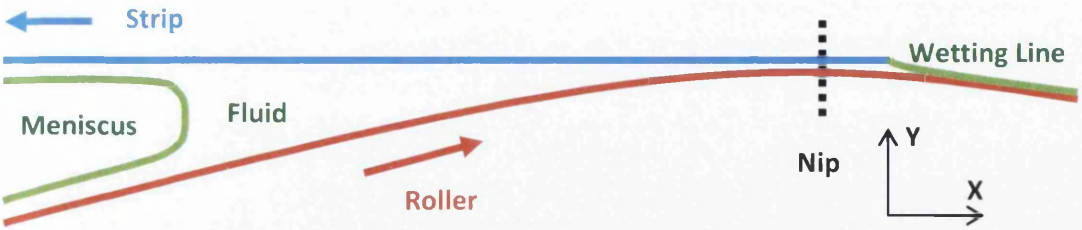

Figure 7.2: Schematic diagram of reverse-roller coating domain

The numerical scheme and simulation, employs a time-stepping finite element approach, semi-implicit Taylor-Galerkin pressure-correction scheme (TGPC). The computational domain is discretised into structured triangle elements. The principal finite element mesh used for the problem description is illustrated in Fig. 7.3 below, with mesh convergence assured through two other mesh choices, a coarser mesh consisting of 650 number of elements, 1563 number of nodes and 433 number of vertex nodes and a finer mesh consisting of 5208 number of elements, 10536 number of nodes and 2925 number of vertex nodes. Solution precision has been resolved on these meshes, without the inclusion of the extended free-surface wetting line, to avoid any additional instabilities stimulated by singularity inclusion. Differences in mesh solutions are found to be less than 0.1% in primary velocity-pressure components. The spatial domain was discretised through structured-meshing triangular elements employing a Taylor-Hood type of finite element, with quadratic velocity and linear pressure complete interpolations. In this choice, velocity nodal degrees-of-freedom are located at all vertex and mid-side nodes, and pressure degrees-of-freedom apply at vertex nodes only. A typical mesh employed is illustrated in Fig. 7.3; consisting of 1550 numbers of elements, 3485 number of nodes, 968 pressure nodes and 768 boundary nodes.

For an incompressible, isothermal laminar flow, the governing system of equations includes those for continuity of mass and momentum transport. Further to these equations, initial and boundary conditions are also required in order to complete the problem specification, from which to derive the corresponding pressure and velocity distributions. In this respect, a combination of Dirichlet and Neumann boundary conditions are imposed on the various variables and the solution process is initiated from rest. These initial conditions are specified by prescribing an initial rest state for the primitive field variables at time, t=0. With respect to free-surface location, traction-free-surface boundaries are assumed at the inflow, meniscus, outflow and wetting regions. These locations are determined via solution of the two equations provided in chapter 4 (eqn 4.67). Initial conditions on these free–surface boundaries are taken as quiescent. Then, to enhance efficiency in convergence to a steady-state, domain solutions are first computed with fixed-location traction-free boundaries, prior to release and completion of the solution search. Remeshing is performed after each time-step to avoid excessive distortion of elements in the boundary zones.

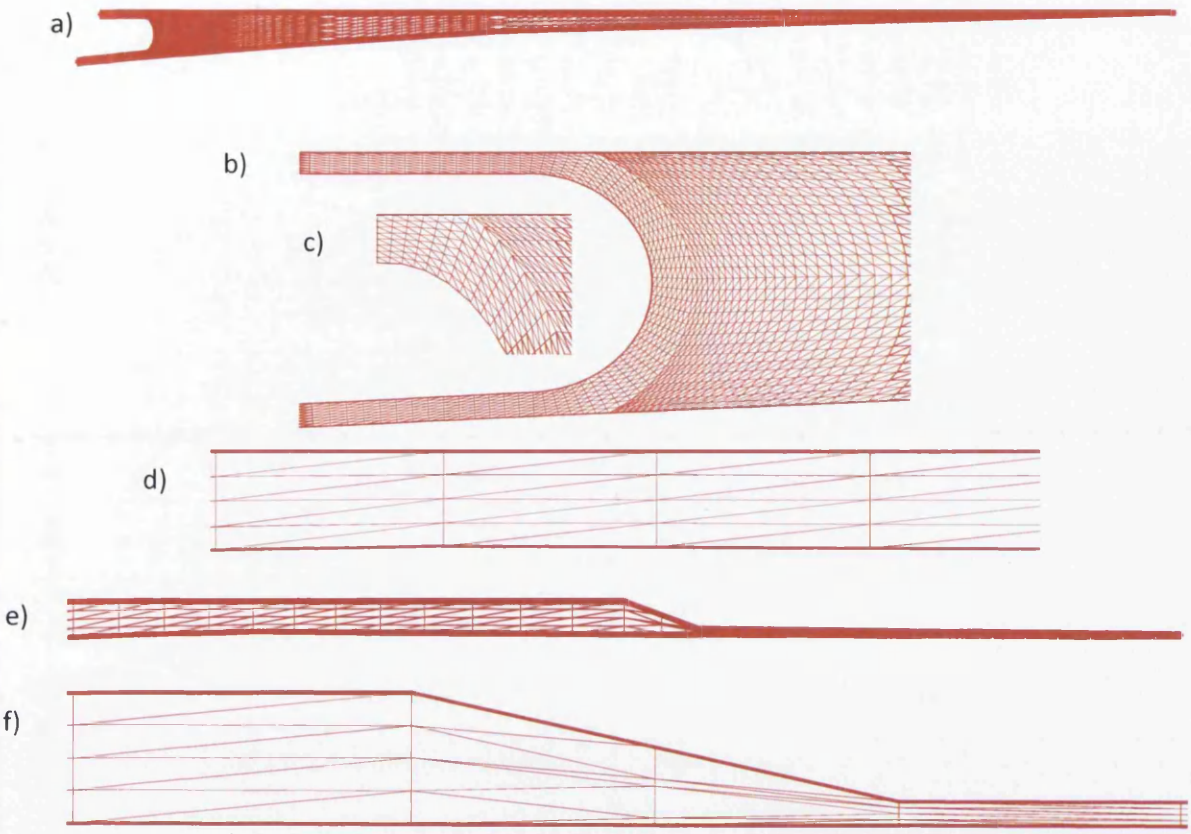

Figure 7.3: Finite element discretization; a) full mesh, b) meniscus region, c) zoomed meniscus, d) nip region, e) wetting region, f) zoomed contact and wetting region

Dynamic contact point adjustment: The contact point where the fluid interfaces meet the moving substrate is considered to be dynamic by allowing freedom of movement through the wetting of the adjacent surface sections. In doing so, when the nodes on the free-surface line segment make contact with the moving substrate, these nodes assume the substrate conditions and a new contact point is formed (see Fig. 7.4). Under such a procedure, the horizontal distance between the new and previous contact point is allowed movement in the forward positive x-direction only to avoid starvation at the nip.

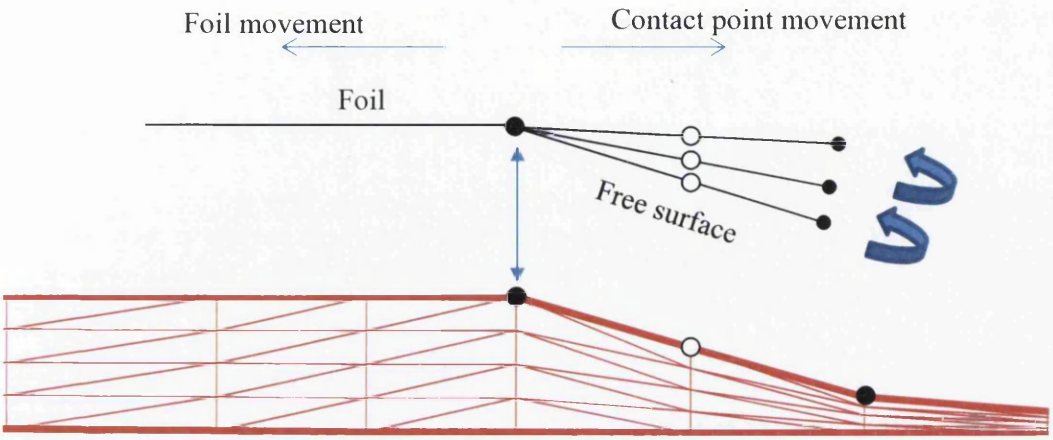

Figure 7.4: Treatment of dynamic contact point

Boundary conditions at the inflow and outflow boundary sections are considered to be those of plug flow (see Fig. 7.5), over which conservation of mass flow is satisfied, viz.

Mass balance, over flow domain from entry to exit with local reference:

$$[Q_{roller} = (V_{roller} h_{roller})] = [Q_{leak} = (V_{leak} h_{leak})] + [Q_{foil} = (V_{foil} h_{foil})] \qquad (7.1)$$

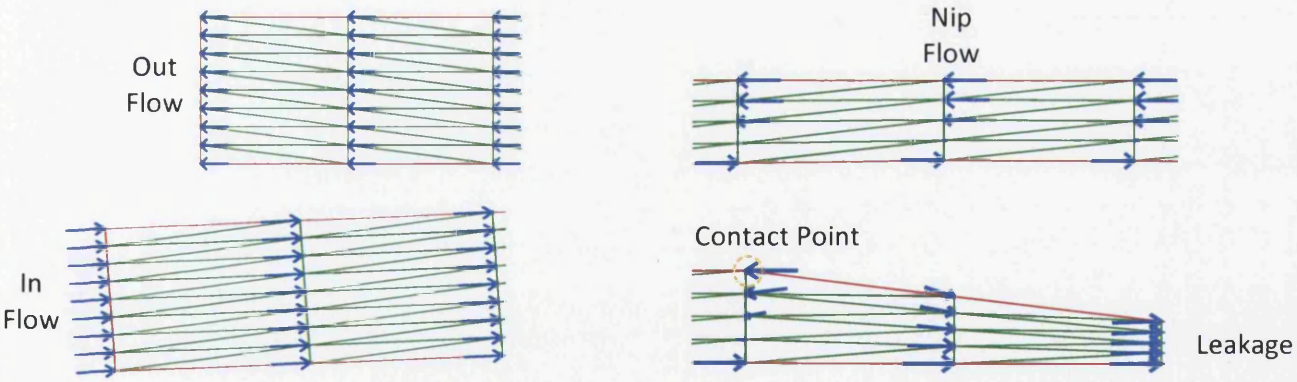

Figure 7.5: Boundary conditions; a) out-flow, b) in-flow, c) nip-flow, d) leakage flow

With respect to lift calculations, these are the mechanical forces that arise between solid and liquid surfaces. Lift forces apply on and normal to the strip-substrate. For a viscous inelastic fluid, the lift may be expressed as,

$$L_{strip} = \int_{\Gamma_{strip}} \left(-p + \tau_{yy}\right) d\Gamma = \int_{\Gamma_{strip}} L_f d\Gamma \tag{7.2}$$

where, $\tau = 2\mu D$, and L_f identifies the distributional lift quantities.

Surface tension considerations: Surface tension effects are analysed through application of interfacial surface tension forces on the free-surface boundaries of the RRC domain (inflow and outflow meniscus region). Both kinematic and dynamic conditions are considered within the surface tension calculation. On such free-surfaces, the kinematic condition ensures that the fluid does not cross such domain frontiers, via Equations (7.3 and 7.4). The dynamic condition of Equations (7.3) relates to a force balance across the free-surface (medium interface), where capillary forces prevail. For a fluid with surface tension coefficient ($\kappa_s = \frac{1}{Ca}$) the force balance at the interface is expressed as:

$$\sigma \cdot n = -p_a \cdot n - \kappa_s \left(\frac{1}{R_1} + \frac{1}{R_2}\right) \tag{7.3}$$

Here, σ is the Cauchy stress, p_a is ambient surrounding pressure, R_1 and R_2 are the principle radii of curvature [Ashmore et al. 2008] and n is the normal vector to the free-surface. In planar flow, R_2 tends to infinity [Tiu et al. 1999], thus for the free-surface boundaries as presented in the RRC domain, R_1 is considered as:

$$R_1 = \begin{cases} \dfrac{\partial^2 h}{\partial x^2} \Big/ \left(1 + \left(\dfrac{\partial h}{\partial x}\right)^2\right)^{3/2} & \text{for rounded meniscus} \quad (7.4) \\ \left(\dfrac{h}{R^2} + \dfrac{\partial^2 h}{\partial x^2}\right) \Big/ \left(1 + \left(\dfrac{\partial h}{\partial x}\right)^2\right)^{3/2} & \text{for the roller side (radius } R\text{)} \quad (7.5) \\ 2\sqrt{\sigma_s / \rho g} & \text{for the foil side \& wetting line} \quad (7.6) \end{cases}$$

Non-Newtonian material modelling: Initially, fluid coating material was considered as Newtonian with constant viscosity. Inelasticity was then introduced through an Ostwald-de Waele Power-law shear-thinning modelling; where power-law index (m=1) corresponds to Newtonian fluid response, and (m<1) for shear-thinning properties. Then, $0.1 \leq m \leq 0.6$, and κ_p is a consistency factor, taken here as unity, so that Newtonian zero-shear-rate viscosity is imposed at and below a unit shear-rate. The power-law model is represented as:

$$\mu(\dot{\gamma}) / \mu_0 = \kappa_p \dot{\gamma}^{m-1} \tag{7.7}$$

In addition, some viscometric data are also provided for a typical coating fluid paint. With associated first and second Newtonian plateaux apparent in the data, it was found more

suitable to appeal to a Carreau model fit (see Chapter 2, Fig. 2.2) to extract a reasonable match to this data, of the form:

$$\mu(\dot{\gamma}) = \mu_\infty + \left(\mu_0 - \mu_\infty\right)\left(1 + \kappa_c{}^2\dot{\gamma}^2\right)^{\frac{m-1}{2}} \qquad (7.8)$$

where additional parameters appear of upper/lower limiting *μ-plateaux*. In this fitting, typical parameter values yield a ratio of $\mu_\infty / \mu_0 = 0.01$ *units*, reflecting a two-decade decline in viscosity levels within the shear-thinning region.

7.3 Viscous flow solutions

Under such dynamic wetting line scenarios, first viscous analysis is launched with restriction to Newtonian constant viscosity rheology for the coating paints. Within the simulation procedures adopted, field solutions were initiated from a rest state, from which internal-domain consistent steady-state fields were pre-calculated that satisfy a fixed free-surface position. This necessitates surface velocity projection to satisfy continuity, reaching temporal-converged steady-state conditions based on a time-stepping relative increment norm tolerance of 10-6, using five mass iterations per Jacobi step. Mass balance is monitored and maintained across the inlet, outlet and leakage regions. The intermediate solutions thus extracted may then be adopted as a close internal-field approximation and initial solution-state for a fully dynamic free-surface calculation.

Numerical solutions are reported non-dimensionally in terms of flow streamline patterns, vortex structures, substrate pressure profiles, substrate distributional lift profiles, shear rate fields (tabulated) and dynamic wetting line locations. The fluid transfer modes in the domain, from the roller to the foil, are established using particle-tracking stream-traces. From Fig. 7.6, no flow reversal is apparent in the solutions at the vicinity of the meniscus. Here, the metered plug-inflow on the roller is observed to develop and travel up to the nip, to pass through to the roller outlet, with a secondary vortex occurring around the nip-region in the contact point vicinity; then most of the flow reverses to be taken up in the form of the coating on the substrate. The flow is characterized by a single large flow structure with two vortex transfer modes: a primary vortex, commencing around the meniscus, and a secondary vortex, between the nip and the contact region (see Fig. 7.6a, 7.6b). These observations concur well with experimental findings as reported in Gaskell et al. [5].

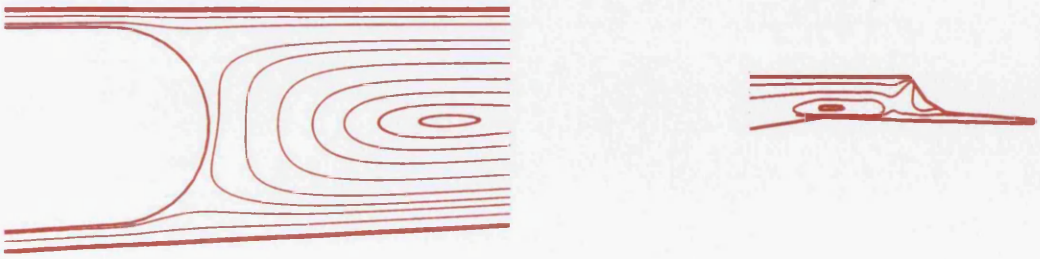

Figure 7.6: Newtonian rheology, vortex patterns around a) meniscus and b) nip region

Fig. 7.7 data illustrates corresponding foil-substrate pressure and distributional lift profiles. Peak-pressures are highly localised to the nip-region at a distance of 2% of foil-length (x=-10, relative to the origin at the narrowest part of the nip-gap), with maximum of $1.83*10^3$ units observed in nip peak-pressure. This pressure spike builds up from a distance of 20% of foil-length considered (500 units), to subsequently and instantly dissipate approaching the contact point. Distributional lift profiles are then dictated by pressure profiles on the substrate, yet increasing slightly more gradually towards the nip (max = $1.15*10^3$ units), before reducing once more to zero at the wetting line.

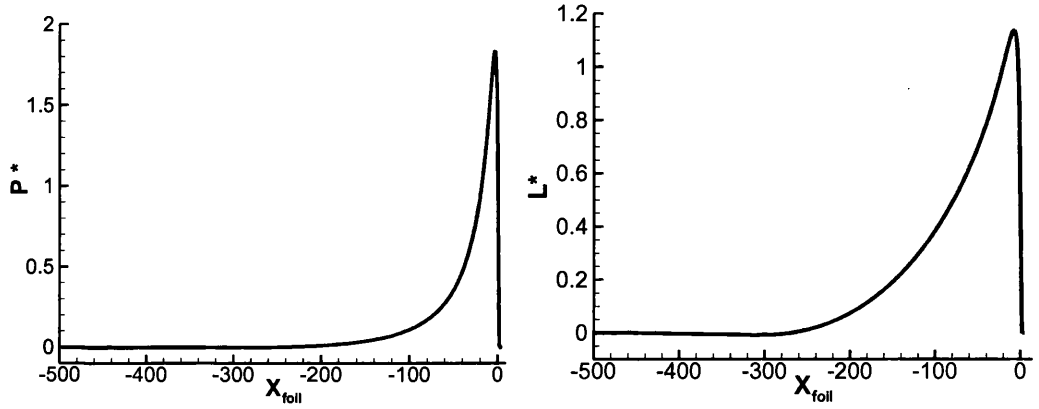

Figure 7.7: Substrate pressure and distributional lift profiles
(P* = Pressure * 10^{-3}, L* = Lift * 10^{-3})

Shear-rate field data at the meniscus and nip-region are provided in Fig. 7.8, with point values tabulated in Table 7.1. These data reveal vanishing shear-rates both on foil-side and roller-side at the meniscus and leakage-outlet, due to the flow conditions around these regions (plug flow). Toward the nip-region around point (x=-8.2), shear rate values are seen to gradually increase, reaching a peak value of 51.9 units at position (x=0.2), and then decrease to 27.8 units at the contact region. Shear rates are observed to increase span-wise across the nip-gap zone, with the maximum rate being biased towards the roller-side of the nip. This is a direct consequence of the secondary vortex and wetting-line presence, as without such features, shear-rate nip-maxima would arise on the foil-substrate (see our earlier findings, Belblidia et al. **[2012]**).

Shear Rates	Foil/Free side	Roller
Meniscus	0	0
Nip	12.2	51.9
Contact Point	11.9	27.8
Leakage	0	0

Table 7.1: Sample shear rates at specific locations in RRC-Domain

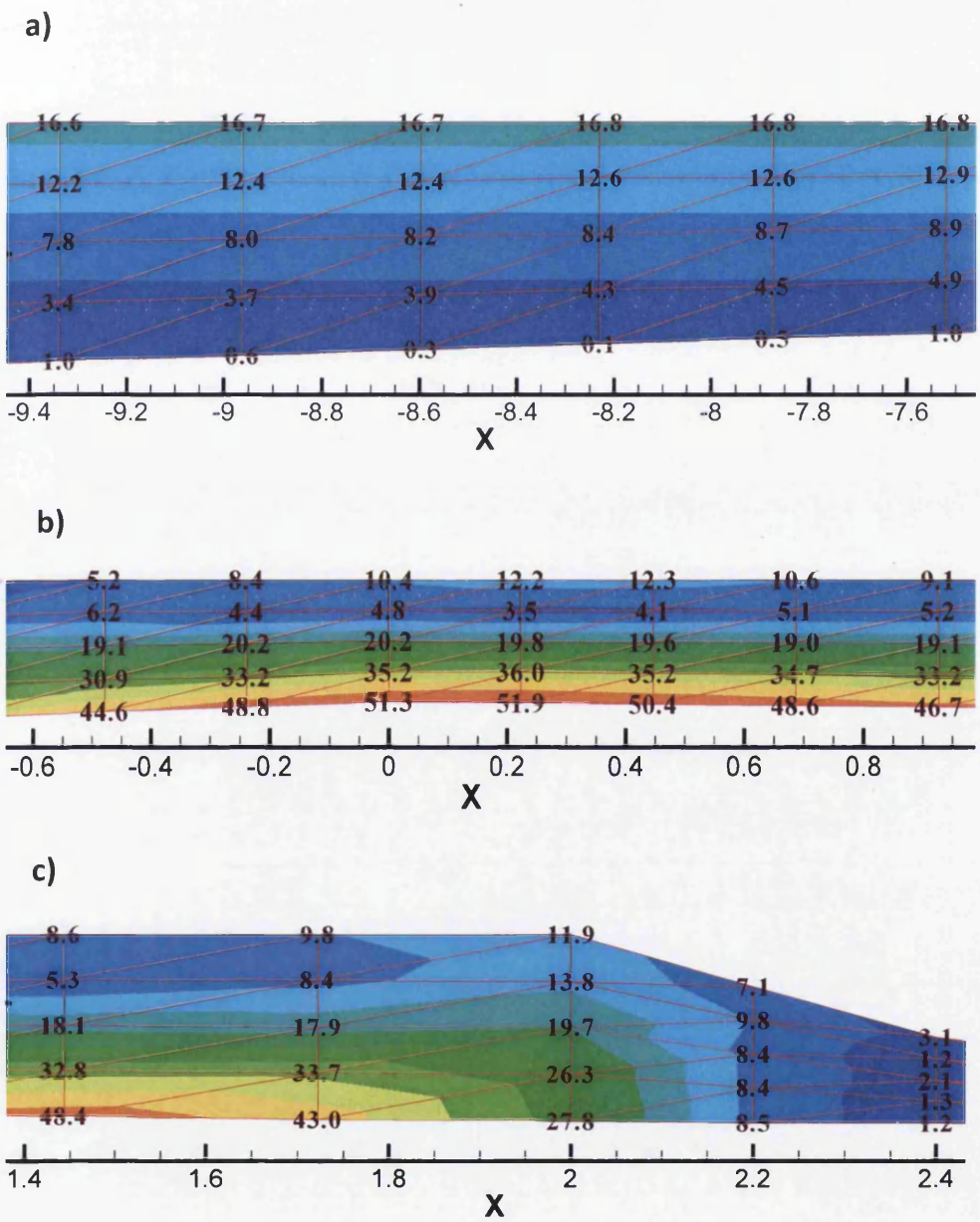

Figure 7.8: Shear-rate fields around the nip region, a) before nip, b) narrowest nip point, c) contact point.

7.3.1 Nip-gap variation and effects

Nip-gap conditions are held as of crucial importance to the overall RRC process, see Tiu et al. [1999]. Hence, analysis next turns to a parametric study on nip-gap width variation, with particular interest in the consequences on pressure and lift profiles. The base reference and standard design setting with Newtonian paint rheology, is of unity speed ratio (V_F=1, V_R=1 unit), and nip-gap of 0.1 units. This represents a nip-gap size of about 0.15μm (10% h, coating thickness) in practice. Then subsequently, four further nip-gap width sizes (s) of 0.005, 0.01, 0.02, 0.05 units have been considered.

Fig. 7.9a reveals the effects of reducing nip-gap size on substrate pressure profiles, whereupon the location of the pressure peak point shifts further towards the narrowest nip-gap point location. Similar trends and patterns are then inherited within the distributional lift profiles on the substrate (see Fig. 7.9b). At smaller nip-gap sizes (s<=0.01), pressure profiles display both exaggerated positive peaks (rises) and negative peaks (dips); the extent of pressure-minima rise with further reduction in nip-gap size. Most rapid pressure and lift variations begin to occur below nip-gap sizes around 5% (s=0.05). Extrema generated at the lowest nip size of 0.5% (s=0.005), are $130*10^3$ units in maximum peak-pressure and $72*10^3$ units in distributional lift. Such influence decays within the nip-zone, indicating that the wetting line acts as pressure relief mechanism, in agreement with the numerical and experimental work of Jang et al. [2009].

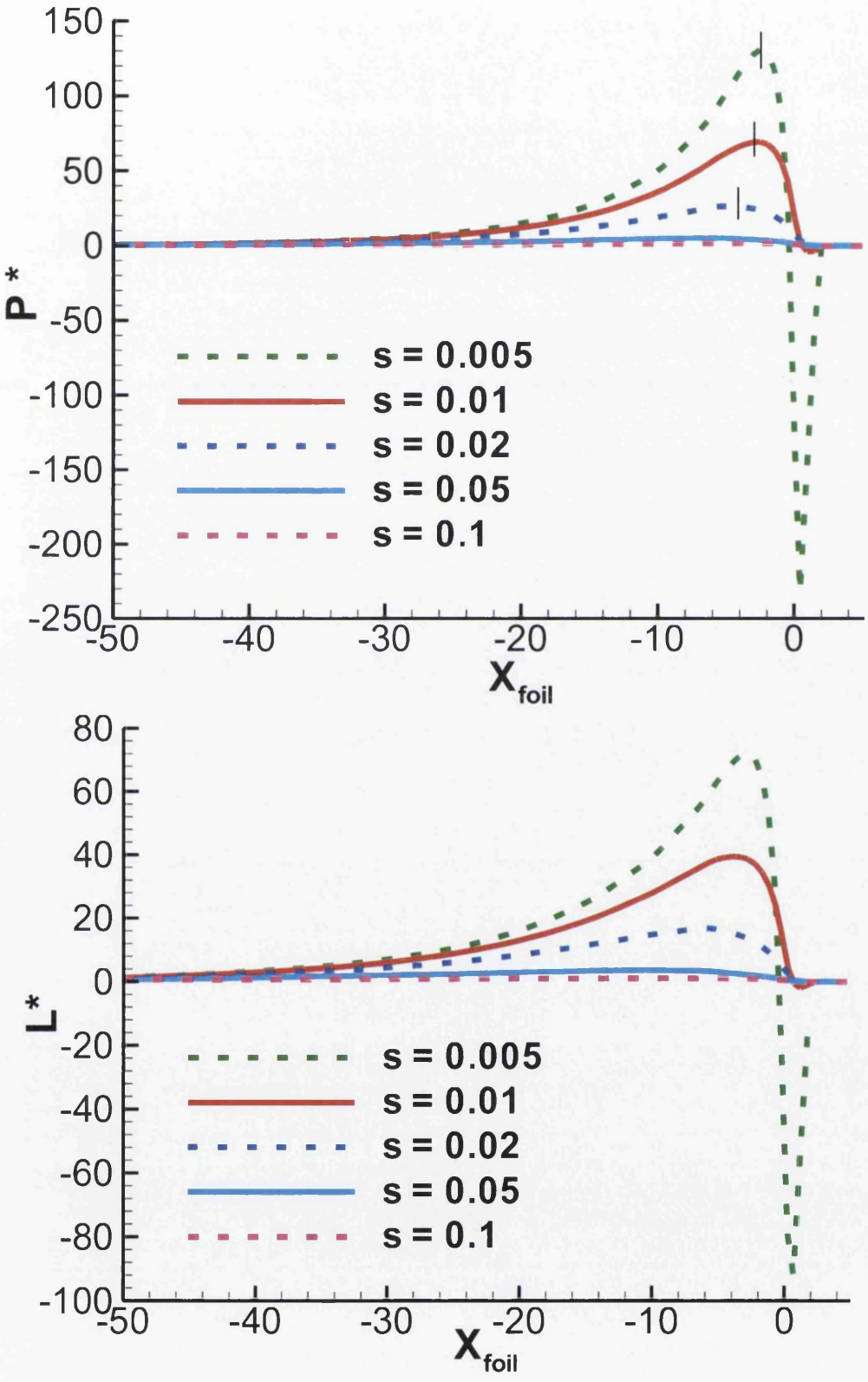

Figure 7.9: Influence of nip-size variation on; a) substrate pressure and b) lift profiles (**P* = Pressure*10^{-3}, L* = Lift*10^{-3}**)

7.3.2 Variation of speed-ratio

In departing from the base equal-balance speed-ratio of unity ($V_{ratio}=V_F/V_R$), here solution effects are investigated by increasing foil-speed relative to the roller $V_{ratio}=1.5$ ($V_F=1.5$, $V_R=1$ units), and vice-versa, increasing roll-speed relative to the foil $V_{ratio}=0.8$ ($V_F=1$, $V_R=1.2$ units). Fig. 7.10 illustrates the consequence of such variation in speed-ratio on streamline patterns over the meniscus and nip-regions. Observations reveal that speed-ratio can indeed have a significant impact on the solution, [see Hao et al. 1999], Benkreira [2002]. When $V_{ratio}=0.8$, streamline patterns are insignificantly affected from the base-case. In contrast with $V_{ratio}=1.5$, streamline patterns reveal a widening of the central vortex at the meniscus and at the nip zones. The downstream meniscus is sucked in, further towards the nip, as is the upstream wetting line, and the size and strength of the nip-zone recirculation is diminished (see circle-insert in Fig. 7.10). Thus, speculation implies that at somewhat larger speed-ratios, both meniscus and nip-zone vortices will merge, as indicated in the experimental observations of Gaskell et al. [2000].

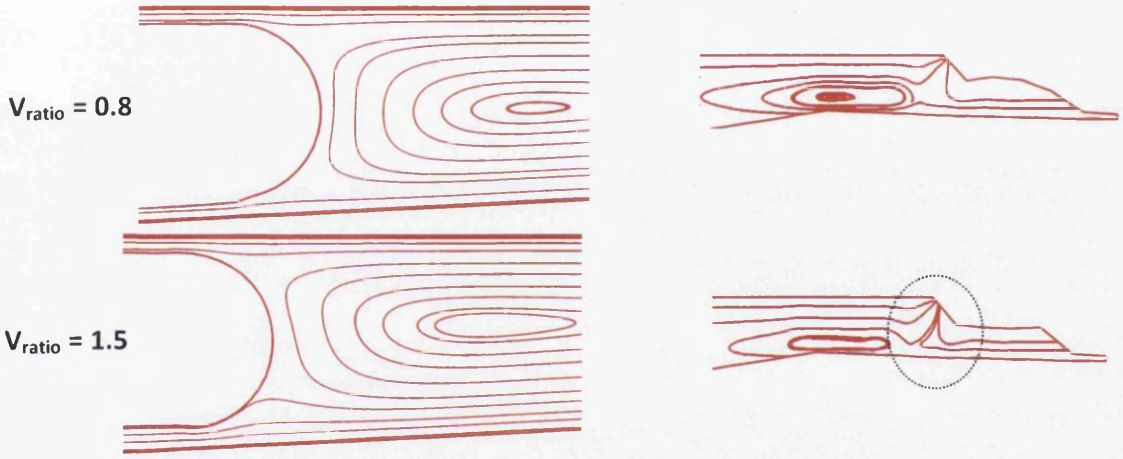

Figure 7.10: Influence of speed ratio (V_{ratio}) on streamline patterns at meniscus and nip regions

Fig. 7.11a & 7.11b presents sets of substrate pressure-profile results for two choices of nip-gap setting s={0.1, 0.01} units, according to speed-ratio adjustment. Most significant rise in pressure-peak occurs with increase of speed-ratio ($V_{ratio}=1.5$) under either design, but also, decreasing adjustment leads to a slight rise in pressure-peak; one notes, a maximum pressure peak of 10^5 for the narrower nip-gap (s=0.01 units), and $2.4*10^3$ for the wider nip-gap (s=0.1 units). The footprint of the pressure rise noticeably switches between nip-gap, being 200/300 for wider nip-gap (s=0.1 units) and 60/100 for narrower nip-gap (s=0.01 units). An interesting observation is that with speed-ratio *decrease*, pressure distribution is barely affected, whilst there is a marked effect upon pressure distribution under speed-ratio *increase* (either design). The location of positive peak-pressure around the nip-region remains unaffected by speed ratio variation for both nip-gap settings.

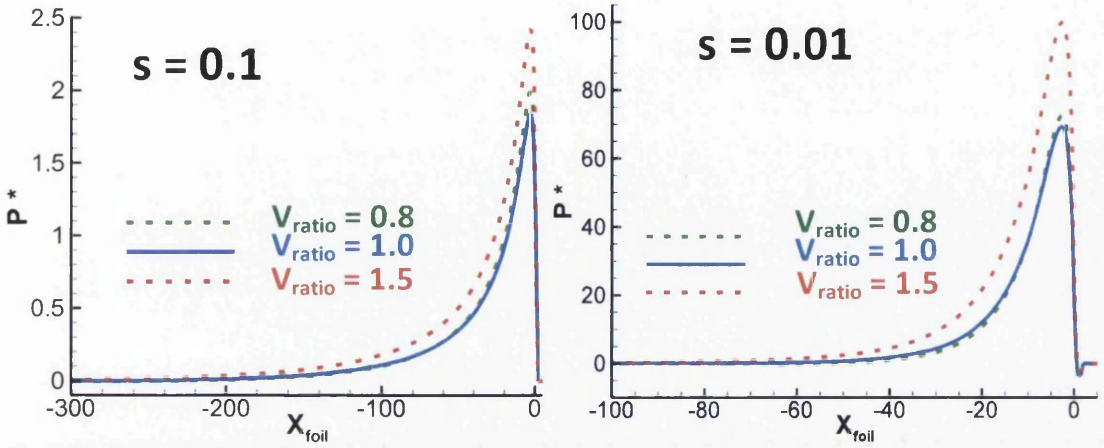

Figure 7.11: Influence of speed ratio (V_{ratio}) on pressure profiles for nip size a) s = 0.1, and b) 0.01 (**P* = Pressure * 10^{-3}, L* = Lift * 10^{-3}**)

7.3.3 Influence of surface tension

First, surface tension effects were analysed under the standard design setting (V_{ratio}=1, s=0.1, Newtonian rheology), considered upon both the meniscus and wetting line surfaces. Solution data are reported in terms of streamline patterns and adjustment of wetting line position (**see** Fig. 7.12), since kinematic conditions were barely affected. Here, one may clearly observe that changes are undetectable in fluid transfer and flow structures, both at the meniscus and nip-regions. In contrast, surface tension plays a major role along the wetting line and within the contact point zone, where a *third vortex* emerges, with its origin close to the contact-point attached to the wetting-line. As surface tension is increased (Ca^{-1} decrease), the contact point on the foil-substrate (vertical dashed line insert) shifts further away from the narrowest nip-gap location. The vertical line insert shows the position of the wetting line-foil contact point for the Newtonian solution without surface tension (x=2.0); once surface tension was introduced, this point shifts away from the initial insert line position to form a new contact point at (x=2.4), where the third vortex appears. As the level of surface tension is increased still further, this vortex now grows and expands causing dramatic reduction in film-leakage; as visible from the adjustment in the third contact-point wetting-line vortex structure, which grows in size and strength.

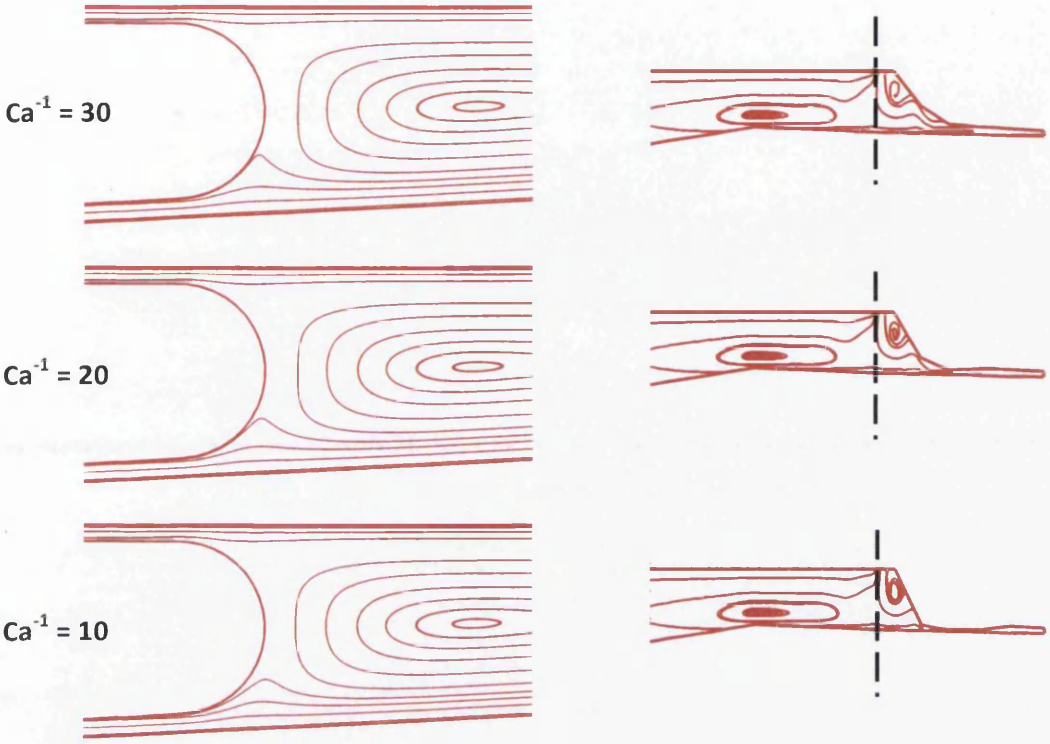

Figure 7.12: Surface tension effects on vortex structure at the meniscus and wetting regions

7.4 Inelastic flow solutions

The next point of study turns to investigating the influence of adjustment in material rheological properties, under standard domain design and RRC process settings (V_{Ratio}=1, s=0.1). In this respect, shear-thinning inelastic models are introduced, representative of industrial paint coatings. Since deformation conditions away from the nip are essentially those of plug-flow (small to vanishing shear-rates) at the inlet, outlet and meniscus regions, hence inelastic shear dependency will only manifest itself within the localised nip-region, where large variation and high shear-rates are exposed. Typical shear-thinning properties analysed are those which cover variation in power law indices, m={0.1,0.3,0.6,1.0}, (κ_p=1).

7.4.1 Power-law model

Vortex Structures: Fig. 7.13 illustrates the various streamlines flow patterns extracted for the power-law shear-thinning model. Previous studies have revealed that rheological material properties can have a significant impact on vortices and flow solution, see Echendu et al. [2011]. Vortex patterns around the meniscus region are shown to be invariant with power-law index reduction both in shape and structure. Here, viscosity levels barely change practically right up to the miniscule nip-zone, where high shear rates occur and shear thinning begins. In the second set of streamline patterns that correspond to those around the

nip-region, adjustment in the transfer vortex is clearly apparent, which expands towards and travels into the nip as shear-thinning influences increase (m decreases).

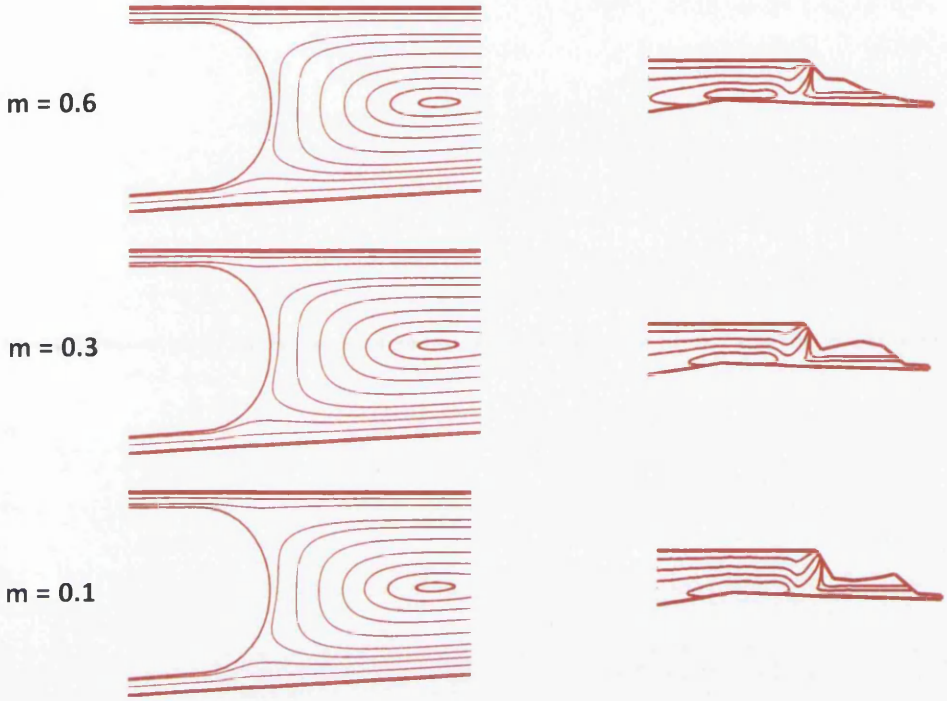

Figure 7.13: Vortex structures for Power-Law fluids at meniscus and wetting regions

Pressure and lift profiles: The effects of shear-thinning on pressure and distributional lift substrate profiles are illustrated in Fig. 7.14. With decline in power-law index (m), maximum peak-pressures decrease and the location of the fluid splitting point shifts slightly further away from the nip. This effect is due to expansion and shifting of the nip-zone vortex itself, which expands further away from the nip and into the extended meniscus zone.

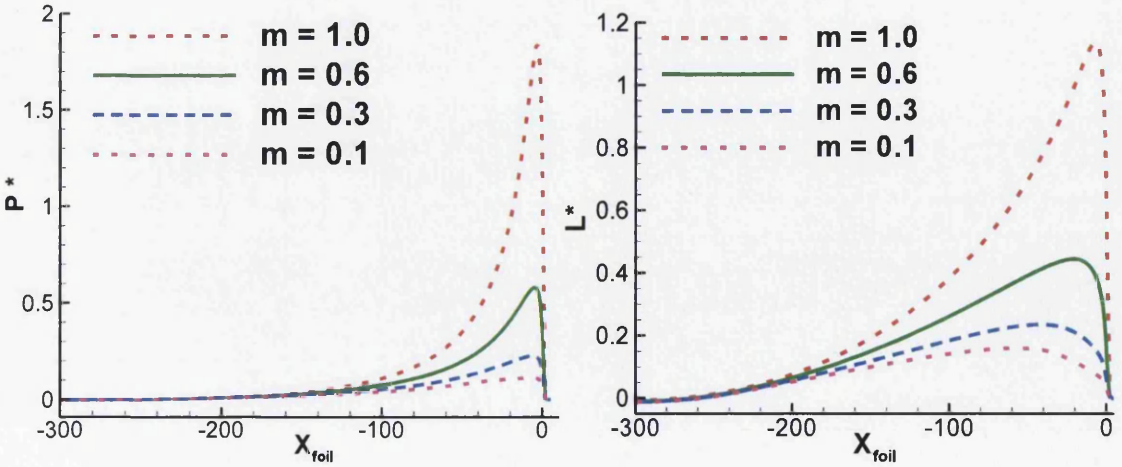

Figure 7.14: Substrate pressure and distributional lift profiles for Power-law fluids
(P* = Pressure * 10^{-3}, L* = Lift * 10^{-3})

Shear rates: Table 7.2 provides some localized and point-wise extrema in shear rate data for these shear-thinning power-law fits in the nip-region. Here, shear rates are generally noted to increase as the power-law index (m) is reduced. For Newtonian fluids (m=1), shear rates hit a maximum of 52 units at the narrowest nip-gap setting (see above Table 7.1); yet, as shear-thinning is introduced and at a maximum thinning rate supported by m=0.1, shear rate maxima at the nip reach extrema of 120 units.

Table 7.2: Sample shear rates for Power-Law fluids

Regions/Power Index	Nip		Contact Point	
	Foil side	Roll side	Foil side	Roll side
m = 0.6	14	79	14	36
m = 0.3	20	106	19	49
m = 0.1	28	120	23	55

7.4.2 Carreau model fit to industrial paint coating

Some viscometric data have been provided for a typical industrial topcoat fluid at a temperature of 40°C, showing viscosity trends over a range of shear rates. The industrial topcoat data provided is fitted with a Carreau model over a range of shear rates (10-6 to 10-1) with parameters (=0.01). This setting is compared against varied second viscosity plateaux (□□/□0=0.1 and 0.005). With these Carreau model fits to the industrial coating data, the range of shear-rates are shifted to low shear-rate values when compared to the Power-law fit (see Chapter 3, Fig. 3.2). Thus interpreted relatively, the industrial coating thins earlier and faster, and at the nip, reaches its second Newtonian plateau value at the extremely high shear-rates encountered there.

Streamlines: From Fig. 7.15, as the viscosity plateau ratio is decreased, the streamline patterns for the Carreau model fit, hardly differ from those observed with the Newtonian solution at the meniscus region. However, some differences are apparent at the downstream nip vortex with the vortex intensity decreasing and expanding into the narrowest nip-gap region. There are no significant changes observed at the wetting line between 0.1≤ ≤0.01, whereas at viscosity plateau ratio =0.005, free-surface bulging arises, which has a tendency to increase the magnitude of the film-leakage. Variations are only expected to occur when fluids are thinning at the nip-region, as shown in the power-law solutions. Hence, under Carreau approximation, the solution at the nip more closely resembles that of a Newtonian fluid with a constant high shear-rate viscosity (of =0.01 units).

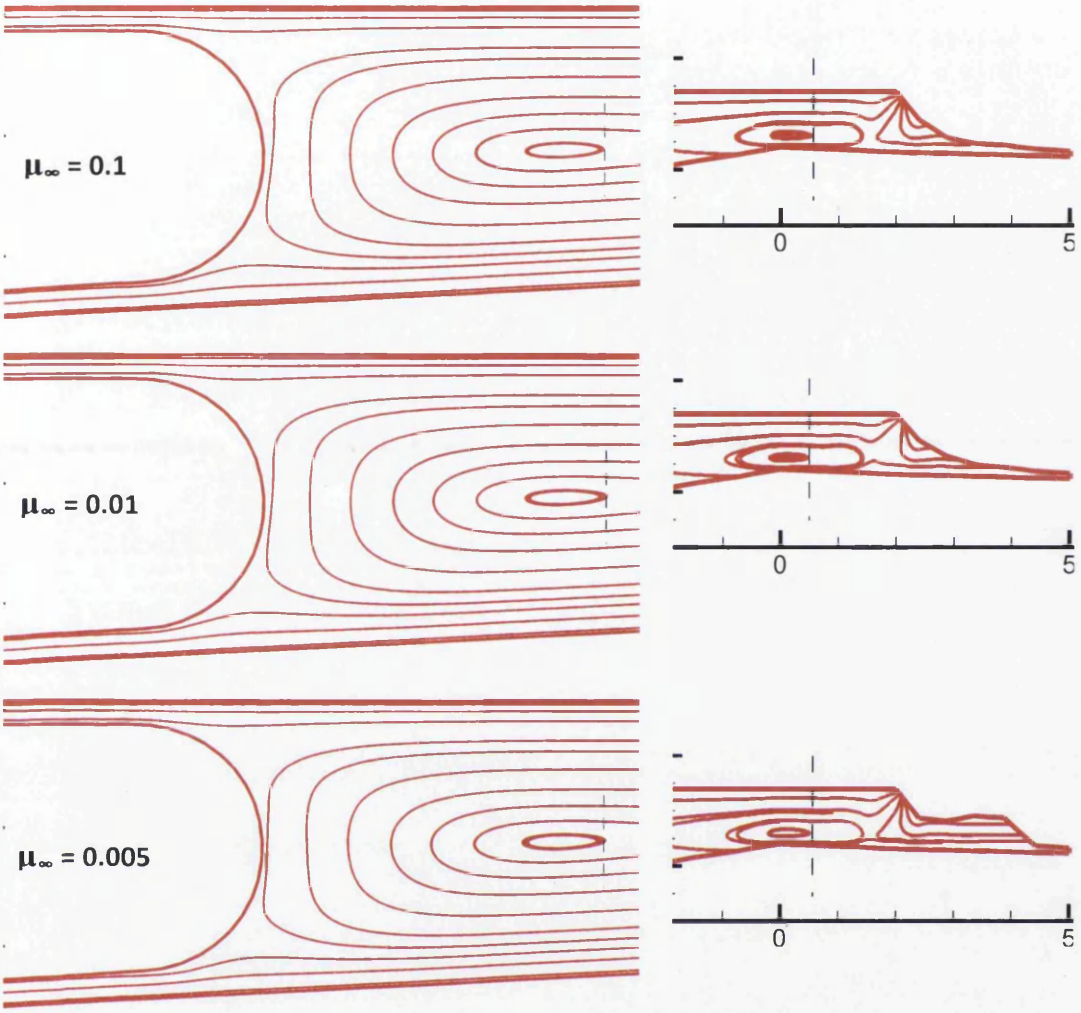

Figure 7.15: Vortex structures for Carreau model fluids at meniscus and wetting regions

Pressure and lift profiles: Conspicuously, Fig. 7.16 shows the effects of pressure and lift profiles on the foil-substrate for varying viscosity plateau ratios ($0.1 \leq \mu_\infty / \mu_0 \leq 0.0005$). The maximum peak-pressure of $0.183 * 10^3$ is observed for $\mu_\infty / \mu_0 = 0.1$; reducing to a positive peak-pressure of $0.018*10^3$ at $\mu_\infty / \mu_0 = 0.01$; and to the lowest peak value of 0.012 at $\mu_\infty / \mu_0 = 0.005$. This manifests a reduction of one order of magnitude when comparing solutions for $\mu_\infty / \mu_0 = 0.1$ to that corresponding to the Newtonian solution; such Carreau solutions are of equivalent magnitude to Power-law solutions with m=0.1. The order of magnitude reduction in pressure increases with decreasing viscosity plateau ratio. This reveals the effect of imposition of the second Newtonian plateau in shear viscosity. Lift profiles also show the same characteristic trends as observed in pressure.

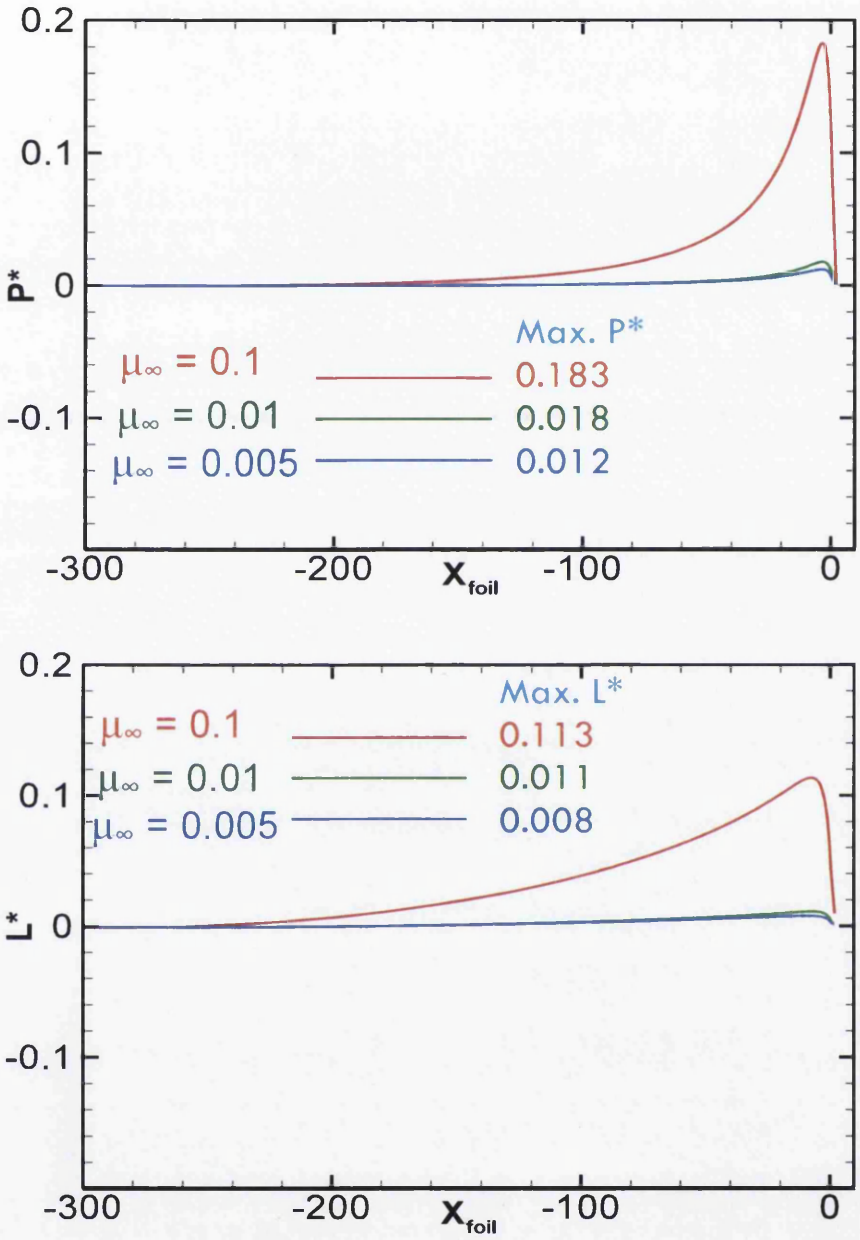

Figure 7.16: Substrate pressure and distributional lift profiles for Carreau model fluids (**P* = Pressure * 10^{-3}, L* = Lift * 10^{-3}**)

7.5 Outcomes-overview

This phase of study has particularly addressed wetting line inclusion in the context of finite element solution for thin-film reverse roller coating, drawing upon free-surfaces and viscous-inelastic paint-coating rheology. The analysis has illustrated solutions through streamline patterns, substrate pressure and distributional lift profiles, demonstrating effects of parameterisation over nip-gap size, speed-ratio and surface tension on dynamic wetting.

Flow streamline patterns reveal two vortex fluid transfer modes within the RRC domain, a large vortex at the meniscus region and a secondary smaller vortex at the nip-wetting region. Both vortices are influenced by variation in foil:roller speed-ratio. As speed-ratio increases, the downstream vortex at the meniscus expands inwards towards the nip-region, whilst the upstream secondary vortex at the wetting region also expands inwards, away from the narrowest nip-region, and reduces the size and strength of the recirculation. As speed-ratio increases, this is held to be physically reasonable as the dynamic wetting line position is pulled inwards towards the nip-gap.

Pressure and lift profiles show positive peak-pressures just before the nip and negative peak-pressures around the contact point (for low nip-gap widths of $s<0.01$). As nip-gap size increases above $s=0.5$, the variation in pressure becomes quite small with correspondingly low positive peak-pressures. At a nip-gap size of $s=0.01$ and above, no negative peak-pressures are observed around the contact region. As roll-speed is increased, positive pressure-peaks only increase at a low rate; whilst comparatively, positive peak-pressures increase rapidly with increase in foil-speed.

Analysis on surface tension reveals that as the capillary number is decreased, the contact point moves in the opposite direction to that of foil-movement, sucking more fluid from the wetting line. This has the effect of stimulating growth in a third vortex around the contact-point region, and apparent reduction in leakage film-width.

Findings on inelastic paint rheology representation, under which shear-thinning is taken into account, reveal that as the power-law index (m) is decreased, positive peak-pressures decrease linearly. Streamline flow patterns show that the primary vortex structure at the meniscus remains undisturbed due to shear-thinning; whereas the minor secondary vortex structure at the nip-zone is seen to expand into the nip-gap. When a typical industrial paint topcoat is matched with a Carreau model fit, predictions reveal two orders of magnitude reduction in localised peak-values of pressure and lift, with the same intensity of vortex transfer structures as observed for a Newtonian paint.

Chapter 8

Reverse roll-coating: viscoelastic PTT flows*

This chapter deals with the viscoelastic modelling of reverse roll coating with dynamic wetting lines. Here, various non-Newtonian viscoelastic paint materials are analysed, appealing to the Phan-Thien Tanner network class of models. These models provide suitable representation for typical polymer solutions, with properties of shear-thinning and strain-hardening/softening. The numerical technique utilizes a hybrid finite element-subcell finite volume algorithm with dynamic free-surface location, drawing upon a fractional-staged, predictor-corrector, and semi-implicit time-stepping procedure. Numerical solutions are investigated following a systematic study, allowing for parametric variation in elasticity (We-variation), extensional hardening-softening (ε), and solvent fraction (β). Under incompressible flow conditions, LPTT and EPTT constitutive equations are used to generate viscoelastic solutions, covering a range of Weissenberg numbers (We) up to critical solution levels. Results are analysed through velocity fields and vortex developments, pressure and lift profiles, shear-rate and stress fields. Various differences are observed comparing solutions under both constitutive models, where the main aim is to analyse flow features as a consequence of adjusting rheology. This is observed principally around the nip and wetting line regions. The solution trends gathered reveal qualitative agreement with comparable theoretical studies.

8.1 Introduction

The main interest here lies in analysis of the reverse roll coating (RRC) procedure with non-Newtonian viscoelastic flows. In this regard, earlier viscous modeling work is built upon [Belblidia et al. 2012, Echendu et al. 2013] from that of previous chapters, which involved RRC with inclusion of dynamic wetting lines and inelastic materials. To date, the development of such procedures has appeared as an active area of research in the literature. The majority of theoretical work has employed Newtonian fluids, with only limited attention being paid to viscoelastic analysis. Nevertheless, industrial coating liquids often display viscoelastic character, containing varying amounts of polymer, which may affect process operating conditions. Hence the pertinence of this chapter, being concerned with the computational modelling of viscoelastic material under reverse roll coating flow configurations, analysing the rheological effects of material functions through parameter variation. The numerical solver utilises a hybrid finite element-subcell finite volume algorithms with dynamic free-surface location, drawing upon a fractional-staged, predictor-corrector, semi-implicit time-stepping procedure. Previous viscoelastic solutions of coating flows were studied by Zevallos et al. [2005] employing Oldroyd-B and FENE-P models for forward roll coating flow. Findings explained the analysis of Graham [2003] on the viscoelastic destabilization of the free-surface meniscus flow field, as in Zevallos et al. [2005], elastic stress was shown to influence the flow near the meniscus, by reducing and eventually eliminating the recirculation with increasing elasticity (We). Triantifilopous [1996] analysed the effects of liquid rheology in coating systems. Theoretical viscoelastic effects include the study of Greener and Middleman [1975] using an empirical constitutive relation to describe the material model, where observations reveal a decreased pressure at low Weissenberg numbers. Over recent years, there has been a considerable shift in emphasis to model paint rheology, away from constant shear viscosity Oldroyd-B models, to those of shear-thinning PTT models and FENE models. In experimental analysis, Tiu et al. [1999] studied the effects of non-Newtonian fluid properties on pre-metered reverse roll coating for hard-hard rolls, finding that the fluid viscosity plays a dominant part in determining the strip-film thickness, while the liquid feed-rate and nip-gap determines the metered film thickness. That study also found that viscoelastic fluids produce thicker, more stable films than do Newtonian fluids. Carvalho et al. [1994], and more recently Lopez et al. [2002b], studied non-Newtonian effects on ribbing instabilities. The former revealed that the lower the flexible polymer content, the lower the critical speed for 3D instabilities to occur.

The present phase of study focuses on the computation of non-Newtonian viscoelastic flow in a reverse roll coating setting with dynamic wetting lines. The computation here employs a Taylor-Galerkin pressure-correction algorithm with a second-order hybrid finite element and finite volume method [Carew et al. 1993, Wapperom et al. 1998]. This is a semi-implicit time-stepping procedure, solving for velocity, stress and pressure over fractional-staged equations. The parent finite element triangle is partitioned to form four child, triangular finite

volume sub-cells. A finite element discretization technique solves the mass and momentum equation with quadratic velocity interpolation on the parent cell, while a finite volume sub-cell-vertex approach solves the constitutive equation for stress, using linear stress interpolation on the child cell. This hybrid scheme is deemed to provide second order accuracy for this study [Webster et al. 2005, Aboubacar et al. 2001, Aboubacar et al. 2005]. The finite element method may be further stabilized through a 'Streamline Upwinding Petrov Galerkin (SUPG)' technique [Carew et al. 1994], combined with a local direct method of recovery for velocity gradient approximation [Hawken et al. 1991, Matallah et al. 1998]. This scheme captures highly accurate discrete representation of the finite element solution. The computational domain involves two free-surface boundary sections; the upstream meniscus and the downstream wetting line. Free-surface movement is determined through a time dependent particle tracking scheme, a local kinematic condition governing the temporal evolution of the deformed domain using a height function [Phan-Thien 1977, Chandio et al. 2003]. Two forms of PTT constitutive model are considered to represent the rheology of typical industrial polymer solutions. A linearised PTT model, which has increasing extensional viscosity property that reaches an elevated plateau at high strain-rates; and the exponential model, which gives decreasing extensional viscosity that reaches a low plateau at high strain-rates. The numerical solutions thus derived explore corresponding vortex structures, pressure and lift profiles, and stress fields, over a range of elasticity (We) and material function parametisation.

Previous computations with this numerical approach, for free-surface flows with viscoelastic (PTT) models, include studies for die-swell flows [Al-muslimawi et al. 2013, Ngamaramvaragul et al. 2000], tube-tooling and wire-coating [Ngamaramvarangul et al. 2002]. Hence, in this chapter, the main aim is to model an industrial polymer coating flow, utilizing these PTT viscoelastic constitutive models for the RRC domain, an application that has received little coverage to date. Details of the analysis focus on the: effects of elasticity (We increase); influence of tension-hardening and strain-softening (LPTT to EPTT comparison); and impact of polymer concentration via change in solvent fraction content.

8.2 Problem specifications

The computational domain is an extension to the geometry analysed in chapter 6, but includes the dynamic wetting line as illustrated in chapter 7. This work is a natural extension of the rheological studies of chapter 7. The viscoelastic models employed are chosen to facilitate approximation to the rheological response under flow of industrial paint coatings.

Under incompressible isothermal conditions, the behaviour of viscoelastic flow is generally governed by the fundamental principle of fluid mechanics expressing the conservation of mass and momentum (see chapter 2).

In the present application, the first model variant adopted is the EPTT model, featuring a shear viscosity with shear-thinning behaviour, as opposed to the constant shear viscosity represented with the Oldroyd-B model (see chapter 3; PTT with f=1). This form of PTT model possesses a strain-softening material response function under classical extensional deformation, which reaches sustained lower asymptotic-limit at large strain-rates. The constant non-dimensional parameter ε largely dictates severity in strain-hardening/softening, with smaller values approaching zero offering the greater extremes (larger Trouton ratios). Depending on the ε-parameter selected, and below a value of 0.5, the EPTT model features initial hardening, prior to subsequent softening upon further rise in strain-rate.

For contrast in rheological characteristic response, EPTT solutions are compared against those for the LPTT model, the linearised functional PTT form. This Linear PTT model also exhibits shear-thinning behaviour, as under EPTT, but reflects only strain-hardening response, which is capped at large strain-rates (sustained-hardening property).

Under ideal shear and extensional flow deformation, corresponding material functions provide a vital guidance against which to interpret solution response in complex flow (mixed shear-extension). In chapter 3, Figures 3.5(a-d), material function plots for the respective PTT models have been presented, considering the relevant parameters, covering functional forms for steady-state shear (η_s) and extensional (η_ε) viscosities, shear stress (τ_{xy}) and first normal stress difference (N_1).

{ε, β}-variation: The parameters considered are in the range of β={0.9,0.1,0.01}, at ε={0.02, 0.15,0.25,0.5}, as displayed in Chapter 3, Figures 3.5(a-d). Under PTT modeling, the selected parameters have been chosen to isolate the effects of shear-thinning, strain hardening/softening and amount of solvent fraction, respectively. Initially, an EPTT flow model was simulated with β=0.9 at extensional viscosity (ε=0.5) up to critical elasticity (We). A change of solvent fraction to β=0.1 and 0.01 reduces the second plateau of shear-viscosity to respective levels, causing an increase in the rate of shear-thinning. Also, there is a reduction in the second plateau of extensional viscosity with change of solvent fraction, which increases levels of strain-softening. In contrast to this, at β=0.1 and ε=0.25, decreasing the extensional viscosity introduces slight hardening, where the extensional viscosity behavior of the EPTT fluid, marginally increases up to a peak level (hardening), and then rapidly decreases (softening) as the strain-rate rises further.

Under LPTT properties, no such softening feature is apparent. LPTT solutions were sought for β=0.9, ε=0.5, and then β=0.1 and 0.01. In terms of shear viscosity, this LPTT fluid possesses almost the same properties as those for the EPTT fluid with the same parameters; with the exception that the EPTT fluid thins a little faster. Notably, however, the terminating extensional viscosity of the LPTT fluid increases up to a plateau-level at high strain-rates; which itself is determined by the ε–parameter setting. At ε=0.5, extensional behaviour is

invariant (practically Newtonian), whereas at ε={0.25,0.15,0.02}, tension-hardening is appreciable, with rise up to limiting plateaux-levels of η_ε= {4.0,7.6,12.4,90.4}.

Such material response is closely matched in both shear viscosity and first normal stress difference, see chapter 3, Figure 3.5d. In extensional viscosity of Figure 2b, noted differences arise over the deformation rate range from 10^{-1} to 10^{4}; and likewise in N_1 at rates above 10^{-1}. Significant differences are observed in all three material functions under the highly-mobile state of β=0.1 and for even smaller solvent fractions; this is apparent in shear above rates of 10^{0}, and in extension above rates of 10^{-1}. For EPTT, {ε, β}={0.5, 0.01} is the more shear-thinning of the two instances in model 3 and model 7. This is also reflected therefore in N_1 (chapter 3, Fig. 3.5d), where peaks and limiting N_1 high-rate plateaux vary; weaker for EPTT than LPTT model. Hence, when {ε, β}={0.25, 0.1}, extensional response is clearly more complex, rich in variation and rate dependent: displaying first strain-hardening in the rate-range 10^{-1} to 10^{1}, prior to softening in the rate-range 10^{1} to 10^{4}.

The solution technique selected is that of the hybrid finite element/finite volume scheme. The formulation employed is the Taylor-Galerkin pressure-correction (TGPC) algorithm, where the semi-implicit form of Carew et al. [1993] is modified, with finite element discretisation for the mass and momentum equations, and a finite volume sub-cell-vertex scheme for the constitutive equation. The TGPC framework combines a Lax-Wendroff time-stepping procedure based on temporal discretisation and Taylor series expansions [Donea 1984], with an incremental pressure-correction (PC) procedure. Under incompressible conditions, the coupled systems of equations are segmented at each time step into a number of fractional stages, which is solved in sequence providing a second-order level of temporal accuracy.

A spatial Galerkin *fe* discretisation is applied on the momentum-continuity equation system and a finite volume method is adopted for the viscoelastic stress constitutive equations. This method employs a cell-vertex scheme based upon fluctuation distribution, where control volume residuals are distributed through an upwinding technique, and medium dual cell approximation is introduced to handle non-homogeneous source-term contributions.

The computational domain is spatially discretised through structured-meshing triangular elements (tessellation) employing a Taylor-Hood type of finite element with six-noded finite element triangles; three vertex nodes and three mid-side nodes. Velocity components are computed through quadratic interpolation functions at the six nodes of the finite element triangle, whereas pressures are computed through linear interpolation functions at the three vertex nodes of the *fe* triangle.

The finite volume approximation is formed from partitioning each finite element (parent) triangle into four finite volume (child) sub-cells. These *fv* subcells are assigned with three vertex nodes and stress components are computed at these vertices through linear interpolation functions.

The meshing used for the computation is that illustrated in chapter 7, Fig. 7.3, and consists of 1550 numbers of elements, 3485 number of nodes, 968 vertex nodes and 768 boundary nodes. Then, solution consistency with mesh convergence has been assured through two other mesh choices; a coarser mesh, consisting of 650 number of elements, 1563 number of nodes and 433 number of vertex nodes; and a finer mesh, consisting of 5208 number of elements, 10536 number of nodes and 2925 number of vertex nodes. Solution precision has been resolved on these meshes, without the inclusion of the extended free-surface wetting line, to avoid any additional instabilities stimulated by singularity inclusion. Differences in mesh solutions are found to be less than 0.1% in primary velocity-pressure components.

Boundary conditions: Dirichlet and Neumann type boundary conditions are adopted. At the flow inlet and outlet, plug flow is assumed. This renders simplicity with vanishing inflow stress components (in plug flow), as the necessary driving boundary conditions on the hyperbolic-type stress equations.

The free-surface location method (see chapter 4) uses a time-dependent prediction technique where the evolution of the deformed domain is estimated from a previous solution through a height function. This strategy was previously applied by Phan-Thien [1977] in extrudate swell. Initial conditions on these free–surface boundaries are taken as quiescent. Then initially, to enhance efficiency in convergence to a steady-state, domain solutions are first computed with fixed-location traction-free boundaries, prior to release and completion of the solution search. Re-meshing is performed after each time-step (see chapter 7 for inclusion of and discrete treatment of the dynamic wetting line).

8.3 EPTT model flow solutions

First, solutions are extracted for which performance of the EPTT model is examined on RRC flow with wetting line inclusion, to investigate the effects of elasticity (We) and influence of the polymeric solution by varying the material parameter (β). At ε=0.25, the main interest lies in elasticity effects (with rising We) and changes in flow structures at different levels of strain-softening and strain-hardening. Steady state solutions are determined taken to a typical time step of $\Delta t=10^{-4}$ with relative increment tolerance of 10^{-6}, whilst employing three mass iterations per embedded Jacobi iterative step. The influence of model parameters are described on vortex structures, pressure and lift profiles, and the component polymeric contribution to the stress tensor.

Table 8.1: Critical states for different constitutive models:

Model	Solvent Fraction β	Extensional viscosity ε	Max. We	Max. P*	Max. τ_{yy}	Max. N_1	Max. τ_{xy}
EPTT	0.9	0.5	0.5	1.7	1.5	1.15	0.5
	0.1	0.5	0.4	0.6	13.7	13.5	3.97
		0.25	0.4	0.7	24.9	24.5	4.43
	0.01	0.5	0.3	0.5	16.5	21.3	9.81
LPTT	0.9	0.5	2.0	1.68	4.53	2.90	1.55
		0.25	1.0		8.74	5.61	2.82
	0.1	0.5	1.0	0.5	37.3	31.7	6.23
		0.25	0.3	1.30	52.6	85.4	13.6
		0.15	0.25	1.39	66.3	111.5	14.2
		0.02	0.12	1.68	111.1	260.0	10.5
	0.01	0.5	0.2	0.79			

The viscoelastic flows studied here present steep stress boundary layers that are attached to the free-surface. As We rises, the stress boundary layer solution-thickness thins. As a consequence, a critical We is encountered, above which the stress gradient cannot be resolved and the computation fails to converge. Table 8.1 reports the various critical terminal We-states reached for the two constitutive models studied.

8.3.1 Elasticity (We) and solvent fraction (β) change

The influence of elasticity on the meniscus and nip-vortex structures is illustrated in Fig. 8.1 and 8.2, respectively, with model parameters of: fixed ε=0.5, and varying $0.01 \leq \beta \leq 0.9$. The meniscus-vortex structure does not show any significant changes due to increase in elasticity for the three solvent fractions analysed. In contrast, one notes some adjustment in the evolution of the shape of the meniscus free-surface at solvent fraction β =0.01; this becomes more deformed due to the increased elastic forces imposed.

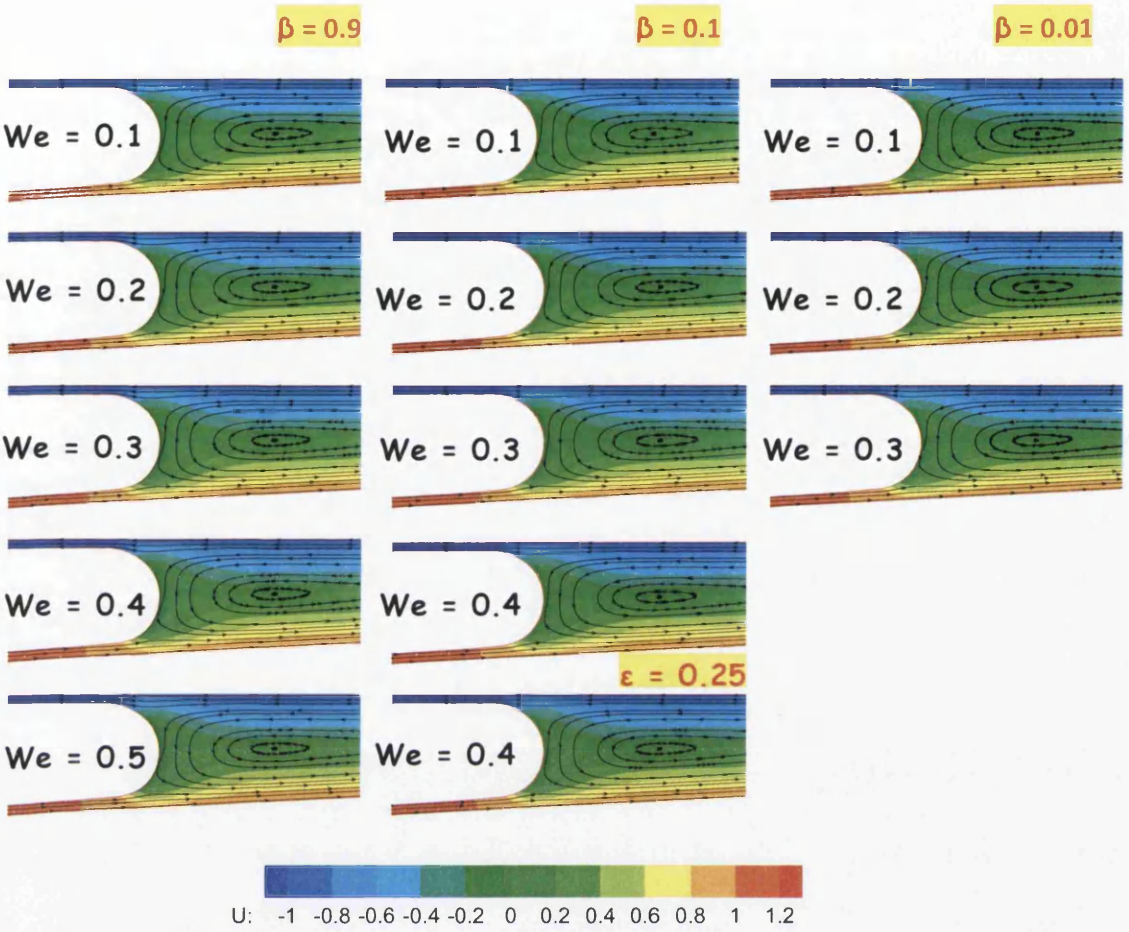

Figure 8.1: Meniscus vortex development, EPTT flow ($\varepsilon = 0.5$)

The influence of elasticity on vortex structure is more apparent at the nip-region and most prominent in Fig. 8.2b and 8.2c. At We=0.1 and β=0.9, the flow is close to Newtonian with recirculation observed in the shear-dominated nip-flow region. With elasticity increase, the recirculation is stretched more and more, and is observed to be compressed laterally and drawn inwards longitudinally, in the direction of the meniscus. At We=0.3 and β=0.01, flow behaviour is far from that of Newtonian response; with the highest shear-thinning rate, vortex distortion, compression and extension are all apparent features.

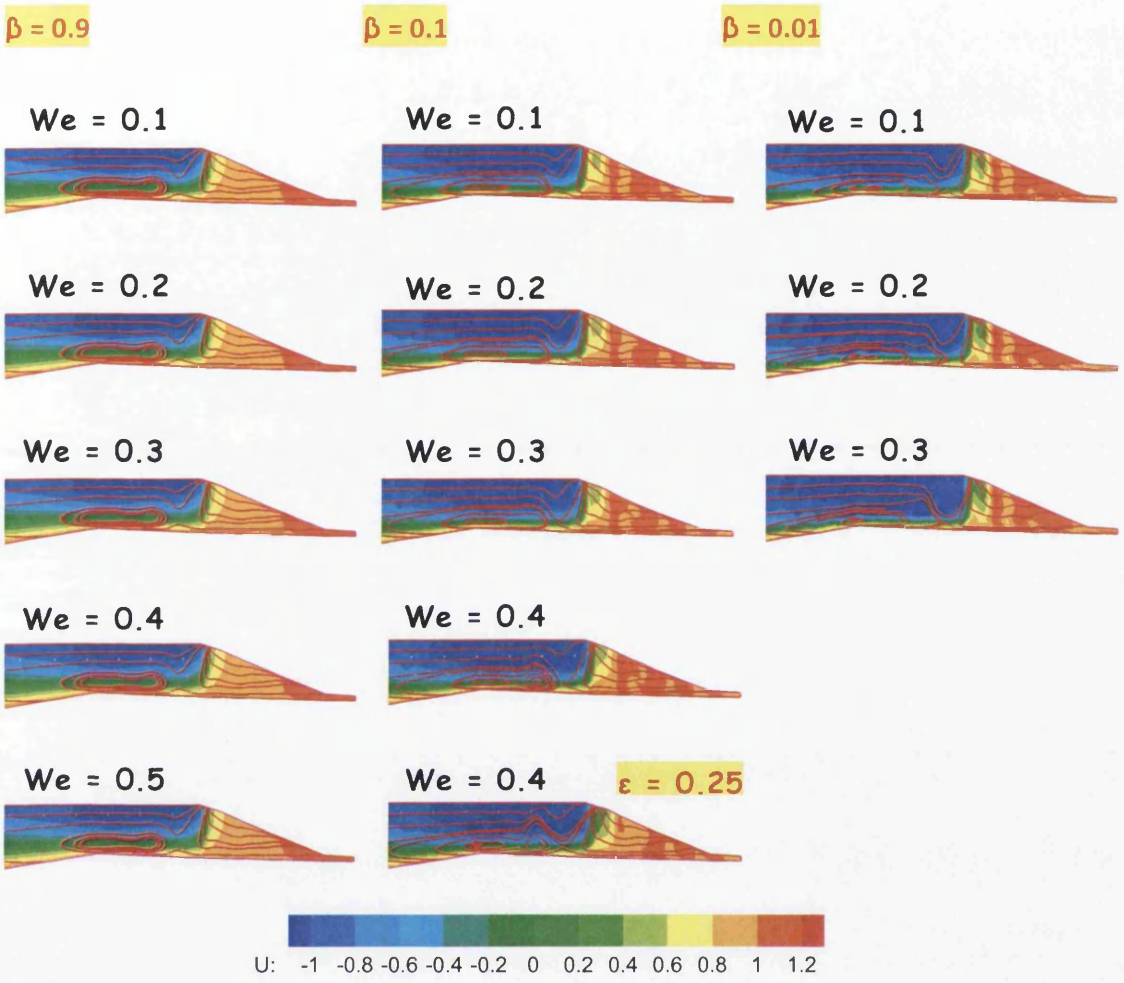

Figure 8.2: Nip vortex development, EPTT flow ($\varepsilon = 0.5$)

Figure 8.3 represents corresponding pressure profiles gathered for EPTT solutions. At β=0.9, differences in peak-pressures are now relatively small and observed to decrease with increasing elasticity (We). Again, the most significant pressure changes are revealed at β=0.01. As elasticity increases from We=0.1 to 0.3, pressure levels decrease from maxima of 1 to 0.5 units (50% reduction; 39% reduction in corresponding lift). Shear-thinning fluids are known to support reduced pressures, and here, shear-thinning dominates these EPTT solutions. Lift levels follow similar trends to those in pressure, revealing the significant level of forces exerted on the foil-substrate as a result of exposure to these viscoelastic nip-flow conditions.

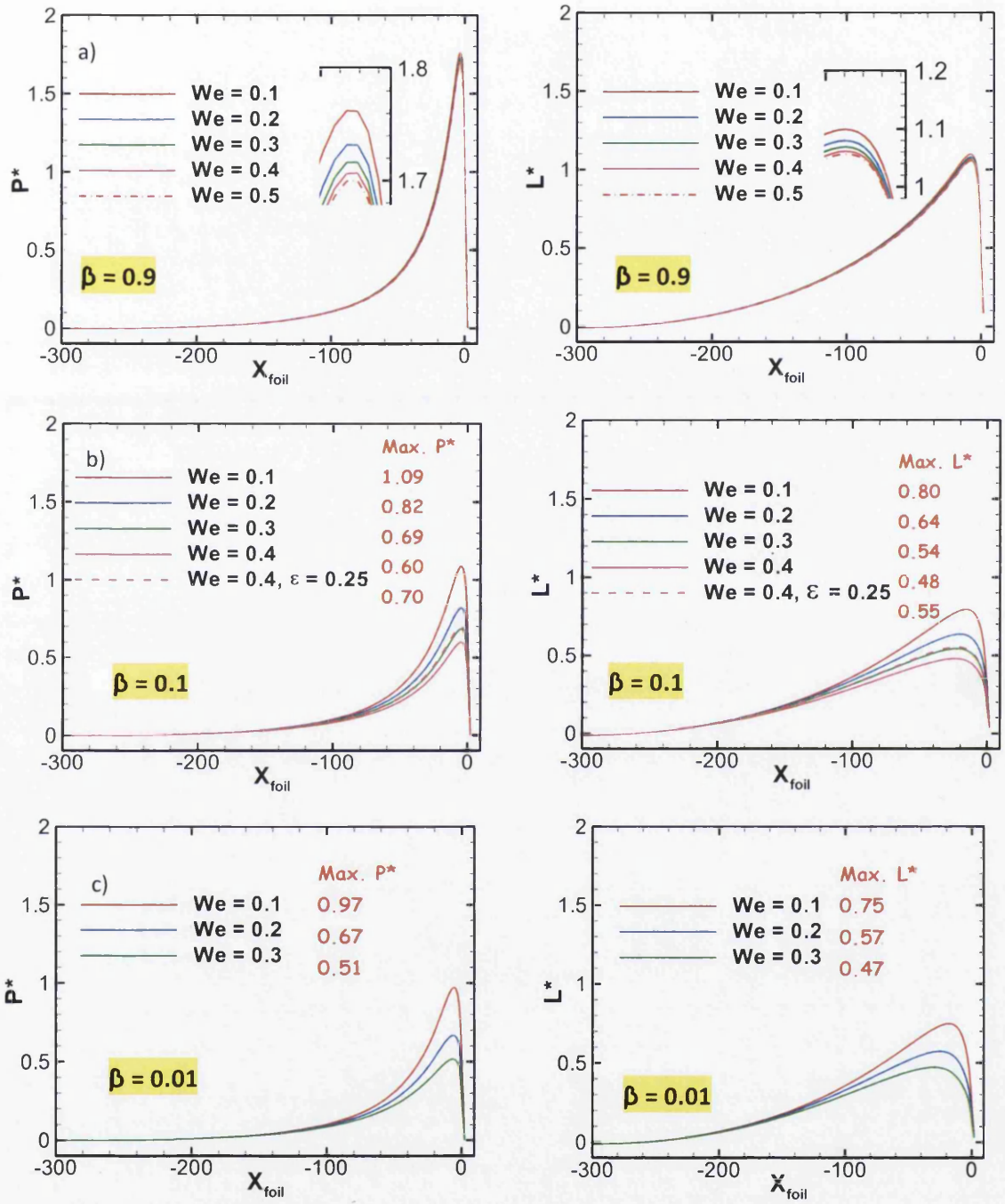

Figure 8.3: Pressure and lift profiles, EPTT flow (ε = 0.5)

From Fig. 8.4, τ_{xx}, and τ_{yy} field development and profiles are presented. These fields show the region of large deformation rate on the roll surface dominated by shear. Here, τ_{xx} is largest on the roll side and decreasing with increase in elasticity (We) for the three solvent fractions analysed. For β=0.9, with the lowest level of shear-thinning, the largest τ_{xx} value

attained was 2.95 at We=0.1, which decreased to 1.13 at We=0.5. At β=0.1, there is one order of magnitude increase in τ_{xx} values to 32.9 at We=0.1, which decreased with increasing elasticity (We) up to 13.2 at We=0.4. Overall, the decreasing effects on the absolute maximum are due to strain-softening influence. For all levels of solvent fraction, τ_{xx} values seem to decrease at almost the same rate (from We=0.1 to 0.3, the values halve). From Fig. 8.4b, the τ_{xx} profiles show a rapid increase on the roll-side at the nip region and a decrease on the foil-side for all solvent fractions considered. There is a crossover point, between the increasing roll τ_{xx}-level and the decreasing foil τ_{xx}-level; this location marks the extent of the outer perimeter of the nip-vortex structure towards the meniscus. Moreover, this crossover point adjusts with decreasing solvent fraction: at β=0.9, the crossover point is observed to lie at x=-3; whereas at β=0.1, this location increases to x=-5. This feature agrees with direct observation from the vortex structure interaction, where the nip-vortex recirculation is seen to expand on the roll surface side into the meniscus-vortex; to almost varnish at β=0.01, We=0.3. τ_{yy} field content reveals significant effects over the contact-point zone, where corresponding largest levels arise. At the contact-point, the fluid comes into contact with the foil and is accelerated rapidly to the speed of the foil; here, a local maxima in τ_{yy} is observed (cross-stream stretching; N_2 effect). The deformation in this flow zone is dominated by extension, which results in a strain-softening response under EPTT approximation. Hence, and as We-levels increase further, such maxima decline still further – a consistent result when We-rise is interpreted through increase in deformation rate. As illustrated in τ_{xx} levels, there is also a one order of magnitude increase when solvent fraction is decreased to β=0.1. There are no τ_{yy} (N_2) effects on the roll side to be observed, as profile levels remain around the zero-level.

N_1 and τ_{xy} fields and profiles are illustrated in Fig. 8.5. This illustrates that evolution trends in the first normal stress differences directly follow from those in their individual constituent normal stress components, with domination by τ_{xx} in those regions where τ_{xx} is most significant, and vice-versa for τ_{yy}. Shear stress reveals a maximum on the foil surface. Here, the fluid undergoes exposure to maximum shearing deformation, due to the change in direction of flow to take up the speed of the foil.

For completeness, nip deformation rates, shear and extension fields and profiles are then shown in Fig. 8.6. Maximum shear-rates are observed on the roll surface, and maximum strain-rates around the contact-point on the foil. When nip-recirculation is generated, the shear-rate is greater than zero and strain-rate in less than zero; a feature observed on the roll side. In contrast on the foil side, the counterpart region, with shear-rate less than zero and strain-rate greater than zero, reveals a stagnant region with no recirculation (see shear-rate fields). The transition occurs when shear and strain-rates reach zero levels, and when this arises, the pressure becomes negative. These significant effects become more amplified with a decrease in solvent fraction up to β=0.01.

Figure 8.4a: Nip τ_{xx} and τ_{yy} development, EPTT flow ($\varepsilon = 0.5$)

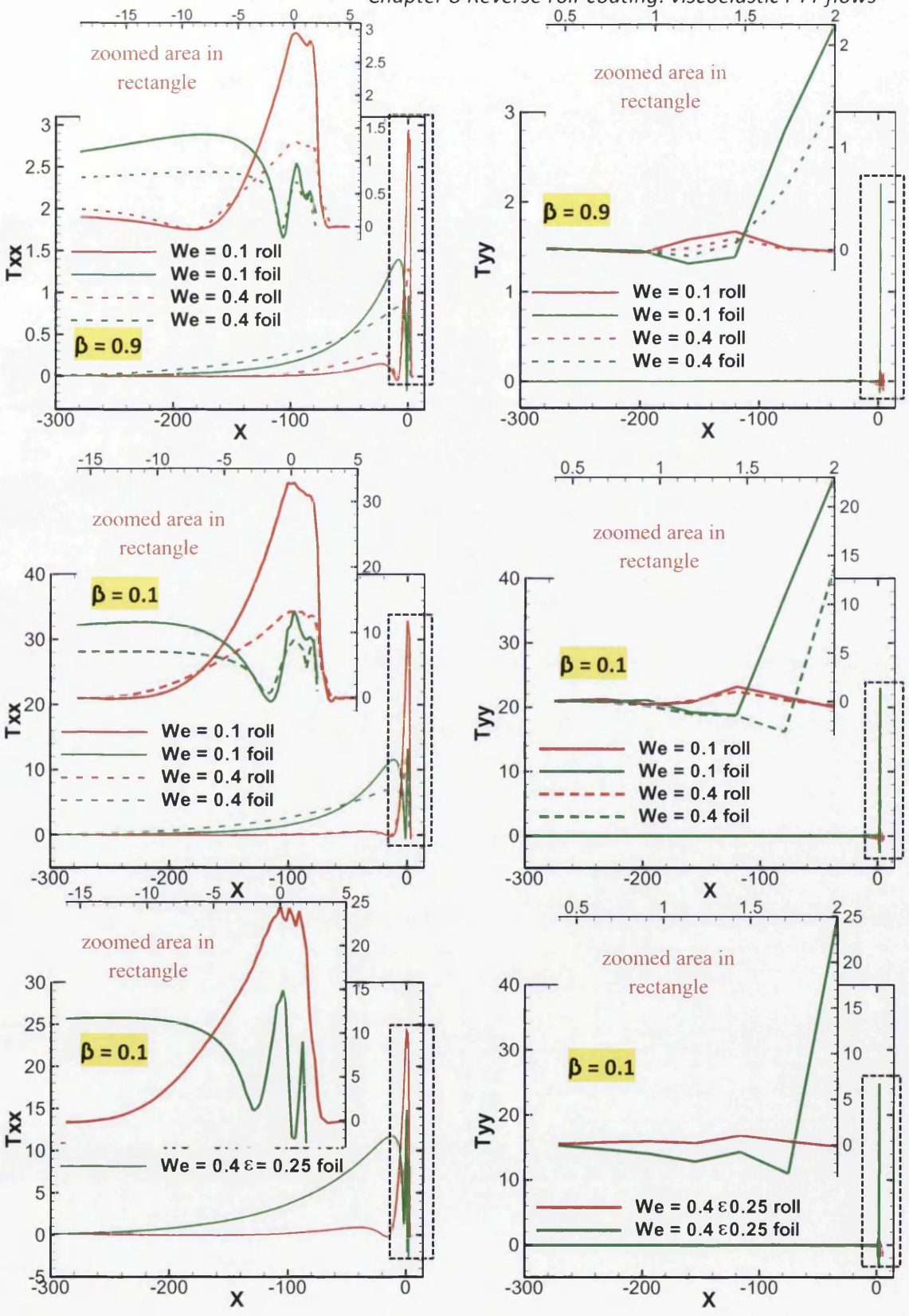

Figure 8.4b: τ_{xx} and τ_{yy} profile, EPTT flow ($\varepsilon = 0.5$)

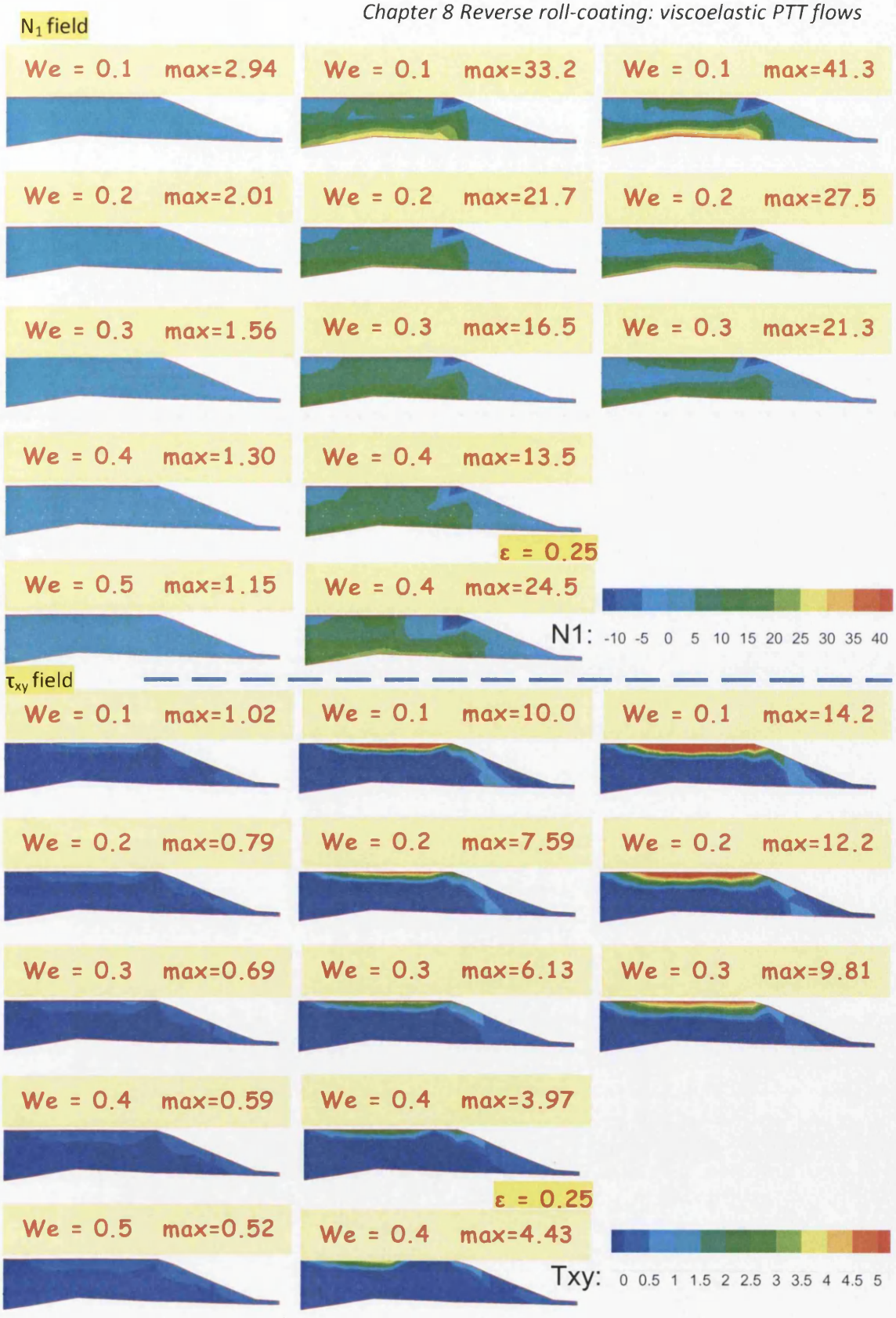

Figure 8.5a: Nip N_1 and τ_{xy} development, EPTT flow ($\varepsilon = 0.5$)

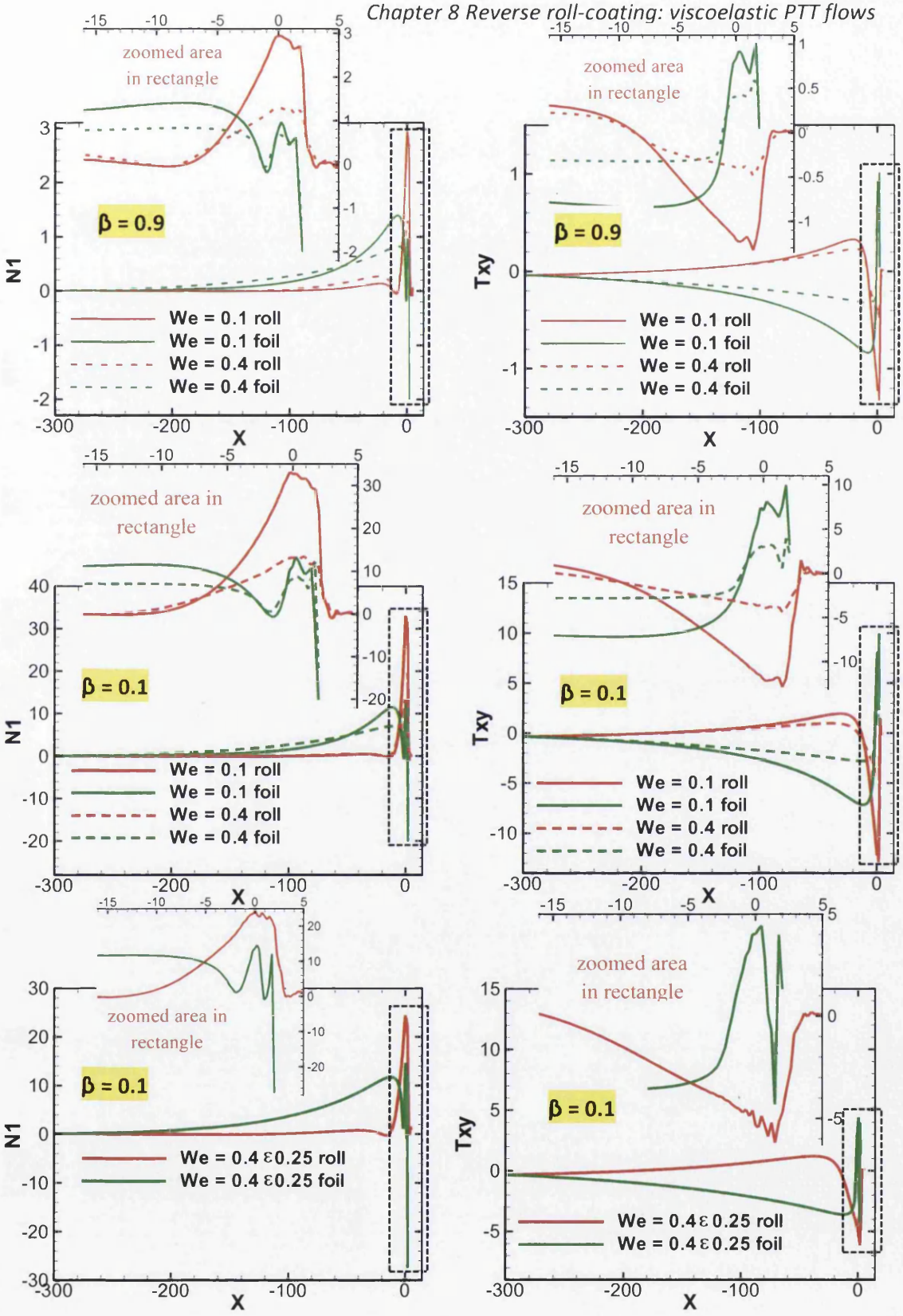

Figure 8.5b: N_1 and τ_{xy} profile, EPTT flow ($\varepsilon = 0.5$)

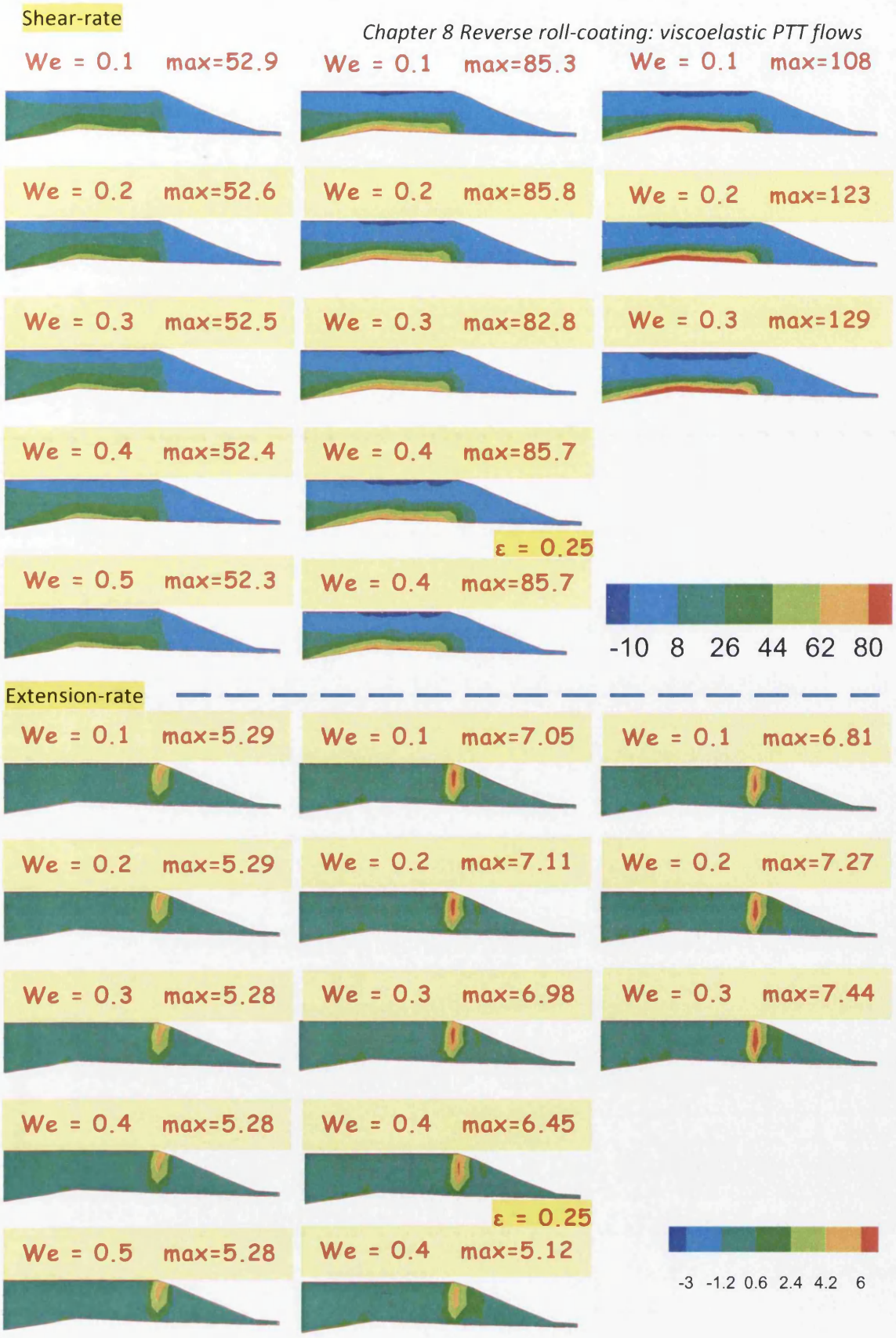

Figure 8.6a: Nip deformation (top) and extension (bottom) rate, EPTT flow ($\varepsilon = 0.5$)

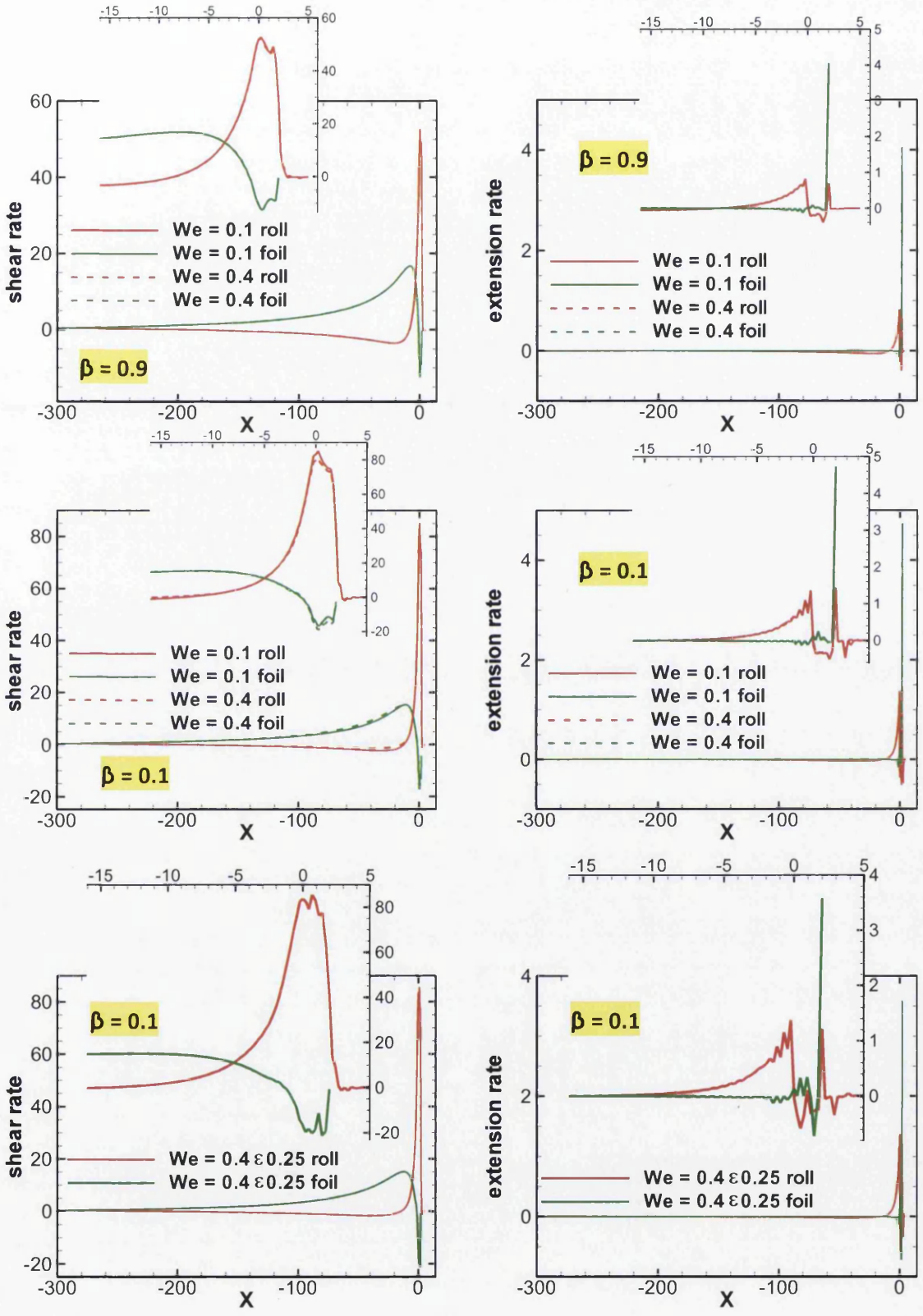

Figure 8.6b: Shear and extension rate profiles, EPTT flow (ε = 0.5)

8.3.2 Effects of strain hardening/softening

In this section, interest focuses on the change in extensional viscosity properties. From Fig. 8.4, at β=0.1 and We=0.4, as extensional viscosity increases (from ε=0.5 to 0.25), with features of both strain-hardening and strain-softening response, a change in the recirculation patterns arises with largest fluid stretching occurring across the domain towards the foil-side; a third vortex then appears and grows in recirculation strength. In Fig. 8.5, peak-pressure levels are seen to increase from 0.6 (at ε=0.5) to 0.7 (at ε=0.25), when comparing at the same level of elasticity (We=0.4). The hardening behaviour in the EPTT solution at ε=0.25, increases the τ_{xx} level on the roll surface from 13.2 to 24.6 units, as shown in Fig. 8.6. Correspondingly, the τ_{yy} levels at the contact-point location are also seen to increase at the same rate. At this location, the flow is dominated by extensional response, so that the impact of strain-hardening is clearly observed, as τ_{yy} increases from 13.7 to 24.9 - almost double at the same level of elasticity. This sort of trend is also reflected in N_1 – a clear demonstration of the impact from strain-hardening.

From the shear stress profiles, peak τ_{xy}-values are only slightly larger in the hardening over the little-to-no strain-hardening instances. So, effects due to shearing are minimal. Yet, as anticipated, there is a rapid drop and increase in peak τ_{xy}-levels at the location where the third vortex emerges and is stretched across the domain towards the foil. Shear-rate values remain about the same, relatively unperturbed, for both levels of extensional viscosity; whereas strain-rates differ, taking values of 5.12 units at ε=0.25 and 6.45 units at ε=0.5.

8.4 LPTT model flow solutions

In contrast to the foregoing, consideration is diverted to numerical solutions derived under the LPTT approximation. Here, solution comparison over parameter variation follows as with EPTT solutions above. The differences in the material functions are represented in chapter 3, Fig. 3.5. First vortex activity is observed and discussed, followed by analysis of stress fields and profiles.

8.4.1 Elasticity (We) and solvent fraction (β) change

Again, observing the meniscus-vortex in Fig. 8.7, there are no apparent solution differences at lower solvent fractions; but at β=0.01, increasing We begins to stimulate the central core vortex and at the nip, the recirculation gradually unfolds and expands inwards, towards the meniscus. The pressure and lift profiles are illustrated in Fig. 8.8. Peak-pressure levels are observed to decline with increasing elasticity and lower solvent fraction, reflecting the dominance of shear-thinning characteristics. An interesting phenomenon is identifed in the normal stresses (see Fig. 8.9). At higher solvent fractions (β=0.9 and 0.1), increasing elasticity (We) decreases the level of τ_{xx}, whereas at low solvent fraction (β=0.01), the fluid becomes more resistant to shear and τ_{xx} levels rise. In all solvent fraction scenarios, as τ_{xx}

decreases, τ_{yy} increases. The absolute maxima occur on the roll surface for τ_{xx} and at the contact-point location on the foil for τ_{yy}. N_1 (Fig. 8.10) follows identical trends as in τ_{xx}, which would indicate the strictly localised nature of N_2-influence (in τ_{yy}).

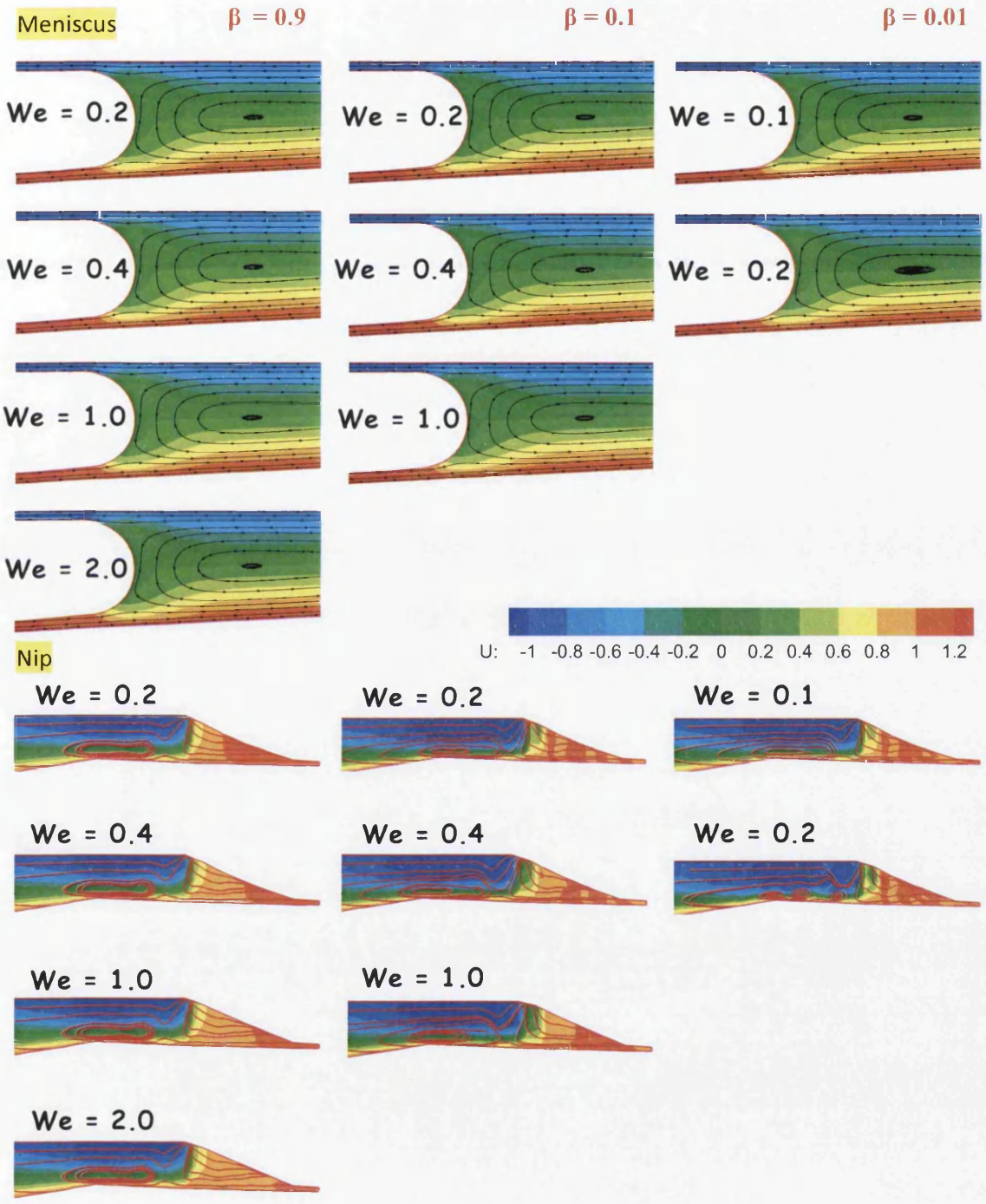

Figure 8.7 Meniscus and nip vortex development, LPTT flow ($\varepsilon = 0.5$)

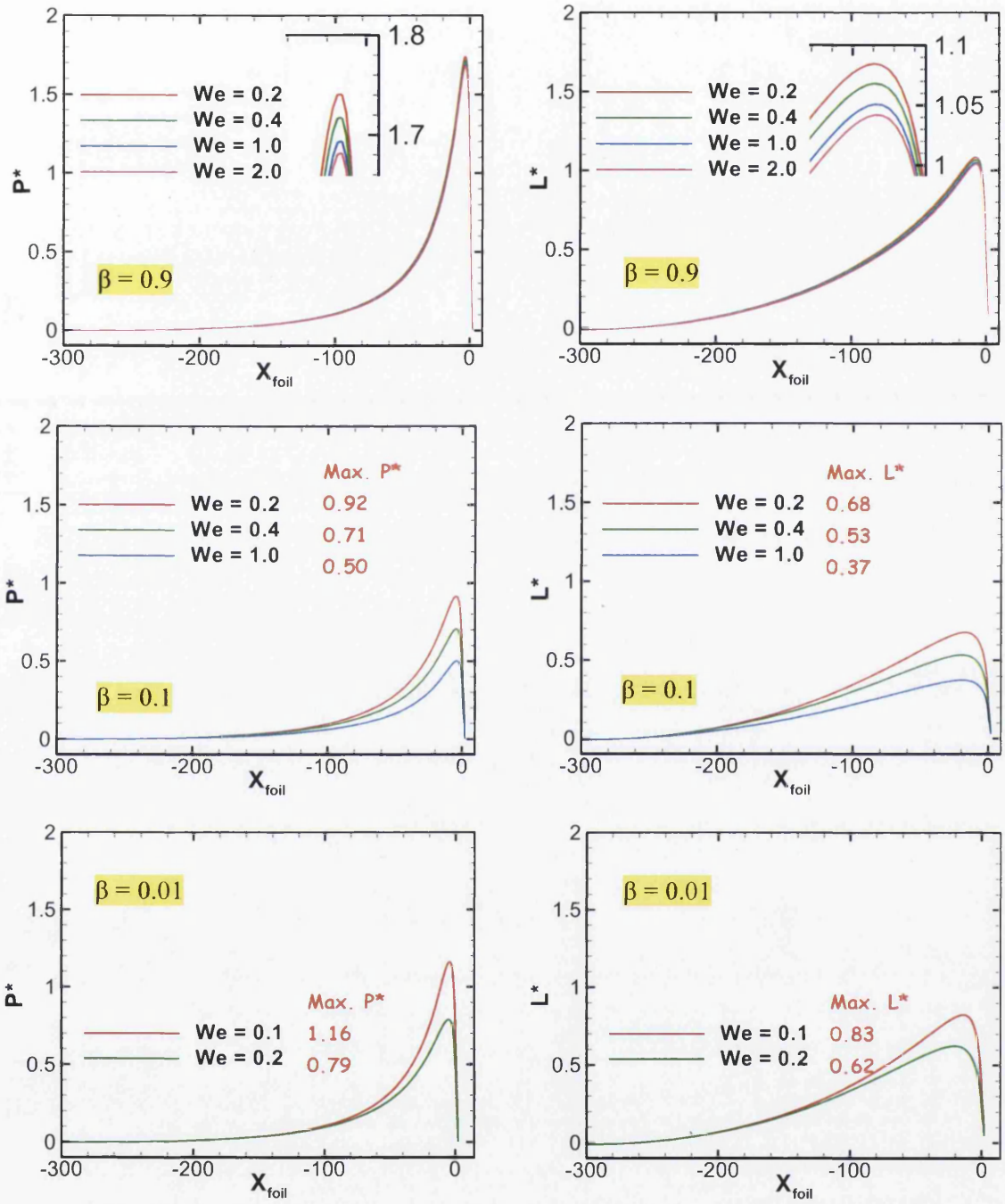

Figure 8.8: Pressure and lift profiles, LPTT flow (ε = 0.5)

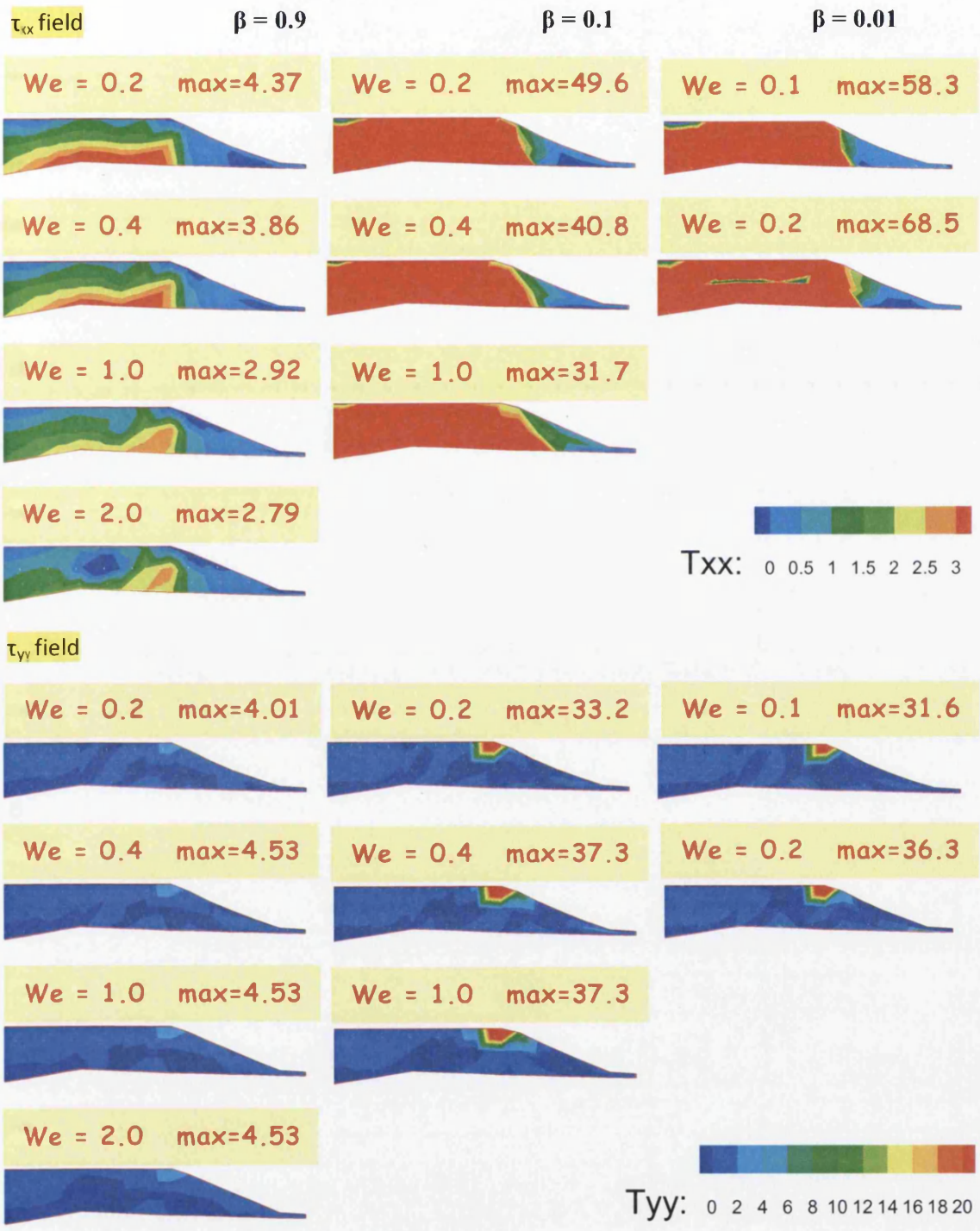

Figure 8.9a: Nip τ_{xx} and τ_{yy} development, LPTT flow ($\varepsilon = 0.5$)

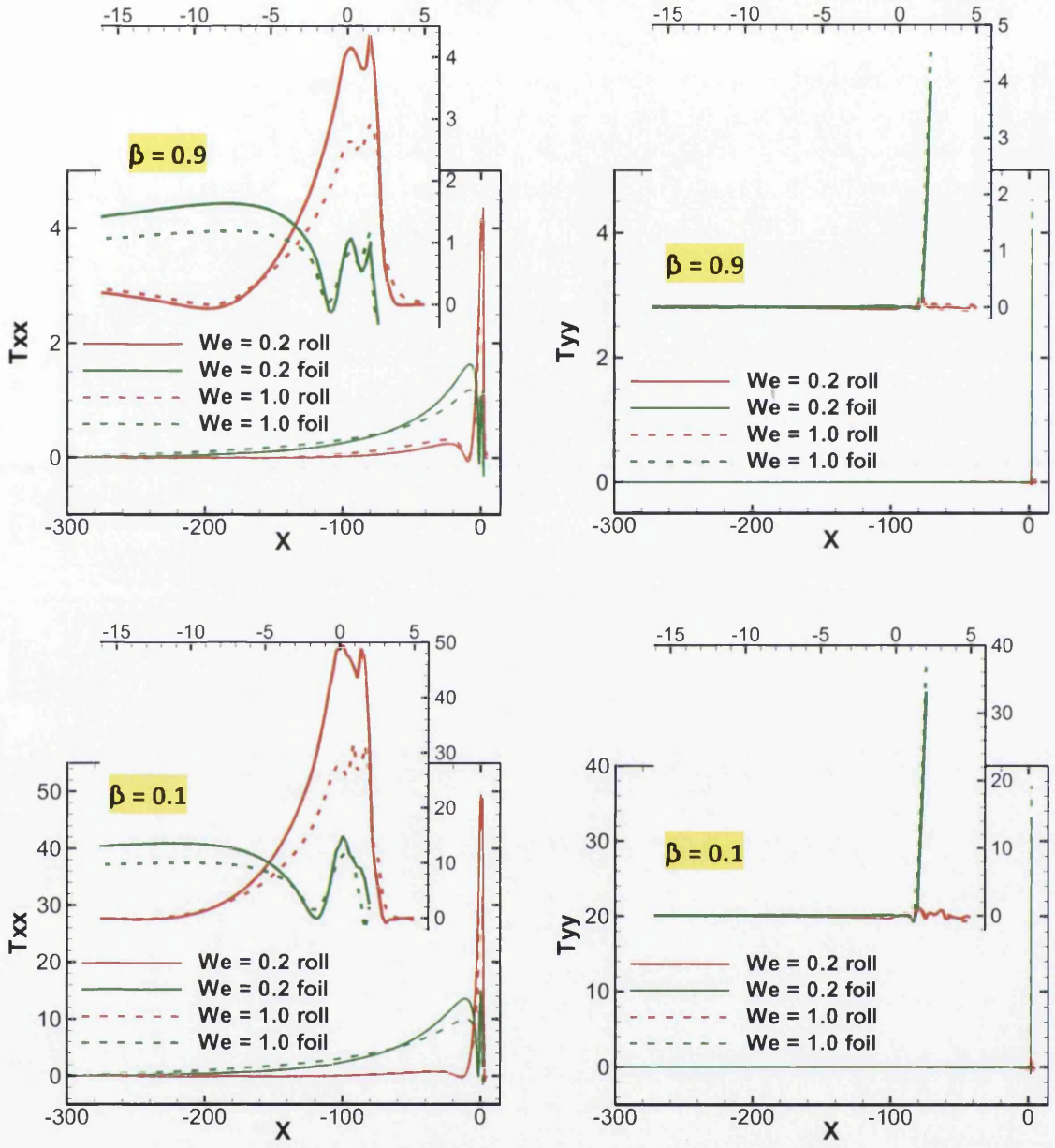

Figure 8.9b: Nip τ_{xx} and τ_{yy} profile, LPTT flow ($\varepsilon = 0.5$)

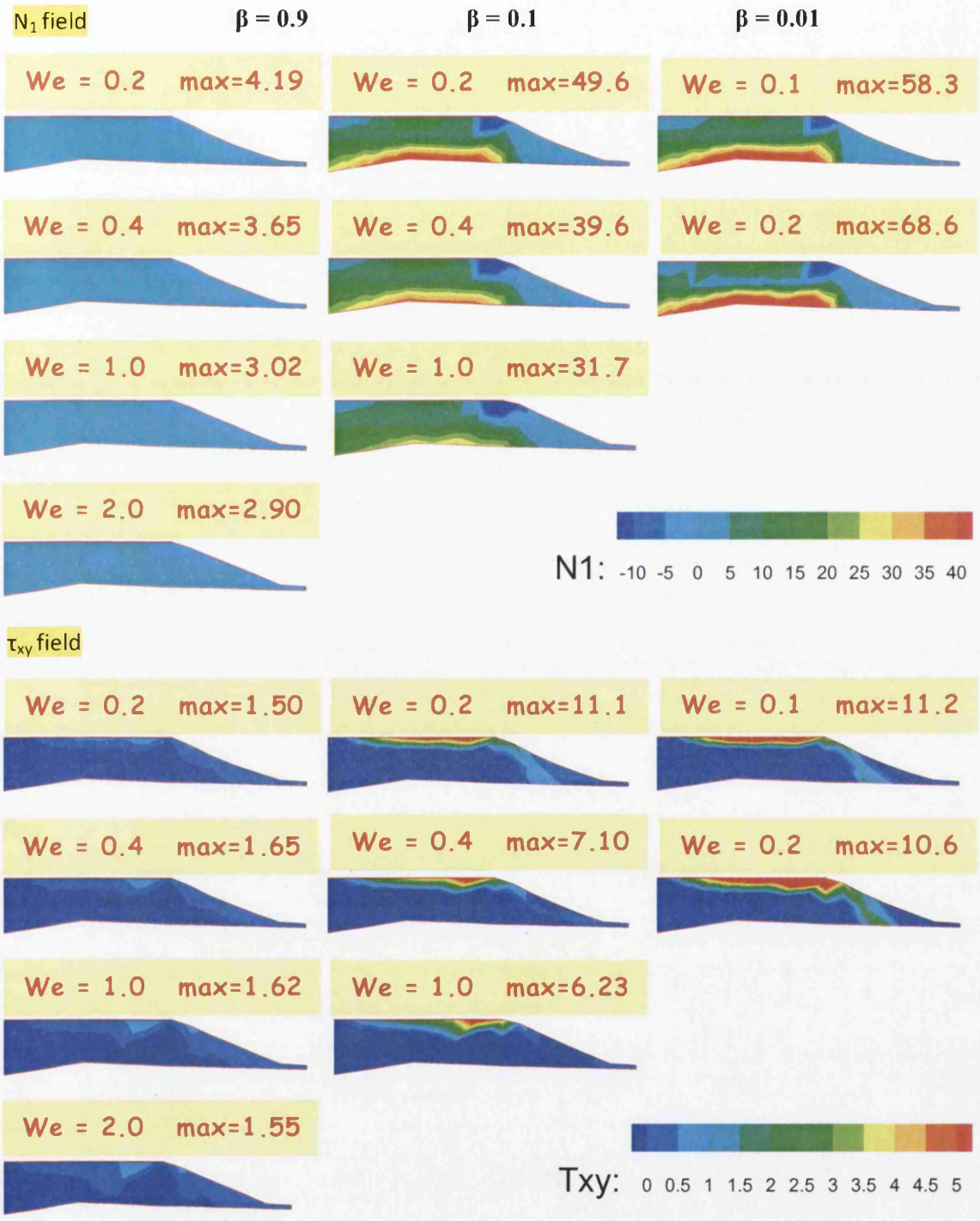

Figure 8.10a: Nip N_1 and τ_{xy} development, LPTT flow ($\varepsilon = 0.5$)

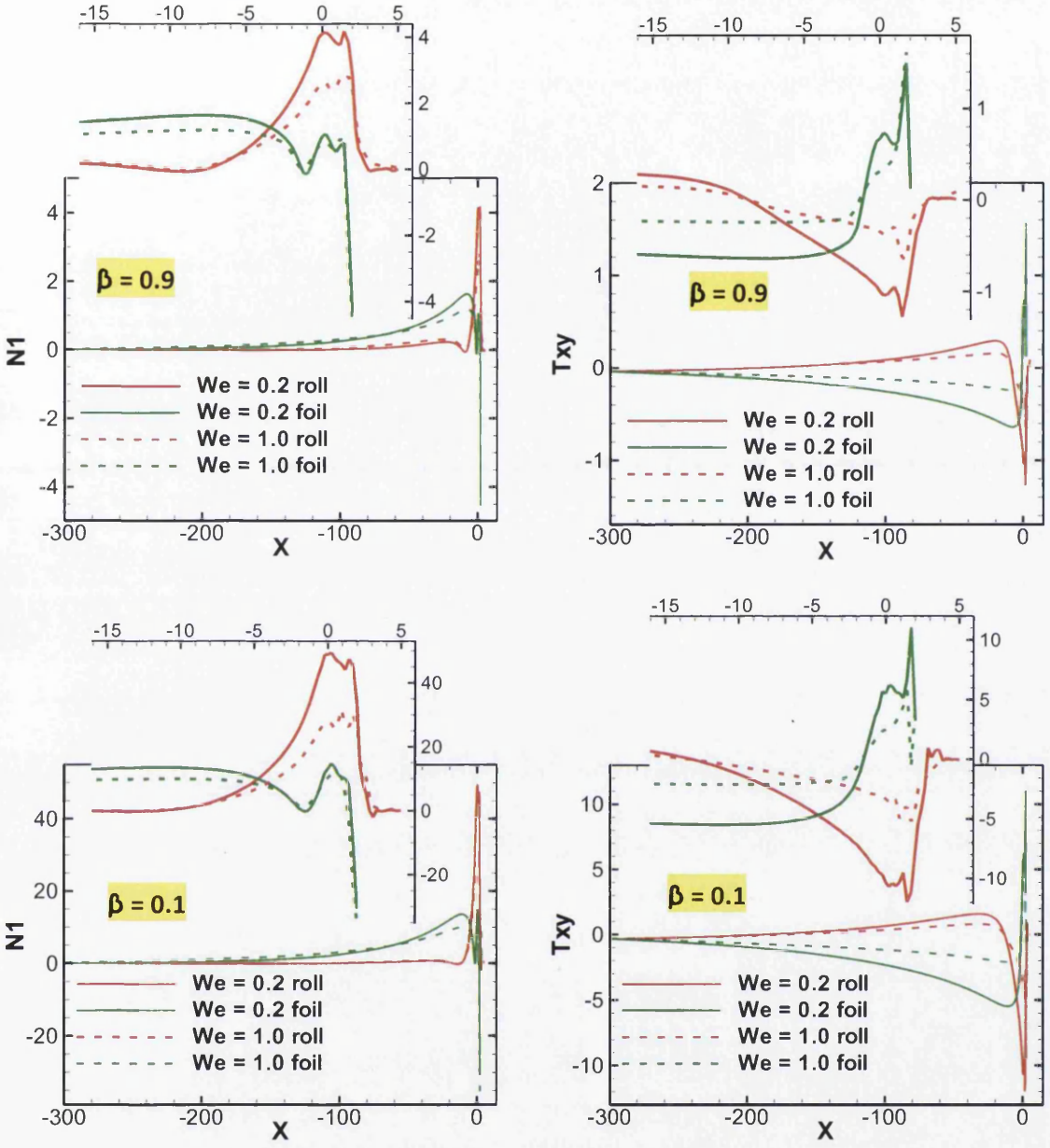

Figure 8.10b: Nip N_1 and τ_{xy} profile for LPTT flow ($\varepsilon = 0.5$)

Shear stress is observed to generally decline with We-increase under all solvent fraction settings. Shear and extension rate fields are shown in Fig. 8.11, with maximum values extracted in Table 8.2. This data is placed into perspective against equivalent industrial expected rates. For each solvent fraction, one may note from Fig. 8.11 that there is little difference in deformation rates with rise in We. At high solvent fraction, shear-rate remains (Fig. 8.11) around the same levels, but below β=0.01, there is a significant increase in shear-rate as We increases. At this β=0.01 solvent fraction level, the viscosity level would appear to be dominated by its second plateau; so change in τ_{xy} is mainly due to shear-rate decline; yet,

τ_{xx} in seen to increase (hence a memory effect). Note that extensional viscosity distribution remains almost constant with no apparent increase, according to strictly localised changes in extension rates that are one order in magnitude smaller than those in shear-rate.

Table 8.2: Comparing shear and extensional rates of different constitutive models to industrial rates.

Model	**Solvent Fraction β**	**Extensional viscosity ε**	**Max. We**	**Max.** $\dot{\gamma}$	**Max.** $\dot{\varepsilon}$
EPTT	0.9	0.5	0.5	52.3	5.28
	0.1	0.5	0.4	85.7	6.45
		0.25	0.4	85.7	5.12
	0.01	0.5	0.3	129	7.44
LPTT	0.9	0.5	2.0	51.2	5.08
	0.1	0.5	1.0	66.7	4.22
	0.01	0.5	0.2	104	7.12
Ind. Data	0.1-0.01	0.15-0.5	Very low	1-50	0.1-10

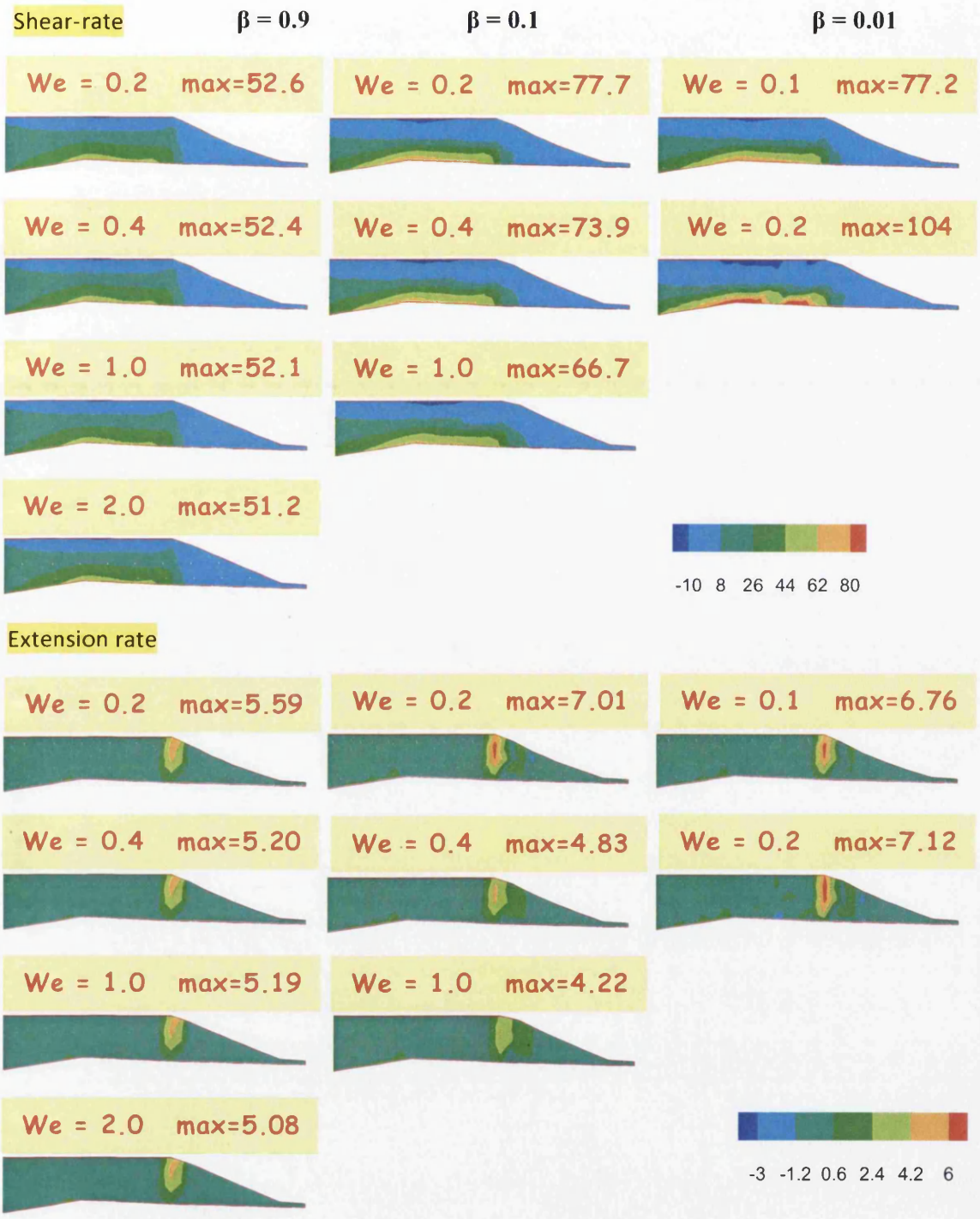

Figure 8.11a: Shear and extension rate, LPTT flow (ε = 0.5)

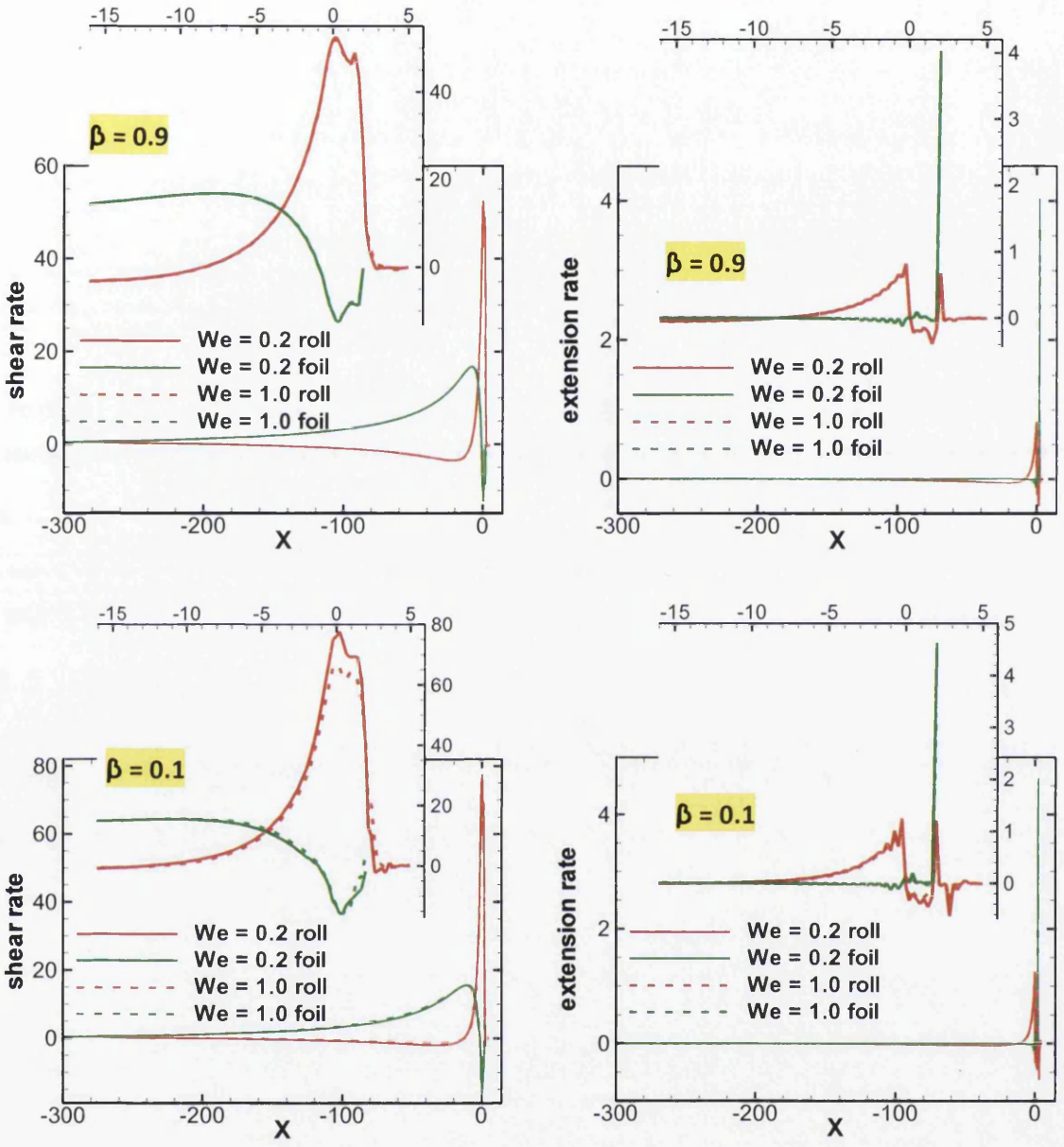

Figure 8.11b: Shear and extension rate profiles, LPTT flow (ε = 0.5)

8.4.2 Effects of increasing levels of extensional hardening

Taking the LPTT model at β=0.1, different levels of extensional viscosity were analysed. This focuses on the effects of changing the second limiting plateau of the extensional viscosity. From Fig. 8.12, increasing extensional hardening from ε=0.25 to 0.02, the vortex structure reduces in recirculation. Localised pressure and distributional lift peak-values increase due to enhanced hardening effects (see Fig. 8.13). The normal stresses increase reflecting a rapid increase in the first normal stress difference (N_1). Then, shear-rates are seen to decrease, as resistance to shear occurs due to increased strain-hardening (Fig. 8.14).

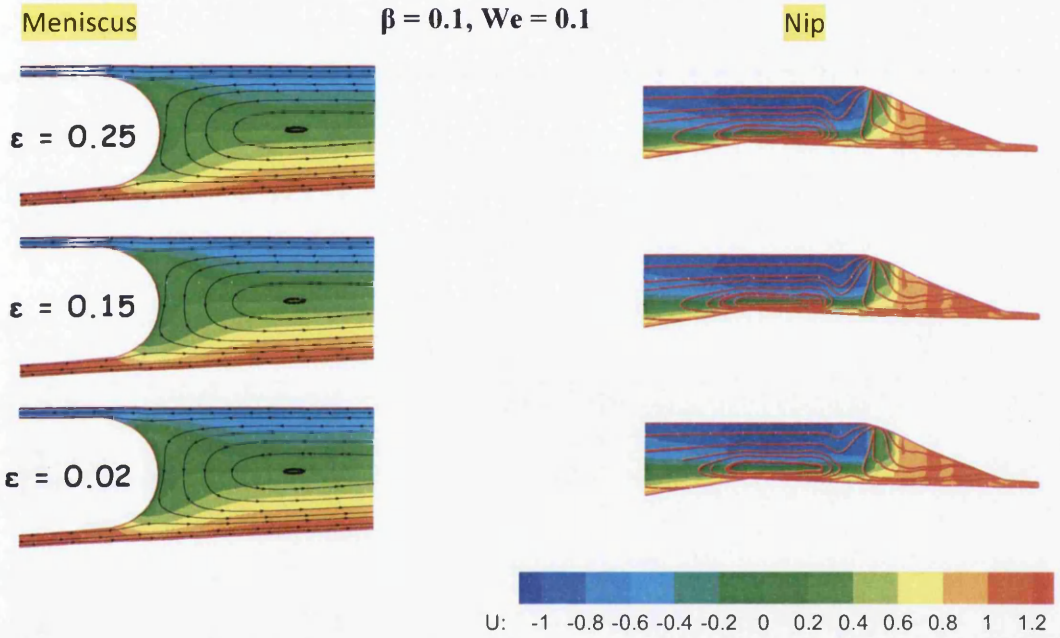

Figure 8.12: Meniscus and nip vortex development, LPTT flow ($0.02 \geq \varepsilon \leq 0.25$)

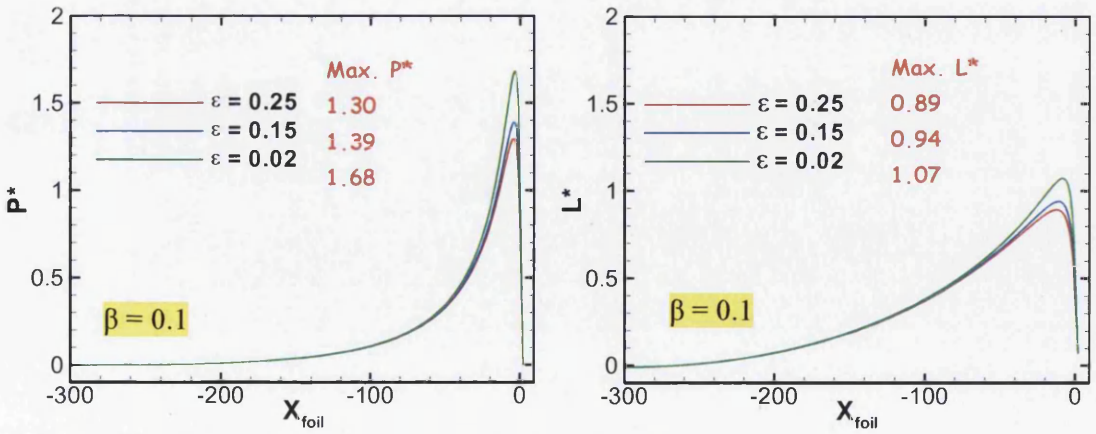

Figure 8.13: Pressure and lift profile, LPTT flow ($0.02 \geq \varepsilon \leq 0.25$)

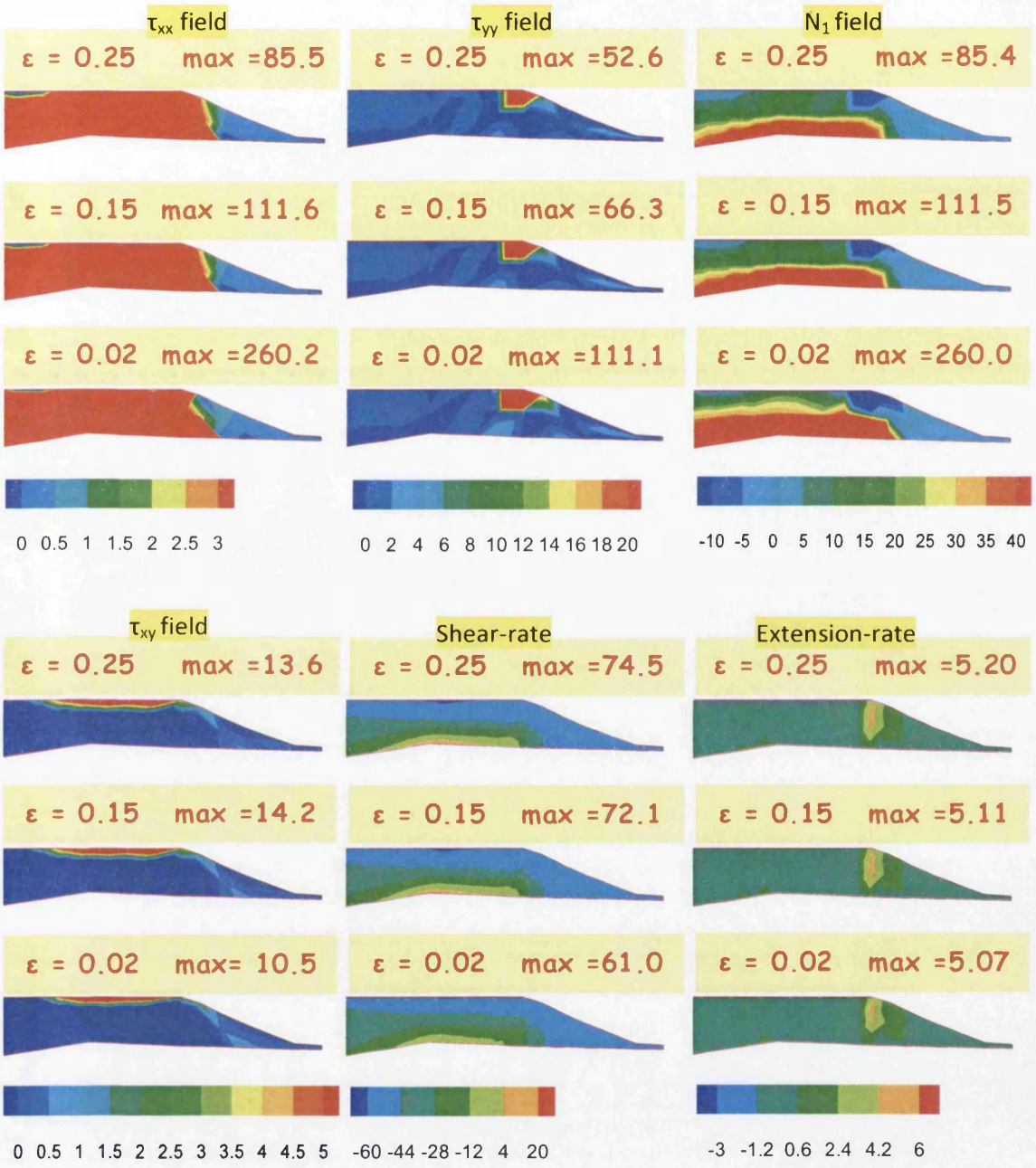

Figure 8.14a: τ_{xx}, τ_{yy}, N_1, τ_{xy}, Shear and extension rate, LPTT flow ($\beta = 0.1$, $We = 0.1$)

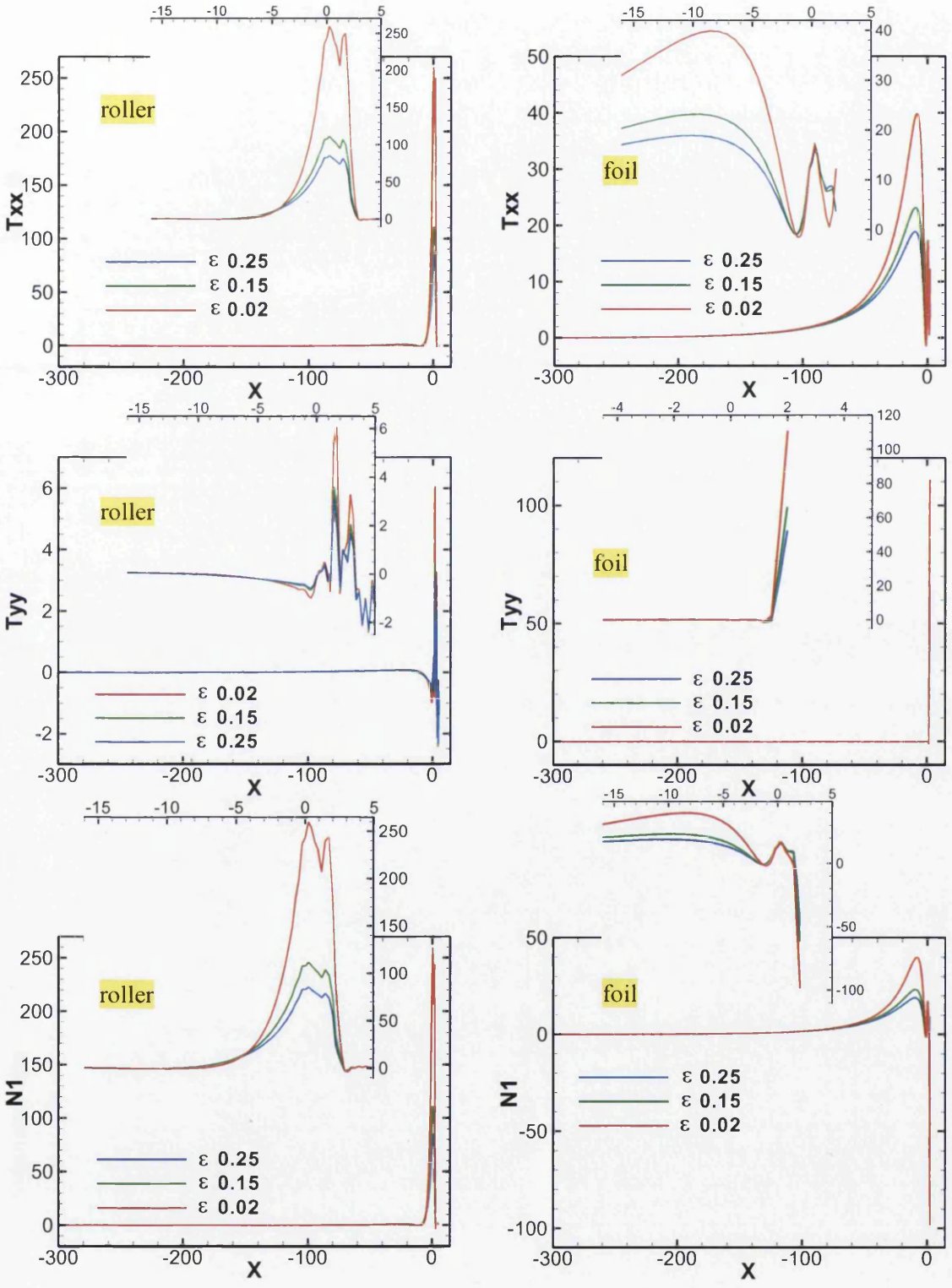

Figure 8.14b: τ_{xx}, τ_{yy} and N_1, LPTT flow ($\beta = 0.1$, We = 0.1)

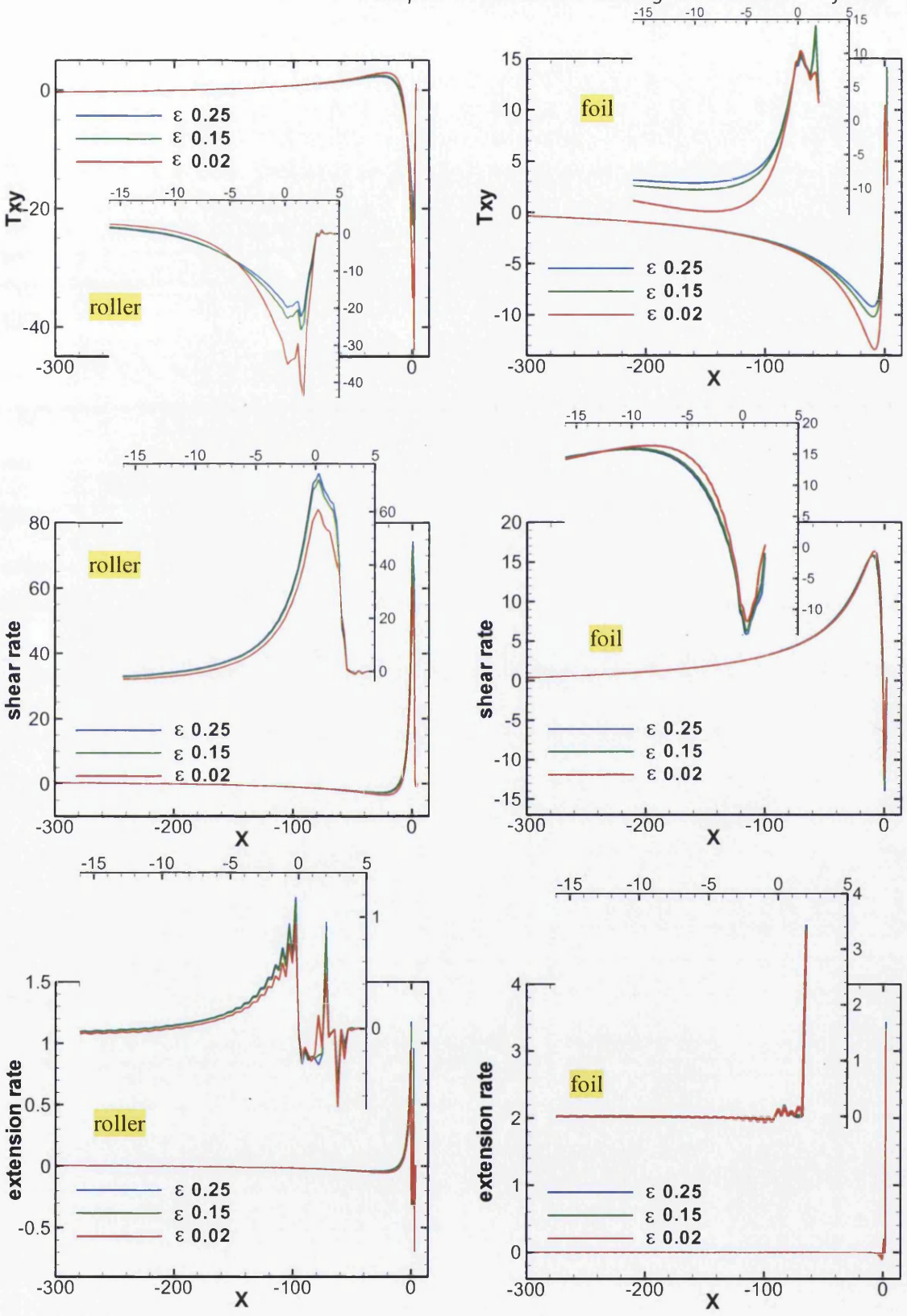

Figure 8.14c: τ_{xy}, shear and extension rate, LPTT flow ($\beta = 0.1$, We = 0.1)

Comparing results directly for the two material constitutive models, Figures 8.15-8.17 show the significant differences gathered between EPTT and LPTT solutions at parameter setting of {β=0.1, ε=0.25}. Slightly larger critical stress states were attained for EPTT(We=0.4) than with LPTT(We=0.3) (note, comparison is conducted at We=0.3). Peak-pressure levels for EPTT are lower than those for LPTT, due to the higher rate of shear-thinning hit for EPTT solutions. Stress levels are much higher with LPTT than EPTT; on account of EPTT strain-softening characteristics, whereas LPTT is strain-hardening. Due to EPTT faster shear-thinning rate, EPTT supports higher shear-rates than does LPTT; noting also the impact of EPTT strain-softening rate, absent under LPTT.

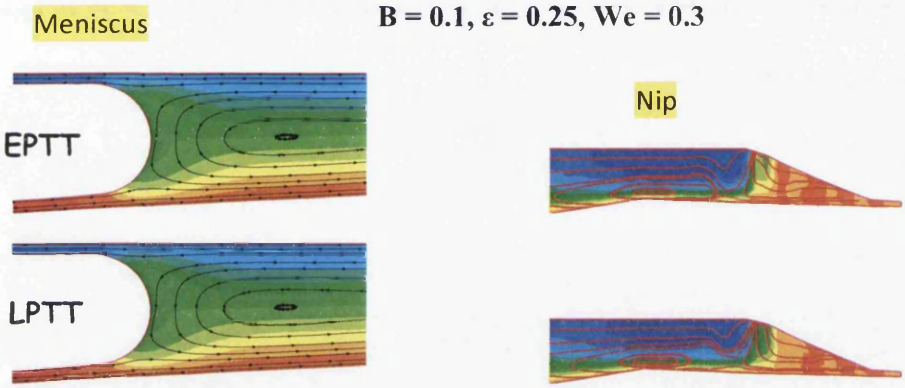

Figure 8.15: meniscus and nip vortex development, EPTT and LPTT flow

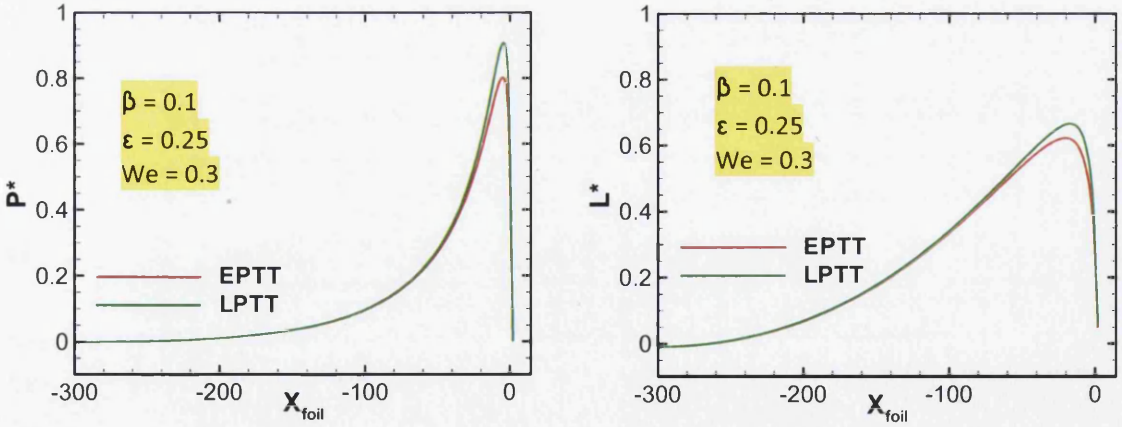

Figure 8.16: Pressure and lift profiles, EPTT and LPTT flow

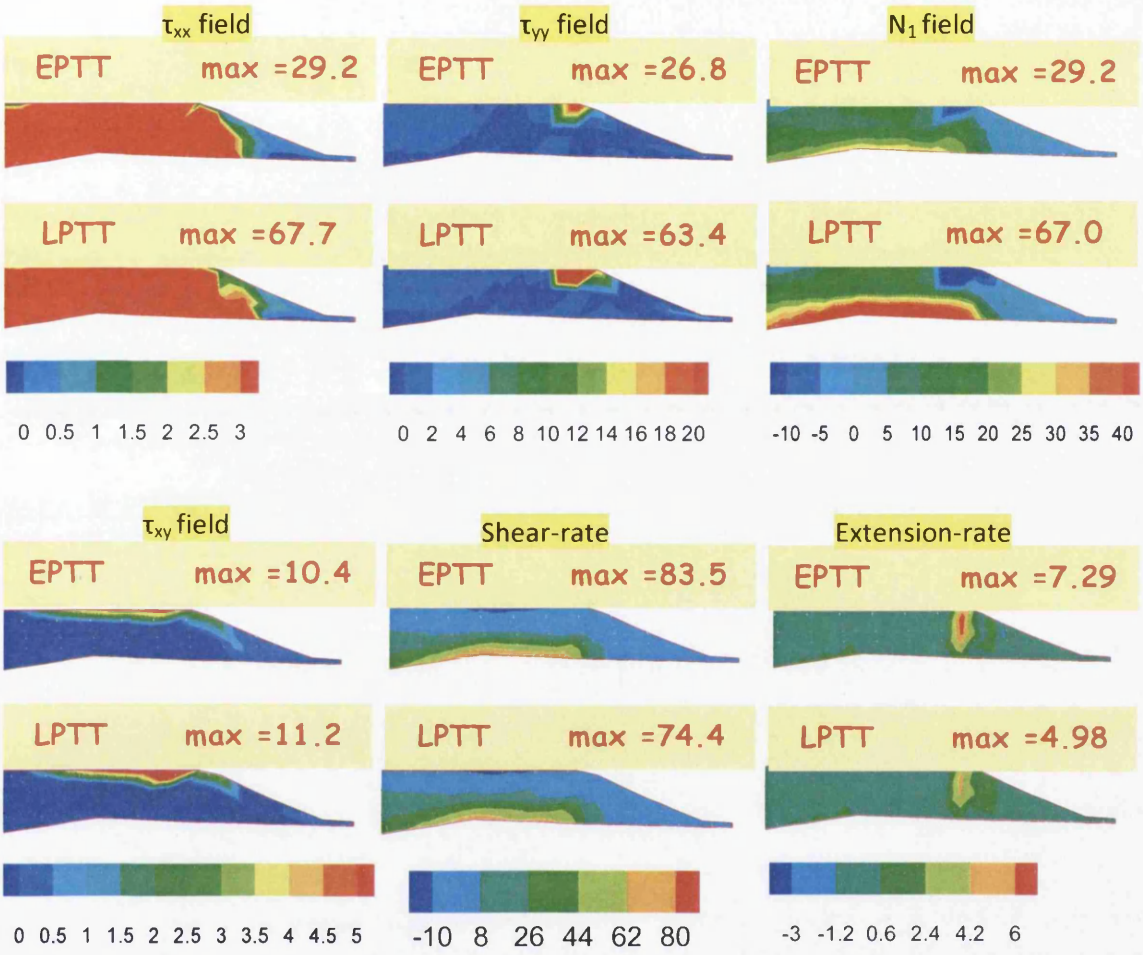

Figure 8.17a: τ_{xx}, τ_{yy}, N_1, τ_{xy}, shear and extension rate, LPTT flow
(β =0.1, ε = 0.25, We = 0.3)

8.5 Outcomes-summary

Numerical solutions have been presented for reverse roll coating with viscoelastic EPTT and LPTT constitutive models, inclusive of wetting line presence. Solution for several parameter pairings have been investigated with different levels of solvent fraction, to reflect highly polymeric fluids, and varying extensional viscosity, to isolate and identify softening and hardening flow response. It has been observed that highly polymeric fluids destabilise the flow at the nip region, as the nip-vortex is stimulated and distorted; this reveals a reduction in overall recirculation as elasticity (We) is increased. On nip-pressures: at larger ε above ε=0.5 (lower levels of extensional viscosity), the localised peak-pressure decreases, a feature

always apparent under EPTT solutions; whereas for LPTT, at low ε below ε=0.25 (larger levels of extensional viscosity), localised peak-pressures are seen to increase. Hence, tension-hardening elevates localised peak-pressures; whilst tension-softening has the opposite effect.

The high stressing levels on the foil-substrate shows the influence of shear/extensional flow on the stagnation region (maximum stress field observed on the foil-side); this tends to pull liquid away from the nip-vortex recirculation, to take up the speed of the foil whilst strengthening the flow in the meniscus recirculation. Under lower shear stressing, as with EPTT over LPTT solutions, the meniscus recirculation reduces more for EPTT than with LPTT solutions; here, there may also be a contribution from the strain-softening property of EPTT, absent under LPTT representation.

Chapter 9

Reverse roll-coating: viscoelastic FENE flows

Viscoelastic FENE constitutive models are considered in the simulation of high-speed reverse roll coating flow with polymeric paint solutions, where wetting lines are incorporated. Both FENE-CR and FENE-P models are utilised to illustrate the influence of shear-thinning in the context of strain-hardening properties. Steady solutions are derived numerically through a time-stepping hybrid finite element-finite volume subcell algorithm with dynamic free-surface location, drawing upon a fractional staged, incremental predictor-corrector, and semi-implicit time-stepping procedure. A systematic computational and rheological study allows for parametric variation in elasticity (We-variation), level of extensional hardening (A_L), shear-thinning and solvent fraction (β). Various problem aspects are investigated to reveal the influence of viscoelasticity on vortex developments, pressure and lift profiles, shear and extension rates, and critical stress states. Specific advantages of the viscoelastic rheological properties are observed by analysing stress and flow structures over a range of Weissenberg numbers. The novel aspects of the work lie in the application of the algorithm to the reverse roll coating process under such viscoelastic flow approximation.

9.1 Introduction

In this chapter, the various influences of extensional flow are analysed in a reverse roll coating (RRC) process, when dynamic wetting lines are involved. In the computational domain, the polymer solutions represented encounter regions of both high shear and extension rates, which demand suitable viscoelastic description. This justifies the selection of a viscoelastic model from the FENE network class of models to represent the spatial-temporal evolution of the extra-stress tensor. Here under RRC flow, particularly FENE-CR and FENE-P models are selected for their richness in rheological properties. The FENE model highlights the key influence of sustained strain-hardening (tension-thickening) behaviour, whilst within shear; the FENE-CR model supports constant shear viscosity, in contrast to FENE-P model which provides shear-thinning response. A principle focus lies mainly in attaining larger elasticity levels with the FENE-option than obtained from the earlier study with PTT fluids [see chapter 8]. Significantly, FENE constitutive models can be solved in two forms of stress variable format, either stress tensor or configuration tensor form. In the earlier study, the PTT fluids utilised the stress tensor form and numerical solutions at critical stress states were achieved for much lower elasticity levels ($We<2$). As a consequence, the current work utilises a *configuration tensor* form of the FENE model, in contrast to the specific *stress tensor* form, in order to investigate these approximations. Some interesting features are observed in the respective numerical solutions for these models and their corresponding material functions aid in distinguishing their common and disparate character.

FENE models have been widely employed in recent computational rheological studies, with a view to simulating the behaviour of polymeric fluids, quantifying the influence of level of extensibility, solvent fraction and elasticity. Most work in the literature has focused on classical shear flows, and the effects of elasticity and levels of extensibility in terms of critical elasticity attained. Lee at al. [2002] studied viscoelastic free-surface flows in slot-coating by finite element methods, comparing the performance of different constitutive models including those of Oldroyd-B, FENE-CR and FENE-P. The authors concluded that increase in the hydrodynamic coating thickness is strongly dependent on the physical properties of the coating fluid. Rocha et al. [2009] studied the effects of extensibility in cross-slot bifurcation flow, employing the stress tensor form with both FENE-CR and FENE-P models. Results reveal that the critical Deborah number reduces as extensibility increases.

Most significantly the complex RRC flow domain reveals the existence of separate high shear and high extension rate zones, which can generate a high degree of accumulated stress; much higher than in comparable channel or simple shear flows. Hence, it is suitable to investigate the influence of different levels of extensibility, polymer:solvent fraction and effects of elasticity. Initially, such RRC flows are modelled utilising a stress tensor form of the FENE-CR model, and then under variable transformation, contrasted against

implementation with configuration tensor form. Notably, due to advantageous numerical stability properties under configuration tensor definition, much larger critical Weissenberg (We_{crit}) stress states have been observed under this configuration form. Consequently, flow simulations are pursued further in this form, whilst addressing material function parametric variation. To investigate the additional influence of shear-thinning, the selection under constitutive models was widened to also include that of FENE-P. In the reverse roll coating application, polymeric fluids are forced through a nip-gap under high shear-rate prevailing conditions, and beyond that meet the coating-substrate (foil) at a contact-point, whilst the foil is travelling at high speed and in reverse direction to that of the roller. A schematic illustration of the RRC domain is shown in [chapter 8], consisting of a cylindrical applicator roll rotating in the forward direction and the foil moving in the reverse direction. The polymeric fluid is conveyed forward by the applicator roll up to the nip-gap, with some penetration and through this zone. Then, flow conditions around the nip and contact-point locations, represent a combination of high-shear and highly-extensional flow. Since the foil-substrate surface is assumed to be a no-slip boundary, moving at high constant speed in the opposite direction to the roller, hence the polymeric coating fluid undergoes some degree of extension. At the contact-point, the material is accelerated rapidly to match the foil-speed, giving rise to a region of intense shear and extension. As such, the RRC process represents a complex combination of shear and extensional flow deformation, created by the combined influences of pressure-driven flow through the nip and drag flow induced by the foil. Although the flow is steady, it experiences changing flow dynamics as it moves through the flow-domain and a non-constant extension rate when subject to extension. In this particular study, a firm objective is to investigate the various effects of different levels of extensibility, amounts of solvent fraction and alternative critical elasticity levels reached. The present numerical findings are deemed valuable support to RRC process control – specifically, in aiding the reduction of undesirable recirculation, quantifying peak-pressure levels generated and in estimating accumulated stress in the coating. A laudable ultimate processing goal is then, to predict and derive optimally suitable flow-process conditions, to preserve uniformly coated foil-substrates where surface defects are avoided.

9.2 Problem specifications

The computational domain is exactly as presented in chapter 8 and provides a natural extension of the rheological studies of Chapter 8. The viscoelastic model is chosen to facilitate flow of industrial fluids. Under incompressible isothermal conditions, the behaviour of viscoelastic flow is generally governed by the fundamental principle of fluid mechanics expressing the conservation of mass and momentum (see Chapter 2). The constitutive model considers a FENE-CR and FENE-P model to reflect constant shear viscosity and extension thickening, and shear thinning viscosity and extension thickening respectively. The first model variant adopted is the FENE-CR model featuring a constant shear viscosity. This form of FENE-CR model possesses an extensional hardening behaviour, capped at high

extensional rates. The finite extensibility parameter L largely dictates severity in strain-hardening, with larger values approaching infinity offering the greater extremes (larger Trouton ratios).

Contrary to the constant shear-viscosity model, the FENE-P model is adopted and exhibits shear-thinning behaviour and extensional thickening capped at high extensional rates.

Under shear and extensional flow deformation, the state of material functions may be taken as an important model reference to interpret anticipated complex mixed-type flow response. In Chapter 3, Figures 3.6(a-c), material function plots for the respective FENE models are presented considering the relevant parameters, covering the steady-state shear (η_s) and extensional (η_ε) viscosities, and the first normal stress difference (N_1).

{L, β}-variation: The parameters considered are, L={5, 3} and β=[0.9, 0.1}, as displayed in chapter 3, Figure 3(a-c). With a base selection of {L = 5, 10} and {β = 0.9}, these choices are made to reflect high and low levels of extensional viscosity. For the FENE-CR model, the parameter selection consist of {L = 3, 5, 10} and {β = 0.9, 0.1}, used to study the impact of variation in strain hardening level and amount of solvent fraction, respectively. The FENE-CR response for β=0.9 and 0.1 at two different L-values (L={3, 5}), is exactly matched in both shear viscosities as unity, whilst there is slightly weakening in first normal stress difference for L = 3, chapter 3, Figure 3(c). In extensional viscosity of chapter 3, Figure 3b, noted differences arise over the deformation rate range from 10^{-1} to 10^{4}; and likewise in N_1 at rates above 10^{-1}. Significant differences are observed in all three functions under the highly-mobile state of β = 0.1; this is apparent in shear above rates of 10^{0} and in extension above rates of 10^{-1}. For FENE-CR, {L, β}={3, 0.1} is the more strain-hardening of all instances considered, which is also reflected therefore in N_1 as weakening at high shear-rates. Hence, under the FENE-P model, the flow behavioral response is clearly more complex, rich in variation and rate dependent: displaying a combination of shear-thinning and strain-hardening in the rate-range 10^{1} to 10^{4}. Here, N_1 levels are considerably weaker than those represented with the FENE-CR model.

Fluid flow simulation was changed to FENE-P fluid at β = 0.9, A_L = 5 and 10, and then β = 0.1 A_L = 3, and 5. In terms of shear viscosity, this type of fluid possesses almost same characteristics as LPTT fluid (see chapter 8) with matching parameters. Extensional viscosity level of FENE-P model increases up to a plateau at high extensional rate. The plateau level depends on the extensional viscosity value (L-parameter) selected.

The solution technique is based on a finite-element discretisation with semi-implicit Taylor-Galerkin/pressure-correction algorithm used to solve the governing equations. This scheme incorporates a time-stepping procedure and a fractional-staged equation methodology over each time-step. The fractional-staged equation procedure is represented in some four phases: first a mass matrix form; second a Poisson-equation type; third, a corrected mass matrix

form; and fourth, a free-surface location stage for surface height (h) (see below). The numerical solvers include: a Jacobi iteration method for the first and third stages, performing three mass iterations per step; and a direct Choleski decomposition method used for stage two. For a reasonable balance between accuracy and stability, a time-step of 10^{-4} is adopted throughout all calculations. The velocity field introduces a piecewise continuous approximation based on quadratic shape functions, and the pressure field is approximated by linear shape functions.

For the extra-stress, a triangular-subcell cell-vertex finite volume approach is developed [8, 9, 10], where a parent finite-element is sub-divided into four child finite-volume subcells. The individual components of the stress tensor, are then approximated by linear shape functions over each finite volume subcell.

The computational domain is spatially discretised through structured-meshing triangular elements employing a Taylor-Hood type of finite element with six noded finite element triangles; three vertex nodes and three mid-side nodes (see chapter 7 & 8 for mesh).

Boundary conditions and free surface tracking method are illustrated in chapter 8.

9.3 FENE-CR model flow solutions

Model performance is first examined by applying FENE-CR in a stress tensor form. The flow is simulated up to critical solution states of We and flow fields are analysed. Observations reveal relatively low critical We solution states as observed for the PTT models. Table 1 shows critical We-levels reached for each simulation. Subsequently, a configuration tensor form of the FENE-CR model has been employed. This provides the ability to reach much larger elasticity levels up to We=11. The reason for this lies in the improved numerical evolution properties available under the configuration form, as can be demonstrated through the corresponding *Det*(τ) fields and the improved precision of boundary condition representation [Hulsen 1988, Hulsen 1990, Wapperrom et al. 1995]. The effects of increasing elasticity and level of strain-hardening at low solvent fraction (β=0.9) are analysed, and then equivalently, for highly polymeric mobile solutions (β=0.1). The analysis highlights the influence of strain-hardening across the domain, as this is one of the key features of the FENE-CR model.

Model	Solvent Fraction β	Finite extensible factor L	Max. We
FENE-CR configuration tensor	0.9	5	11
		10	2.8
stress tensor	0.9	**5**	**0.4**
FENE-P	0.9	5	11
		10	1.6
	0.1	5	0.3
		3	1.2
Zevallos (FENE-P)	0.59	1-10	11.0

Table 9.1: Critical states for different constitutive models.

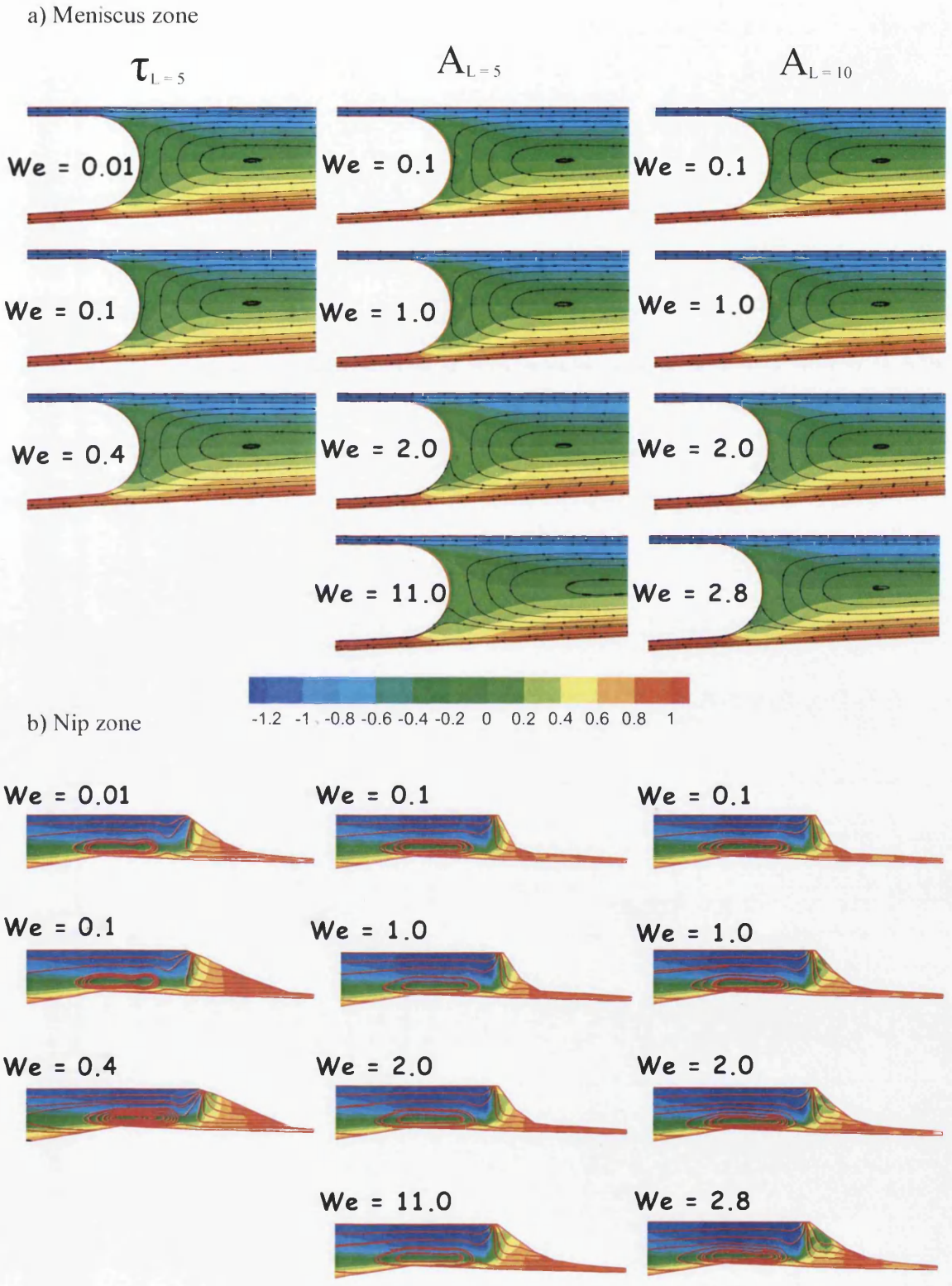

Figure 9.1: a) Meniscus and, b) Nip vortex development for FENE-CR flow ($\beta = 0.9$)

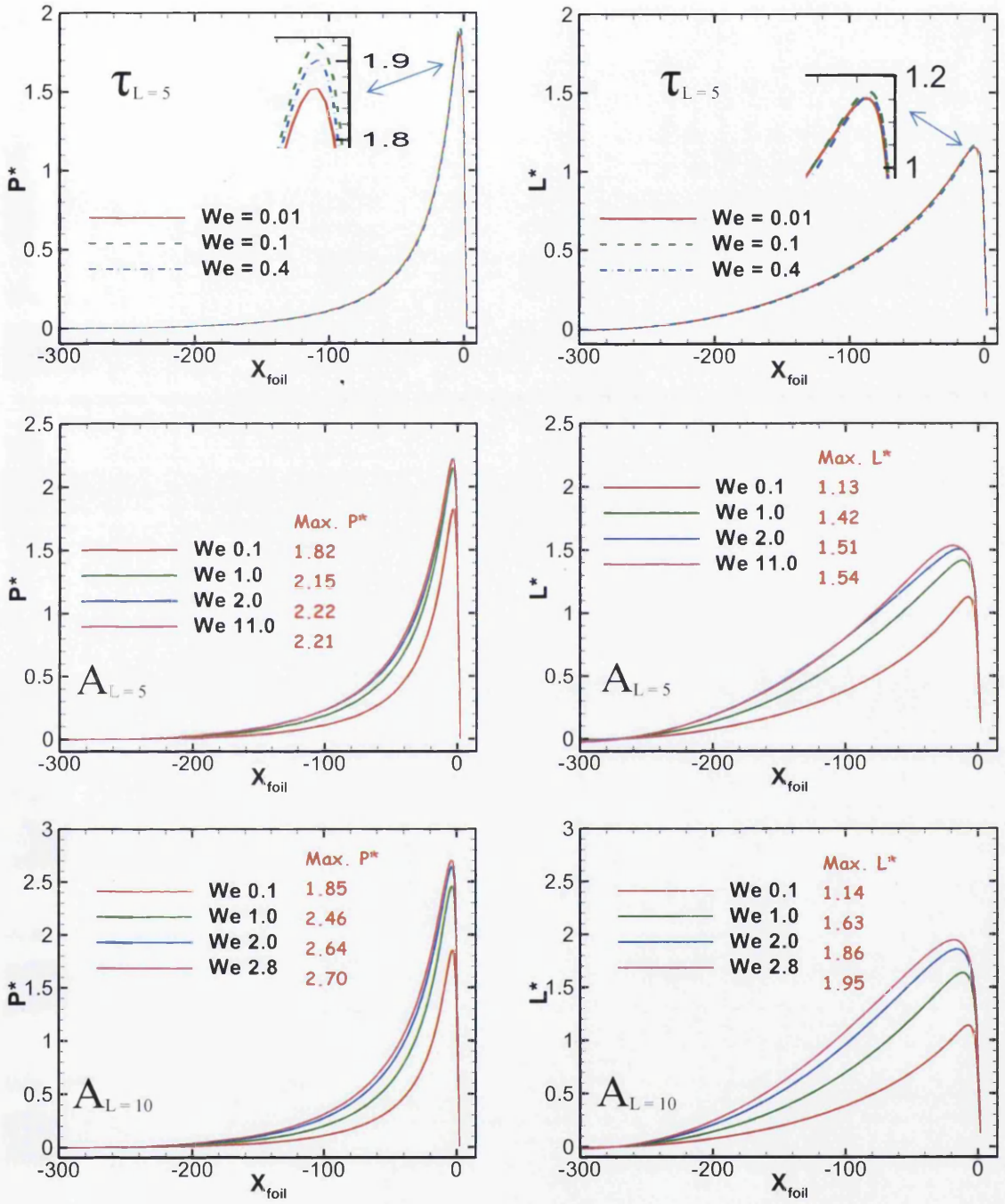

Figure 9.2: Pressure and lift profiles for FENE-CR flow ($\beta = 0.9$)

a) N_1-fields

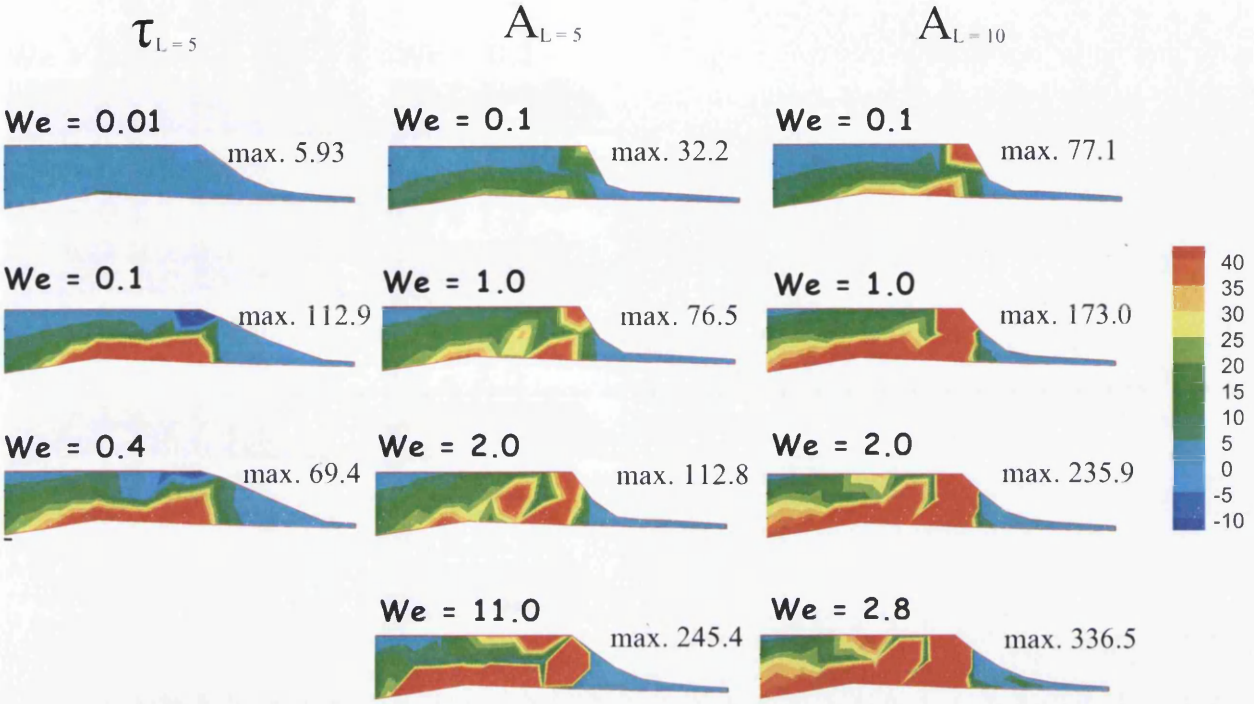

b) τ_{yy}-fields

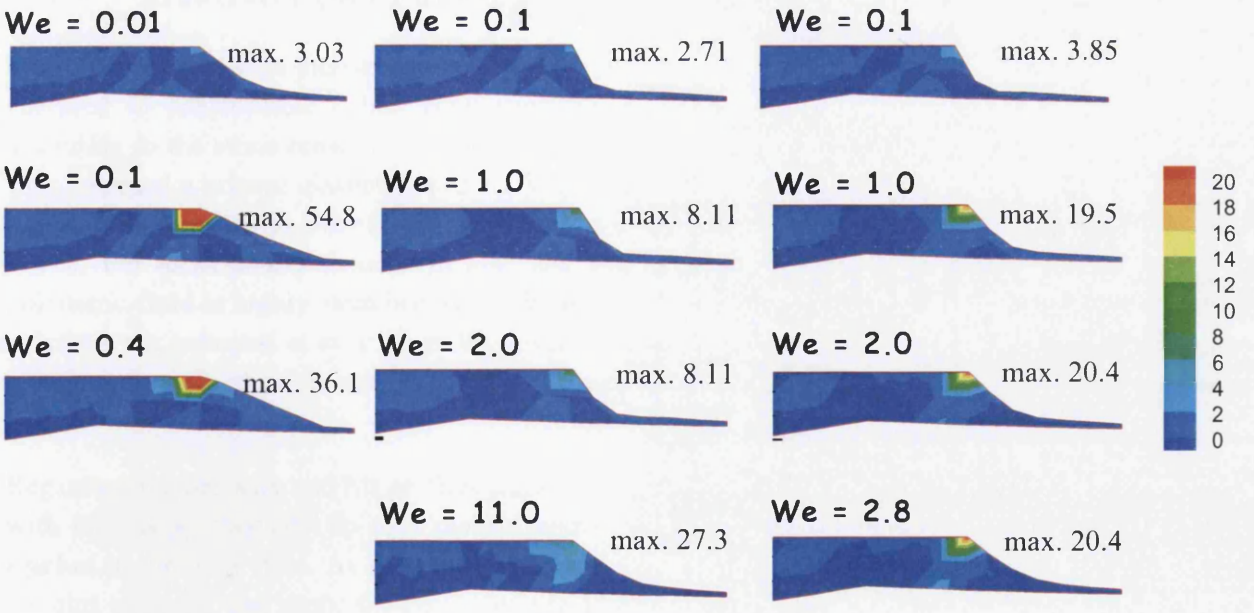

Figure 9.3: a) N_1 and, b) τ_{yy} nip development for FENE-CR flow ($\beta = 0.9$)

c) τ_{xy}-fields

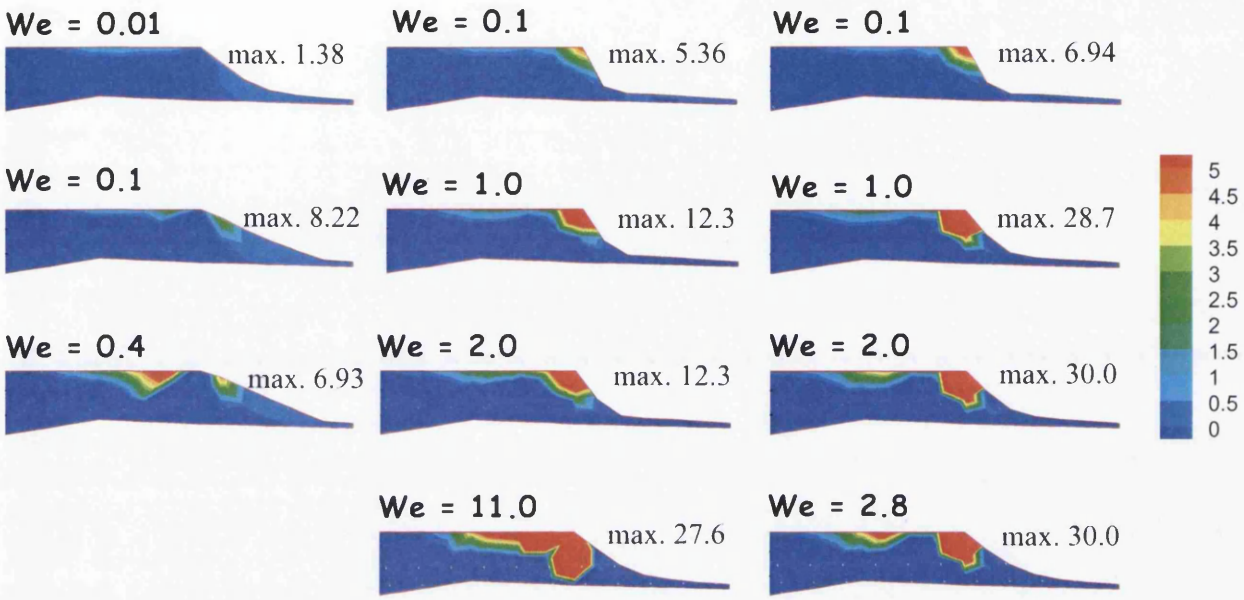

Figure 9.3: c) shear stress nip development for FENE-CR flow ($\beta = 0.9$)

9.3.1 Elasticity (We) and Extensional hardening change (A_L)

From Fig. 9.1 and with increasing elasticity, the meniscus and nip-region flow structures are analysed in considerable detail, comparing the influences on respective flow solutions, according to the stress tensor and configuration tensor variable-base used. The stress tensor form attained a critical elasticity level of We=0.4, whereas the configuration form reached higher critical states at We=11. Observations reveal that at higher elasticity levels above We=2, the recirculation reduces in size and meniscus shape becomes deformed as the polymeric fluid is highly stretched along the directions of the moving boundary. As further solutions are extracted at ever larger We-levels, more fluid tends to be picked up by the foil, reducing the strength of the recirculation at the nip-region, whilst increasing the leakage flow height.

Regarding the pressure and lift profiles shown in Fig. 9.2, localised peak-pressure levels rise with increasing elasticity up to a plateau above We=2.0, where the extensional viscosity reaches its limiting state. As such and with increasing strain-rate, the extensional viscosity remains constant, and hence the peak-pressure also remains around a constant level. The lift profile reflects the forces on the foil due to pressure, and also peaks locally around the nip-region where the pressure does likewise.

The first normal stress differences (N_1) are identified in Fig. 9.3a. Here, N_1-levels are larger around the nip on the foil-substrate side and about the contact-point zone. The values reached particularly reflect the levels of N_1 in extension, as the flows reaches a region of high deformation rate (in extension and shear) at this location. The FENE-CR model features a constant shear viscosity and hardening extensional viscosity, therefore N_1-levels are more related to extensional effects. The τ_{yy} levels observed in Fig. 9.3b are much greater at the contact-point zone, where strain-rates are maximum and increasing. Shear stress development at the nip-region is illustrated in Fig. 9.3c. Here, shear stress levels are observed to rise with increasing We up to critical solution states, and accumulate around the contact-point zone.

As extensional viscosity level is increased up to A_L=10, numerically converged critical elasticity solution states are seen to be much lower, at We=2.8, and above We=2 up to the critical solution level, flow structures around the meniscus are deformed with more stretching apparent of the polymeric fluid. At the nip-region itself, vortex structures are stretched inwards towards the meniscus as more fluid is picked up by the foil-substrate. Leakage flow height also increases. The pressure and lift peak levels at this level of hardening, are greater than that observed at A_L=5, and also increase with increasing elasticity. N_1 fields show a doubling in maximum levels, as compared to the lower extensional hardening scenario. τ_{yy}-values reach a plateau above We = 2, due to the critical strain-rate being attained; also the same observation applies to the shear stress fields.

9.4 FENE-P model flow solutions

Under extracted FENE-P solutions, the shear viscosity is thinning with increasing shear-rate, and N_1 is weakening under the present complex flow deformation conditions. Yet in terms of extensional viscosity, levels attained are much lower than under FENE-CR solutions. As such, the FENE-P material functions correspond to those of the LPTT model (see Fig. 9.7); yet the difference is that the FENE-P models are solved in configuration variable form.

9.4.1 Influence of shear-thinning

Different amounts of solvent fraction have been investigated (β=0.9 and 0.1) and also different levels of hardening (A_L=5 and 10). At high solvent fraction, and low hardening, critical elasticity levels attained were much higher at We=11. Herein, the meniscus shape also deforms in solutions above We=2; where accordingly the central core vortex expands, with less recirculation strength, as the polymeric fluid is stretched and pulled by the rotating roll and foil.

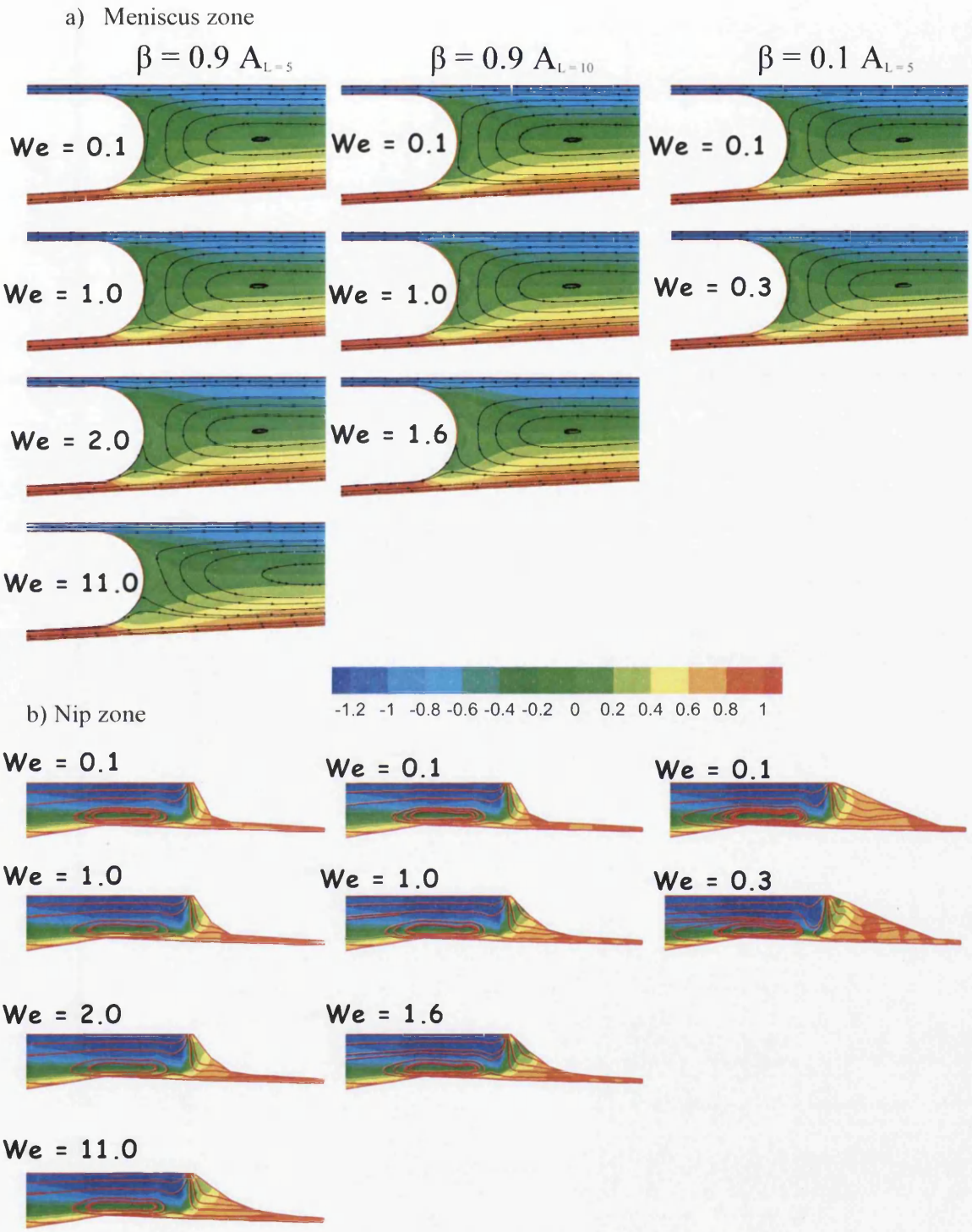

Figure 9.1: a) Meniscus and, b) Nip vortex development for FENE-P flow (β = 0.9 and 0.1)

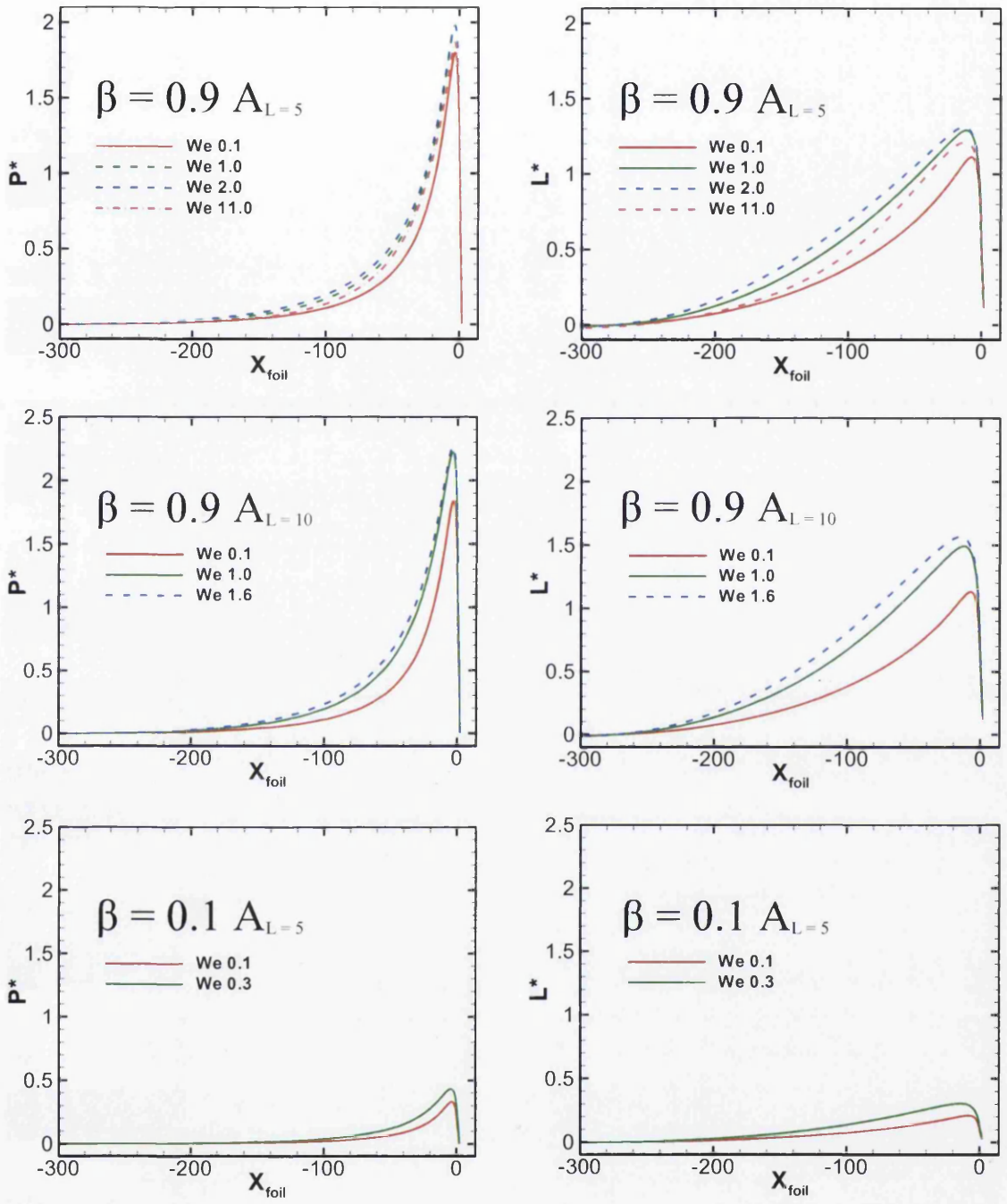

Figure 9.2: Pressure and lift profiles for FENE-P flow (β = 0.9 and 0.1)

a) N_1-fields

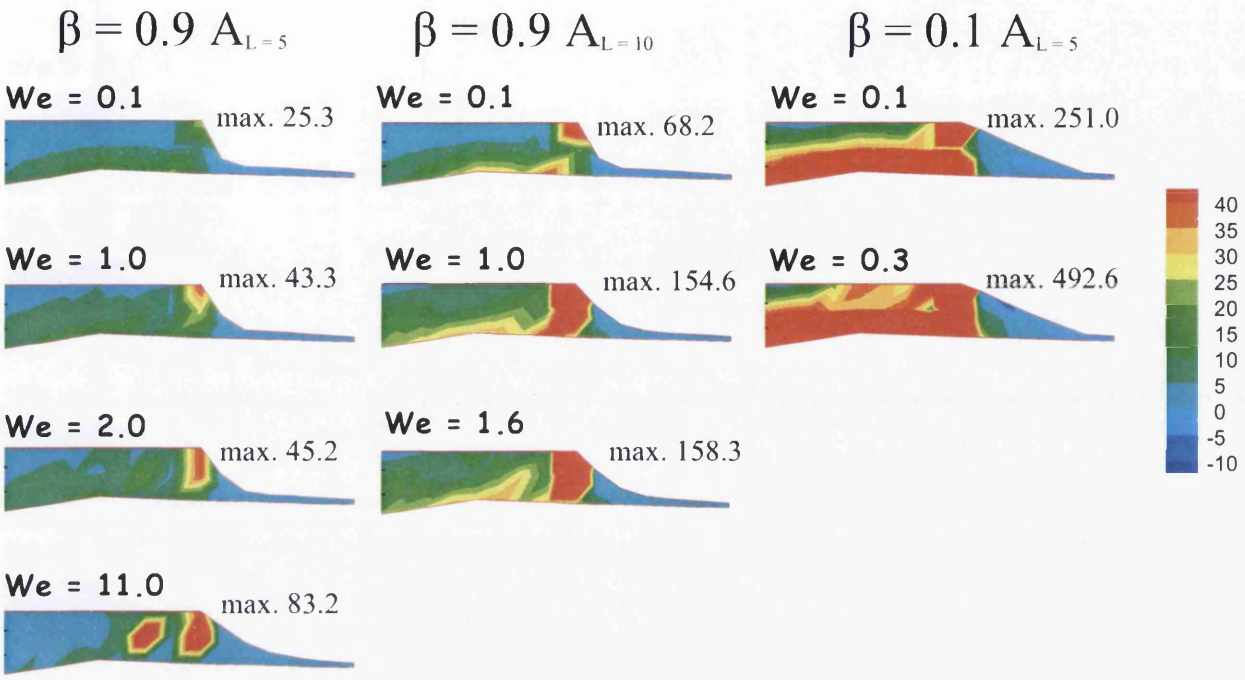

b) τ_{yy}-fields

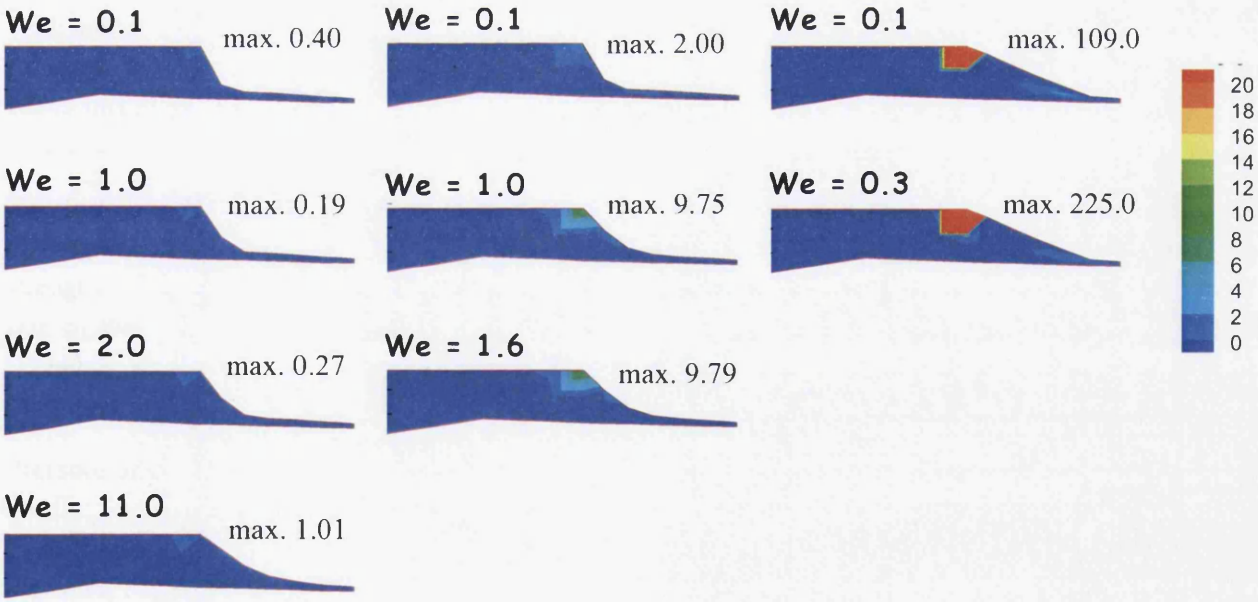

Figure 9.3: a) N_1 and, b) τ_{yy} nip development for FENE-P flow ($\beta = 0.9$ and 0.1)

c) τ_{xy}-fields

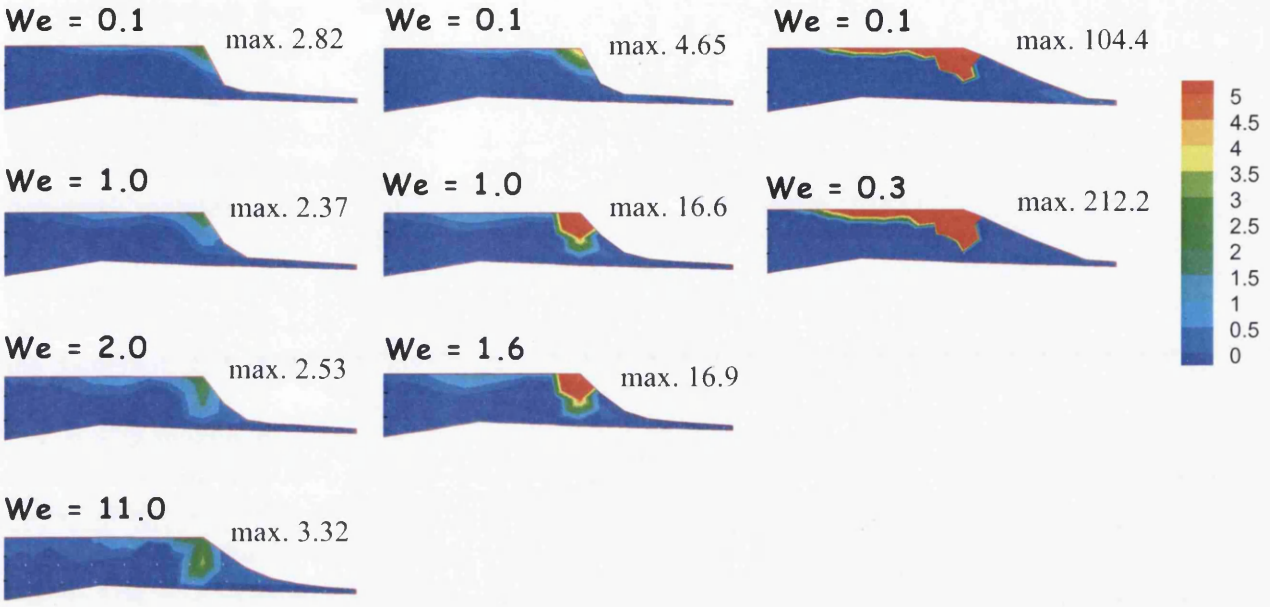

Figure 9.3: c) shear stress nip development for FENE-P flow (β = 0.9 and 0.1)

With increase in strain-hardening (A_L=10), the critical stress states reduce dramatically in solutions up to We=1.6, for which meniscus-shape deformation is apparent and this feature arises much earlier than observed for A_L=5. For highly polymeric fluids (β=0.1, A_L=5), the critical solution We-state attained is reduced even further, now being only up to We=0.3.

The influence of shear-thinning is more apparent in vortex structures observed around the nip-region and for the highly-polymeric mobile-flow solutions. Here, recirculation size and strength increases and is seen to expand inwards towards the meniscus, with an increase in size of the leakage flow zone. Previous research studies, both experimental and numerical [Echendu et al. 2011], concur with this finding, as observation would indicate that shear-thinning tends to often stimulate vortex enhancement.

Pressure and lift profiles demonstrate rising peaks with increasing elasticity for all solvent fractions analysed (see Fig. 9.2). Notably, peak levels reach a plateau above certain critical stress states (We=1.5), corresponding to when extensional viscosities also reach their plateaux. Although peak levels attained are much less than those observed under FENE-CR solution; this is due to the influence of shear-thinning for both high-solvent and highly-polymeric flows. For the highly-polymeric mobile solutions, the peak-pressure levels reduce even more.

From Fig. 9.3(a-c), the various states of stress development are observed. N_1 is seen to increase at the contact-point zone and also with increasing elasticity. As the level of strain-hardening increases from $A_{L=5}$ to $A_{L=10}$, the maximum in N_1 values triples and stress states reach high levels. As solvent fraction is decreased from β=0.9 to 0.1, N_1 maximum values are one order of magnitude larger than those obtained for high-solvent solutions. In addition for high-solvent solutions, τ_{yy} levels are much lower, lying in the range of zero to unity; whereas with their highly-polymeric counterparts, maximum τ_{yy}-levels are ~$O(10^2)$. With highly-polymeric mobile solutions, the fluid is highly shear-thinning and high levels of deformation-rate are generated; hence, more significant polymer extension is encountered at the contact-point zone, as seen in τ_{yy} fields. In shear stress fields of Fig. 9.3c, accumulated stress build up is observed on the foil-side, due to the high strain-rate attained in that region, and the higher the polymeric content, the larger the maximum shear stress generated.

For highly-polymeric mobile solutions, comparison was also performed on the two constitutive models for strain-hardening parameter settings of (A_L=3 and A_L=5). Observations show that shear-thinning properties stimulate vortex activity, and the vortex structure (size/strength) is also much less at lower strain-hardening levels (seen at the nip-region, Fig. 9.4). In addition (Fig. 9.5), pressure and lift levels are also much lower at low A_L and with these FENE-P solutions.

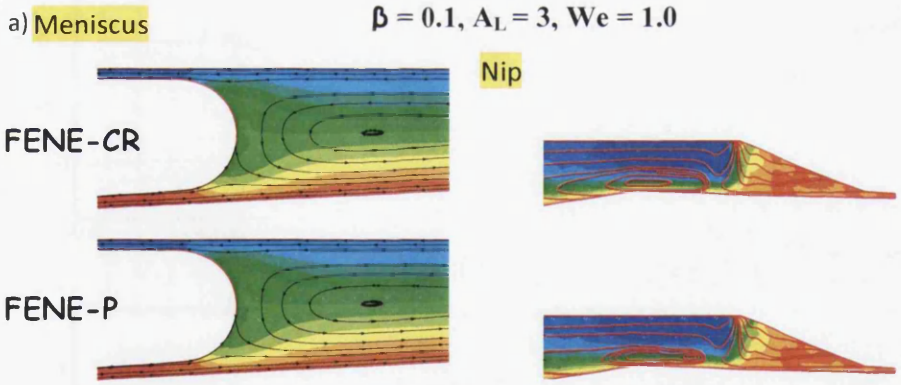

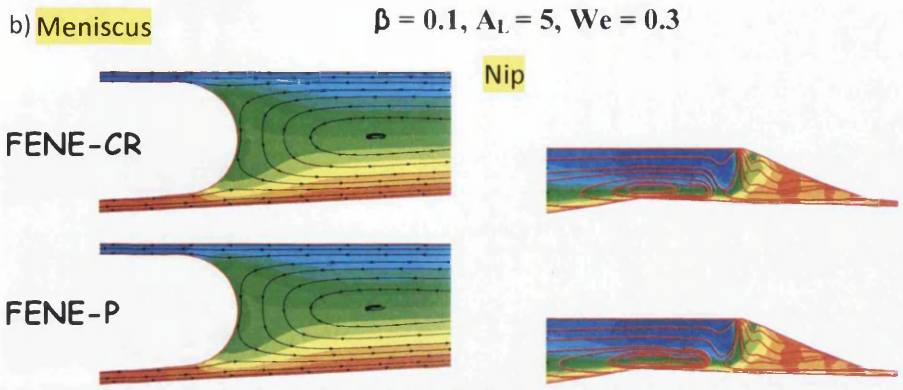

Figure 9.4: meniscus and nip vortex development for FENE-CR and FENE-P flow, β = 0.1,
a) A_L = 3, We = 1.0
b) A_L = 5, We = 0.3

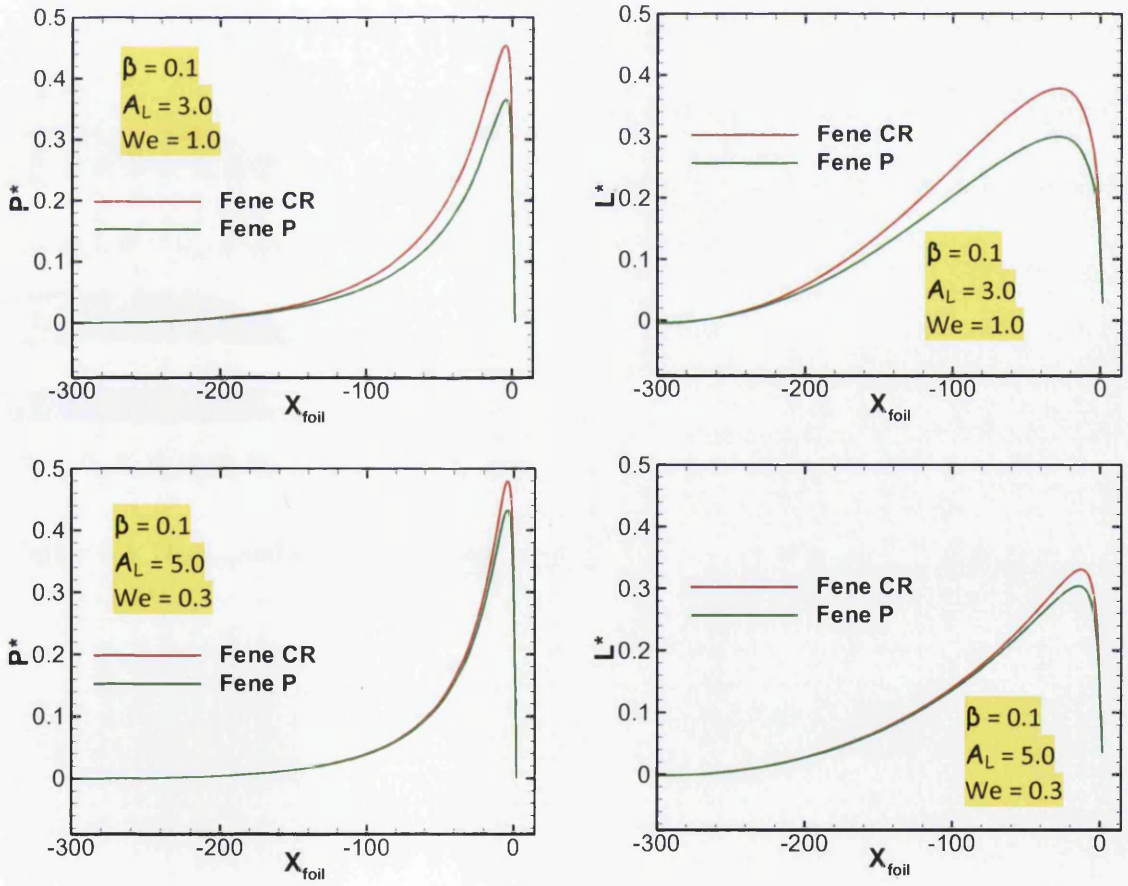

Figure 9.5: Pressure and Lift Profile for FENE-CR and FENE-P flow (β = 0.1)

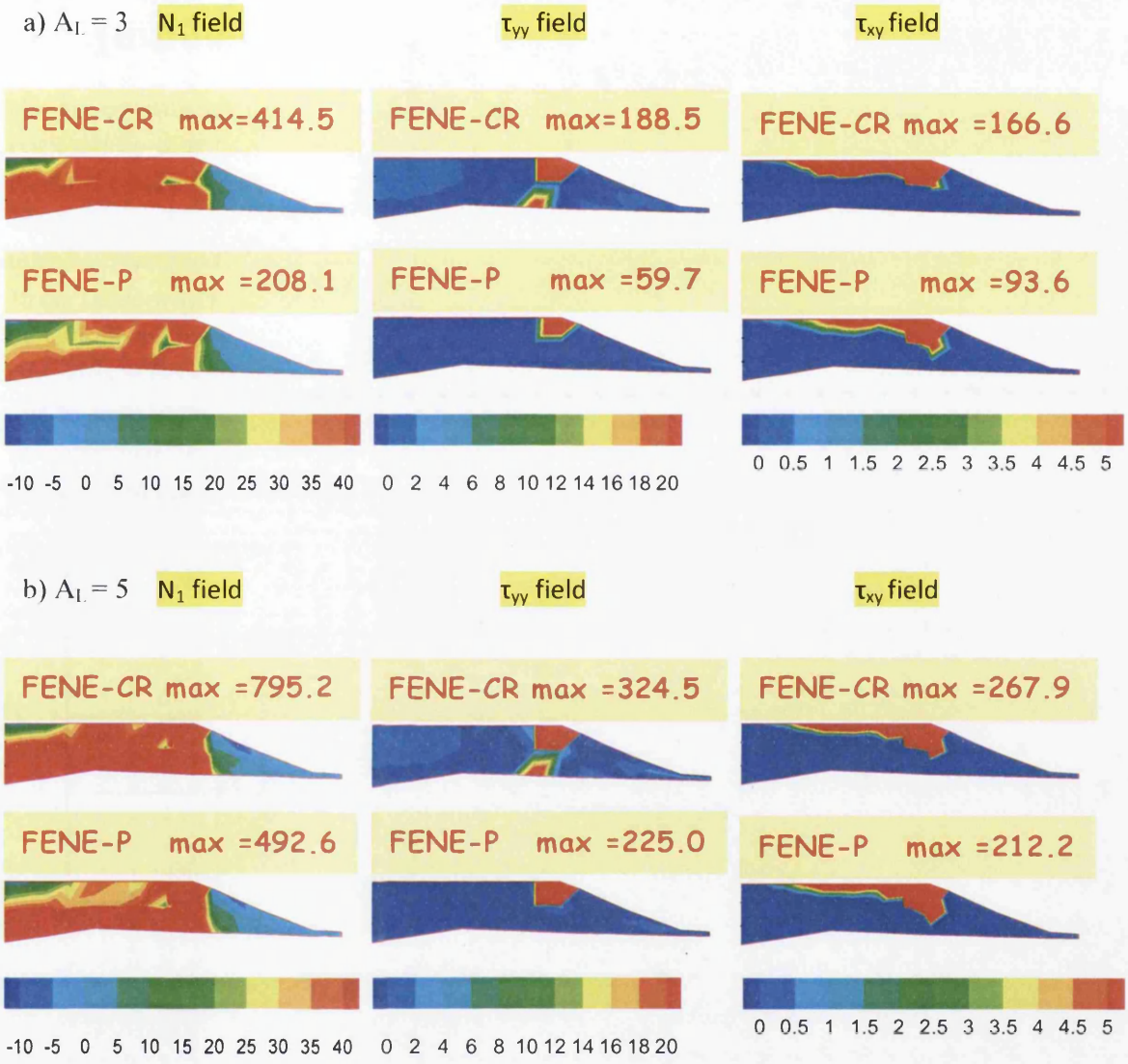

Figure 9.6: N_1, τ_{yy} and shear stress nip development for FENE-CR and FENE-P flow ($\beta = 0.1$) a) $A_L = 3$, b) $A_L = 5$.

9.5 Comparison of FENE and PTT solutions (influence of shear-thinning/strain-softening)

Having investigated the FENE class of models, one can interrogate differences in rheological response by direct comparison against the class of PTT models. Since the PTT form resides in stress tensor variables alone, and to preserve equitable comparison basis, below the FENE versions are also considered in this same form. In this fashion, the influence of shear-thinning may be quantified by comparing, for example, the differences in solution response between stress fields with FENE-CR and LPTT models [see Fig. 9.8-9.10], when extensional viscosity behaviour is matched and shear-thinning properties are disparate. Likewise, the direct comparison between FENE-P and EPTT, under comparable shear-thinning properties, allows one to unambiguously associate with the strain-softening properties of EPTT, as distinct from the sustained hardening of FENE-P (as with LPTT). The respective material behaviour are presented in Fig. 9.7.

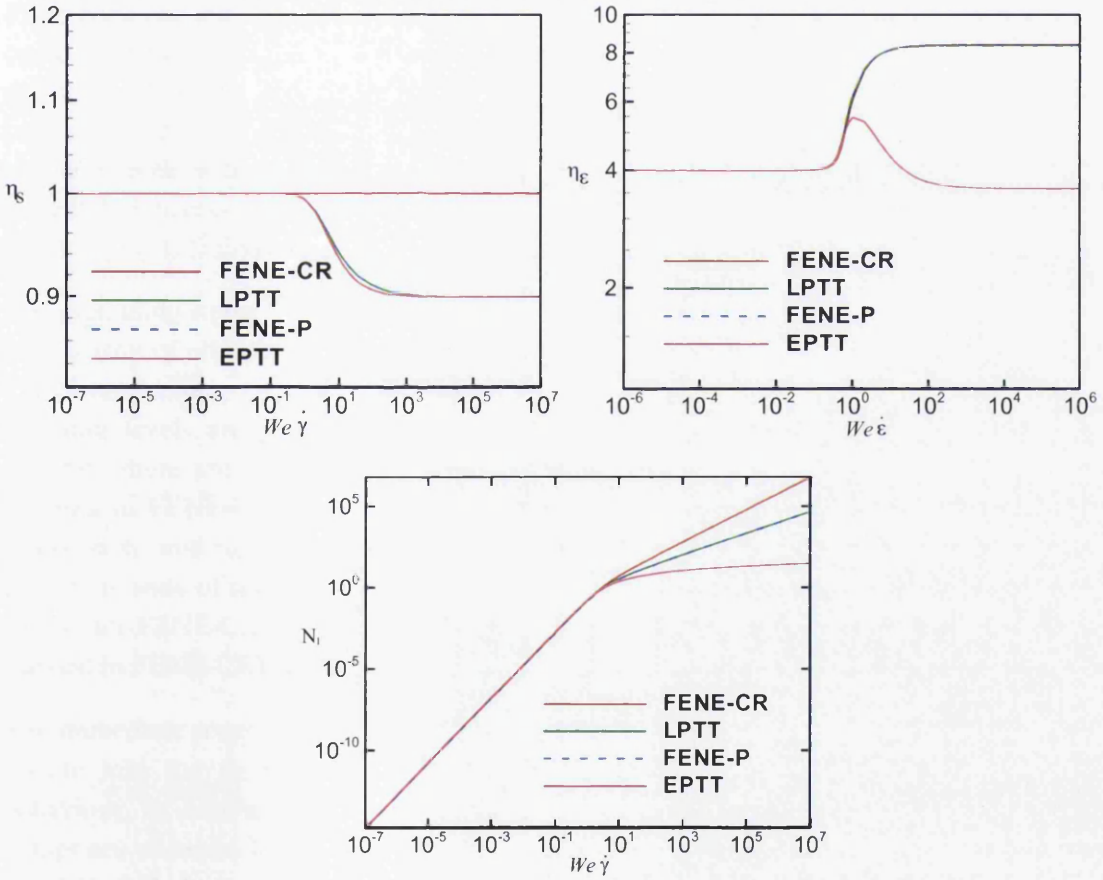

Figure 9.7: Material function plots comparing model behaviour for FENE and PTT materials; ($\beta = 0.9$, $L = 5.0$, $\varepsilon = 0.042$)
a) Shear viscosity b) Extensional viscosity c) N_1

Firstly, on the influence of shear-thinning, the extensional viscosity behaviour of FENE-CR(L=5) is matched to that of LPTT(ε=0.042). For this setting, the critical elasticity solution state reached is We=0.4 for FENE-CR and We=0.1 for LPTT; which reveals that numerical solution becomes less tractable as shear-thinning is introduced. Here, meniscus deformation is relatively unaffected, whereas nip vortex structure is slightly stimulated, proving larger than that observed under constant shear viscosity FENE-CR solution. Secondly, wetting-line solution response is interrogated for cases FENE-P(L=5) and EPTT(ε=0.042), where one may identify the impact of EPTT strain-softening under comparable levels of shear-thinning. In this instance and with EPTT solutions, the dynamic wetting line is pushed out further away from the nip-zone by the coating fluid, causing an overall measurable increase in leakage flow; the meniscus region remains unaffected. This is apparent in the outer-domain shape changes in Fig.9.8 below.

In Fig. 9.9, corresponding pressure profiles are illustrated, contrasting separately the highly-localised influences of shear-thinning and strain softening, across the various models on offer. Here one may observe, that increase in both shear-thinning and strain softening effects, cause reduction in highly-localised peak-pressure levels, which are strictly manifest over the nip-region. Notably, shear-thinning is roughly twice as strong a reducing influence on peak-pressures, than that attributable to strain-softening. There is a one unit reduction in peak pressure levels with regards to the influence of shear-thinning (FENE-CR = 1.9 to LPTT = 1.8units), whereas with strain-softening, a half unit reduction is observed for the peak pressure levels (FENE-P = 1.85 to EPTT = 1.8units).

Corresponding stress field development in N_1, τ_{yy} and τ_{xy} are provided in Fig. 9.10. A direct comparison of all stress maxima is extracted from the summary data provided in Table 9.2. On *shear-thinning influence*, with FENE-CR and LPTT comparison under Fig. 9.10a, the stressing levels are generally observed to be less under LPTT than FENE-CR solution. Notably, there are large and *significant effects due to shear-thinning in N_1-fields*, where maxima in FENE-CR are some *five-times* larger than with LPTT (ratio 5:1). LPTT-stress fields, in τ_{xy} and τ_{yy}, are also reduced by about one-half, from those of FENE-CR flow. The maximum state of shearing in the field is observed within the nip-region on the roll-side (e.g. see N_1 for FENE-CR), while the maximum state of extension is exposed within the τ_{yy} field (largest in FENE-CR), around the contact-point region on the foil-side.

The immediate comparison between FENE-P and EPTT stress solutions of Fig. 9.10b permits insight into the isolation of strain-softening effects. One notes that EPTT extensional behaviour, in contrast to that of LPTT and FENE-P, is considerably more complex; it comprises of initial hardening, and then subsequently, strain-softening at higher strain-rates (see Fig. 9.7). In contrast, shear-thinning trends essentially replicate those under FENE-P but slightly earlier than observed for the LPTT and FENE-P model behaviour. Notably again, between FENE-P and EPTT N_1-solutions, there are large and *significant effects due to strain-softening impacting on N_1*. Here, maxima in FENE-P are now *three-times* larger than with

EPTT flow (ratio 3:1). Note in addition on FENE models alone, that N_1-levels also reduce by a factor of about one-third between FENE-CR to FENE-P, attributable again to thinning influence (as extensional properties are replicated in this comparison).

Significant features are further observed in the τ_{yy} and τ_{xy} stress fields of Fig. 9.10b, where EPTT solutions reach larger stressing-levels than those extracted under FENE-P flow. Notably, critical EPTT elasticity solution levels reached lie around We=0.1[1]. The level and positioning of τ_{yy}, around the contact-point/wetting-line zone, indicate the relative strength and impact of N_2-effects (biaxial cross-stream stretching of the coating fluid), as dependent upon the fluid-coating rheology and its bearing on the overall reverse roll coating process itself. In all these *FENE-solutions*, it is conspicuous that N_2 influence versus that of N_1, is about *fifty percent less*. In stark contrast, the trend is completely opposite under all *PTT solutions* and irrespective of softening presence, generating a *relative increase of twenty-five percent* from N_1 to N_2-levels. Moreover, softening itself also plays a role here in LPTT to EPTT normal-stressing levels, being responsible for some twenty percent reductions; hence, evidence of being within the high strain-regime, where softening has an impact.

Much of the explanation for these findings may be exposed by switching to comparison over shear (τ_{xy}) stress fields, between FENE-CR of Fig. 9.10a to FENE-P of Fig. 9.10b. From this, one may gather the strong impact that shear-thinning has imposed on FENE-P solutions (which also, has a knock-on effect on τ_{yy}–maxima). As one might anticipate, such shear-thinning influence is much less prominent in the comparison between LPTT and EPTT solutions, as both these models support this property. Moreover, it is conspicuous that both τ_{xy} and τ_{yy}–maxima for FENE-P show reduction from those of EPTT.

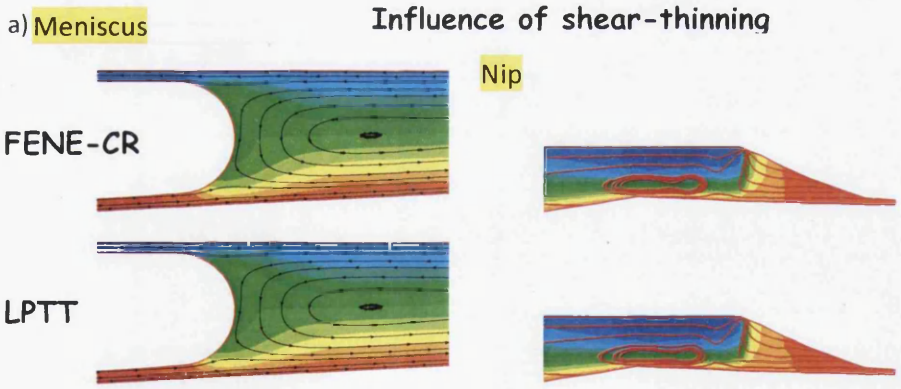

[1] We_{crit}=0.1 for EPTT is notably, much reduced over simple viscometric flows; or yet, even under complex mixed shear-extensional flows at lower deformation-rates than exposed here in these non-industrial flows.

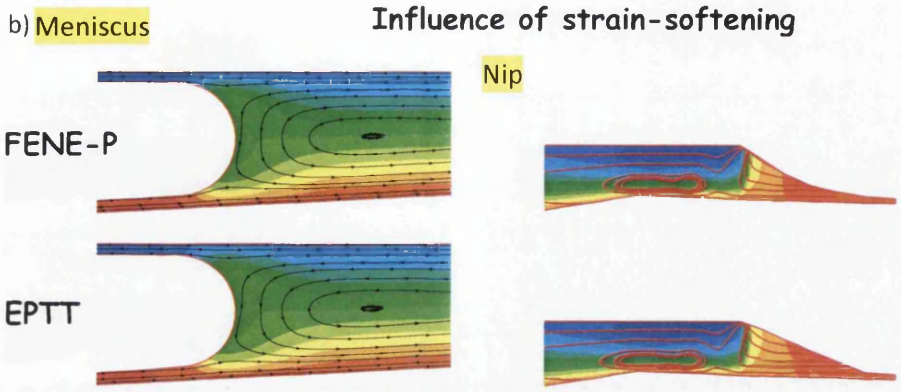

Figure 9.8: Meniscus and nip vortex developments, $\beta = 0.9$, We = 0.1

a) Influence of shear-thinning, (FENE-CR, $\tau_L = 5$, LPTT, $\varepsilon = 0.042$)

b) Influence of strain softening, (FENE-P, $\tau_L = 5$, EPTT, $\varepsilon = 0.042$)

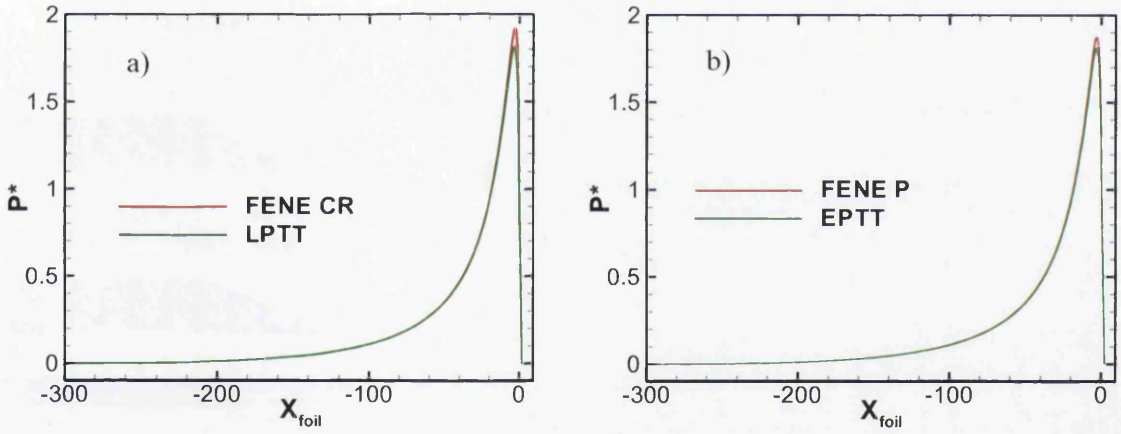

Figure 9.9: Pressure profiles, $\beta = 0.9$, We = 0.1

a) Influence of shear-thinning, (FENE-CR, $\tau_L = 5$, LPTT, $\varepsilon = 0.042$)

b) Influence of strain softening, (FENE-P, $\tau_L = 5$, EPTT, $\varepsilon = 0.042$)

a) Influence of shear-thinning

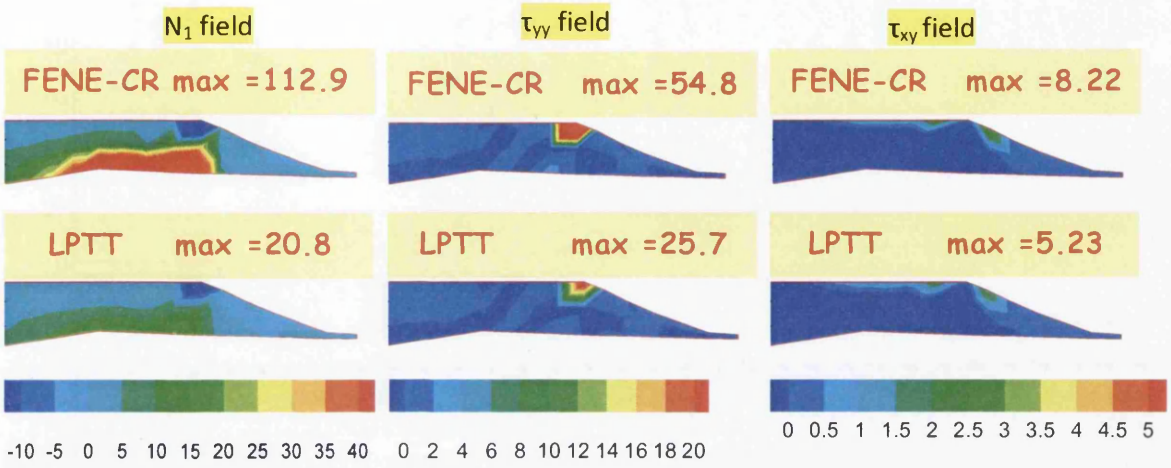

b) Influence of strain-softening

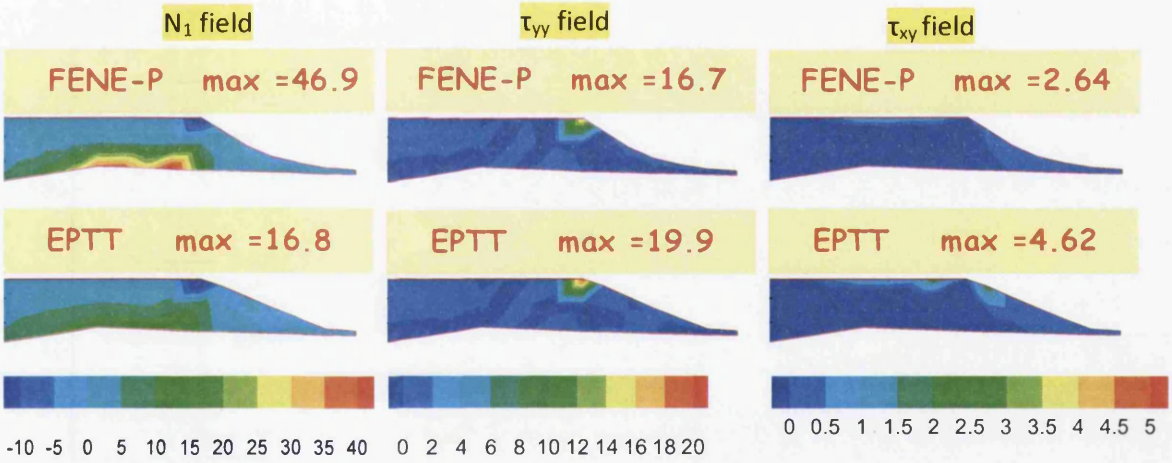

Figure 9.10: N_1, τ_{yy} and shear stress nip development ($\beta = 0.9$), We = 0.1

a) Influence of shear-thinning, (FENE-CR, $\tau_L = 5$, LPTT, $\varepsilon = 0.042$)

b) Influence of strain-softening, (FENE-P, $\tau_L = 5$, EPTT, $\varepsilon = 0.042$)

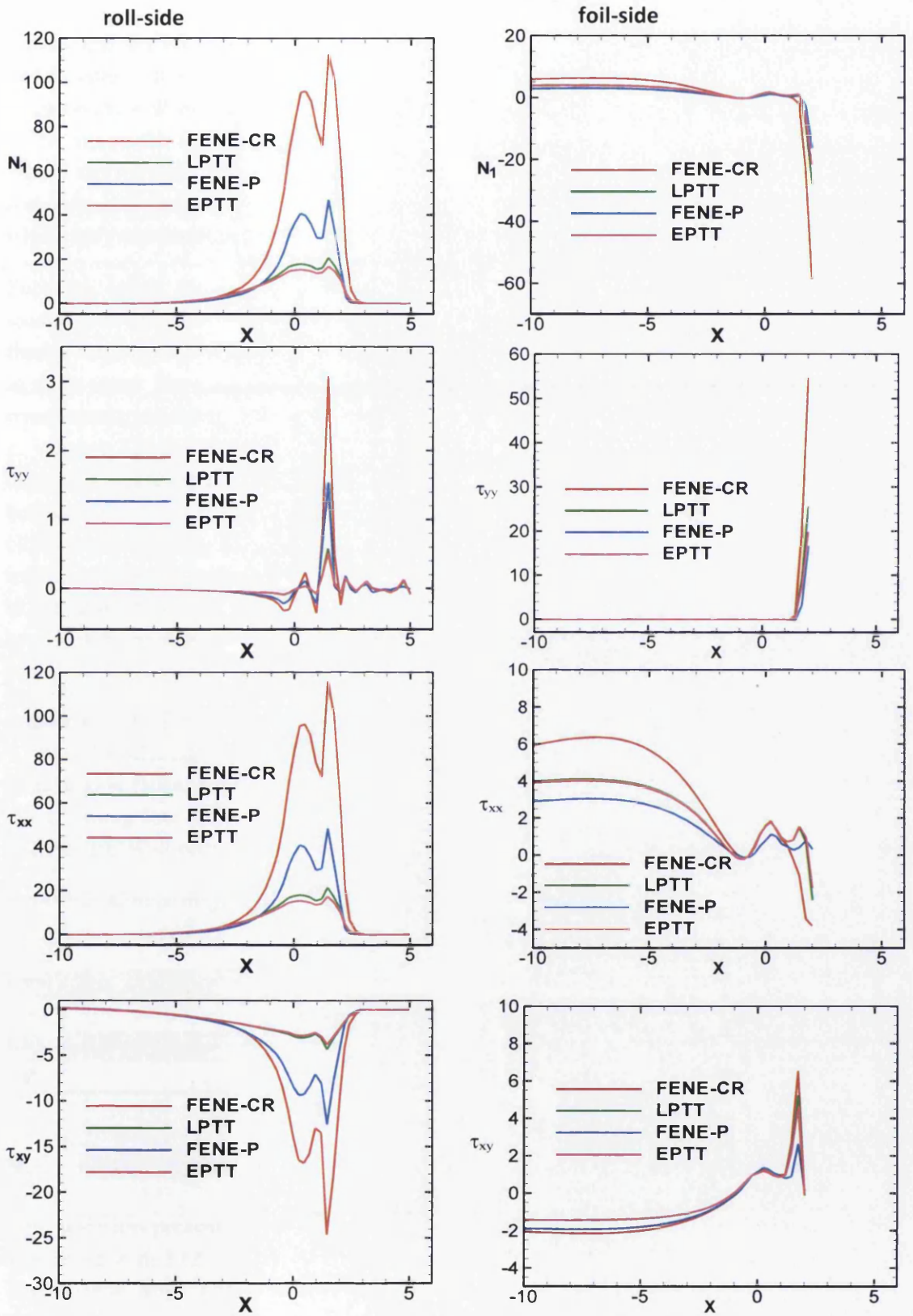

Figure 9.11: N_1, τ_{yy}, τ_{xx} and τ_{xy} nip profiles ($\beta = 0.9$), We = 0.1, FENE($\tau_L = 5$), PTT($\varepsilon = 0.042$)

Finally and for all models, quantitative and local comparison on N_1 ($=\tau_{xx}-\tau_{yy}$), τ_{xx}, τ_{yy} (N_2) and τ_{xy} (shear-stress) profiles is achieved in Fig. 9.11. Overall: (i) normal stressing is *twice as large on the roll-side than that on the foil-side*; (ii) this is more concentrated in peak-values to the nip on the foil-side, being more distributed over a wider roll-surface region about the nip on the roll-side; (iii) *N_2 dominates in N_1 on the foil-side, and τ_{xx} dominates in N_1 on the roll-side*; (iv) absolute shear stress maxima is one-quarter of normal stress on the roll-side, whilst only one-tenth on the foil-side.

Focusing solely on roll-side results and considered in rising order, N_1 and τ_{xx}, EPTT-solutions reveal the lowest peak levels, followed by those for LPTT, then FENE-P, and finally the largest in FENE-CR. This pattern and relative proportional rise is also replicated in shear stress. Here, sustained strain-hardening FENE solutions strongly dominate their PTT counterparts; doubling in value to FENE-P levels (with shear-thinning present), and tripling in value to FENE-CR levels (without shear-thinning). Hence, extensional deformation has a dominant influence on the roll-side. It is also noted that there is a distinction in response between the two models of FENE-P and LPTT, which share common hardening response and close shear-thinning. Moreover, the close levels of LPTT and EPTT, indicate the marginal influence of strain-softening, present under EPTT; and just how miniscule this is in contrast to the more dominant hardening influence. The consistently lower viscometric N_1 for PTT over FENE versions, also leads to their distinct differences in levels here too.

In contrast on the foil-side, peak N_1-levels (remarkably - totally dominated by N_2) are much greater for FENE-CR (by 2.5 times), than with any of the other three shear-thinning model versions: declining in the order of LPTT, EPTT and FENE-P results. Hence, shear deformation (shear-thinning) has a dominant influence on the foil-side around the contact-point/wetting-line zone. Note that, the most extreme reduction in this respect is associated with the FENE-P result.

Table 9.2: Comparing stress maxima values for all models

Model	**Max. N_1**	**Max. τ_{yy}**	**Max. τ_{xy}**
FENE-CR	112.9	54.8	8.22
LPTT	20.8	25.7	5.23
FENE-P	46.9	16.7	2.64
EPTT	16.8	19.9	4.62

9.6 Outcomes-overview

This study has presented an investigation for reverse roller coating viscoelastic flow, primary concerned with FENE-based modelling, but with extended consideration to PTT solutions. The reverse roller coating problem is one that manifests industrial levels of shear and

extensional deformation, for which modest levels of elastic solution are anticipated. Under the FENE class, numerical solutions have been extracted under both stress tensor and configuration tensor forms. Under this variable transformation, the configuration tensor form has proven itself to reflect superior numerical evolution properties, as was originally intended, which in turn render numerical solutions tractable to impressively larger critical elasticity states. The study has been divided into separate phases: initially, FENE-CR solutions were compared and contrasted between stress and configuration tensor form, analysing the effects of increasing elasticity up to critical states. Configuration tensor solutions reached We=11, whilst stress tensor forms only attained the much more modest level of We=0.4, under identical parameter settings of (β=0.9 and L=5.0). Then influence of level of extensibility were observed for L parameter value (L=10) and high solvent flow (β =0.9). Here much lower elasticity levels were attained at We = 2.8. And highly polymeric mobile flows were simulated, also for high and low level of extensibility (L =5 and 3). In contrast to the constant shear viscosity FENE-CR flows, shear thinning FENE-P flows were simulated to match same level of extensibility as in FENE-CR flows and to study the influence of shear-thinning and level of extensibility. Critical elasticity states attained were observed to be much lower at We = 1.6 for L parameter (L=10) than that seen for the FENE-CR flow at We = 2.8. Highly polymeric FENE-P flows were also introduced with enhanced shear-thinning, where significant influences are observed with regards to critical states, reduced peak pressure levels and simulated and extending vortex structures.

Subsequently, FENE model solutions have been compared against those for PTT models, to positively shed light on segregated shear-thinning and strain-softening influences within the process. Both shear-thinning and strain-softening, stimulate vortices and destabilise the flow around the wetting region, leading to an overall increase in quantity of leakage flow. Overall, viscoelasticity effects are found to expand vortices, as the meniscus itself deforms with the moving boundaries. Shear-thinning and strain-softening properties, on the other hand, stimulate vortex growth, where vortices grow into and across the nip zone, ultimately to merge with the meniscus vortex, becoming one large momentum-transfer mode.

In terms of peak pressure levels observed at the nip, shear-thinning is roughly twice as strong a reducing influence on peak-pressures, than that attributable to strain-softening. Comparing the various solutions generated, one may conclude that maxima in pressure (restrained to the nip-zones), is directly linked with viscosity levels. This is evidenced by shear-thinning fluids, which generate lower peak-pressure levels than observed with constant shear-viscosity fluids. Likewise regarding extensional properties, strain-softening fluids tend to lower peak-pressure levels over their strain-hardening counterparts.

Overall, normal stressing is *twice as large (shear stress quadruples) on the roll-side against that on the foil-side*; *N_2 dominates in N_1 on the foil-side, and τ_{xx} dominates in N_1 on the roll-side.* Hence, shear deformation (shear-thinning) has a dominant influence on the foil-side around the contact-point/wetting-line zone.

Chapter 10

Concluding remarks

This final chapter provides an overview and general summary to the body of research undertaken with addition suggestions for fruitful lines to follow in future work. The achievements of this study are presented and the logic behind the analysis is discussed and clarified. All main aims and objectives have been accomplished, for which the solution fields produced are in excellent agreement with theoretical hypothesis and experimental evidence. Employing various coating material through a reverse roll coating application, it has been shown how the dynamics of the flow influences the coating process. As such, the major achievements of this work lie in the understanding of the rheological properties of coating flows and their influence on the manufacturing process in actual operation. The material model approximations implemented are those of Newtonian, inelastic and viscoelastic type. The process has been modeled numerically extending a finite element based algorithm to incorporate free surface treatment of the meniscus and wetting lines. The computational technique appeals to semi-implicit Taylor-Galerkin methodology. Under viscoelasticity, appeal has been made to a finite volume technique to represent stress solution, from which a hybrid finite element-finite volume method has emerged. The algorithm has been validated and shown to lie in excellent agreement with both counterpart numerical solutions and experimental data. As such, this predictive technology provides an effective tool for the computational modeling of reverse roll coating applications. Initially, the studies focused on

a related two dimensional combined and separating flow configuration, using Newtonian fluids and introducing yield stress concepts (see chapter 5). This problem was deemed suitable to mimic the reverse roll coating application, yet without the inclusion of free surfaces, it provided a suitable starting point for validation of the numerical method and introduction to the numerical aspects of such flow problems. In the study phases to follow, several constitutive equations were considered to define the rheology of the coating fluid, including viscous inelastic and viscoelastic PTT and FENE class of models.

The research has been divided into distinct phases to aid in the understanding of the aims and objectives of the work. Chapter 2 introduces the fundamental principles of fluid mechanics, highlighting the basic assumptions taken in the computational approximation of such an industrial flow process. In particular, the research considers the application of the process to the solution of non-Newtonian flows. To achieve this, several constitutive equations have been pursued to model the rheological response of the coating material and to facilitate this, it is helpful to attempt flow classification. The rheological properties of suitable coating flows are introduced and studied in chapter 3. The numerical algorithm incorporates a free surface technique to address the problem requirements of coating flows, as described in chapter 4.

In this context, the first problem and flow domain considered was that of the combined-separating flow configuration, with viscous, inelastic and viscoplastic materials. This problem was one of a planar Poisuielle unidirectional and reversing flow, into and out of a channel with a flow splitting partition and a central gap in the partition. This benchmark problem was chosen to mimic the flow reversal of reverse roll coating, and findings were taken in comparison against previous numerical and experimental data. This study provided the necessary insight into the numerical solution of such flows before progressing to more complex reverse roll coating flows. The results were found to lie in excellent agreement with comparable studies reported in literature. A Herschel-Bulkley fluid model was applied, with a power-law model and a yield stress approximation. Unyielded power law solutions were found to stimulate vortices with increased shear-thinning. Whereas for Bingham model solutions, higher levels of inertia were required to obtain the same level of vortex formation as observed under shear-thinning. Under Herschel-Bulkley modeling, and at larger yield stress levels, vortices were eliminated with the appearance of unyielded regions.

In chapter 6, the reverse roll coating application was investigated, for which several pressure relief mechanisms have been identified. Here, viscous and inelastic materials were utilised to model the coating material rheology and several process operating conditions were analysed: including speed ratio, nip-gap, slip conditions and elastohydrodynamic effects. For such viscous material approximations, and with increasing foil speed, some degree of meniscus deformation was observed in the direction of the moving foil. As the nip-gap size was reduced, peak pressure levels increased accordingly, followed by associated levels of lift. At this stage and whilst avoiding wetting line inclusion, slip conditions were investigated to predict the influence of wetting on peak pressures at the nip region. Observations accordingly, have revealed a reduction in localized peak pressure levels at this nip region. An elastomer rubber cover on the roller was also implemented (in both static and dynamic modes of implementation), accounting for both with positive and negative nip-gaps. Findings have

shown oscillations in pressure around the nip zone; the lower the elastic constant (greater hardness) of the rubber covers, the larger the displacement observed.

Subsequently for the RRC application, a wetting line region was introduced into the problem approximation in Chapter 6. Then, viscous inelastic materials were studied, suitable for some paints, under surface tension considerations and different process conditions. The RRC domain consists of both shear and extension-dominated regions; therefore a generalized Newtonian model was initially employed. The corresponding flow problems were solved numerically and process operation and instabilities analysed. The flow around the nip realized a localized region of high shear rate influence. The material functions indicate the general description of such flows and their distributions throughout the domain demonstrate this fact. Under surface tension, a stagnation zone is observed around the contact point. Inelastic fluids, such as those governed by the power-law model, of constant thinning form in the power-law regime, have the propensity to eliminate this nip-region recirculation and also of lowering peak pressure levels.

With a keen interest in non-Newtonian fluid mechanics, attention was turned towards viscoelastic solutions and complex RRC flow, with highly elastic coating liquids (polymeric paint constituents). For this purpose, material modeling was switched to viscoelastic representation, where memory effects and normal stress influences may be analysed. Appeal has been made to PTT models, to identify the influence of increasing elasticity (We-variation), covering a number of instances of high-solvent and highly-mobile polymeric fluids. The first such model adopted was that of the EPTT (exponential) model, with shear-thinning and strain-softening behaviour at high extension rates. Different strain-softening levels were compared and contrasted for various solvent fractions. Solutions fields attained critical elasticity states in the range of We=0.5. Such a critical We-state becomes much less for highly polymeric mobile solutions. Notably, localized peak pressure levels have been observed to decline with increasing elasticity due to the increase in the rate of softening. A second PTT model variant employed is that of the LPTT (linear) model, which supports shear-thinning and sustained strain-hardening properties. Herewith, pressure levels are observed to rise with increasing elasticity, in contrast to findings with the counterpart strain-softening EPTT model – hence, exposing the dependence upon sustained strain-hardening properties. At high solvent fractions, critical We-states attained were larger for LPTT-solutions in the range of 2.0; whereas for highly polymeric fluids, EPTT fluids were considerably easier to solve computationally, and reached larger critical We-states than for their LPTT counterparts.

In yet other attempts to reach higher elasticity levels, FENE constitutive equations have also been employed to model the coating material, specifically, in FENE-CR and FENE-P form. Different variable-forms of FENE-CR utilized include a stress tensor form and a configuration tensor form. The stress tensor form attained similar critical elasticity levels as those reached for the PTT models (also of stress tensor form), whereas the configuration form was found to be superior in numerical stability, and as such reached higher elasticity states up to We=11. Numerical solutions obtained with the FENE-CR model, reveal a rise in localized peak pressure levels with increasing elasticity, due to sustained strain-hardening effects. Although the FENE-CR model displays a constant shear viscosity (as with

Newtonian approximation), critical stress states are observed to be much higher than all other models investigated (FENE-P and PTT). In contrast, the FENE-P model possesses shear-thinning and sustained strain-hardening effects. The FENE construct equations realize a configuration tensor form, and it is under this variable form, that they are capable of reaching higher elasticity levels at high solvent fraction. In relative terms and for highly polymeric mobile solutions, the critical levels of elasticity reduced due to increased shear-thinning. Yet, peak pressure levels attained were much lower than those gathered under FENE-CR solutions.

When FENE-CR(A_L=5) and LPTT(ε=0.042) solutions are compared and contrasted for high-solvent fraction mobile solutions (β=0.9), both in stress tensor form, the main rheological differences lie in the constant shear viscosity behaviour of FENE-CR and shear-thinning effects of LPTT. Here, FENE-CR solutions attain a critical elasticity level of We=0.4, whereas LPTT only reaches the modest critical elasticity level of We=0.1. Observations reveal that shear-thinning fluids are much more complex to solve for under RRC flow configuration, and hence, reach much lower We-critical levels than apparent for constant shear viscosity fluids. In contrast, FENE-P(A_L =5) and EPTT(ε =0.042) solutions are compared to reveal the influence of strain-softening, Both shear-thinning ad strain softening, stimulates vortices and destabilises the flow around the wetting region leading to an overall increase in leakage flow. In terms of peak pressure levels observed at the nip, shear-thinning is roughly twice as strong a reducing influence on peak-pressures, than that attributable to strain-softening.

From the corresponding numerical results derived, the following general conclusions are highlighted below for the reverse roll coating process operation:

- Shear-thinning fluids at the nip region, eliminates vortices
- Under surface tension, stagnation is observed around the contact point
- Peak pressure levels directly relates to viscosity levels
- Increasing strain-rate increases pressure-levels for hardening fluids and reduces pressure-levels for softening fluids
- Under uniaxial extension, critical elasticity levels are considerably higher for shear-thinning fluids, whereas for planar extensional flows observed herein, higher critical elasticity levels are much more difficult to attain with higher levels of shear-thinning.

Overall, the flow of coating fluids through an industrial reverse roll-coating application represents a grand rheological challenge which necessitates suitable process operation, its proper description and control of the flow properties. To this end, the solvent and polymer model described herein predicts an ideal model amenable to practical studies. They provide close intelligent predictive tool for industrial processes. The novelty of the work lies in the treatment of the dynamic contact point to avoid starvation of the nip in a reverse roll coating process. Also previous research studies have experimentally examined different polymer solutions, and recently, Zevallos has presented findings on forward roll coating with FENE-P models. In the current work, viscoelastic models are analysed in a general manner, in their application to reverse roll coating flow, when considering rheological variation of the coating fluids and analysis of such influences on the process operation. In the case of inelastic

approximation, shear-thinning stimulates vortices. For viscoelasticity, strain-softening and hardening also stimulate vortices and stretching of the polymeric fluid. Significant τ_{yy} effects on the contact foil-side have been observed for extension flows which reveal a novel and important aspect of the industrial reverse roll coating process. Furthermore, shear-thinning fluids have been observed to influence the levels of τ_{yy} attained at this contact foil-side region, and therefore, reduce its peak. Normal stressing is *twice as large on the roll-side than on the foil-side*; *N_2 dominates in N_1 on the foil-side, and τ_{xx} dominates in N_1 on the roll-side.* Hence, shear deformation (shear-thinning) has a dominant influence on the foil-side around the contact-point/wetting-line zone. At the same time, this research also demonstrates the stimulation and consequences of biaxial extension.

Having analysed the rheological properties of coating flows and its influences on the process operation, further attention may now be focused on other pressing problem issues, viz:

- More complex modeling of an elastomer covered roll and its influence on the flow dynamics at the nip and contact region (say under viscoelasticity)
- Analysing the effects of complex rheological properties such as, under White-Metzner and/or pom-pom modeling, suitable to match a typical industrial coating
- Three dimensional flow simulation studies
- Three-roll system modeling in two or three dimensions
- Wet-film weight prediction
- Wetting and /or peeling effects of the dynamic contact region

References

Abdali, S.S., Mitsoulis, E., Markatos, N.C.,
Entry and exit flows of Bingham fluids
J. Rheol. 36(2), 389–407.T.C. (1992)

Aboubacar M, Webster MF.,
A cell-vertex finite volume/element method on triangles for abrupt contraction viscoelastic flows
J. Non-Newtonian Fluid Mech. 106, 98:83 (2001)

Aboubacar, M., Aguayo, J.P., Phillips, P.M., Phillips, T.N., Tamaddon-Jahromi, H.R., Snigerev, B.A., Webster, M.F.,
Modelling pom-pom type models with high-order finite volume schemes
J. Non-Newtonian Fluid Mech. 126, 207–220 (2005)

Afonso, A. M., Alves, M. A., Poole, R. J., Oliveira, P. J., Pinho, F. T. ,
Viscoelastic flows in mixing-separating cells
J. Eng. Math. 71, 3–13 (2011)

Alexandrou, A. N., Le Menn, P.,
Flow instabilities of Herschel-Bulkley fluids
J. Non-Newtonian Fluid Mech 116(1), 19-32 (2003)

Alexandrou, A. N., Mcgilvreay, T.M., Burgos, G.,
Steady Herschel–Bulkley fluid flow in three-dimensional expansions
J. Non-Newtonian Fluid Mech. 100, 77–96 (2001)

Al-Muslimawi, A., Tamaddon-Jahromi, H.R., Webster, M.F.,
Simulation of Viscoelastic and Viscoelastoplastic Die-swell Flows
Journal of Non-Newtonian Fluid Mechanics, 191, 45-56, (2013)

Ascanio G, Carreau PJ, Brito-De La Fuente E, Tanguy PA.,
Forward Deformable Roll Coating at High Speed with Newtonian Fluids
Chem. Eng. Res. Design. 82, 390-397 (2004)

Ascanio, G., Carreau, P.J., Tanguy, P.A.,
High speed roll coating with complex rheology fluids
Experimental in fluids, Vol. 40, 1-14, (2006a)

Ascanio G, Ruiz G.,
Measurement of pressure distribution in a deformable nip of counter-rotating rolls. Measure
Sci. Tech. 17, 2430-2436 (2006b)

Ashmore, J., Shen, A., Kavehpour, H., Stone H., McKinley, G.,
Coating flows of non-Newtonian fluids; weakly and strongly elastic limits
J. Eng Math. 60: 17-41 (2008)

Baloch, A., Townsend, P., Webster, M.F.,
On two and three dimensional expansion flows
Comp. Fluids, 24(8), 863-882 (1995)

Baloch, A., Townsend, P., Webster, M.F.,
On the Simulation of Highly elastic complex flows
J. Non-Newtonian Fluid Mech. 59 111 – 128 (1995)

Baloch, A.,
Numerical Simulation of Complex Flows of Non-Newtonian Fluids
Ph.D. Thesis, University of Wales, Swansea, (1994)

Barrett, J.W., Morton, K.W.,
Approximate symmetrisation and Petrov-Galerkin methods for diffusion-convection problems
Comp. Meth. Appl. Mech. Eng., 45, 97-122, (1984)

Barnes, H.A., Hutton, J.F., Walters, K.,
An Introduction to rheology
Elsevier, Amsterdam (1989)

Barnes, H.A.,
Handbook of Elementary Rheology
INNFM (2000)

Belblidia F, Matallah H, Puangkird B, Webster MF.,
Alternative subcell discretisations for viscoelastic flow: Stress interpolation
J. Non-Newtonian Fluid Mech. 146, 59-78 (2007)

Belblidia, F., Tamaddon-Jahromi, H.R., Echendu, S.O.S., Webster, M.F.,
Reverse roll Coating Flow: A computational investigation towards high speed defect free coating
Mechanics of Time-dependent Material (accepted for publication 2012).

Benkreira, H., Edwards, M.F., Wilkinson, W.L.,
Roll coating of purely viscous liquid
Chem. Eng. Sci., Vol. 36, 429-434, (1981)

Benkreira, H., Edwards, M.F., Wilkinson, W.L.,
Ribbing instabilities in the roll coating of Newtonian fluid
Plastic rubber Process Application, Vol. 2, 137-144, (1982a)

Benkreira H, Edwards MF, Wilkinson WL.,
Mathematical modelling of the reverse and metering roll coating flow of Newtonian fluids
Chem. Eng. Sci. 37, 277-282 (1982b)

Benkreira H, Patel R, Edwards M.F., Wilkinson W.L.,
Classification and analyses of coating flows
J. Non-Newtonian Fluid Mech. 54, 437-447 (1994)

Benkreira, H.,
Dynamic wetting in metering and pre-metered forward roll coating
Chem. Eng. Sci., Vol. 57, 3025-3032, (2002a)

Benkreira, H.,
Experimental study of dynamic wetting line reverse roll coating
*AI*ChEJ., Vol. 48, 221-226, (2002b)

Benkreira H, Khan M.I.,
Air entrainment in dip coating under reduced air pressures
Chem. Eng. Sci. 63, 448-459 (2008)

Benkreira H, Ikin J.B.,
Dynamic wetting and gas viscosity effects
Chemical Engineering Science 65, 1790–1796 (2010)

Benque, J.P., Labadie, G., Ronat, J.,
A new finite element method for the Navier-Stokes equations coupled with a temperature equation
Proc. 4th Int. Conf. Finite Element Methods in Flow Problems, Eds. Tadahiko K, 295-301, (1982)

Bingham, E.C.,
Fluidity and plasticity
McGraw-Hill, New York (1992)

Bird, R.B., Dai, G.C., Yarusso, B.J.,
The rheology and flow of viscoplastic materials
Rev. Chem. Eng., 1, 1-70 (1983)

Bird, R.B., Armstrong, R.C. and Hassager, O.,
Dynamics of polymeric liquids: fluid Mechanics
John Wiley and Sons, New York. 2nd Edition, Vol. 1, (1987)

Brooks, A.N., Hughes, T.J.R,
Streamline upwind Petrov-Galerkin formulations for convection dominated flows with particular emphasis on the incompressible Navier-Stokes equations
Comp. Meth. Appl. Mech. Eng., 32, 199-259, (1982)

Carew, E.O., Townsend, P., Webster, M.F.,
A Taylor-Petrov-Galerkin algorithm for viscoelastic flow
J. Non-Newtonian Fluid Mech., 50, 253-287 (1993)

Carew, E.O., Townsend, P. and Webster, M.F.,
Taylor-Galerkin algorithm for viscoelastic flow; Application to a model problem
Num. Meth. PDE, John Wiley and Sons, Inc., 10, 171-190. (1994)

Carew, E.O.A., Townsend, P., Webster, M.F.,
On a discontinuity capturing technique for Oldroyd-B fluids
J. Non-Newtonian Fluid Mech., 51, 231-238 (1994)

Carvalho, M.S., Scriven, L.E., Anderson, T.J.,
Ribbing instability in forward deformable roll coating
Coating conference-TAPPI, 99-104, (1994)

Carvalho, M.S., Scriven, L.E.,
Capillary and viscoelastic effects on elastohydrodynamic lubrication in roller
J Tribo-trans., ASME, Vol. 118, (4) 872, (1996)

Carvalho, M.S., Scriven, L.E.,
Deformable roll coating flows: steady state and linear perturbation analysis
J. Fluid Mech. **339**, 143-172 (1997a)

Carvalho, M.S., Scriven, L.E.,
Multiple States of a Viscous Free-surface Flow: Transition from pre-metered to a metering flow
Int. J. Num. Meth. Fluids, vol.24: 813-831 (1997b)

Casson, N.,
Rheology of disperse systems
Ed. C.C. Mill, Pergamon Press, Oxford (1959)

Chandio, M.S., Matallah, H., Webster, M.F.,
Numerical Simulation of Viscous Filament Stretching Flows
Int. J. Num. Meth. Heat Fluid Flow 13, 899-930 (2003)

Chandio M.S, Webster M.F.,
Numerical Simulation for Reverse Roller-Coating with Free-surfaces
ECCOMAS proceedings, Computational Fluid Dynamics Conference, 4-7 Sept., Swansea, UK, (2001)

Chandio, M.S., Webster M.F.,
Numerical Study of Transient Instabilities in Reverse Roller Coating Flows
Int. J. Num. Meth. Heat Fluid Flow, Vol. 4, 375-403, (2002a)

Chandio, M.S., Webster M.F.,
Numerical Simulation for Viscous Free-surface Flows for Reverse Roller-Coating
Int. J. Num. Meth. Heat Fluid Flow, Vol. 4, 434-457, (2002b)

Chandio, M.S., Webster, M.F.,
Numerical simulation for viscous free surface flows for reverse roller-coating
Int. J. Numerical methods in heat and fluid flow 12, 434 (2002c)

Chhabra, R.P., Richardson, J.F.,
Liquid mixing, Non-Newtonian Flow in Process Industries
Butterworth-Heinemann, Oxford, 324–391 (1999)

Chilcott, M.D., Rallison, J.M.,
Creeping flow of dilute polymer solutions past cylinders and spheres
Journal of Non-Newtonian Fluid Mechanics 29, 381-432, (1988)

Chorin, A.J.,
Numerical solution of the Navier-Stokes equations
Mathematics of computation 22, 745-762, (1968)

Clough, R.W.,
The finite element method in plane stress analysis
Proceedings of the secon ASCE Conference on electronic conputation (1960)

Cochrane, T., Walters, K., Webster, M. F.,
On Newtonian and non-Newtonian flow in complex geometries
Philosophical Transactions of the Royal Society A, 301, 163–181 (1981)

Cohu, O., Magnin, A.,
Experimental investigations on roll coating with deformable rolls: The mechanics of thin film coatings
Proceedings of First European Symposium, 179-188, (1995a)

Cohu, O., Magnin, A.,
Rheometry of paints with regard to roll coating process
Journal of Rheology, Vol. 39, (4) 785-797, (1995b)

Cohu, O., Magnin, A.,
Forward roll coating of Newtonian fluids with deformable rolls: an experimental investigation
Chemical Engineering Science, Vol. 52, (8) 1339-1347 (1997)

Courant, R.,
Variation Methods for the solutions of Problems of Equilibrium and Vibration
Bull. Am. Math. Sol., Vol. 49, (1943)

Coyle, D.J., Macosko, C.W., Scriven, L.E.,
Film splitting flows of shear-thinning liquids in forward roll coating
AIChEI, Vol. 33, (5) 741-746, (1987)

Coyle, D.J.,
Linear squeeze theory of deformable roll coating
AIChE spring National Meeting, Orlando, (1990)

Coyle D.J., Macosko C.W., Scriven L.E.,
The fluid dynamics of reverse roll coating
AIChE J; 36, 161-174 (1990b)

Coyle D.J., Macosko C.W., Scriven L.E.,
Reverse roll coating of non-Newtonian liquids
J. Rheology. 34, 615-636 (1990c)

Crotchet, M.J., Keunings, R.,
Finite element analysis of die swell of a highly elastic fluid
Journal of non-Newtonian Fluid Mechanics, 10, 339-356 (1982)

Crotchet, M.J., Davies, A.R. and Walters, K.,
Numerical Simulation of Non-Newtonian Flow
Rheology series, 1, Elsevier Sci. Pub, Amsterdam. (1984)

Cross, M.,
Rheology of non-Newtonian fluids: a new flow equation for pseudoplastic systems
Journal of colloidal science, 20, 417-437 (1965)

Donea, J.,
A Taylor-Galerkin method for convective transport problems
Int. J. Num. Meth., 20, 101-119, (1984)

Douglas, J., Russel, T.F.,
Numerical methods for convection dominated problems based on combining the method of characteristics with finite element or finite difference procedures
SIAM J. Num. Anal., 19, 871-885, (1982)

Echendu, S.O.S., Belblidia, F., Tamaddon-Jahromi, H.R., Webster, M.F.,
Modelling with viscous and Visco-plastic materials under mixing and separating flow configurations
Mechanics of Time-dependent Materials, Vol. 15: 407-428 (2011)

Echendu, S.O.S., Thammaddon-Jahromi, H.R., Webster, M.F.,
Modelling reverse roll coating with dynamic wetting lines and inelastic material
Accepted for publication in Applied Rheology (2013)

Fernando R.H., Glass J.E.,
Dynamic Uniaxial Extensional Viscosity (DUEV) Effects in Roll Application II. Polymer Blend Studies
J. Rheology 32, 199-213 (1988)

Fourcade E., Bertrand F., Réglat O., Tanguy P.A.,
Finite element analysis of fluid--solid interaction in the metering nip of a metering size press
Comp. Meth. Appl. Mech. Eng 174, 235-245 (1999)

Fox, E.A., Gex, V.E.,
Single phase blending of liquids
A.I.Ch.E. J., vol. 2, 539–544 (1956)

Gaskell, P.H., Savage, M.D., Summers, J.L., Thompson, H.M.,
Modelling and analysis of meniscus roll coating
J. Fluid Mechanics Vol. 298: 113-137 (1995)

Gaskell P.H., Innes G.E., Savage MD.,
An experimental investigation of meniscus roll coating
J. Fluid Mech. 355, 17-44 (2000)

Gostling M.J., Savage M.D., Young A.E., Gaskell P.H.,
A model for deformable roll coating with negative gaps and incompressible compliant layers
J. Fluid Mech. 489, 155-184 (2003)

Graham, M.D.,
Interfacial hoop stress and instability of viscoelastic free surface flows
Physics fluids, 15, 1702-1710 (2003)

Greener, J., Middleman, S.,
A theory of roll coating of viscous and viscoelastic fluids
Polymer Engineering and Science, 15(1):1-10 (1975)

Hao Y., Haber S.,
Reverse roll coating flow
Int. J. Num. Meth. Fluids. 30, 635-652 (1999)

Hawken, D.M., Tamaddon-Jahromi, H.R., Townsend, P., and Webster, M.F.,
A Taylor Galerkin based algorithm for viscous incompressible flow
International Journal for numerical methods in fluids 10, 327-351 (1990)

Hawken, D.M., Townsend, P., Webster, M.F.,
A comparison of gradient recovery methods in finite-element calculations
Comm. Appl. Num. Meth., 7, 195-204, (1991)

Hernnikoff, A.,
Solution of Problems of Elasticity by the Frame-Work Method
ASME J. Appl. Mech. **8**, A619–A715, (1941)

Holland, F.A., Bragg, R.,
Fluid flow for chemical engineers
Edward Arnold, Second edition, (1995)

Hulsen, M.A.,
Some properties and analytical expressions for plane flow of Leonov and Giesekus models
J. Non-Newtonian Fluid Mech., 30, 85-92 (1988)

Hulsen, M.A.,
A sufficient condition for a positive definite configuration tensor in differential models
J. Non-Newtonian Fluid Mech., 38, 93-100(1990)

Jang, J. Y., Chen, P.Y.,
Reverse Roll Coating Flow with Non-Newtonian Fluids
Communications in Computational Physics, Vol. 6, No. 3, 536-552 (SCI &EI) (2009)

Jayanti, S.,
Hydrodynamics of jet mixing in vessels
Chem. Eng. Sci., vol. 56, 193–210 (2001)

Keshtiban, I.J., Bumroong, P., Tamaddon-Jahromi, H.R., Webster, M.F.,
Generalised approach for transient computation of start-up pressure-driven viscoelastic flow
J. Non- Newtonian Fluid Mech., vol 151, 2-20, (2008)

Lee, A.G., Shaqfeh, E.S.G., Khomami, B.,
A study of viscoelastic free surface flows by the finite element method: Hele–Shaw and slot coating flows
J. Non-Newtonian Fluid Mech., 108, 327–362 (2002)

Lopez, F.V., Rosen, M.,
Rheological effects in roll coating of paints
Latin America Applied Research, Vol. 32, 247-252, (2002a)

Lopez, F.V., Pauchard, L., Rosen, M., Rabaud, M.,
Non-Newtonian effects on ribbing instability
J. Non Newtonian Fluid Mechanics, Vol. 103, 123-139, (2002b)

Mackerle J.,
Coatings and surface modification technologies: a finite element bibliography (1995-2005)
Model. Simul. Mater. Sci. Eng. 13, 935-979 (2005)

Macosko, C.W.,
Rheology: principles, measurement and applications
Wiley-VCH Publisher, Inc., New York, (1994)

Marouche, M., Anne-Archard, D., Boisson, H.C.,
A numerical model of yield stress fluid in a mixing vessel
Applied Rheology, 12, 182–191 (2002)

Matallah, H., Townsend, P., Webster, M.F.,
Recovery and stress-splitting schemes for Viscoelastic flows
J. Non-Newtonian Fluid Mech., 75, 139-166, (1998)

Maxwell, J.C.,
On the dynamic theory of gases
Philosophical transactions Series I 157, 49-88, (1867)

Mmbaga J.P., Hayes R.E., Bertrand F.H., Tanguy P.A.,
Flow simulation in the nip of a rigid forward roll coater
Int. J. Num. Meth. Fluids. 48, 1041-1066 (2005)

Morrison, F.A.,
Understanding rheology
Oxford University Press, Inc., New York, (2001)

Mysels, K.J.,
Flow of thickened fluids
US Patent No. 2 492 173, December 27, (1949).

Nicosia, M.A.,
A planar finite element model of bolus containment in the oral cavity
Computers in Biology and Medicine, 37, 1472 – 1478 (2007)

Nicosia, M.A., Robbins, J.,
The fluid mechanics of bolus ejection from the oral cavity
Journal of Biomechanics, 34, 1537–1544 (2001)

Nicosia, M.A., Brasseaur, J.G.,
A Mathematical Model for Estimating Muscle Tension in vivo during Esophageal Bolus Transport
J. theor. Biol. 219, 235–255 (2002)

Ngamaramvaranggul, V.,
Numerical Simulation of Non-Newtonian Free-surafce flows
PhD. Thesis, University of Wales Swansea, Swansea, UK (2000)

Ngamaramvaranggul, V., Webster, M.F.,
Simulation of Pressure-Tooling Wire Coating Flow with Phan-Thien/Tanner Models
Int. J. Num. Meth. Fluids, vol 38, pp 677-710, (2002).

Oldroyd, J.G.,
On the formulation of rheological equations of state
Proc. Roy. Soc., A200, 523-541, (1950)

Owens, R.G., Philips, T.N.,
Computational Rheology
Imperial College Press, London, (2002).

Papanastasiou, T.C.,
Flow of materials with yield
Journal of Rheology, Vol 31, 385-404, (1987)

Peterlin, A.,
Hydrodynamics of macromolecules in a velocity field with longitudinal gradient
Journal of polymer science Part B: Polymer letters 4, 287-291 (1966)

Phan-Thien, N., Tanner, R.I.,
A new constitutive equation derived from network theory
J. Non-Newtonian Fluid Mechanics, Vol. 2, 353-365, (1977)

Phan-Thien, N.,
A non-linear network viscoelastic model
J. Rheology, Vol. 22, 259-283, (1978)

Phan-Thien, N.,
Influence of wall slip on extrudate swell: a boundary element investigation
J. Non-Newtonian Fluid Mechanics, Vol. 26, 327-340, (1988)

Raithby, G.D., Torrance, *K.E.,*
Upstream-weighted differencing schemes and their application to elliptic problems involving fluid
Comp. Fluids, 2, 191-206 (1974)

Ramaswamy, B.,
Numerical Simulation of Unsteady Viscous Free-surface Flow
J. Comp. Phys., Vol. 90: 396-430 (1990)

Ritz, W.,
Critical researches on general electrodynamics
Annales de Chimie et de Physique, Vol. 13, p145, (1908)

Rocha, G.N., Poole, R.J., Alves, M.A., Oliveira, P.J.,
On extensibility effects in the cross-slot flow bifurcation
J. Non-Newtonian Fluid Mech., 156, 58–69 (2009)

Rudman, M., Blackburn, H.M., Graham, L.J.W., Pullum, L.,
Turbulent pipe flow of shear-thinning fluids
J. Non-Newtonian Fluid Mech. 118(1), 33 – 48 (2004)

Savreux, F., Jay, P.,
Viscoplastic fluid mixing in a rotating tank
Chemical Engineering Science 62(8), 2290-2301 (2007)

Sendilkumar, K., Kalaichelvi, P., Perumalsamy, M., Arunagiri, A., Raja, T.,
Computational Fluid Dynamic Analysis of Mixing Characteristics inside a Jet Mixer for Newtonian and Non Newtonian Fluids
World Congress on Engineering and Computer Science, 120 – 128 (2007)

SHIODE, H., Tamal, H., Isaki, T.,
Flow simulations of dynamic wetting line at a reverse roller coater using VOFMethod
Journal of the society of Rheology Japan, Vol. 37, No. 2: 59 – 64 (2009)

Sizaire R., Legat V.,
Finite element simulation of a filament stretching extensional rheometer
J. Non-Newtonian Fluid Mech. 71, 89–107 (1997)

Struijs, R., Deconinck, H., Roe. P.L.,
Fluctuation splitting for the 2d Euler equations
Von Karman Institute for Fluid dynamics, Technical Report series (1990-01)

Sujatha, K.S., Matallah, H., Banaai, M.J., Webster, M.F.,
Computational predictions for viscoelastic filament stretching flows: ALE methods and free-surface techniques (CM and VOF)
J. Non-Newtonian Fluid Mech. 137, 81-102, (2006)

Tanner, R.I.,
Constitutive model for V11th Workshop on numerical computations in viscoelastic flows
Private Communication, (1989)

Tanner, R.I., Walters, K.,
Rheology: An historical perspective
Elsevier, Amsterdam; Oxford (1998)

Tanner, R.I.,
Engineering Rheology
Oxford University Press, Inc., New York (2000)

Tamaddon-Jahromi, H.R., Ding, D.P., Webster, M.F., Townsend, P.,
A Taylor Galerkin Finite Element Method for Non-Newtonian flows
Int. J. Num. Meth. Eng., 34, 741-757 (1992)

Tamaddon-Jahromi, H.R., Webster, M. F.,
Transient behaviour of branched polymer melts through planar abrupt and rounded contractions using pom–pom models
Mech. Time-Depend. Mater., 15: 181–211,(2011)

Temam, R.,
Sur L'approximation de la solution des equations de Navier-Stokes par la method des pas fractionnaires II
Archiv. Ration. Mech. Anal. 32, 377-385 (1969)

Tiu, C., Wang, L., Liu, T.J.,
Non-Newtonian effects of pre-metered reverse roll coating
J. Non-Newtonian Fluid Mech. 87: 247 (1999)

Toms, B.A.,
Some observations on the flow of linear polymer solutions through straight tubes at large Reynolds numbers
Proceedings of the international rheology congress, 135-142, (1948)

Townsend, P., Webster, M.F.,
An algorithm for the three-dimensional transient simulation of non-Newtonain fluid flows
G.E. Pande, J. Middleton, Int. Conf. Numerical method in Engineering; theory and applications – NUMETA 87, Kluwer, T12/11-11 (1987)

Triantafillopoulos N. G.,
Paper Coating Viscoelasticity and its Significance in Blade Coating
Atlanta, GA: TAPPI Press; (1996)

Van Kan, J.,
A second-order accurate pressure-correction scheme for viscous incompressible flow
SIAM. J. Sci. Stat. Comput., 7, 870-891 (1986)

Walters, K., Webster, M.F.,
On dominating elastic-viscous response in some complex flows
Philos. Trans. R. Soc. London, A308, 199-218 (1982)

Wapperom, P., Hulsen, M.A.,
A lower bound for the invariants of the configuration tensor for some well-known differential models
Journal of Non-Newtonian Fluid Mechanics, 60, 349-355 (1995)

Wapperom, P., Webster, M.F.,
A second-order hybrid finite-element/volume method for viscoelastic flows
Journal of Non-Newtonian Fluid mechanics 79, 405-431 (1998)

Wapperom, P., Webster M.F.,
Simulation for viscoelastic flow by a finite volume/element method
Comp. Meth. Appl. Mech. Eng. 180, 281-304 (1999)

Warner, H.R.,
Kinetic theory and rheology of dilute suspensions of finitely extendible dumbbells
Industrial and Engineering Chemistry fundamentals 11, 379-387 (1972)

Webster, M.F.,
A technique to solve incompressible non-Newtonian flow problems
Journal of Non-Newtonian Fluid Mechanics, 20, 227-240 (1986)

Webster, M.F., Tamaddon-Jahromi, H.R., Aboubacar, M.,
Time-dependent algorithms for viscoelastic flow-finite element/volume schemes
Numer. Meth. Part. Diff. Eqns. 121, 272-296, (2005)

Zevallos G.A., Carvalho M.S., Pasquali M.,
Forward roll coating flows of viscoelastic liquids
J. Non-Newtonian Fluid Mech. 130, 96-109 (2005)

Zienkiewicz, O.C., Taylor, **C.L.**,
The Finite Element Method: Basic formulation and Linear Problems
McGraw-Hill, London 4th Rev. Ed., 1, (1989)

Zhu, H., Kim, Y.D., De Kee, D.,
Non-Newtonian fluids with a yield stress
J. Non-Newtonian Fluid Mech, 129 (3), 177 – 181 (2005)

Zisis, Th., Mitsoulis, E.,
Viscoplastic flow around a cylinder kept between parallel plates
J. Non Newtonian Fluid Mech. 105, 1–20 (2002)

Publications

S. O. S. Echendu, F. Belblidia, H. R. Tamaddon-Jahromi, M. F. Webster, Modelling with viscous and viscoplastic materials under combining and separating flow configurations, Mechanics of Time-Dependent Materials (November 2011) Volume 15, Issue 4, pp 407-428

F. Belblidia, H. R. Tamaddon-Jahromi, **S. O. S. Echendu**, M. F. Webster, Reverse roll-coating flow: a computational investigation towards high-speed defect free coating, Mechanics of Time-Dependent Materials (January 2013)

Echendu, S.O.S., Tamaddon-Jahromi , H.R., Webster, M.F, Modelling Reverse Roll Coating flow with dynamic wetting lines and inelastic shear thinning fluids, Appl. Rheol. (2013) to be published

S.O.S. Echendu, H.R. Tamaddon-Jahromi, and M.F. Webster, Computation of Non-Newtonian Viscoelastic Phan-Thien Tanner Flow model in Reverse Roll coating with Dynamic Wetting Line, to be submitted

S.O.S. Echendu, H.R. Tamaddon-Jahromi, and M.F. Webster, Modelling Polymeric flows in Reverse Roll coating processes with Dynamic Wetting Lines, under preparation

S.O.S. Echendu, J.E. Lopez-Aguilar, H.R. Tamaddon-Jahromi and M.F. Webster, Elastohydrodynamic lubrication of the contact point on a Reverse Roll Coater through Hooke's model implementation and non-Newtonian fluids, under preparation